UNIVERSITY OF SOUTHAMPTON

FACULTY OF ENGINEERING AND PHYSICAL SCIENCES

Crop Systems Engineering

Enhancing the Study of Plant Root and Soil Interactions using Radiocontrast Agents in X-ray Computed Tomography Imaging

By

Callum Paul Scotson

Thesis for the degree of Doctor of Philosophy

February 2021

University of Southampton

Abstract

Faculty of Engineering and Physical Sciences

Crop Systems Engineering

Thesis for the degree of Doctor of Philosophy

Enhancing the Study of Plant Root and Soil Interactions using Radiocontrast Agents in X-ray Computed Tomography Imaging

Callum Paul Scotson

X-ray computed tomography (XCT) is a non-destructive 3D imaging technique now commonly employed for imaging plant and soil systems. In particular it is increasingly being utilised to capture plant root/ soil structures, in place of traditional destructive dissection techniques. One of the major challenges in the use of the technology is the similar X-ray attenuation characteristics of plant roots and soil-water which results in a low contrast to noise ratio between these materials – particularly when imaging larger soil samples. Where similar issues of poor contrast occur within biomedical imaging, these issues are overcome with the use of radiocontrast agents (solutions or suspensions containing elements with high X-ray attenuation characteristics). The aim of the research presented in this thesis is to investigate novel strategies for the application of various contrast agents in order to enhance the study of plant and soil structures and to then use contrast agents in innovative applications to capture the movement of solutes through soil and roots.

I begin with a review of the current literature, determining the key requirements of contrast agents for imaging biological tissues: minimal toxicity, low reactivity, stability and mobility. From this review of the literature I determined that nanoparticulate contrast agents are best suited to tissue specific accumulation as a functionalised contrast agent. However, the challenge in utilising nanoparticulate contrast agents for this role is the instability of nanoparticles in soil conditions. I also determine that non-ionic iodinated contrast agents are well suited to fluid flow tracing applications owing to their mobility, potential low viscosity and comparatively low reactivity with organic tissues.

In the first scientific research chapter, published as Scotson *et al.*, (2019), I present work in which we stabilised gold nanoparticles for use in soil environments using a polymer coating and demonstrate for the first time that high concentrations of nanoparticles are capable of producing contrast against soil in XCT. The second scientific chapter, published as Scotson *et al.*, (2020a), investigates the innovative use of an iodinated contrast agent as an XCT-visible analogue for field applied soluble-agrochemicals in order to trace the movement of solutes through flat or ridge and furrow soil surface geometries and assess the impact of surface ponding. We observe that plant roots can reduce the infiltration depth of solutes, though this effect is localised to likely root-dense regions, but that surface ponding can negate this - especially within furrows. In the final scientific chapter we present a manuscript, published as Scotson *et al.*, (2020b), in which we construct an original and novel experimental system to allow for application of contrast agents directly to *in vivo* plant roots in soil which is also compatible with synchrotron XCT imaging. Using a combination of synchrotron XCT imaging and synchrotron X-ray fluorescence mapping we are able to capture internal plant solute transport and visualise anatomical features. These represent significant advances in developing new techniques for using contrast agents in plant and soil studies and demonstrates the capacity for contrast agents to trace solute movement in soil and plant systems.

Table of Contents

List of Figures

List of Tables

Publications

First Author

Scotson, C. P., van Veelen, A., Williams, K. A., Koebernick, N., Fletcher, D. M., & Roose, T. (2020). Developing a system for in vivo imaging of maize roots containing iodinated contrast media in soil using synchrotron XCT and XRF. *Plant and Soil*, 1-19.

Contribution: Study design, experimental system design / construction, SRXRF data acquisition, SRXCT data acquisition, image analysis development, data analysis and manuscript writing.

Scotson, C. P., Duncan, S. J., Williams, K. A., Ruiz, S. A., & Roose, T. (2020). X-ray Computed Tomography Imaging of Solute Movement through Ridged and Flat Plant Systems. *European Journal of Soil Science.* 1-17.

Contribution: Study design, XCT data collection, image analysis development, running image analysis, construction of the soil resistivity system, soil resistivity experiments, data analysis and manuscript writing.

Scotson, C. P., Munoz-Hernando, M., Duncan, S. J., Ruiz, S. A., Keyes, S. D., Van Veelen, A., Dunlop, I., & Roose, T. (2019). Stabilizing gold nanoparticles for use in X-ray computed tomography imaging of soil systems. *Royal Society open science*, 6(10), 190769.

Contribution: Study design, UV-Vis data acquisition, ICP-MS data acquisition, XCT data acquisition, applying PEG coating, SEM data acquisition, data analysis, manuscript writing.

Middle author

Petroselli, C., Williams, K.A., Ghosh, A., McKay Fletcher, D., Ruiz, S. A., Gerheim Souza Dias, T., **Scotson, C. P.** & Roose, T. (2020) Time-Resolved Monitoring of Phosphorus Release from a Fertilizer Pellet and its Mobility in Soil Using Microdialysis and X-ray Computed Tomography. *Soil Science Society of America Journal*.

Contribution: Experimental / study design, experiment setup and microdialysis data acquisition

Van Veelen, A., Koebernick, N., **Scotson, C. P.**, McKay-Fletcher, D., Huthwelker, T., Borca, C. N., MosselMans, F. W. & Roose, T. (2020). Root-induced soil deformation influences Fe, S and P: rhizosphere chemistry investigated using synchrotron XRF and XANES. *New Phytologist*, 225(4), 1476-1490.

Contribution: Sample preparation and data acquisition

Hughes, N., Askew, K., **Scotson, C. P.,** Williams, K., Sauze, C., Corke, F., Doonan, J., H., & Nibau, C. (2017). Non-destructive, high-content analysis of wheat grain traits using X-ray micro computed tomography. *Plant Methods*, *13*(1), 76.

Contribution: XCT data acquisition, image processing development and data analysis

Keyes, S. D., Cooper, L., Duncan, S., Koebernick, N., McKay Fletcher, D. M., **Scotson, C. P.**, Van Veelen, A., Sinclair, I., & Roose, T. (2017). Measurement of micro-scale soil deformation around roots using four-dimensional synchrotron tomography and image correlation. *Journal of The Royal Society Interface*, 14(136), 20170560.

Contribution: XCT data acquisition, data analysis / interpretation and assistance with manuscript preparation

Conference Presentations

Tomography for Scientific Advancement (ToScA), University of Portsmouth: September 2017

- 15 minute oral presentation: Optimising gold nanoparticles for use in soil X-Ray CT.

Mechanical Engineering Postgraduate Research (PGR) conference, University of Southampton: January 2018

- 15 minute oral presentation: Optimising gold nanoparticles for use in soil X-Ray CT.

Mechanical Engineering Postgraduate Research (PGR) conference, University of Southampton: January 2018

- Poster presentation: X-ray Computed Tomography Imaging of Solute Movement through Ridged and Flat Plant Systems.

Rhizosphere 5 Conference, Saskatoon, Canada: July 2019

- 15 minute oral presentation: X-ray Computed Tomography Imaging of Solute Movement through Ridged and Flat Plant Systems.
- **Rhizosphere 5 Conference PhD Student Award** for achievements in crop root research during my PhD and previous research work.

Tomography for Scientific Advancement (ToScA), University of Southampton: September 2019

- 15 minute oral presentation: X-ray Computed Tomography Imaging of Solute Movement through Ridged and Flat Plant Systems.

Declaration of Authorship

Print name: Callum Paul Scotson

Title of thesis: Enhancing the Study of Plant Root and Soil Interactions using Radiocontrast Media in X-ray Computed Tomography Imaging

I declare that this thesis and the work presented in it is my own and has been generated by me as the result of my own original research.

I confirm that:

1. This work was done wholly or mainly while in candidature for a research degree at this University;

2. Where any part of this thesis has previously been submitted for a degree or any other qualification at this University or any other institution, this has been clearly stated;

3. Where I have consulted the published work of others, this is always clearly attributed;

4. Where I have quoted from the work of others, the source is always given. With the exception of such quotations, this thesis is entirely my own work;

5. I have acknowledged all main sources of help;

6. Where the thesis is based on work done by myself jointly with others, I have made clear exactly what was done by others and what I have contributed myself;

7. Parts of this work have been published as:

Scotson, C. P., Duncan, S. J., Williams, K. A., Ruiz, S. A., & Roose, T. (2020). X-ray Computed Tomography Imaging of Solute Movement through Ridged and Flat Plant Systems. *European Journal of Soil Science.*

Scotson, C. P., Munoz-Hernando, M., Duncan, S. J., Ruiz, S. A., Keyes, S. D., Van Veelen, A., Dunlop, I., & Roose, T. (2019). Stabilizing gold nanoparticles for use in X-ray computed tomography imaging of soil systems. *Royal Society open science*, 6(10), 190769

Scotson, C. P., van Veelen, A., Williams, K. A., Koebernick, N., Fletcher, D. M., & Roose, T. (2020). Developing a system for in vivo imaging of maize roots containing iodinated contrast media in soil using synchrotron XCT and XRF. *Plant and Soil*, 1-19.

Signature: **Date:**

Acknowledgements

Firstly, I would like to thank my primary supervisor, Professor Tiina Roose of the University of Southampton, for the opportunity to undertake my PhD research and the academic guidance and support she has provided. I would also like to thank the µ-VIS X-ray Imaging Centre at the University of Southampton for facilitation of the X-ray computed tomography experiments and the European Research Council (ERC) who have funded this PhD and made this work possible.

To my co-supervisors, Dr Nicolai Koebernick and Dr Arjen van Veelen, who have provided invaluable support and shaped my research for the better in more ways than I can count – thank you. Arjen, you have taught me much about research, technologies and techniques which I would never have approached let alone implemented within my own work without you. You have been a valued mentor and friend. Nico, I cannot thank you enough: a real inspiration of mine, friend and a genuinely kind man for whom I have nothing but respect and gratitude. Thank you both not only for your advice and support in the completion of my thesis but also in my future career and beyond.

I would also like to express my gratitude to Dr Samuel Keyes for his invaluable input, advice and on-going investment in my success and future career. Despite departing to embark on a new career journey of his own, Sam has always been there to listen, provide support and to reassure me that I am on the right track and for that I will forever be grateful.

Thanks also go to my family and in particular to my partner, Megan Woolley, for their support through these past few years. I could not have got this far without them. To my mum, dad and sister, thank you for always believing in me and for all the time you have given to me and sacrifices you have made for me. Meg, you have always been there for me with unwavering kindness and love when I found myself the most unsteady and unsure. We have made the most wonderful memories together during our time in Southampton and I can't wait to see what the future holds for us. Dw i'n caru ti.

To the other members of the 'Rooty' group, past and present, it has been my pleasure to call you my colleagues but most of all my friends. In particular I must thank my fellow PhD students (now graduates!) with whom I have shared this journey, Dr Daniel McKay Fletcher and Dr Simon Duncan. You are both remarkably smart men and I have no doubt you will go onto achieve great things. Your kindness and friendship is greatly valued. I can think of no better example to give of your friendship than the sympathetic restraint of your celebrations after Scotland retained the Calcutta Cup following a 38-38 draw against England in the Six Nations (we all know I would not have been nearly as gracious).

Finally, to all of my friends and loved ones, both in Southampton and beyond, thank you for your loyal friendship and for the offers of rest & relaxation throughout my PhD. There are a great deal too many of you to name you all individually, but I am sure that you will know who you are.

1 An Introduction to the Use of Contrast Agents to Enhance X-Ray CT Imaging of Plant Root and Soil Systems

1.1 Introduction to X-ray Computed Tomography

X-ray computed tomography (XCT) is a non-destructive and non-invasive imaging technique, commonly employed for imaging organic tissues. It has widespread use within biological research and clinical applications (Kalender, 2006), but has increasingly been utilised within plant and soil science research (Mooney *et al.*, 2012; Roose *et al.*, 2016).

X-rays, a form of electromagnetic radiation with wavelengths between 0.01 and 10 nm, are conventionally generated by a vacuum tube in which a high voltage is used to accelerate electrons from a cathode to an anode (Michael, 2001). More specifically, these electrons are accelerated from the cathode towards the metal 'target' anode (usually molybdenum, tungsten or platinum), with some of the energy re-emitted as X-rays from the point of impact. A proportion of these are projected from the vacuum tube through an exit 'window' to create the focused beam used for X-ray imaging (Wildenschild et al., 2002). The energy of X-rays generated (usually measured in keV) is dependent upon the energy of the electrons used to excite the target (with the tube potential often measured in kVp). In most commercial XCT apparatus, the photon energy averages to approximately one third of the tube potential. The process of XCT imaging most fundamentally requires an X-ray source and an X-ray-sensitive detector. In the beam path between the source and the detector an object of interest is placed. The focused X-ray beam emitted from the source passes through the object and to the detector.

The object (in the instance of most industrial CT scanners) or alternatively the X-ray source and detector (in the instance of medical CT scanners) are incrementally rotated. The raw data captured during scanning, which are called 'projections', consist of a set of line integrals. These line integrals are essentially a representation of the total beam attenuation as it passes through the object in a straight line (Mooney et al., 2012). Projections are captured throughout each rotation. In an idealised case, the intensity of each pixel is the integrated attenuation of the incident energy by all material along a straight path from the pixel to the X-ray point source (Wildenschild et al., 2002). The capacity of a material to reduce X-ray radiant flux is called the attenuation coefficient. The

projections are reconstructed to produce image 'slices'; essentially solving the inverse radon transform, usually as a filtered back projection. Within these slices the grey-level of each location within the object is a function of the local X-ray attenuation. Higher attenuation coefficients are generally represented as brighter voxel values in reconstructed data (Mooney et al., 2012; Lusic & Grinstaff, 2013). Two-dimensional horizontal image slices, normal to the rotation axis, can be 'stacked' to form the full 3D representation of the object.

X-ray CT imaging relies upon a sufficient proportion of incident X-rays passing through the object to the detector (i.e. 'transmission' ratio). This means that for particularly large or dense objects higher X-ray energies are required for penetration. However, since most materials will preferentially attenuate lower energy X-ray photons (Flannery et al., 1987), the use of elevated energies correlates with diminishing contrast between the attenuation coefficients of different materials. In such instances segmentation, and therefore analysis and visualisation, of different features becomes more complex. This is because pixel intensity thresholds (an important component of many simple segmentation workflows) become increasingly ineffective under low contrast-to-noise (CNR) conditions.

1.2 X-Ray Computed Tomography in Plant and Soil Science.

X-ray CT offers the opportunity to retrieve three-dimensional spatial information for root morphological features such as branching, tortuosity and length, in addition to interactions with different phases comprising the soil domain. These features are difficult to study using other methods whilst the plant root system is still intact within soil. Two of the most prolific extant techniques for root study, root washing and root growth in hydroponic/ gel systems, result in the loss of spatial information and require growth within media not representative of true soil behaviour, respectively (Mooney *et al.*, 2012). During root washing, not only is spatial information lost but can it also be difficult to avoid damaging the root systems by removing delicate features such as secondary roots and root hairs during the washing procedure (Böhm, 1979). Whilst hydroponic/ gel systems do not require destruction of the samples for visualisation, the behaviour of roots within the porous media structures of soil aggregates cannot easily be replicated using hydroponic/ gel systems and thus mechanical root behaviour can be altered (Clark *et al.*, 1999; Thompson & Holbrook, 2004).

1.2.1 Challenges of Using X-Ray CT in Plant and Soil Science

Though XCT has become widespread in plant/soil research, the very similar X-ray attenuation coefficients of root material and the soil-water means that often very poor contrast is attained between features of interest (Kaestner *et al.*, 2006; Mooney *et al.*, 2012). This poor contrast has two major effects on XCT use in plant and soil science applications. Firstly, segmentation of the plant roots within the image often involves a complex multi-step computational workflow in which considerable user-interaction can be necessary. Secondly, comparatively low X-ray energies are generally required in order to achieve an acceptable level of contrast within the image. However, these low energies limit the size of sample that can be imaged. Often this means that sample size is limited to juvenile plants only. Therefore, this limits the applicability of XCT for studying the behaviour and mechanisms present in mature plants and larger soil volumes (Mooney *et al.*, 2012).

These same issues are often encountered within biomedical XCT imaging of soft tissues where a common solution to the minimal innate contrast is the use of contrast agents (Lusic & Grinstaff, 2013). Contrast agents comprise an element of high attenuation coefficient - for example iodine, barium or metal particles - either as ions in solution or as a particulate suspension. A contrast agent's high attenuation coefficient is typically associated with a high Z number and therefore with increased radio-density. This high attenuation coefficient raises the CNR and enables the agent to highlight regions that would otherwise be indistinguishable from other tissues during XCT imaging.

It is largely because of their widespread use within clinical contexts that biomedical contrast agents are the focus of much research and development work. For example, the investigation of gold nanoparticles as a contrast agent has been largely a product of biomedical research (Hainfeld *et al.*, 2006; Lee *et al.*, 2013). However, there are currently very few examples of the use of contrast agents within plant research, with extant studies most often employing staining of harvested material as opposed to *in vivo* approaches (Ahn *et al.*, 2010; Dhondt *et al.*, 2010; Blonder *et al.*, 2012). If existing insights and approaches for the use of contrast agents within living organic tissues were to be transferred from biomedicine to plant and soil science, the inherent CNR difficulties presented by XCT imaging of plant and soil systems could be addressed.

1.2.2 Desirable Traits for Plant and Soil Contrast Agents

By examining the characteristics of contrast agents against desirable criteria for plant and soil science applications, the different classes of contrast agent can be assessed for suitability. The aim is to maximise enhanced contrast whilst minimising toxic effects.

Lusic and Grinstaff (2013) identified a list of requirements for CT contrast agents to be used in clinical contexts, many of which are similarly applicable to plant and soil science applications. Their initial assertion is that it is necessary for a contrast agent to enhance the absolute CT attenuation of the target tissue to at least twice that of 'background' material and/or fluid. For example, iodine based contrast agents attenuate X-rays significantly more than both distilled water (Abdul Razak *et al.*, 2013) and typical organic soft tissues (Anderson *et al.*, 2010). The attenuation coefficient of iodine is an order of magnitude greater than that of such organic material (including soil organic material) across a range of X-ray energies. Hence, iodine is commonly incorporated in contrast agents as the principal attenuating component.

An important consideration for the attenuation properties of a contrast agent is the molar percentage of the X-ray attenuating element within a single molecule or particle of the contrast agent. By utilising species which contain a high molar percentage of the 'active' element, the relative volume of contrast agent that will need to be administered can be decreased. This also decreases any potential toxic effects these molecules may have (Golshahi *et al.*, 2014). However, this should not be confused with dilution. A contrast agent can be supplied diluted provided the X-ray attenuating material accumulates to a higher concentration at the target surface - for example, in the instance of functionalised contrast agents (Sun *et al.*, 2009).

A well-defined K-edge is also of benefit to contrast agents. The K-edge is the photon energy at which an incident photon will induce ejection of an electron from the K shell of the atom. An electron from the next shell out will then take the place of the ejected electron, causing the release of a photoelectron. This mechanism is called the photoelectric effect, and it significantly increases the attenuation of the material (Coursey *et al.*, 2010). Therefore, if the energy of the X-ray beam is equal to, or slightly greater than, the K-edge of the contrasting material it can significantly enhance the contrast provided (Coursey *et al.*, 2010; Clark *et al.*, 2013). This is denoted by ***Figure 1***.

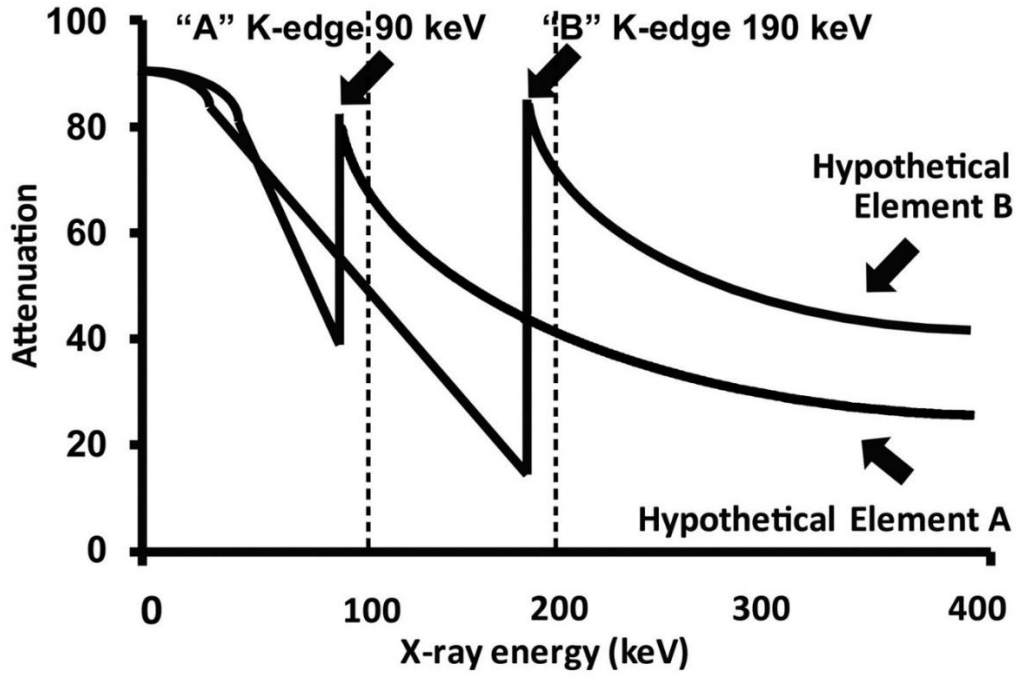

Figure 1. *A diagram illustrating the effect of the K-edge on the attenuation achieved for two hypothetical elements: A and B. Figure from Coursey et al. (2010).*

Further to possessing favourable properties for X-ray attenuation, it is important that a contrast agent is able to be distributed preferentially in/ upon the region of interest. It should not be significantly present within 'background' regions. This may be through a passive process of accumulation, or as the result of functionalisation – for example, the methods utilised by Effersoe *et al.,* (1990) to use functionalised gold nanoparticles to capture damaged bone tissue or Zhang *et al.,* (2010) who used the iodinated contrast agent iohexol to monitor renal function, respectively. In either case the spatial distribution of the agent must be maintained, as excessive leaching of the contrast agent into other areas, for example from roots into the soil, may lead to a 'bleaching' effect within the image. This would negate any contrast benefit sought by the addition of the agent (Mattrey & Aguirre, 2003).

It is also asserted by Lusic and Grinstaff (2013) that the retention time of contrast agents for biomedical use should be ideally not more than four hours, though this consideration arguably does not concern plant systems in the same way. In many respects, for high resolution root and soil imaging the opposite may well be true. Whilst retaining the agent for longer periods within plant living tissue may exacerbate damaging effects on plant tissue, a lifespan of considerably more than four hours in the plant may be required when both the imaging time and the time taken for translocation of agents through the plant are considered (Keyes *et al.*, 2017b). Scan times for

imaging soil systems can be comparatively long (for example relative to soft tissue imaging) since long exposure times may be required to achieve sufficient X-ray transmission through dense soil samples.

Sufficient and efficient translocation of contrast agent to the desired region, for instance the root system, must be considered. For example, it may be necessary to introduce the agent to above ground plant material in order to ensure perfusion of the root system without contamination of the soil. This would allow for translocation of the agent through leaf and stem vasculature to the root system, as demonstrated by *Keyes et al.* (2017b). Alternatively, contrast agents could be applied to the soil but functionalised for adhesion to a particular organic surface; a method demonstrated in the biomedical domain (Sun *et al.*, 2009). In this case it would be desirable for the agent to translocate efficiently to target surfaces without binding to growth media. This minimises image bleaching effects.

Given that contrast agents are generally translocated through aqueous phases, Lusic and Grinstaff (2013) also state that the agents should form stable solutions or suspensions of low viscosity under expected aqueous conditions. For example, they should maintain stability at the expected pH and ionic strength of the fluid. This principle also applies to use in plants and soils, though additional complications are present in these cases. Soil water solutions and plant fluids are relatively heterogeneous compared to typical mammalian biological fluids. For example, the pH of soil-water solutions produced from UK agricultural field soils ranges between approximately 4 and 8 (Tinker & Nye, 2000) with additional variation present in intra-substrate niches. Within intra-substrate niches plant root secretions can significantly alter the pH in the localised rhizosphere: soils with a bulk pH of 4 and 7 can undergo a pH change of about 1 localised to several millimetres of soil closest to the root surface (Tinker & Nye, 2000). By contrast, for a healthy human adult it is unusual for blood pH to vary from the baseline of approximately 7.59 by more than 0.1 (Sinet *et al.*, 1985). Therefore, contrast agents for use within plant and soil systems will need to be stable as solutions or suspensions over a broad range of conditions (such as pH, salinity and surface charge) to ensure consistent behaviour and effectiveness.

Additionally, contrast agents and resulting metabolites ideally should not exhibit excessive toxicity and should be biologically unreactive. Unacceptable phytotoxic effects would involve damage to root tissues to an extent to which they would begin to behave abnormally and thus no longer be representative of typical root systems. As an extreme example, lead (Pb), a radiodense element and thus potential contrast agent (Yu & Watson, 1999), has been observed to significantly impede root length and elongation rate at concentrations above 100 µg Pb / L (Pahlsson, 1989).

An alternative consideration closely related to phytotoxicity is the potential for osmotic stress effects within plant tissues as a result of contrast agent addition. Where a contrast agent, particularly of high osmolality, remains in a region of tissue at a high concentration it will lower the osmotic potential. This will induce osmotic stress by drawing water from surrounding tissues in an effort to restore a higher water potential. Osmotic stress can lead to cell and plant death and as such may significantly affect plant behaviour (Xiong & Zhu, 2002). This is of particular significance as removing water from tissues will affect turgor and thus alter internal plant structures.

The final consideration that applies to plant systems is the particle or molecular size of the contrast agents relative to characteristic scales of plant vasculature and cell wall pores. The larger the particles or molecules of a contrast agent are, the longer it is likely to take for translocation through cells and vasculature towards the desired region. As previously mentioned, this rate can be of significant importance. However, smaller particles or molecules of contrast agent increase the risk of 'leaching' into surrounding tissues by translocating too readily through plant tissues. For example, it would be unwise to use a nanoparticulate contrast agent for which the particles were smaller than 10 nm, which is the approximate size of root cell wall pores (Asli & Neumann, 2009), as this would likely lead to such a leaching effect.

1.2.3 Contrast Agent Categories

Three categories of contrast agent will be compared to these criteria. These categories represent the agents most commonly used in biomedical applications and/or those most promising for consideration in plants and soils: iodinated, metal nanoparticulate and other assorted agents (Yu & Watson, 1999; Hainfeld *et al.*, 2006; Lusic & Grinstaff, 2013). Ultimately, they will be compared for their suitability in performing one of two functions: acting either as a non-functionalised flow tracer for operations such as visualising hydrological flows, or as a functionalised agent providing contrast via accumulation on targeted surfaces or in tissues.

1.3 Iodinated Contrast Agents

Iodinated contrast agents are generally separated into two categories: ionic and non-ionic. Agents in these classes vary from one another in several important characteristics previously identified, such as osmolality and bio-reactivity. Because of these varied characteristics, different agents interact differently with organic material which can be an important factor when assessing suitability for a particular application (Singh & Daftary, 2008; Lusic & Grinstaff, 2013).

1.3.1 Non-ionic

For several decades, non-ionic iodinated contrast agents have been used as non-specialised tracer contrast agents to enhance internal vascular networks and gastrointestinal tracts (Gertz *et al.*, 1985; Blachar *et al.*, 2001; Lusic & Grinstaff, 2013). They possess attributes that are particularly favourable for these biomedical applications. These are attributes which could lead to a similar utility in equivalent plant and soil imaging scenarios – for example, when mapping plant root vasculature in soil.

Non-ionic iodinated contrast agents are generally less reactive compared to ionic alternatives (Aspelin, 2006). This is because non-ionic agents usually consist of one or more fully substituted aromatic rings. The lack of reactivity is often an advantageous trait in applications involving biological tissues. Studies have repeatedly observed that human cells display more severe symptoms of toxicity in the presence of ionic agents compared to non-ionic equivalents (Haller & Hizoh, 2004; Heinrich *et al.*, 2005; Hasebroock & Serkova, 2009; Sendeski, 2011). For example, Heinrich *et al.* (2005) observed that renal cell function was impeded significantly more by the ionic contrast agent ioxithalamate than by ioversol, iomeprol, iodaxinol and iotrolan, which are all non-ionic. This was concluded to be in part a result of the bio-reactive nature of the ionic molecules. The differences in plant and animal cells mean that such results do not necessarily apply to plant cells, but there is unfortunately little literature on the cytotoxic effects of ionic contrast agents in plants.

However, environmental research suggests that non-ionic contrast agents present some phytotoxic effects, though perhaps not as severe as those presented by ionic species. Zhang *et al.* (2016) observed a significant reduction (approximately 50%) in the root length of four species of aquatic plant (*T. latifolia, P. australis, I. pseudacorus and J. effusus*) grown within hydroponic systems containing 10 mg iodine / L of the non-ionic contrast agent Iohexol for twenty-four days. The work by Keyes *et al.* (2017b) is the only example within the literature where iodinated contrast agents have been applied to plants in order to image root systems in soil. This was achieved by submerging the cut faces of leaf petioles of plant specimens within reservoirs of both ionic and non-ionic contrast agents, allowing passive transport to the root system via the plant vasculature. When using iodinated contrast agents to image root systems they observed that optimal contrast was achieved by the non-ionic contrast agent Iopamidol at an iodine concentration of 75 mg I / mL (***Figure 2***). This concentration is significantly higher than the concentration used by Zhang *et al.* (2016) though it was not applied to the plant for nearly as long - only 24 hours (Keyes *et al.*, 2017b). These toxicity

effects therefore indicate that there are limitations to the perfusion time-scales of non-ionic contrast agents when used for plant tissue imaging. This is an important consideration for time resolved studies or those which require long scan times.

Perhaps the most important benefit of non-ionic iodinated contrast agents is their osmolality. Osmolality is the concentration of solute particles within a solution per kilogram. This is reported to be at least four times lower than for ionic iodinated contrast agents of comparable iodine concentration (Aspelin, 2006). As stated, contrast-agent-induced osmotic shock may cause significant plant tissue damage. Given osmotic shock is often closely associated with the osmolality of the supplied contrast agent (Lusic & Grinstaff, 2013), osmolality could be an important consideration. Keyes *et al.* (2017b) noted that where an ionic and non-ionic contrast agent were applied to winter pea plants, the incidence of apparent osmotic shock effects were reduced by using a non-ionic agent. In the case of ionic contrast agents, osmotic shock was visible after one day of perfusion as dehydration and decolouration of leaf tissue to which the contrast agents were applied and also as leaking of contrast agent material into the soil via the root cortex. Where this osmotic shock was present within the roots, it had the potential to induce root shrinkage, leading to unrepresentative root morphology and bleaching of soil resulting from apoplastic transport of the agent during leakage.

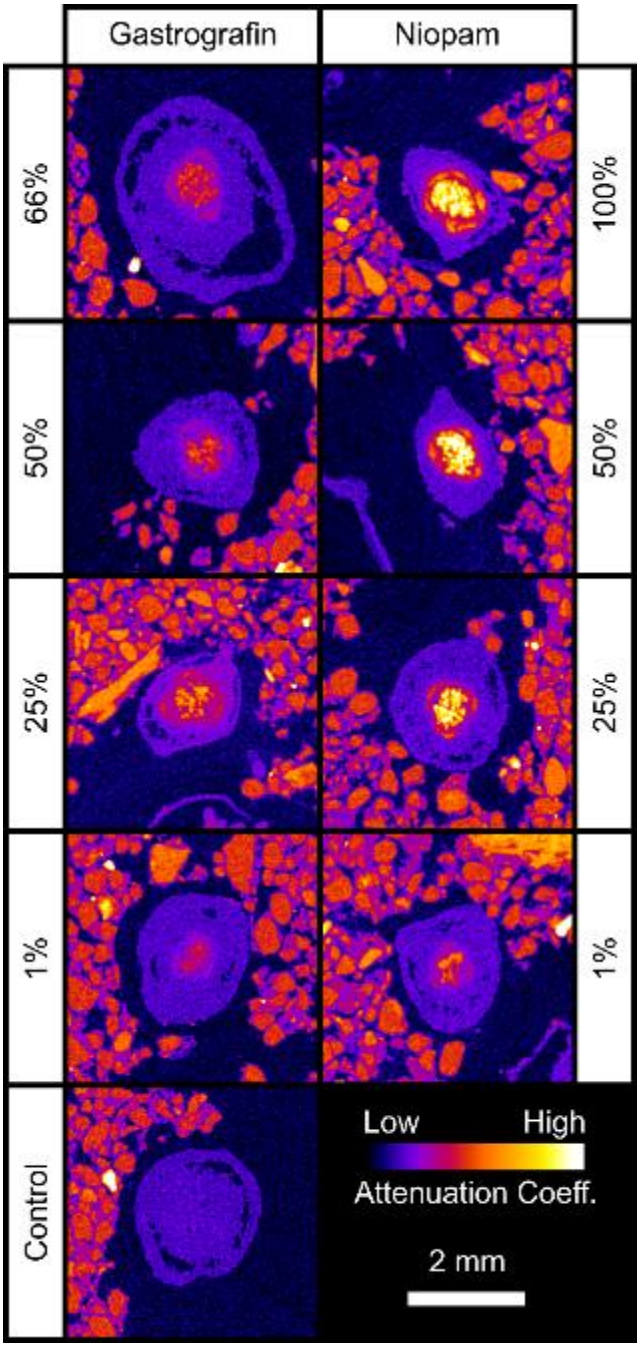

Figure 2. *Heat map images of relative attenuation coefficients of two iodinated contrast agents in winter pea root systems across a range of concentrations. The two contrast agents used were Gastrografin (ionic) and Niopam (also called Iopamidol and non-ionic). Figure from Keyes et al. (2017b).*

Another important feature of non-ionic iodinated contrast agents is the capacity to provide better contrast *in vivo* than ionic equivalents per unit of contrast agent applied. This is thought to be because ionic contrast agents are susceptible to osmotic dilution as they draw water from

surrounding biological tissues due to their higher osmolality (Lusic & Grinstaff, 2013). Therefore, lower concentrations of non-ionic contrast agents may be required to achieve the same target contrast, further reducing osmotic effects. For example, Keyes *et al.* (2017b) observed less contrast was provided by Gastrografin (ionic) compared with Iopamidol (non-ionic) as is visible in ***Figure 2***. It is possible that this could have been at least in part a result of osmotic dilution.

As discussed earlier, contrast can be enhanced by imaging samples just above their K-edge (which for iodine is 33.2 keV). Some work has been undertaken to assess the viability of this approach for plant imaging using iodinated contrast agents. Karunakaran *et al.* (2015) demonstrated the effectiveness of this approach. The non-ionic contrast agent Ioversol was used to undertake synchrotron phase contrast imaging of wheat seed spikes and canola stems at an effective X-ray energy of 33.4 keV (***Figure 3***). The resulting images indicated the potential for using non-ionic iodinated contrast agents as an effective flow tracer in phytological systems. This is because good contrast was achieved and the contrast agent was successfully translocated by the plant vasculature.

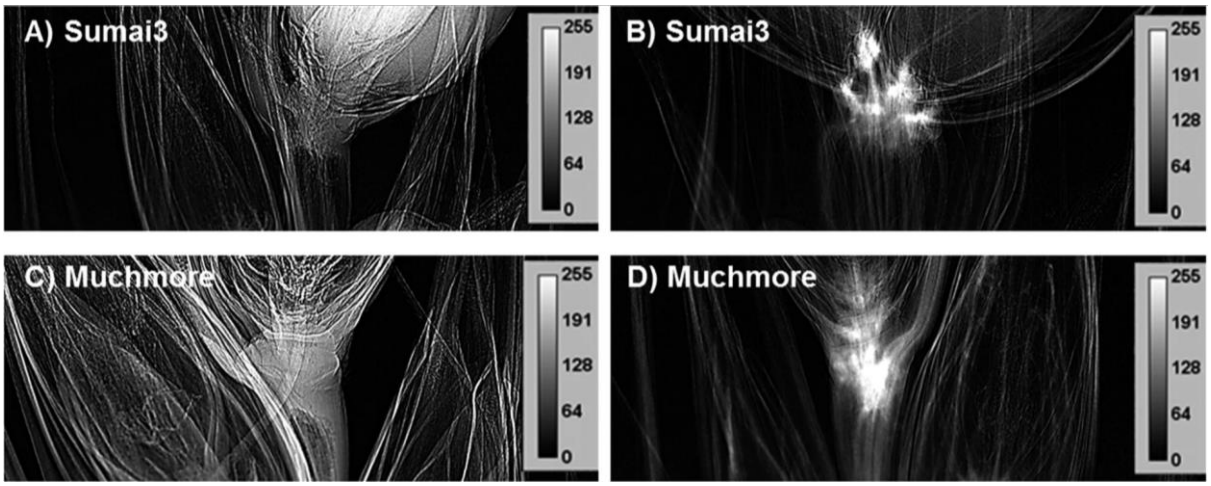

Figure 3. *Radiographic images captured of wheat spikes from two cultivars captured before (A and C) and after (B and D) the introduction of iodine. Images A and C were captured at 18 keV and images B and D were captured at 33.4 keV with an effective pixel size of 8.75 µm. Figure from Karunakaran et al. (2015).*

These results regarding the translocation of contrast agents are in agreement with Keyes *et al.* (2017b). They similarly suggest that translocation via plant vasculature is a promising avenue to deliver contrast agents to intact, soil borne root systems without contaminating the soil itself.

However, whilst the imaging was undertaken *in vivo*, the experimental system did not include a number of the complications presented by imaging root material in soil using non-synchrotron X-ray sources (Karunakaran *et al.*, 2015). Firstly, these samples were imaged in an air background, which, being far less attenuating than soil, allows lower X-ray energies to be used whilst maintaining sufficient X-ray transmission. In addition, synchrotron facilities enable the use of a narrow (often monochromatic) spectrum of photon energies, and maintaining a precise and narrow energy peak (such as the 33.2 keV K-edge of iodine) is much more difficult to achieve using polychromatic sources (as used in laboratory based CT systems). To achieve similar results using a polychromatic source filtering is necessary to remove undesired low energy spectral components. However, filtering reduces total flux which in turn increases necessary scan times. Long scan times are incompatible with imaging of unstable soil samples – such as where there is movement of soil-water or active root growth displacing soil particles.

Non-ionic iodinated contrast agents possess further limitations beyond their potential phytoxicity. As a result of their ease of translocation through biological tissues, they can often undergo severe loss of contrast within organic material due to extravasation and equilibration. This makes meaningful imaging of specific regions difficult (Mattrey & Aguirre, 2003). If applied to a plant root-imaging context this could mean for example that xylem, phloem and root cortex material become indistinguishable and thus information is lost. Their comparative mobility also indicates that leaching of agents along a concentration gradient from roots into soil may be an additional concern. This would particularly be the case where contrast agent molecules are at or below the size of cell wall pores, and where the agent is required to remain within the root system for a prolonged period prior to imaging. It is possible that contrast gains from non-ionic agents, due to reduced osmotic dilution effects compared to ionic agents, could be cancelled out due to higher rate of equilibration (Mattrey & Aguirre, 2003).

There does not appear to be any literature regarding the equilibration of contrast agents within plant tissues, however there are numerous examples in the biomedical literature. Whilst not an ideal source of comparisons, such studies may inform the relative equilibration behaviour of non-ionic iodinated contrast agents within biological tissues in general. Studies have repeatedly observed that, whilst such events are rare in human patients (<3% rate of occurrence), instances of extravasation into surrounding tissues can lead to up to 40% of the administered agent being lost from the vascular domain (Sistrom *et al.*, 1991; Federle *et al.*, 1998; Wang *et al.*, 2007). This represents a substantial loss in attainable contrast between vasculature and background, particularly if the background becomes contaminated with the agent.

1.3.2 Ionic

The major benefit of ionic iodinated contrast agents is that there is far more literature regarding their application as a contrast agent in plant tissues in comparison to non-ionic equivalents. This is possibly due to the relative availability of ionic iodine agents (such as potassium iodide), despite the more severe osmotoxicity and cytotoxicity associated with of this class of agent.

One example is Blonder *et al.* (2012) who soaked harvested *Quercus virginiana* and *Eucalyptus microtheca* in a mixture of 2% iodine and 4% potassium iodide (ionic) for two days. These were imaged using an XCT synchrotron beamline and two commercial µCT scanners, both with and without the addition of the iodine mixture. The synchrotron images were produced using both absorption and phase contrast. It was observed that it was not possible to reliably visualise leaf venation, even using the synchrotron facility, without the application of the contrast mixture. Where the leaves were soaked in the contrast mixture it was possible to visualise all major and minor venation using both the synchrotron and commercial XCT scanners (***Figure 4***). This demonstrated that the iodinated contrast agent had remained within the leaf venation long enough to provide useful contrast, and had not equilibrated into surrounding leaf tissue over the imaging timescale.

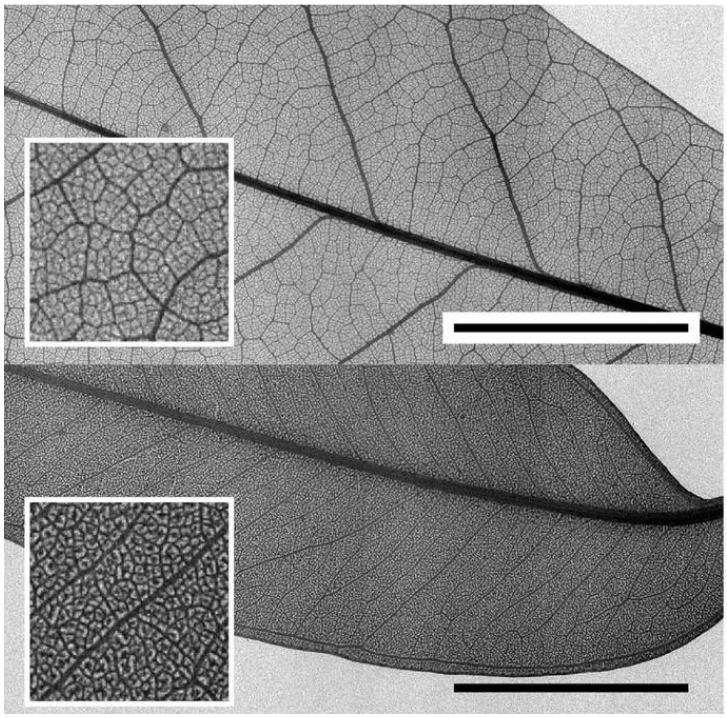

Figure 4. *X-ray radiography images captured using a commercially available µCT scanner of Quercus virginiana (top) and Eucalyptus microtheca (bottom) leaves. The leaves had been soaked in a 2% iodine and 4% potassium iodide mixture for two days. The line is 1cm. Figure from Blonder et al. (2012).*

Similar to the above application, Dhondt *et al.* (2010) undertook high resolution XCT imaging of *Arabidopsis thaliana* stem, hypocotyl, flower and leaf material. It was possible to capture CT images with a voxel size of 13.8 µm and of sufficient quality to visualise floral organs without the need of a contrast agent. Dhondt *et al.* (2010) also managed to capture CT images at a cellular resolution (0.8 µm), though this required dehydration of the plant material with alcohol before staining it with potassium iodide (KI) solution for 24 hours. The iodine appeared to remain confined to the xylem/ phloem vasculature and intracellular spaces.

The ionic contrast agent Gastrografin was used by Kemmochi and Maru (2004) to identify and map regions of diseased cabbage (*Brassica oleracea capitata*) tissue using radiography. In order to achieve this, the roots of plants removed from soil were submerged in the contrast agent for between fifteen to twenty hours. Diseased regions of the root vasculature were distinguished from healthy regions by their comparatively poor contrast enhancement. The major achievement of this work was the ability to discriminate between xylem and cortical tissues – demonstrating a potential for ionic contrast agents to be used for the identification of specific tissues.

Despite the successes of the above work, it was not undertaken in soil, and usually not *in vivo*. Where Keyes *et al.* (2017b) applied the ionic contrast agent Gastrografin to winter pea (*Pisum sativum* L. cv. frisson) material at concentrations approaching the as-supplied values, osmotoxicity issues were reported to be severe. At high concentrations it was hypothesised that the osmotoxicity of Gastrografin had induced dehydration of root cortical cells causing a rapid efflux of fluid (including Gastrografin) into surrounding soil. Not only did this cause significant damage to root material, such that long-term time resolved imaging would not appear possible, but also polluted surrounding soil with high concentrations of Gastrografin. This made segmentation more difficult.

There are substantially more examples of the use of ionic as opposed to non-ionic contrast agents in hydrology and porous media flow tracing applications as well as in plants (Clausnitzer & Hopmans, 2000; Wildenschild *et al.*, 2002; Anderson *et al.*, 2003; Taina *et al.*, 2008). Anderson *et al.* (2003) used KI as a flow tracer for estimating porosity and hydraulic conductivity in soil cores. The KI presented sufficient contrast against the soil and water to enable discrimination of flow fronts within the CT images, exposing small-scale heterogeneities within porous media. In addition to this, the high attenuation coefficient of the KI relative to background material meant that the relatively high X-ray energies required to penetrate 76 mm-thick soil cores could be used whilst retaining a sufficient CNR within the image.

In a similar application to that described above, Clausnitzer and Hopmans (2000) used sodium iodide (NaI) to trace the flow of a front through a glass bead porous media system. This system was used as an analogue of fluid movement through soil. The iodinated contrast agent provided a distinguishable flow front. Additionally, since attenuation increases linearly with sodium concentration, it was possible to estimate the relative concentration of NaI from the attenuation coefficient it provided within the image, and thus map preferential routes through the porous media (Clausnitzer & Hopmans, 2000). The implication of these porous media studies is that small-molecule ionic contrast agents, such as KI and NaI, are well suited to use in porous media, particularly as flow front tracers. In the context of a plant root system, it appears they could potentially be used, for example, to map the flow front of convection routes through soil resulting from root water uptake.

1.3.3 Monomeric versus Dimeric Contrast Agents

Many clinical, small-molecule iodinated contrast agents have an aromatic structure – either monomeric or dimeric. Generally, these are more stable and less toxic than aliphatic iodinated structures. In addition to decisions relating to ionic versus non-ionic iodinated contrast agents, the choice of monomeric or dimeric structure may also be a further consideration. This is often true of medical applications (Heinrich *et al.*, 2005; Aspelin, 2006; Schild *et al.*, 2006). Since dimeric iodinated contrast agents are composed of two aromatic iodinated rings, the iodine atom count per molecule is increased and they usually provide a lower osmolality solution for a given concentration of iodine (Jost *et al.*, 2009). This could reduce the risks of osmotoxicity, as previously described. However, dimeric agents are often more viscous than their monomeric counterparts (Jost *et al.*, 2010). This increased viscosity would not only suggest that translocation times through porous media or organic tissues could be increased but also could mean such contrast agents are unsuitable for use as an XCT-visible analogue for water in tracing applications. Therefore, if the contrast agent is required to trace water flow or would need to be translocated at a higher rate then perhaps monomeric contrast agents may be the preferential choice.

It is important to note that these differences are only slight. Schild *et al.* (2006) examined the behaviour of monomeric and dimeric agents when used as blood-pool contrast agents in human patients. Overall, a similar incidence of adverse reactions were observed in monomeric and dimeric treatments. The only significant difference in behaviour noted between the two structures was that of delayed effects which were more common in the dimeric treatment group. This is possibly a

result of a slower translocation rate due to increased viscosity, meaning it took longer for dimeric agents to reach sensitive tissues.

1.4 Heavy Metal Nanoparticle Contrast Agents

An alternative to using iodinated contrast agents, with the strengths and weaknesses outlined above, is the use of metal nanoparticle suspensions. Metal nanoparticle suspensions have increasingly generated interest as X-ray CT contrast agents due to their ability to behave much like aqueous solutions whilst often being relatively easy to functionalise (Lusic & Grinstaff, 2013). Given their use as contrast agents is still only a relatively recent development within biomedical science (Hainfeld *et al.*, 2006; Rabin *et al.*, 2006; Lusic & Grinstaff, 2013), there is very little literature on their use in plant and soil settings. However, the literature that is available on this topic suggests they are very promising – particularly as a functionalised, and often tissue specific, contrast agent.

1.4.1 Gold Nanoparticles

Of the research that has been undertaken into metal nanoparticles, much of the emphasis is on gold, which possesses a number of beneficial traits for use as a contrast agent. Gold is highly unreactive, interacts little with most biological tissues, and therefore supposedly presents minimal risk of toxicity in most biological scenarios (Hainfeld *et al.*, 2006). In addition, gold has a well-defined K-edge (80.7 keV), a high density and atomic number. This makes it a particularly strong X-ray attenuator compared to biological soft tissues and even to most other iodinated contrast agents; gold nanoparticles (AuNPs) can achieve up to 2.7x the contrast of iodinated agents under equivalent conditions (Lusic & Grinstaff, 2013).

No evidence has been found in the literature detailing the use of AuNPs as a contrast agent in plant roots in soil. However, there are limited examples of their application to imaging of above ground, *ex vivo* plant material. Ahn *et al.* (2010) used AuNPs to trace flows through rice (*Oryza sativa*) leaf xylem. They achieved this by drying rice leaf sheaths, and submerging the material in a suspension of ~20 nm AuNPs until the leaf sap had been replaced by the suspension. The particles had been surface-modified with low molecular weight ligands to optimise their properties (such as hydrodynamic size and zeta-potential) for this application. Low molecular weight ligand coatings were chosen because they allow a reduced coating thickness compared to the standard polymeric coatings. This means a higher density of AuNPs could be achieved on target tissues. The coating was also used because it shortened the distance between the gold surface and the functional group

on the end of the ligand (trialled for optimal hydrodynamic behaviour), meaning these functional groups could be more densely held to the coating surface (Hostetler *et al.*, 1996). The resulting images from this experiment achieved sufficient contrast to distinguish the xylem from surrounding tissues, and to allow for time resolved movement flow tracing (***Figure 5***). It was also observed that the AuNPs did not appear to undergo any equilibration into neighbouring tissues from the xylem. However, given that the plant material used was *ex vivo* and harvested (dry), this research yields limited insights regarding the effectiveness or stability of AuNPs when applied to living plant tissues.

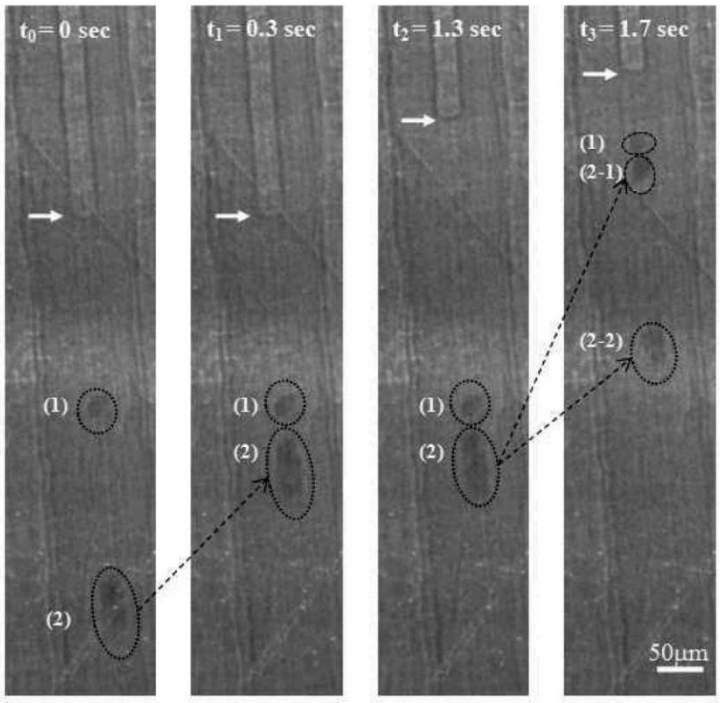

Figure 5. *Gold nanoparticles (highlighted by rings) used to trace sap flow through the xylem of rice leaf sheaths. The images left to right are consecutive time steps. (1) and (2) are the two initial gold nanoparticle cluster positions. Arrows indicate how these two clusters separate and merge over time with variable velocities. Figure from Ahn et al. (2010).*

Where phytotoxicity studies have been undertaken, AuNPs have shown only limited evidence of adverse effects and only after relatively long periods of exposure. Sabo-Attwood *et al.* (2012) grew tobacco (*Nicotiana xanthi*) seedlings in a hydroponic system and then transferred them after approximately four days into either a 3.5 nm or an 18 nm citrate-capped AuNP suspension. The duration of time the seedlings spent within this solution varied between 3 and 30 days. They noted that 3.5 nm AuNPs entered via the root into xylem vasculature, observing some aggregated AuNPs

detectable within root cell cytoplasm, suggesting some equilibration had taken place. These 3.5 nm AuNPs also induced leaf necrosis after fourteen days of exposure, which suggests a plant inoculated continuously within AuNPs over an extended period may express symptoms of phytotoxicity (***Figure 6***). The 18 nm AuNPs were not detected within the plant vasculature and instead remained agglomerated on the surface of the roots, indicating that AuNP uptake by roots is size-selective. It should be noted that this assessment was undertaken in juvenile plants, and that more mature plants may have a greater capacity to tolerate AuNPs.

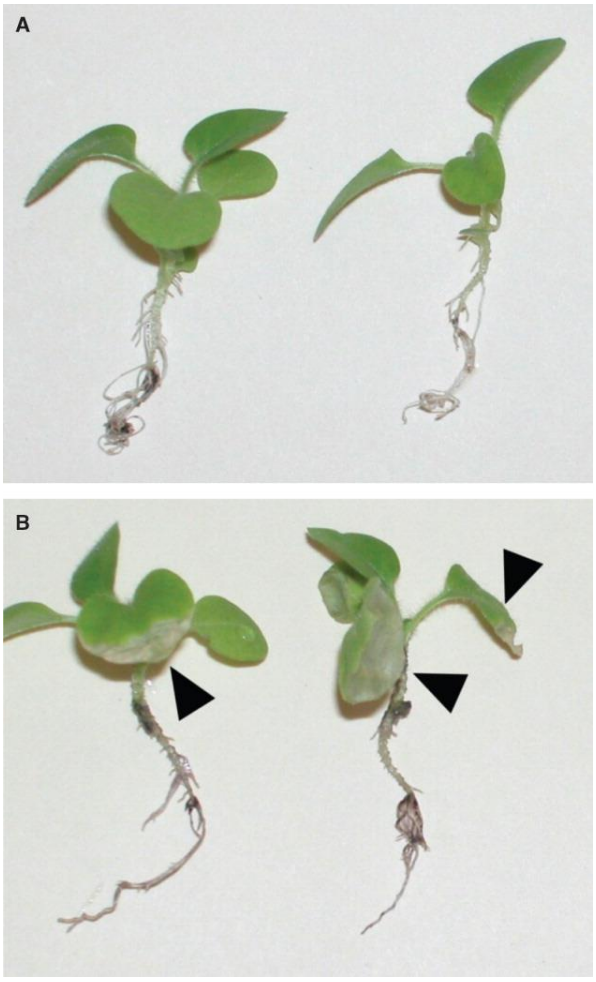

Figure 6. *Tobacco (Nicotiana xanthi) seedlings that were (A) grown within a hydroponic system as a control and (B) transferred from the hydroponic system after four days into a solution of 3.5 nm gold nanoparticles for a further 14 days. There is visible incidence of leaf necrosis present in the seedlings transferred into the gold nanoparticles (marked by black arrows) in (B). Figure from Sabo-Attwood et al. (2012).*

Rather than applying a coating optimised for hydrodynamic behaviour, AuNP coatings are often functionalised for accumulation on specific biological tissues or materials (Geso, 2007). There are no examples within the literature of such functionalisation for plant tissues, though there are many examples from biomedical applications, which set a promising precedent for their future use in plants. For example, Sun *et al.* (2009) used heparin functionalisation of a polymer coating on AuNPs to induce accumulation on murine liver tissues. It was demonstrated that functionalised AuNPs have the potential to provide significantly improved contrast compared to both the native contrast and an equivalent iodinated contrast agent, eXIA-160 (***Figure 7***). Because of the functionalisation-induced accumulation on the liver tissues, a greater quantity of the AuNP contrast agent was retained within the liver for the duration of imaging compared to the iodinated agent. If functionalised coating could be developed for accumulation on plant root surfaces, this could enhance the CNR ratio present within plant root and soil systems.

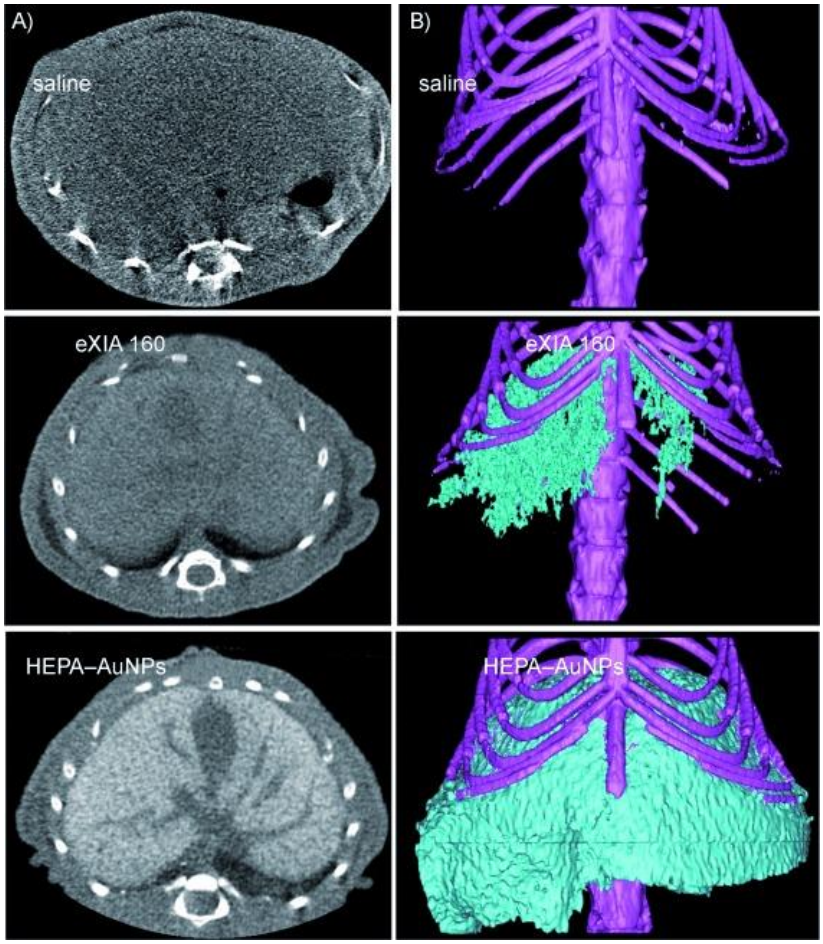

Figure 7. *X-ray CT 2D horizontal slices (left) and 3D visualisations (right) comparing the contrast provided by saline (top), eXIA-160 (middle) and HEPA coated gold nanoparticles (bottom). This study functionalised gold nanoparticles with heparin to induce accumulation on murine liver tissues and then compared the contrast produced by these functionalised nanoparticles with an equivalent iodinated contrast agent (eXIA-160) and with the native contrast present without any contrast agents. Contrast within the liver tissues provided by the agents is denoted by the cyan in the 3D visualisations and the purple in the 3D visualisations represents bone material. This figure demonstrates that the functionalised nanoparticles (bottom) had the potential to provide significantly improved contrast compared to both the native contrast (top) and the equivalent iodinated contrast agent, eXIA-160 (middle). Figure from Sun et al. (2009).*

However, the work of Sun *et al.* (2009) does expose a possible limitation of AuNP suspensions, since high concentrations must be reached in order to achieve sufficient contrast in XCT imaging. It was noted by Xu *et al.* (2008) that between 2.5 mg Au / mL and 5 mg Au / mL is necessary to obtain significant contrast against water in X-ray CT imaging and according to Sun *et al.* (2009) approximately 15.7 mg Au / mL was necessary to achieve equivalent contrast to the iodinated eXIA-

160 contrast agent (***Figure 8***). Whilst the eXIA-160 contrast agent did contain around 53.3 mg I / mL, supporting the assertion of Lusic (Lusic & Grinstaff, 2013) that AuNPs can provide up to 2.7x the contrast per unit of attenuating agent, it is likely more difficult to supply 15.7 mg Au / mL. Firstly, AuNPs at such concentrations are considerably more expensive than iodinated contrast agents. This may well mean it is prohibitively expensive to undertake large-scale experiments. Secondly, AuNPs tend to destabilise (aggregate and/ or settle out of a stable suspension)at high concentrations (Bergen *et al.*, 2006). Finally, viscosity will also be increased at high concentrations such that the translocation to the target region may be reduced. The necessity to reach high concentrations reaffirms the need for functionalisation. If AuNPs can be induced to accumulate locally to the high concentrations required for sufficient contrast, their application at unstably high concentrations may not be necessary.

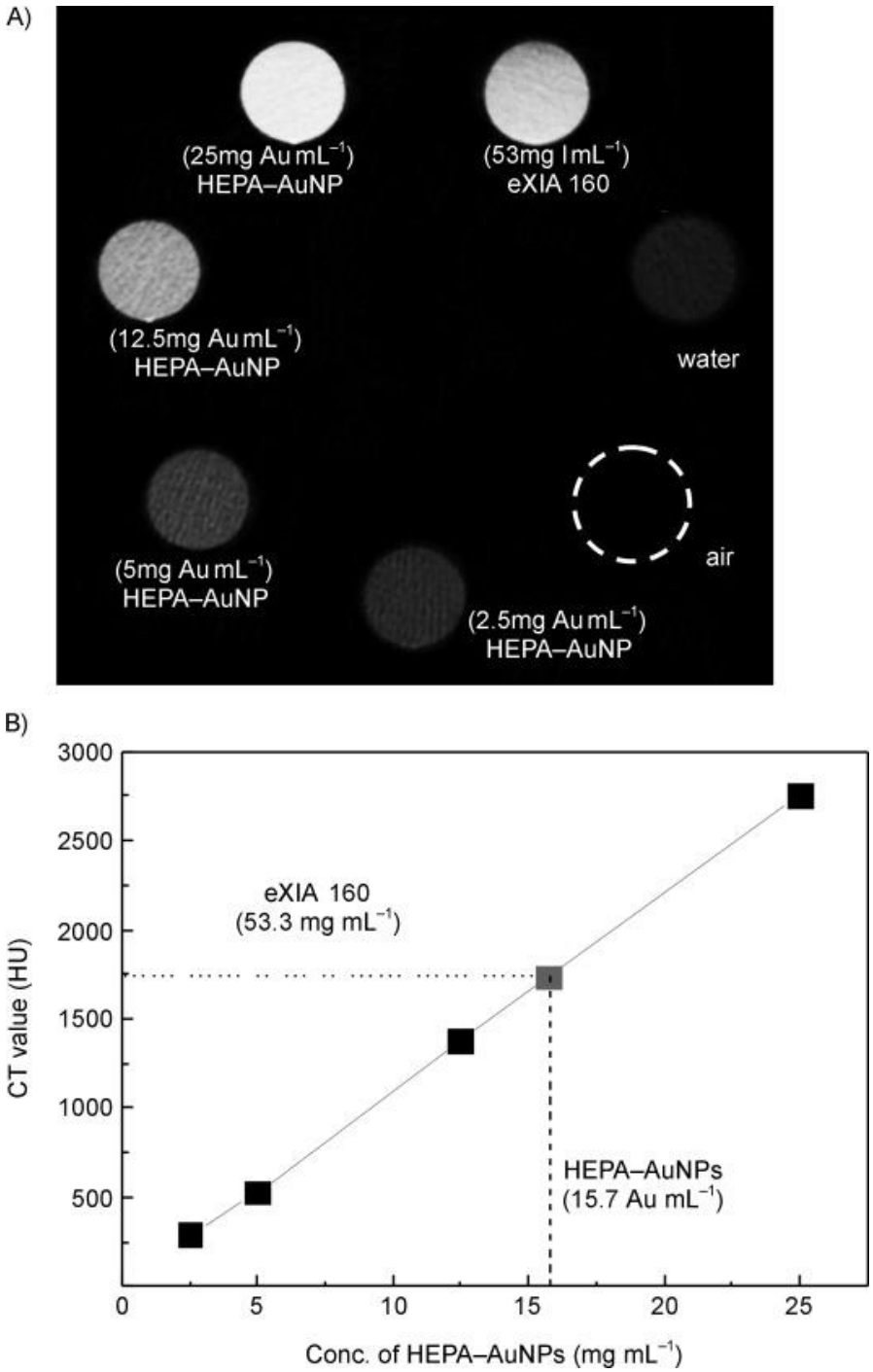

Figure 8. *XCT contrast assessment of gold nanoparticle nanoparticles at varied concentrations in comparison with an iodinated contrast agent, eXIA-160. (A) is a 2D image slice of phantoms containing the contrast agents and (B) is a plot of the concentration of gold nanoparticles and the CT value (in Hounsfield units) they produce. Equivalent contrast was achieved between the gold nanoparticles and the eXIA-160 contrast agent at approximately 15.7 mg Au / mL. Figure from Sun et al. (2009).*

A prominent consideration for the use of AuNPs as a contrast agent within biological systems is that they can be prone to instability and aggregation in environments that are saline, acidic and/ or contain matter with strong surface charges (Diegoli *et al.*, 2008; Zakaria *et al.*, 2013). All these effects may strongly and negatively influence their transport and other behaviour. In addition to functionalisation for targeted accumulation, the goal of enhancing the stability of AuNPs in adverse conditions is a strong motivation for employing coatings (Bergen *et al.*, 2006). For example, Bergen *et al.* (2006) noted that where a polyethylene glycol (PEG) coating was applied to AuNPs, the severity of aggregation could be significantly reduced in the presence of adverse salt conditions (***Figure 9***). This was true of both positively and negatively charged AuNPs at a range of particle sizes.

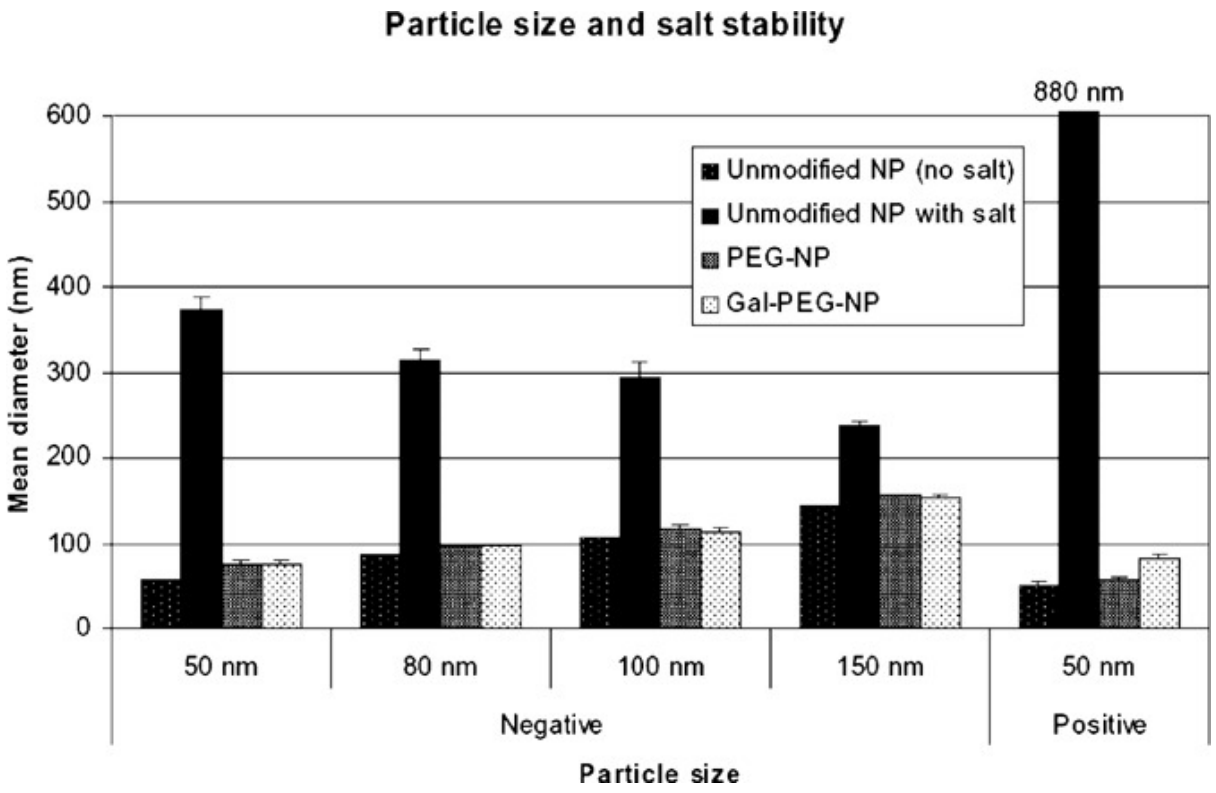

Figure 9. *A graph displaying the presence of aggregation of nanoparticles in saline conditions before and after PEG coating. The salt concentration used was 150×10^{-3} M NaCl. Where non-coated nanoparticles are exposed to the saline conditions the mean diameter is significantly increased suggesting aggregation has taken place. Figure from Bergen et al. (2006).*

1.4.2 Bismuth Sulphide Nanoparticles

Bismuth sulphide is another non-radioactive heavy metal that has previously been trialled as contrast agent, though to a more limited extent than gold. Research undertaken by Rabin *et al.*

(2006) used polymer coated bismuth sulphide nanoparticles to image the vasculature, liver and lymph nodes in mice and returned positive results. The coated nanoparticles they produced were capable of an X-ray attenuation five times greater than achieved using equivalent concentrations of iodinated agents. The human toxicity profile was reported to be similar to currently used iodinated contrast agents, and the stability of the suspensions would only begin to become compromised above around 0.25 M Bi^{3+}. Though it was reported that approximately 0.55 M Bi^{3+} was required to provide equivalent contrast to a 2.4 M iodine solution (300 mg I / mL), the concentration of iodine used by Keyes *et al.* (2017b) to achieve contrast was only 75 mg I / mL. Therefore, this reported 0.25 M Bi^{3+} stability limit should be in excess of the concentration needed for application to root imaging. The XCT images of the bismuth sulphide nanoparticles in mice demonstrate the potential for obtaining good contrast in localised regions (***Figure 10***).

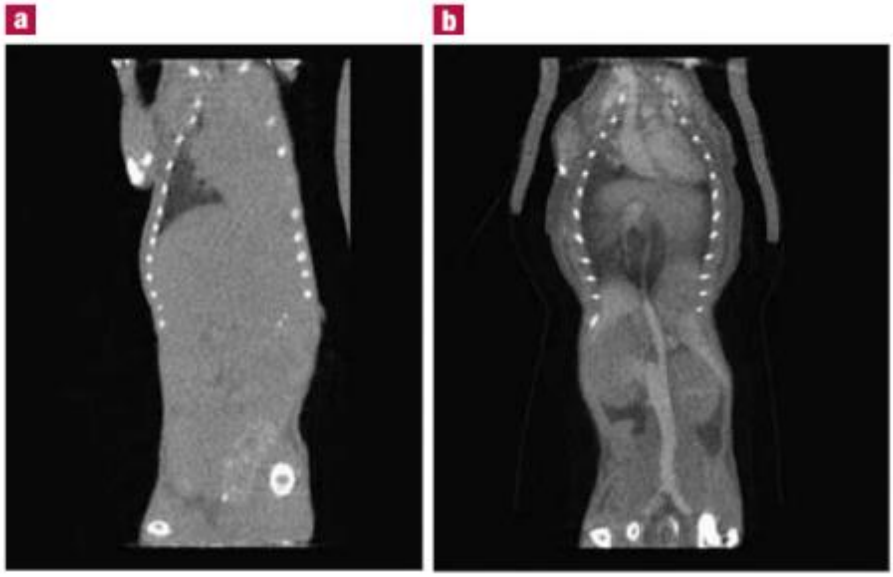

Figure 10. *A reconstructed X-ray CT image of a live mouse before (a) and after (b) the intravenous administration of bismuth sulphide nanoparticles. Image b displays the significant contrast enhancement of large vascular vessels and the heart provided by the addition of bismuth sulphide nanoparticles as a contrast agent. Figure from Rabin et al. (2006).*

Similar to AuNP functionalisation, there is also some limited evidence of bismuth sulphide nanoparticles being used as a tissue specific contrast agent. Kinsella *et al.* (2011) used bismuth sulphide nanoparticles labelled with a "homing peptide", LyP-1. This peptide targets and becomes bound to breast tumour lymphatic vessels (Zhang *et al.*, 2012), and this bismuth sulphide- peptide

complex was used to image breast cancer tumours in mice. The peptide-labelled bismuth sulphide particles were recorded at three times the concentration of non-labelled Bi_2S_3 particles in tumour tissues, and meaningful (tumour contrasted) CT images were captured. This demonstrated the possibility of functionalised bismuth sulphide nanoparticles as an alternative contrast agent to AuNPs.

This research by Kinsella *et al.* (2011) did however indicate that a significant proportion (the exact ratio was unknown) of the nanoparticles had been reduced in radius and were thought to have degraded to ionic bismuth. In addition to this, a similar proportion of ionic bismuth was found aggregated in lung tissues neighbouring the breast tumour regions. Whilst not overtly toxic, bismuth is thought to affect protein synthesis, protein mediated transport mechanisms and cell viability in plants (Babula *et al.*, 2008). If bismuth sulphide nanoparticles were applied to plants *in vivo* and a similar degradation were to take place, then plant health could be significantly impacted. Ultimately, the major limitation of bismuth sulphide nanoparticles as a contrast agent in plants is the lack of literature regarding both their use as a contrast agent and effect on plant growth and development. It is noted by Babula *et al.* (2008) and Kinsella *et al.* (2011) that literature regarding bismuth phytotoxicity and the use of bismuth sulphide as a contrast agent, respectively, is limited at present and requires much further work.

1.5 Other Contrast Agents

In addition to iodinated and nanoparticle systems, there are other classes of agents which have been used to varying extents as biomedical contrast agents. The reason for their inclusion within this 'other' section is that they are anticipated to be prohibitively phytotoxic or otherwise unsuitable for application to plant systems. However, they shall be briefly summarised and these assertions of unsuitability justified nonetheless.

Cesium chloride has previously been used as an XCT contrast agent in porous media imaging. Schnaar and Brusseau (2005) used cesium chloride to identify the behaviour of liquid phases within three porous media as a function of the porous media texture. Cesium chloride produced adequate contrast within the liquid phase for characterisation by image processing. However, it is believed that the cesium chloride may affect the behaviour of the liquid phase by decreasing the contact angle at primary particle surfaces by up to 15-20° (Barranco *et al.*, 1997). Shalygo *et al.* (1998) observed that, where barley (*Hordeum vulgare* L.) leaves were incubated with cesium chloride, photodynamic leaf lesions developed within 24 hours. This was caused by an inhibition of the

enzyme uroporphyrinogen III decarboxylase responsible for tetrapyrrole biosynthesis (tetrapyrrole being a photo-desensitiser). This adverse reaction to cesium chloride renders it unsuitable for use as a contrast agent in plant systems.

Barium sulphate suspensions have for many decades been used for gastro intestinal X-ray imaging. It is low cost, considerably more X-ray attenuating than human soft tissues (Bontrager & Lampignano, 2013) and can be administered orally as a suspension (know colloquially as a 'barium meal'). Despite its widespread medical use, it is likely not suitable for use in plant and soil systems. The concentrations of barium sulphate suspensions used for clinical CT imaging result in a very viscous suspension (Li *et al.*, 1992; Anderson *et al.*, 2010), such that mobility of the material through soils and plant vasculature would be insufficient for effective translocation. Furthermore, it has often been noted that barium sulphate mixtures are prone to agglomeration when kept at high concentrations for prolonged periods (Smith & Puddington, 1960; Balastre *et al.*, 2002; Pieper *et al.*, 2012). This would likely further increase the viscosity of the mixture, reducing its appropriateness for soil and plant systems.

It should be noted that there are likely many alternative potential contrast agents not currently explored in detail within the existing literature – even fewer contrast agents are explored specifically within biomedical literature. For example, other radiopaque heavy metals could theoretically act as effective contrast agents with regards to generating contrast, though toxicity effects would have to be considered. Many potential alternative contrast agents, including heavy metals, could exert toxic effects on biological tissues and this is likely why they are not currently explored in biomedical literature. However, such toxic effects would not necessarily preclude them from use in soil imaging applications.

1.6 Contrast Agents in Soil Imaging

In addition to using contrast agents within plant tissues to enhance XCT imaging, there is much scope for utilising contrast agents in soil. Radiographic contrast agents can be used within porous media soil systems to map macropore structure, identify organic matter, assess preferential solute transport and quantify 3D patterns of fluid movement. Much of this information could be otherwise difficult to capture in intact soil systems containing live plants if using traditional methods such as dissections or soil coring.

Iodinated contrast agents are particularly suited to use as flow tracers in porous media as they possess numerous beneficial traits. As mentioned previously, iodinated contrast agents are

generally comparatively unreactive (Aspelin, 2006; Lusic & Grinstaff, 2013). This is of particular importance for scenarios in which contrast agents are to be used in systems containing live organic tissues or where it is necessary that the contrast agents can translocate freely through porous media structures without becoming immobilised. Further to this, the high solubility of iodinated contrast agents and potential to possess a viscosity similar to water means that such contrast agents can act as an ideal analogue for mobile solutes in flow tracing settings. For these reasons, iodinated contrast agents are widely used to map gastrointestinal and vascular flow in biomedicine and clinical practice (Gertz et al., 1985; Blachar et al., 2001; Lusic & Grinstaff, 2013).

There are several examples within the literature of the use of ionic iodinated contrast agents for soil porous media flow imaging using XCT. For example, Heijs *et al.* (1996) used KI to investigate moisture distribution patterns in both a clay-rich soil and a water repellent sandy soil. By comparing XCT images of the soils when dry with images of the soils containing KI enriched water, they were able to capture the soil bulk density, moisture distribution patterns and determine macropore networks. Similarly, Koestel and Larsbo (2014) used time-lapse XCT imaging to capture the preferential flow patterns of KI solutions through soil columns under steady state hydraulic conditions. With this technique they were able to observe that solute transport primarily occurred in just two macropores and from these macropores the KI solution then diffused into the surrounding soil pore space – therefore by-passing much of the soil matrix. Using such a time-lapse imaging regime it becomes possible to capture all manner of time-resolved data, including capturing the interactions between root water uptake and fluid flow dynamics in soil. For example, iodinated contrast agents could be used as an XCT-visible analogue for agrichemical solutes in order to study infiltration patterns through soil.

Radiographic contrast agents have also been used to locate soil organic matter in soil. Peth *et al.* (2014) developed a technique in which XCT-visible osmium is used to stain soil organic matter in soil samples with contrasting carbon contents. Using synchrotron XCT imaging it was possible to capture heterogeneous distributions of soil microbes and plant-derived organic matter and relate this data to the pore network of the soils. Rawlins *et al.* (2016) also used osmium to stain soil organic matter and were able to study the influence of the accessibility and distribution of soil organic matter on soil microbial respiration. From this work they were able to deduce that soil aggregate surface area can affect soil microbes' access to soil organic matter and therefore alter microbial respiration rates. However, a major consideration for the use of osmium is the risk of toxic effects on biological tissues - in particular in the oxidised form, osmium tetroxide, which can cause substantial damage to biological tissues (Brunot, 1933; Griffith, 1974; Smith *et al.*, 1974; McClellan,

2001). It is therefore not possible to use osmium for time-resolved experiments which are to include *in vivo* plant tissues as the substantial tissue damage would likely affect plant behaviour.

It is important to note that a number of challenges are presented with regards to the use of contrast agents in soil. The heterogeneous nature of soil pH, salinity and surface charge has already been mentioned in section 1.2.2 'Desirable Traits for Plant and Soil Contrast Agents', however soils also present additional difficulties. The structure of soil porous media is generally complex and therefore it can be difficult to anticipate fluid dynamic behaviours within soil networks. Though much work has been undertaken to investigate such behaviours, for example the work of Koestel and Larsbo (2014) mentioned above, this makes it difficult to design experiments when the patterns of fluid flow over time are unknown. The complex structure of soil porous media also creates practical difficulties for the application of the contrast agents to the soil system. Given that macropores can dominate preferential fluid flow (Koestel & Larsbo, 2014), some methods for introducing contrast agents into soil may be unsuitable, such as injection. Instead, it may be preferable to apply contrast agents to exposed surfaces of the soil system, though this could require a greater amount of time for translocation to a desired site within the soil. These are important considerations when designing practical imaging experiments.

1.7 Summary and Conclusions

The relative suitability of different contrast agents for plant and soil applications has been considered, with a focus on agents already used in such contexts as well as those with promising attributes that may suit such applications. These were compared against criteria deemed necessary for successful use as either flow tracers or as functionalised, tissue-specific contrast agents. Whilst it is unfortunate that there is limited literature regarding the use of contrast agents within plant and soil systems, there are a number of extant toxicity and imaging studies in the biomedical domain, which were used to provide insight into potential behaviour in phytological systems. The relative benefits and limitations of the main candidates (ionic iodinated, non-ionic iodinated and AuNP contrast agents) are presented below in ***Table 1***.

Following this review, it is apparent that iodinated contrast agents are well suited to flow tracing and non-specialised, whole organ imaging. Non-ionic contrast agents possess particularly advantageous attributes for this application, commonly available in forms with low viscosity, low osmolality and comparatively minimal phytotoxic effects. Iodinated contrast agents are also the only contrast agent class for which there is direct evidence of application to CT imaging of soil-borne

roots. However, if contrast agents are required to remain contained within vasculature, or there is risk of 'leaching' into soils, then ionic alternatives could be considered. This is because ionic iodinated contrast agents are less prone to equilibration.

With regard to tissue-specific contrast agents, the capacity for functionalisation of metal nanoparticles is beneficial. The advantage of AuNP systems is the relative abundance of literature regarding their use as a functionalised X-ray contrast agent, their use in plants, and an existing understanding of potential phytotoxic effects. Research into coating methodologies is well advanced, and a number of the possible challenges in adaptation for plant and soil use may be mitigated by the ability to draw upon existing research from other domains. However, from the limited literature available, bismuth sulphide nanoparticles may be a less toxic and more stable alternative to AuNPs at equivalent concentrations. The most pressing limitation surrounding the use of bismuth sulphide nanoparticles is the lack of literature regarding their phytotoxicity and transport behaviour in plants.

The two other extant contrast agents systems investigated are highly unlikely to be suitable for use in plant root imaging. Cesium chloride is excessively toxic to plants causing severe lesions in leaf tissues within only 24 hours. Barium sulphate requires application at such a high concentration that viscosity becomes prohibitively high, and suspensions are prone to agglomeration, further contraindicating their use in the small transport vessels of plants.

Ultimately, the behaviour of all the contrast agents discussed requires further research in plant systems in order to enable development of protocols suitable for plant science applications. Hopefully in time this could provide similar utility and benefit to the mature protocols used in the biomedical sciences. The major challenges to be addressed in all scenarios is optimising the contrast agent toxicity and stability against the degree of contrast enhancement attainable.

Table 1. *A comparison of the relative benefits and limitations of ionic iodinated, non-ionic iodinated and gold nanoparticle contrast agents.*

Characteristic	Ionic Iodinated	Non-Ionic Iodinated	Gold Nanoparticles
Viscosity	Viscosity often similar to water though variable with dilution	Monomeric variants potentially have lower viscosity than dimeric variants	Dependent on nanoparticle concentration. Low viscosity if applied at low concentrations
Phytotoxicity	Comparatively high osmolality. Can cause osmotoxic shock.	Comparatively low osmolality. Low reactivity.	Small particles (≤3.5 nm) observed to induce leaf necrosis in tobacco seedlings
Flow Tracer	Well suited to use as a flow tracer owing to viscosity and low cost	Well suited to use as a flow tracer provided viscosity is low though cost can be greater than some ionic variants	Concentrations necessary to achieve sufficient contrast in suspension are expensive. Possibility of instability at high concentrations
Functionalised	Not functionalised	Not functionalised	Can be functionalised for accumulation on specific surfaces/ tissues
Used in Soils Before	Widely used for soil imaging applications	Little evidence of use in soil – ionic alternatives are used instead	Not used in soil imaging. Too expensive relative to ionic iodinated alternatives
Used in Plants Before	Used to image *ex vivo* leaf material and *in vivo* root material. Observed to induce root tissue damage.	Used to image *ex vivo* leaf material and *in vivo* root material. Observed to induce comparatively less root tissue damage.	Not previously used in plant XCT imaging. Only previously used in bioremediation applications, assessing phytotoxicity and microscopy imaging.

1.8 Thesis Aims and Structure

Informed by the conclusions of the literature review, the aims of the research presented in this thesis were to develop approaches to enhance the study of plant and soil structures using different contrast agent classes and to then apply the contrast agents to capture the movement of solutes through soil and roots. The scientific chapters of this thesis are in the form of three research papers

adapted for this thesis – two of which are published whilst the third is currently submitted and undergoing peer-review.

In Chapter 1 the potential of AuNPs as a future candidate contrast agent for use in plant and soil imaging was highlighted. However, in the review of the literature it is noted, based on biomedical research, that a challenge in utilising AuNPs for this application is the instability of AuNP suspensions in the presence of acids, salts and strong surface charges. Polymer coatings have been identified as a solution to these instability issues. In Chapter 2, published as Scotson *et al*., (2019), we characterise the aggregation of non-coated AuNPs and successfully achieve the stabilisation of AuNPs within soil conditions using a polyethylene glycol coating. This paper represents a significant development in the use of AuNPs as a contrast agent in plant root and soil imaging settings.

It was also apparent from the review of the literature in Chapter 1 that iodinated contrast agents are well suited to fluid flow tracing applications in porous media and soil. In Chapter 3, published as Scotson *et al*., (2020a), we use a non-ionic iodinated contrast agent to capture fluid flow through flat and ridged soil surface geometries using XCT imaging and compare experimental imaging results with simulation results of models based on the work of Duncan *et al*., (2018a; 2018b). We use the iodinated contrast agent as an analogue for agrichemical solutes to study the influence of soil surface geometry, plant roots and soil surface ponding on patterns of solute infiltration and vulnerabilities to solute leaching. This study provides insights into factors which affect solute uptake efficiency and demonstrates the efficacy of iodinated contrast agents for studying fluid flow patterns in plant and soil systems.

In Chapter 4 we present a manuscript, currently submitted for publication and under peer review, in which we design and construct an experimental system for applying iodinated contrast agents directly to roots in soil which is compatible with *in vivo* synchrotron XCT imaging. The translocation of iodinated contrast agent movement through plant vasculature from the roots to the leaves is captured using a combination of synchrotron XCT and synchrotron X-ray fluorescence mapping. Using our experimental system iodinated contrast agents can overcome contrast to noise ratio issues of roots in soils to aid segmentation of roots, capture internal fluid flow in roots and root anatomical features which otherwise would likely require destructive techniques.

Finally, in Chapter 5 we provide a summary of the work undertaken and discuss how this research contributes towards achieving the aims of this thesis. We also note limitations of the studies presented and provide examples of the opportunities for further work and development.

2 Stabilising Gold Nanoparticles for use in X-ray Computed Tomography Imaging of Soil Systems

2.1 Authors

Callum P. Scotson[1], Maria Munoz-Hernando[2], Simon J. Duncan[1], Siul A. Ruiz[1], Samuel D. Keyes[1], Arjen van Veelen[1], Iain E. Dunlop[2], Tiina Roose[1]

[1]Bioengineering Sciences Research Group, Mechanical Engineering, Faculty of Engineering and Physical Sciences, University of Southampton, Southampton, UK

[2]Department of Materials, Faculty of Engineering, Imperial College London, London, UK

2.2 Abstract

This investigation establishes a system of gold nanoparticles that show good colloidal stability as an X-ray computed tomography (XCT) contrast agent under soil conditions. Gold nanoparticles offer numerous beneficial traits for experiments in biology including: comparatively minimal phytotoxicity, X-ray attenuation of the material and the capacity for functionalisation. However, soil salinity, acidity and surface charges can induce aggregation and destabilise gold nanoparticles, hence in biomedical applications polymer coatings are commonly applied to gold nanoparticles to enhance stability in the *in vivo* environment. Here we first demonstrate non-coated nanoparticles aggregate in soil-water solutions. We then show coating with a polyethylene glycol (PEG) layer prevents this aggregation. To demonstrate this, PEG-coated nanoparticles were drawn through flow columns containing soil and were shown to be stable; this is in contrast with control experiments using silica and alumina-packed columns. We further determined that a suspension of coated gold nanoparticles which fully saturated soil maintained stability over at least five days. Finally, we used time resolved XCT imaging and image based models to approximate nanoparticle diffusion as similar to that of other typical plant nutrients diffusing in water. Together, these results establish the PEGylated gold nanoparticles as potential contrast agents for XCT imaging in soil.

2.3 Introduction

X-ray computed tomography (XCT) is a mature technology for biomedical and clinical imaging (Kalender, 2006), and is increasingly used for non-destructive 3D imaging of soil and plant root systems (Mooney *et al.*, 2012; Roose *et al.*, 2016). However, the ability to distinguish easily between soil and plant roots remains a challenge due to overlapping X-ray attenuation of soil pore water and root material (Mooney *et al.*, 2012), in which the resulting poor contrast can complicate image segmentation. Contrast issues also limit sample sizes – the higher X-ray energies required to penetrate larger samples are proportionally less sensitive to attenuation. As a result, the maximum attainable contrast-to-noise ratio (CNR) generally decreases as sample diameter increases (Attix, 2008).

When similar issues occur within biomedical soft tissue imaging, it is common practice to use solutions or suspensions containing radiopaque elements as contrast agents (Lusic & Grinstaff, 2013). A recently introduced class of contrast agent is gold nanoparticles (AuNPs), which have become the focus of much biomedical research interest. This is due to the numerous beneficial traits they present. One such notable trait is the capacity for functionalisation (Sperling & Parak, 2010; Ahn *et al.*, 2013). Functionalisation is the addition of a functional group or protein structure either directly onto the AuNP or onto a coating which envelopes the AuNP (Sperling *et al.*, 2008; Sperling & Parak, 2010). Functionalisation will often be applied to induce accumulation upon specific materials or biological tissues. This is as opposed to tracer contrast agents which are used to trace liquid flows where the intention is that the contrast agent will remain in solution or suspension (Lusic & Grinstaff, 2013). There are numerous applications of functionalised AuNPs as contrast agents in biomedical research (Geso, 2007; Sperling *et al.*, 2008; Sperling & Parak, 2010). For example, Sun *et al.* (2009) used a functional heparin coating on AuNPs to induce accumulation on murine livers and produced much improved contrast against un-treated tissue.

An additional beneficial trait of AuNPs exploited in biomedical applications is the high density and atomic number which cause AuNPs to be X-ray attenuating – possessing considerably greater attenuation than iodinated contrast agents at equivalent concentrations (Lusic & Grinstaff, 2013). The contrast provided by AuNPs has often been observed to be up to 2.7 times greater than iodinated equivalents (Xu *et al.*, 2008; Sun *et al.*, 2009). Therefore, lower concentrations of AuNPs can achieve comparable contrast to iodinated contrast agents.

In contrast to these advantageous traits however, AuNPs have previously been observed to become unstable and undergo aggregation when exposed to strong surface charges, salinity and acidity (Diegoli *et al.*, 2008; Tourinho *et al.*, 2012; Zakaria *et al.*, 2013). These are all common conditions in

both soil and biological systems. In biomedical research, the application of a Polyethylene Glycol (PEG) coating to the surface of AuNPs has previously been found to overcome the destabilising effects of saline and/ or acidic conditions (Bergen *et al.*, 2006; Sperling & Parak, 2010). Therefore, such coatings ensure stability of the AuNPs in suspension. The PEG coating also replaces the need for stabilising agents in the solvent, such as citrate solution, which cannot be maintained in most biological systems.

While the utility of AuNPs is frequently explored in biomedical applications and research, use of AuNPs as an XCT contrast agent has not been attempted for plant roots in soil. AuNPs have seen limited use as a radiographic contrast agent in plants and only in non-soil-borne tissues. However, they have presented promising results in the few studies in which AuNPs were applied to *ex vivo* plant material. For example, Ahn *et al.* (2010) submerged dried rice leaf sheaths in an AuNP suspension. The xylem vessels of the leaf sheaths then filled with the AuNP suspension through capillary action, and resulted in the AuNP suspension significantly improving radiographic contrast of xylem structures. However, the use of dried plant tissue outside of soil is unrepresentative of the *in vivo* and *in situ* processes. Furthermore, the domain in which XCT has demonstrated great potential is for imaging roots in soil.

In addition to those traits exploited in biomedical applications, AuNPs offer a number of favourable traits that particularly relate to use in soil and plant root systems. In particular, AuNPs present comparatively less phytotoxicity relative to alternative contrast agents such as iodinated equivalents (Sabo-Attwood *et al.*, 2012; Taylor *et al.*, 2014). For example, when tobacco (*Nicotiana xanthi* L.) seedlings were exposed to AuNP suspensions, the AuNPs only appeared to induce visually observable leaf damage after fourteen days of exposure (Sabo-Attwood *et al.*, 2012). By comparison, Keyes *et al.* (2017b) exposed winter pea (*Pisum sativum* L. cv. frisson) to an iodinated contrast agent (Gastrografin) and observed severe tissue damage after one day. It is noted that different species may tolerate such contrast agents to a different extent, however the scarcity of literature on the subject makes direct comparisons difficult. Additionally, Sabo-Attwood *et al.* (2012) only exposed juvenile plants to AuNPs, which should have a lower capacity to tolerate AuNPs as the particles could only be dispersed over a relatively smaller volume of tissue. Sabo-Attwood *et al.* (2012) also highlighted that the range of available AuNP particle sizes enables selective uptake by organic tissues. Smaller AuNPs (3.5 nm) were observed to have reached the leaves whereas the larger size of AuNPs used (18 nm) were not detected within the plant vasculature, but instead remained agglomerated on the surface of the roots.

At present however, the full potential of AuNPs as a contrast agent for use in soil systems has not been realised, because they are susceptible to aggregation or degradation and do not remain in suspension, *i.e.* they destabilise (Nowack & Bucheli, 2007; Hotze *et al.*, 2010; Tourinho *et al.*, 2012). This in turn compromises the transport of the AuNPs through soil pore spaces and prevents them from targeting tissues for functionalisation. AuNPs in soil are not only exposed to salinity and acidity, as in biomedical applications, but also the destabilising effects of soil particulate surface charges. Furthermore, the pH and salinity conditions in soil-water solution or plant tissue fluids are likely more heterogeneous than mammalian fluids. For example, in a healthy human adult it is unusual for blood pH to vary from the baseline of approximately 7.4 by more than 0.1 (Sinet *et al.*, 1985), whilst the pH of soil solutions from UK soils range between approximately 4 and 8 (Tinker & Nye, 2000) with additional variation present in intra-substrate niches. For AuNPs to be successfully transferred from current biomedical applications to plant root and soil systems, stability of the AuNPs must be achieved in these complex biogeochemical environments. It is therefore important to establish whether PEG coating procedures, used in biomedical applications to overcome destabilising effects, are sufficient for use in soil systems.

The aim of this investigation is to ensure stability of AuNPs under different soil conditions. This includes the use of a PEG polymer coating to mitigate destabilising properties of the soil environment. We hypothesised that non-coated gold nanoparticles (NC-AuNP) would become destabilised if exposed to the strong particle surface charges, salinity or acidity, which often characterise soil systems. Further, we hypothesised that application of a PEG coating to gold nanoparticles (PEG-AuNP) would mitigate against these destabilising effects and keep the AuNPs within a stable suspension. In order to assess the effects of PEG coating on AuNP stability in soil, the following procedures were undertaken. First, the stability of NC-AuNPs was assessed using a selection of soil-water solutions, with the degree of aggregation quantified using ultraviolet-visible spectroscopy (UV-Vis). Based on the results of this stability test, the AuNPs underwent a PEG coating procedure and were tested for stability in soil-water solutions a second time. Following stabilisation in soil-water, the PEG-AuNP suspensions were assessed for their stability when drawn through flow columns of porous media. The suspensions were first assessed in columns containing alumina and silica particles, which possess strong surface charges, to characterise AuNP behaviour when destabilised by particles in a 'soil-analogue' porous medium. Scanning electron microscopy (SEM) was used to further characterise AuNP destabilisation in the columns, and a mathematical model was used to estimate a lower bound of the buffer power for AuNPs in silica and alumina. The stability of the PEG-AuNP suspensions was trialled in the soils using flow columns containing the soils and by fully saturating the soils with a concentrated suspension of the PEG-AuNP. Finally, the

utility of PEG-AuNPs as tracer contrast agents was assessed by estimating the diffusion rate of AuNPs in soil water, using a combination of time resolved XCT imaging and mathematical modelling.

2.4 Materials and Methods

2.4.1 Preparation of Soil-Water Solutions

To quantify the influence of real soil-water acidity and salinity on NC-AuNP and PEG-AuNP stability, soil-water solutions were first prepared. These were extracted by centrifugation from samples of three soils excavated from field locations across the UK. Those three field locations were in the following regions: Bangor, Dundee and Nottingham and the three soils are referred to by their geographical origin hence forth (detailed information about the three soils is given in ***Table 2***).

Table 2. *Information on the three field soils used in this investigation including: soil type and geographic location of origin.*

Soil Name	Soil Type	Geographic Origin
Bangor	Sand-textured Eutric Cambisol	Abergwyngregyn, North Wales, UK (53.014'N, -4.001'W)
Dundee	Sandy-loam Dystric Cambisol	South Bullionfield, James Hutton Institute, Dundee, UK (56.273'N, - 3.041'W)
Nottingham	Sandy-loam Eutric Cambisol	University of Nottingham farm, Bunny, Nottinghamshire, UK (52.860'N, -1.141'W)

For the preparation of the soil-water solutions, each soil was sequentially sieved using British Standard geotechnical sieves (Glenammer Engineering, Ayr, UK) of 2 mm and 1.18 mm aperture size. From the <1.18 mm fraction of each soil type, a homogenised 10 g was placed into a 50 mL centrifuge tube, 15 mL of UHQ water (ultrapure water – water purity Type 1 as described by ISO 3696) was added, and the tube was shaken vigorously for one minute. All tubes were then agitated on laboratory rollers for 48 hours, allowing the soil water solution to equilibrate.

The tubes underwent centrifugation using a Sorvall Legend XTR (Sorvall, UK) at 8000 revolutions per minute (RPM) for 30 minutes at 20 °C in order to separate the solids from the soil solution. After centrifugation, the supernatant was removed from each tube using a 10 mL syringe in series with a 0.45 µm Millex HA syringe filter tip. This step removed soil particles that may have re-suspended following centrifugation. The resulting soil-water solutions contained many of the soil-borne acids

and salts. Therefore, these solutions were used to test the stability of the AuNPs under acid and salt conditions representative of those expected in soil environments. This protocol was executed twice for each of the three soil types: once when stored at room temperature and another where they were kept in a 3 °C fridge. This was to ensure changes of acidity with temperature could be considered. Ionisation can increase with temperature thus more H^+ ions will become active and the solution will become more acidic.

2.4.2 pH of Assay of Soil-Water Solutions

The pH was determined for the three soil-water solutions. The pH test panel comprised both sets of soil-water solutions for each of the three soils: those stored at room temperature and those stored at 3°C. Measurement of pH was conducted 24 hours after preparation using an Accumet AB150 pH testing probe (Fisher Scientific, UK). A three point calibration using pre-prepared buffer solutions at pH 4.01, 7.00 and 10.00 was used to ensure accuracy of the pH measurements.

2.4.3 Characterisation of Soil-Water Solution Composition

In order to characterise the composition of the soil-water solutions, high resolution Inductively Coupled Plasma Mass Spectrometry (HR-ICP-MS) was conducted using a Thermo Fisher Scientific ELEMENT 2XR (Thermo Fisher Scientific, UK) at the National Oceanography Centre, Southampton. A sub-sample of each of the three soil-water solutions was prepared for ICP-MS using a multi-step digestion procedure. The initial step in the digestion procedure was the addition of 2.5 mL aqua regia to 1 mL of the soil-water solution to digest and oxidise the potential colloids and the majority of the dissolved organic matter. This solution was left on heat plates in a fume cupboard until the aqua regia had evaporated. Following this, 6 M hydrochloric acid (HCl) was applied to the soil-water solutions to digest any remaining organic matter and once again left on heat plates in a fume cupboard for the HCl to evaporate. The final stage of the sample preparation was the addition of 3% nitric acid (HNO_3), which contained beryllium, indium and rhenium as internal standards. These were used as standards since they were unlikely to be found within the samples, had few spectral inferences with analytes of interest and would be chemically stable in these solutions.

2.4.4 Assessment of AuNP Stability in Soil-Water Solutions using UV-Vis

Ultraviolet-visible spectroscopy (UV-Vis) is often used for determining AuNP size (Kim *et al.*, 2005; Haiss *et al.*, 2007; Kim *et al.*, 2008; Zakaria *et al.*, 2013), and to indicate the prevalence of

aggregation or degradation of AuNPs as a result of instability. UV-Vis, using a Shimadzu UV-1800 spectrometer (Shimadzu, Japan), was used to assess stability of AuNPs in the soil-water solutions and to inform whether it was necessary to coat the AuNPs in order to enhance stability and prevent aggregation.

For the UV-Vis analysis, 100 nm AuNPs (Sigma Aldrich, UK) at the manufacturer-supplied concentration of $3.84x10^{-2}$ mg Au/ mL were added to aliquots of each of the three soil solutions. AuNPs of 100 nm size were chosen for two reasons. Firstly, were plants to be included within experimental setups of future work, 100 nm AuNPs are too large to be taken up through pores in plant root cell walls (Asli & Neumann, 2009). Secondly, the polymer coating procedure, described in section 2.4.5 Polymer Coating Process, required several rounds or centrifugation. The ease of performing centrifugation is considerably improved for larger particle sizes as they possess a greater mass and thus require a lower RPM for successful centrifugation. Time-resolved UV-Vis analysis was undertaken on the following samples for NC-AuNP and PEG-AuNP suspensions: soil solution mixed with AuNPs, soil solution, UHQ water, and UHQ water mixed with AuNPs. The total volume of each aliquot was 4 mL, at a ratio of 1 mL AuNP to 3 mL of either soil solution or UHQ water.

2.4.5 Polymer Coating Process

The polyethylene glycol polymer used for the coating process was an α-methoxy-ω-mercapto PEG (CH_3O-PEG-SH) with a molecular weight of 5 kDa (Rapp Polymere, France). A standard PEG coating protocol (Jokerst *et al.*, 2011) was applied wherein the stabilising citrate suspension in which the AuNPs are supplied is replaced by the stabilising PEG coating. To attach the PEG chains to the surface of the AuNPs, the PEG polymers were first dissolved in UHQ water at a concentration of 5 mg PEG / mL UHQ. A suspension of 100 nm AuNPs at a concentration of $3.84x10^{-2}$ mg Au / mL (Sigma Aldrich, UK) was then mixed with the PEG-UHQ solution at a ratio of 1:1. The mixture was wrapped in foil to avoid light exposure and then left to incubate for one hour at room temperature. This suspension of PEG-AuNP complexes was then purified using a centrifugation method. For the purification, 80 mL of the suspension was split evenly across two 50 mL Falcon™ tubes with 40 mL in each tube. These were then centrifuged using a Thermo Scientific Heraeus Biofuge Primo R Centrifuge for 15 minutes at a force of 5000 RCF. Following centrifugation, the PEG-AuNP formed a pellet in the base of the centrifuge tube above which was a supernatant largely consisting of excess dissolved PEG and citrate buffer from the initial AuNP suspension. This supernatant was removed to prevent any possible osmotic effects which may have been induced by the excess PEG and the

remaining pellet of PEG-AuNP was re-suspended using UHQ water to a volume of 20 mL per Falcon™ tube. These Falcon™ tubes were again centrifuged for 15 minutes at a force of 5000 RCF and the supernatant was removed though this time the pellet of PEG-AuNPs were resuspended to a total volume of 1 mL per Falcon™ tube. The two 1 mL volumes were then transferred into 1.5 mL Eppendorf tubes. Centrifugation was undertaken once more using the 1.5 mL Eppendorf tubes for 15 minutes at 4000 RCF. Following centrifugation 800 µL was removed from each of the 1 mL mixtures to leave 200 µL of PEG-AuNPs at a concentration of 3.84 mg Au / mL – the concentration to be used in XCT imaging. Given that there were two Eppendorf tubes this led to a total output of 400 µL of PEG-AuNP suspension.

2.4.6 Assessment of Gold Nanoparticle Stability in Soil

To ascertain the influence of soil particle surfaces on PEG-AuNP transport and stability, a dynamic column transport experiment was set up. In this experiment, both single-material soil-analogues and the field soils were studied. Alumina (Al_2O_3) and silica (SiO_2) powders were chosen as initial substrates to examine the influence of 'worst case scenario' contrasting surface charges in the absence of salinity and pH effects. Silica has a point of zero charge at pH ~3 (Kim & Lawler, 2005) whilst alumina has a point of zero charge at pH ~9 (Kosmulski, 2009). The PEG-AuNPs were anticipated to aggregate within this material, thus the intention was to characterise aggregation within a porous medium as a point of reference and comparison for PEG-AuNP stability in the subsequent soil column experiments. Any spatial pulse movement in the experimental system was observed and quantified using XCT imaging every 24 hours and scanning electron microscopy (SEM) imaging was used to characterise the interaction between silica, alumina and PEG-AuNPs in greater detail. The system was then also represented using a mathematical model to quantify a lower bound estimation for the buffer power of PEG-AuNPs in silica and alumina.

Experimental Assessment of Gold Nanoparticle Stability in Soil

Experimentally this system was constructed using 1 mL syringes, with a length of 70 mm and internal diameter of 4.88 mm, for the column (***Figure 11***). These syringes were held tip down in a vertical orientation. To prevent granular media from leaving the system, cotton wool was placed at the base of the syringe and lightly packed to fill a depth of 4 mm from the base. A silicon-rubber O-ring was then placed above the wadding to secure it in place (***Figure 11***). For the soil-analogue experiment, the syringes were filled with either silica particles of 150-250 µm (Sigma Aldrich, UK),

alumina particles of 50-200 µm (Fischer Scientific, UK), or an equal mixture of both to a depth of 4 cm above the O-ring. The SiO_2 and/ or Al_2O_3 particles were then saturated by injecting UHQ water from the column base using a syringe pump (Harvard PHD 3000, Harvard, US) at a rate of 0.05 mL/ min until the meniscus was level with the upper surface of the granular media.

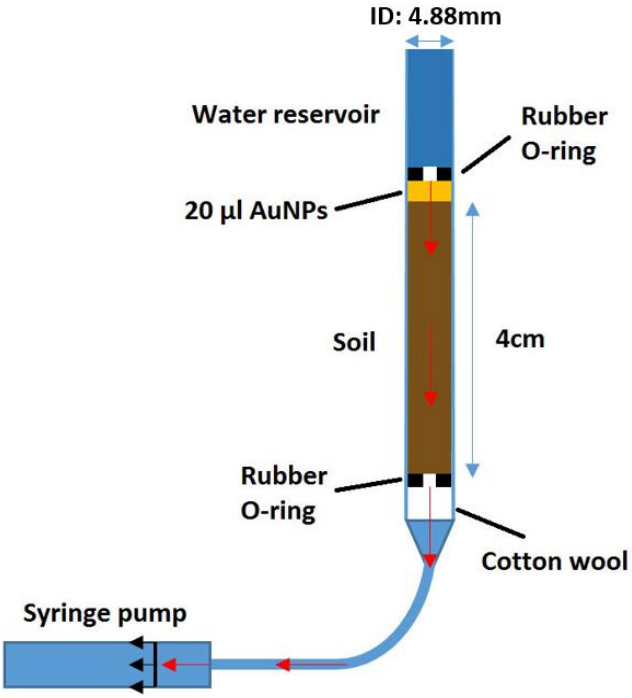

Figure 11. *Diagram of the constructed experimental system to be used for both soil-analogue and soil columns. Red arrows indicate the movement of water through the saturated system.*

Once the column was fully saturated, a 20 µL pulse of PEG-AuNPs at a concentration of 3.84 mg Au / mL was introduced at top of the saturated material via pipette. This concentration, 100 times the concentration of the suspension as supplied from the manufacturer, was used to provide contrast in XCT assessments (Xu *et al.*, 2008; Sun *et al.*, 2009). Another O-ring containing cotton wool in the central aperture was introduced directly above the PEG-AuNPs. This additional O-ring and cotton wool was to prevent flush-back of the PEG-AuNPs during the addition of 0.5 ml of UHQ water above the O-ring (***Figure 11***). The UHQ water added above the O-ring provided the reservoir of fluid required for a constant-flux operation. The constant-flux was applied by drawing fluid through each column with the syringe pump at the pre-determined rate of 0.5 µm s^{-1} – the average maximum velocity of water movement through soil to plant roots (Tinker, 1976). The use of a syringe pump allowed the flux to be set to 0 µm s^{-1} during imaging, reducing the incidence of movement artefacts, or 'blurring' and streaks, during image acquisition. Though the syringe pump is stopped for the duration of imaging, there will still be diffusion taking place. However, given the

short duration of the imaging the diffusion is negligible relative to the flux induced when the syringe pump is running. A total of nine separate replicates of the system were manufactured, providing three replicates each of silica, alumina and the silica/alumina mixture. For the soil experiments, the syringes were filled with field soils in place of the soil-analogue powders. The experimental system with soil was otherwise identical. This soil column system was replicated nine times: three times for each of the three soils.

XCT imaging of the columns was undertaken once daily for a period of three days. After setting the flux to 0 μm s^{-1}, each sample was loaded into an XTH 225 L Industrial CT Scanner (Nikon, UK), and a 2D radiograph of the entire column was acquired at 40 kVp. A plot of average attenuation coefficient with distance down the column was produced to find the depth of the AuNP concentration peak maxima. A tomograph was acquired using a field of view centred on the peak including 2.4 mm of material either side of the peak position. The parameters for the XCT imaging are given in ***Table 4***. Once the imaging was complete the flux was reimposed. The reconstruction was undertaken using CTPro 3D (Nikon, Tokyo, Japan) using a fine scale dual centre of rotation detection.

Image processing of 3D reconstructions was carried out using FIJI (Schindelin *et al.*, 2012). First, a grey-level threshold was defined using the minimum and maximum grey values induced by AuNP accumulation (180 to 500 in a 32bit image, as assessed across multiple positions in different scans). A 3D median filter was then applied using a kernel of 5 pixels in the X, Y and Z axes. This removed the influence of individual pixels of anomalously high grey value. The maximum grey value in each image slice down the column was then recorded and plotted. This was used to capture the AuNP pulse position.

For the silica and alumina systems, SEM was used to further characterise the nature of AuNP and silica/ alumina interaction following the column experiments. Samples were prepared by sectioning a 3 mm horizontal region of each syringe column which contained the AuNPs and the silica or alumina. These samples were air dried and then carbon coated using an Edwards Auto 306 Thermal Evaporator (Edwards, UK). The coating was between 15-20 nm thick of carbon and was applied using 'fine' pumping. SEM imaging was then undertaken in a full vacuum using a Leo 1450 VP SEM (Zeiss, UK) at a range of magnifications from 50 to 30,000×.

UV-Vis analysis, using a Shimadzu UV-1800 spectrometer (Shimadzu, Japan), was also used on extractions of soil-water solutions from the soil columns to assess PEG-AuNP stability. This was applied to the imaged soil columns post-imaging in addition to a further set of non-imaged soil flow columns. For the imaged flow columns, the soil-water solution was extracted basally post-imaging

and then UV-Vis analysis was immediately undertaken. The non-imaged flow column experiments were identical in setup to the imaged columns (***Figure 11***). However, prior to undertaking UV-Vis analysis on basally extracted soil-water solutions, the solutions were left to stand for 3 hours in order for soil particles to precipitate out of suspension. The material which had not precipitated, including the AuNPs in suspension, was then extracted for centrifugation at 4000 RCF for 15 minutes using a Sorvall Legend XTR (Sorvall, UK). The supernatant was removed, the precipitated AuNPs were resuspended using UHQ to the initial concentration added to the columns (20 µL) and then UV-Vis analysis was undertaken. This centrifugation and resuspension would enable the concentration of AuNPs added at the start of the experiment to be compared with that of AuNPs extracted from the base of the columns at the end of the experiment.

Modelling Buffer Power Approximation for Silica and Alumina

Governing Equation

In order to determine a lower bound estimate for the buffer power of AuNPs in silica and alumina, we constructed a mathematical model to simulate the experimental results shown in ***Figure 16***. To represent the experimental set up of the flow column system as shown in ***Figure 11***, we used a one-dimensional advection-diffusion equation. Parameters are given in ***Table 3***. This takes the form

$$(\phi + b)\frac{\partial c}{\partial t} = D_e \frac{\partial^2 c}{\partial x^2} - V\frac{\partial c}{\partial x}, \qquad \boldsymbol{x} \in \Omega, \tag{1}$$

where ϕ[$m^3\ m^{-3}$] is the porosity of the porous media (approximated from the known size of sieved particles inside the syringe barrel – the dimensions of which are also known), *c* is the normalised concentration of AuNPs based on the mass concentration [$kg\ m^{-3}$], *b* is the buffer power of the PEG-AuNPs, V [$m^3\ s^{-1}\ m^{-2}$] is the volumetric flux of water, D_e [$m^2\ s^{-1}$] is the effective diffusion coefficient for the AuNPs adjusted for impedance caused by the porespace steric conditions in the silica and alumina, and Ω is the 1D domain that represents the column shown in ***Figure 11***. The buffer power within this equation is, in effective terms, the capacity for a material to become immobilised or 'bound' on a surface. We assume that the transition between the states of 'bound' and dissolved happen instantaneously and thus are not time dependent. The concentration of bound AuNPs is written as a ratio between the adsorption rate and dissolution rate multiplied by the concentration of AuNPs in solution.

Since the flow column system was fully saturated, we assumed the effective diffusion coefficient takes the power form and used the expression by Nye (1977; Roose & Fowler, 2004) *i.e.*,

$$D_e = D\phi^3, \tag{2}$$

where D is the diffusion coefficient of the PEG-AuNPs in free liquid. The diffusion coefficient D was derived from the Stokes-Einstein equation for the diffusion of spherical particles through a liquid that has a low Reynold's number. The Stokes-Einstein equation is given by

$$D = \frac{Tk}{6\pi\eta r}, \tag{3}$$

where T is the absolute temperature, k is the Boltzmann constant, η is the suspension viscosity (we assume this suspension is water) and r is the hydrodynamic radius of the particle.

Boundary Conditions

For the boundary condition at the top of the flow column system, an O-ring and cotton wool were placed at the top of the column to prevent flush-back of the PEG-AuNPs during the addition of 0.5 mL of UHQ water above the O-ring (***Figure 11***), *i.e.*, the AuNPs were insulated within the column and not able to leave. Hence, to replicate this condition mathematically, we imposed a no flux condition so that the AuNPs were contained within the domain and are unable to leave the domain, *i.e.*,

$$D_e \frac{\partial c}{\partial x} - Vc = 0, \qquad \boldsymbol{x} \in \partial\Omega_{\boldsymbol{T}}, \tag{4}$$

where $\partial\Omega_{\boldsymbol{T}}$ is the boundary at the top of the domain.

Since we aimed to capture the results seen in ***Figure 16***, *i.e.*, there is no movement of the AuNPs over 24 hours, we noted that the AuNPs did not reach the base of the domain and bound to the particle surface at the top of the system. Since the domain is sufficiently large to avoid any AuNPs reaching the base of the domain, we imposed another no flux boundary condition, *i.e.*,

$$D_e \frac{\partial c}{\partial x} - Vc = 0, \qquad \boldsymbol{x} \in \partial\Omega_{\boldsymbol{B}}, \tag{5}$$

where $\partial\Omega_{\boldsymbol{B}}$ is the boundary at the base of the domain. To validate the insulating condition, we checked there was zero concentration on $\partial\Omega_{\boldsymbol{B}}$ throughout the simulation when the model results matched the experimental results.

Initial Conditions

The domain length was 0.04 m and an initial condition of PEG-AuNPs was imposed in the first 0.002 m of the domain to replicate the experimental system, *i.e.*,

$$c|_{t=0} = \begin{cases} 1 & 0 \text{ m} \leq \boldsymbol{x} \leq 0.002 \text{ m} \\ 0 & 0.002 \text{ m} < \boldsymbol{x} \leq 0.04 \text{ m} \end{cases}. \tag{6}$$

Table 3. *Parameter values used for the convection diffusion model to simulate the movement of AuNPs through the silica and alumina column.*

Parameter	Symbol	Value	Reference
Porosity of soil	ϕ	0.4	(van Genuchten, 1980)
Diffusion coefficient of AuNPs	D	$7\text{x}10^{-12}$ m^2 s^{-1}	-
Effective diffusion coefficient of AuNPs adjusted for soil porosity	D_e	$4.5\text{x}10^{-13}$ m^2 s^{-1}	-
Volume flux of water	V	$5.0\text{x}10^{-8}$ m s^{-1}	(Tinker, 1976)
Buffer power of silica/ alumina	b	70	-
Viscosity of water	η	$8.9\text{x}10^{-4}$ Pa s^{-1}	(Street *et al.*, 1996)

2.4.7 Confirmation of AuNP XCT Contrast and Stability

This experimental system consisted of 1 mL syringes (BD Plastipak, UK) that were cut halfway down (at the 0.5 mL graduation mark). The syringe tip halves were held tip down with a rubber bung placed inside at the base and the top region of each syringe was discarded. Above this basal bung,

these syringes were filled to the top with soil which was fully saturated with a suspension of PEG-AuNPs at the concentration of 3.84 mg Au / mL. The syringes were then transferred into the XTH 225 L Industrial CT Scanner and underwent XCT imaging using the same imaging parameters as described in ***Table 4***.

Table 4. *The parameters used for the X-ray CT imaging of the column based experimental system*

Parameter	**Value**
Voltage (kVp)	40
Power (W)	15
Exposure (ms)	708
Analogue Gain	24
Binning	x2
Number of Projections	1001
Frames per Projection	2
Target Material	Mo
Detector	Perkin Elmer 1621 Flat Panel
Detector Dimensions (Pixels^2)	2000
Pixel Size on Detector (µm^2)	200
Detector Dimensions (cm^2)	40
Source to Sample Distance (mm)	14.64
Source to Detector Distance (mm)	755.03
Filtration	None
Resulting Pixel Resolution (µm^2)	8
Resulting Scan Time (mins)	25

2.4.8 Assessing the utility of gold nanoparticles as a tracer

Experimental Imaged System

The experimental setup for estimating AuNP diffusivity consisted of a 1 mL syringe held tip down and connected to a syringe pump at the basal tip (Harvard PHD 3000, Harvard, US). Within the syringe Bangor soil aggregates sieved to between 1.18 and 2 mm was placed until it had achieved

a depth of 3 cm (***Figure 12***). The Bangor soil was then fully saturated with AuNPs at a concentration of 2.5 mg Au / mL. This concentration was distinguishable from UHQ water and soil but without the risk of producing considerable artefacts within the XCT images that might have been produced at higher AuNP concentrations. Above the soil fully saturated with AuNPs, UHQ was added to the top of the system until a depth of 3 cm was achieved.

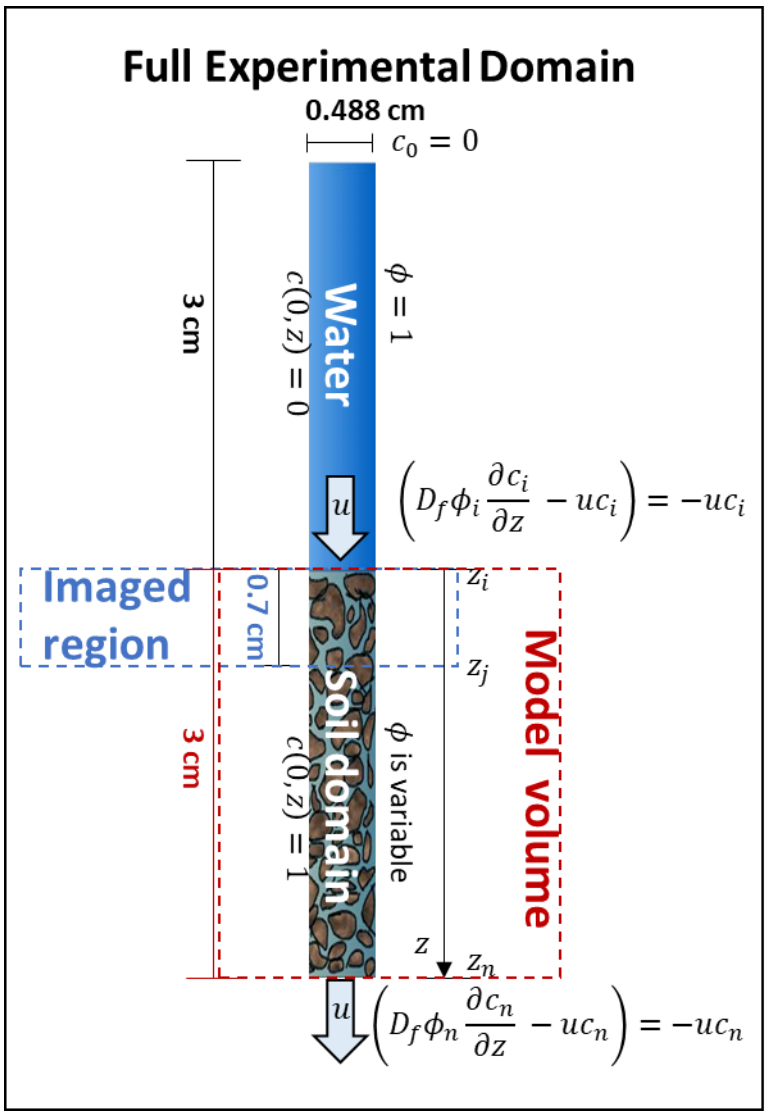

Figure 12. *Modelling experiment of gold nanoparticles as a flow tracer. From the entire experimental domain, the simulations only consider the soil subdomain. The model utilizes a zero gradient at the top and bottom boundaries of the soil domain considering the full experiment. The model is used to fit data obtained from the imaged region (the top 0.7 cm of the soil domain) in order to estimate the diffusivity of gold nanoparticles in free water.*

This system was XCT imaged every hour for three hours. Between images the syringe pump applied a flux of 1 µL / min for a duration of 30 minutes. The XCT parameters used for this imaging were the same as those for previous experiments (***Table 4***). The region of the experimental system that was imaged during XCT imaging was from the surface of the soil to 0.7 cm beneath the soil surface. This would enable the 'transition' zone, the region in which the advection and diffusion at the soil-water interface could be observed, to be captured in detail.

These images were kept as 32bit images and not downscaled to 8bit such that greater grey value range could be maintained. The image processing for this dataset consisted of cropping the image such that only the inside of the syringe remained. A grey value threshold of between 220 and 360 was applied leaving only the liquid phase (AuNP suspension/ water) within the image. The area and mean average grey value of each vertical z slice was then recorded to provide the porosity and average grey value, respectively, of the liquid phase with depth.

Modelling of Gold Nanoparticle Advection-Diffusion

In order to assess the utility of using the AuNPs as a flow tracer, the AuNPs diffusivity required quantification. The experimental system was modelled with a focus on the soil domain (***Figure 12***). The soil domain is considered to be fully water saturated. AuNP concentrations in the soil pore space are used based on the normalised average image grey value intensities for a slice at a given depth value, assuming the grey values to be proportionate to AuNP concentrations. The concentrations are normalised based on the following formulation:

$$c(t,z) = \frac{\tilde{c}(t,z) - mean\left(\tilde{c}(t_f)\right)}{mean\left(\tilde{c}(t_0)\right) - mean\left(\tilde{c}(t_f)\right)}, \tag{7}$$

where $\tilde{c}(t,z)$ [mol m^{-3}] is the solute concentration at a given time and depth, t_0 [s] is the initial time of the experiment, t_f(=7200 s) is the final time of the experiment, and $mean\left(\tilde{c}(t_0)\right)$ and $mean\left(\tilde{c}(t_f)\right)$ [mol m^{-3}] are the mean values of the concentration across the domain at the initial and final time points respectively. The mean values are calculated as:

$$mean(\tilde{c}(t_k)) = \frac{1}{n-i}\sum_{j=i+1}^{n}\tilde{c}(t_k, z_j)\,, \tag{8}$$

where z_i [m] is assumed to be the soil surface and z_n [m] is the bottom boundary of the soil domain (***Figure 12***). Transport of AuNPs in the water phase was modelled based on the advection-diffusion equation:

$$\frac{\partial(\phi c)}{\partial t} + \frac{\partial}{\partial z}(uc) = \frac{\partial}{\partial z}\left(D_f \phi \frac{\partial c}{\partial z}\right), \qquad z \in [z_i, z_n], \tag{9}$$

where ϕ [m^3_{fluid} m^{-3}_{bulk}] is the soil porosity (constant in time since the system is in saturation, though changes with depth where image derived porosity values are used), c [-] is the normalized concentration of AuNPs, u [m^3_{fluid} $m^{-2}_{surface}$ s^{-1}] is the flux value governed by the pumps flow rate and the syringe cross-sectional area, and D_f[m^2 s^{-1}] is the diffusivity of AuNPs in free water. Diffusivity is considered constant. The water flux is also assumed constant throughout the soil domain. The porosity is considered time independent - there is no evidence of significant porosity changes with time, as demonstrated by the lack of movement artefacts in XCT images of the soil columns. In the experiment, water is pulled through the soil domain, ultimately flushing out the AuNPs out of the soil system. Considering all of the experimental constraints, the model, initial conditions, and boundary conditions could be expressed as:

$$\begin{cases} \phi \frac{\partial c}{\partial t} = \frac{\partial}{\partial z}\left(D_f \phi \frac{\partial c}{\partial z} - uc\right), \ z \in [z_i, z_n] \\ c = 1, \ t = 0 \\ \frac{\partial c}{\partial z} = 0, \ z = z_i \\ \frac{\partial c}{\partial z} = 0, \ z = z_n \end{cases}. \tag{10}$$

Within this equation, $\frac{\partial c}{\partial z}$ does not imply a zero flux condition. This implies an outward flux of AuNPs corresponding to the advection which is driven by the volumetric water flux.

Two porosity scenarios are considered when running the simulations. The first scenario considers a fixed average porosity throughout the soil domain of $\phi = 0.4$ m^3_{fluid} m^{-3}_{bulk}. The second scenario considers a spatially varying porosity for the first 0.7 cm depth based on the experimentally determined porosity values at each slice. For both scenarios, the model is fit to the data based on an optimisation routine by treating the diffusivity as a fitting parameter. The objective function is created based on sum of the squared difference between the model results and the data points:

$$\epsilon = \sum_{k=0}^{f} \sum_{j=i}^{n} \left(c_{mod}(t_k, z_j) - c_{dat}(t_k, z_j)\right)^2, \tag{11}$$

where c_{mod} [-] are the modelled normalised concentration values, c_{dat} are the normalised experimental concentrations, t_k [s] is a given time point, and z_j [m] is the depth of a given slice. Numerical solution and optimization were all conducted using Matlab 2016a (Mathworks, Inc., Natick, MA, USA) via a custom built Crank-Nicolson scheme (*i.e.* implicit method to preserve numerical stability for a wider range of time steps) for solving the PDEs and using the fmincon function for the optimization (Crank & Nicolson, 1996).

2.5 Results

2.5.1 Characterising Soil-Water Solutions

The pH values for the Bangor, Dundee and Nottingham soil-solutions stored at room temperature were 7.12, 7.25 and 7.83, respectively. For the refrigerated soil-water solutions, the pH values were 6.33, 6.72 and 7.19, respectively. Therefore, all soil-water solutions were of near-neutral pH and there was only minimal variation in pH between the three soils, but Dundee and Bangor soils were slightly more acidic than the Nottingham soil. The ICP-MS results suggested that the Dundee soil contained higher concentrations of aluminium, iron, magnesium, potassium, rubidium and caesium (***Table 5***). Additionally, the Bangor and Nottingham soils contained higher levels of calcium. These elemental concentrations may influence the behaviours of AuNPs in these three different soils.

Table 5. *The selected results of ICP-MS assessment of soil-water solutions. Elements displayed are those which display variation in concentration between soils.*

	Element						
Soil	**Mg (ppb)**	**Al (ppb)**	**K (ppb)**	**Ca (ppm)**	**Fe (ppb)**	**Rb (ppb)**	**Ce (ppb)**
Bangor	2579	28	1658	13	25	0.56	0.14
Dundee	307	328	2969	1	394	1.34	0.43
Nottingham	3571	36	2126	16	35	0.72	0.17

2.5.2 Gold Nanoparticle Stability in Soil-Water Solutions

UV-Vis analysis of AuNPs with UHQ water indicated the characteristic peak for stable 100 nm AuNPs between wavelengths of 572 and 580 nm (***Figure 13***). This spectrum was used as the reference for AuNP stability against which the UV-Vis spectra of AuNPs suspended in soil-water solutions were compared. These samples also allowed determination of erroneous background peaks.

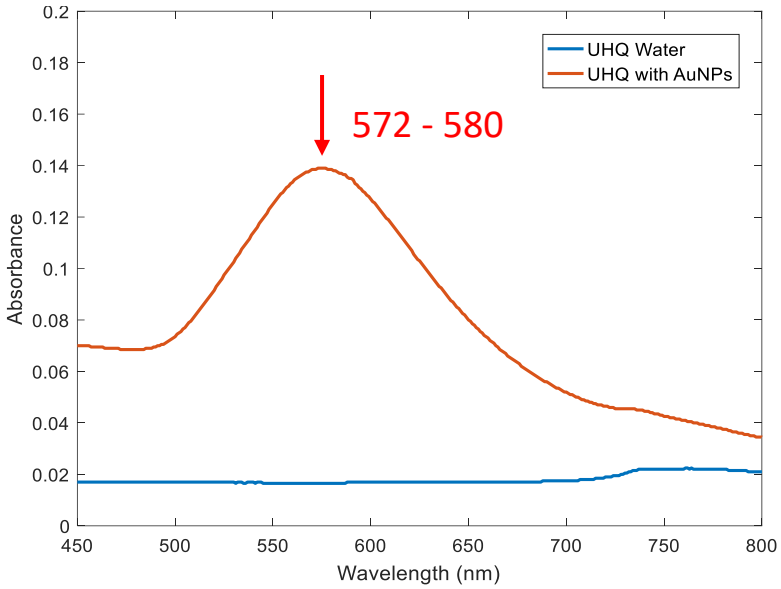

Figure 13. *The characteristic absorbance peak of 100 nm AuNPs in UHQ water using UV-Vis analysis. The blue line represents UHQ water without the addition of AuNPs and the orange line represents UHQ water 24 hours after the addition of AuNPs. The red arrow and adjacent numeric values indicate the AuNP peak position.*

When NC-AuNPs were added to soil-water solutions, the UV-Vis spectroscopy results revealed the degradation of the characteristic peak between the wavelengths 572 and 580 nm in all instances (***Figure 14*****a, c, e**) when compared to the AuNP reference spectrum (***Figure 13***). This indicates that the NC-AuNPs had become destabilised. The NC-AuNPs became destabilised within the Bangor and Nottingham soil-water solutions before 24 hours and within the Dundee soil-water solution between 24 and 72 hours. The increase in absorption between wavelengths of approximately 200 to 500 nm, present in all soil solutions, is likely noise resulting from dissolved organic carbon in the soil-water solution. Peacock *et al.* (2015) investigated a range of wavelengths for detecting dissolved organic carbon in upland catchments in the UK and determined that the strongest correlations between dissolved organic carbon and absorbance were at 230 nm, 254 nm and 263 nm. In addition, Cook *et al.* (2017) were able to use UV-Vis at a wavelength of ~270 nm to detect the level of dissolved organic carbon in tropical peatlands. These wavelength values are within the range in which we detect noise within the UV-Vis data of this investigation.

The UV-Vis experiment was then repeated using the PEG-AuNPs. In this instance the peak between wavelengths of 572 and 580 nm persisted, and the relative concentration of 100 nm AuNPs (as indicated by background and peak height ratio) remained constant over a seven day period (***Figure 14*****b, d, f**). This suggested that the PEG-AuNPs had remained stable.

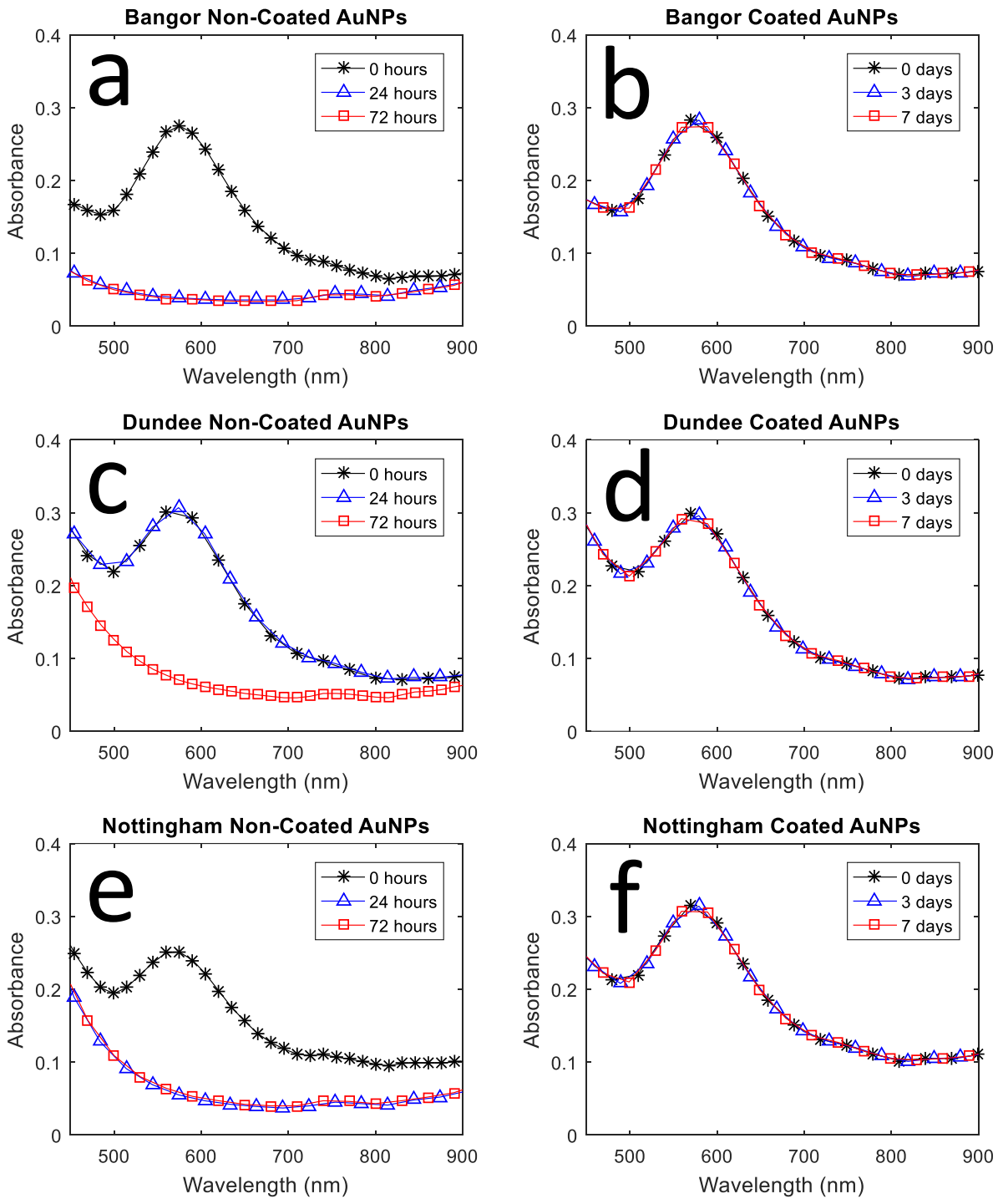

Figure 14. *Confirmation of the stability of PEG coated AuNPs in soil-water solutions of the Bangor, Dundee and Nottingham soils using UV-Vis analysis. The UV-Vis analyses of non-coated AuNPs in Bangor (a), Dundee (c) and Nottingham (e) soil solutions at time steps of zero, 24 and 72 hours from initial AuNP addition, are on the left side. The UV-Vis analyses of PEG coated AuNPs in Bangor (b), Dundee (d) and Nottingham (f) soil solutions at time steps of zero, three and seven days from initial AuNP addition, are on the right side. The data presented for each solution is an average of three replicates. The standard deviation was too small to display in all cases (SD < 0.01 in absorbance).*

2.5.3 Assessment of Gold Nanoparticle Stability in Porous Media

Silica and Alumina Experimental Results

XCT images of silica and alumina columns demonstrated that destabilisation of PEG-AuNPs was primarily characterised by almost immediate accumulation of the AuNPs on both silica and alumina surfaces in all experiments. This accumulation occurred within an hour in all cases and was detectable only one hour after the addition of the PEG-AuNPs to the column. The accumulation was observed in the top few millimetres of each column as a layer of high grey value voxels on the exterior surfaces of particles (***Figure 15*** **&** ***Figure 16***). These voxels were of such high grey value that they can be segmented from silica and alumina using a simple grey value threshold (***Figure 22***). In fluid-filled pore spaces immediately adjacent to the silica and alumina particles that had AuNPs accumulated on their surface, grey levels were similar to pure UHQ water. This indicates a drop of suspended concentrations of AuNPs within the solution after this one hour period. The regions which appear to contain few silica or alumina particles in ***Figure 15*** are not macropores. Instead, these images were captured at very top of the silica and alumina columns and these regions are the result of capturing the uneven surface of the silica and alumina in a horizontal plane.

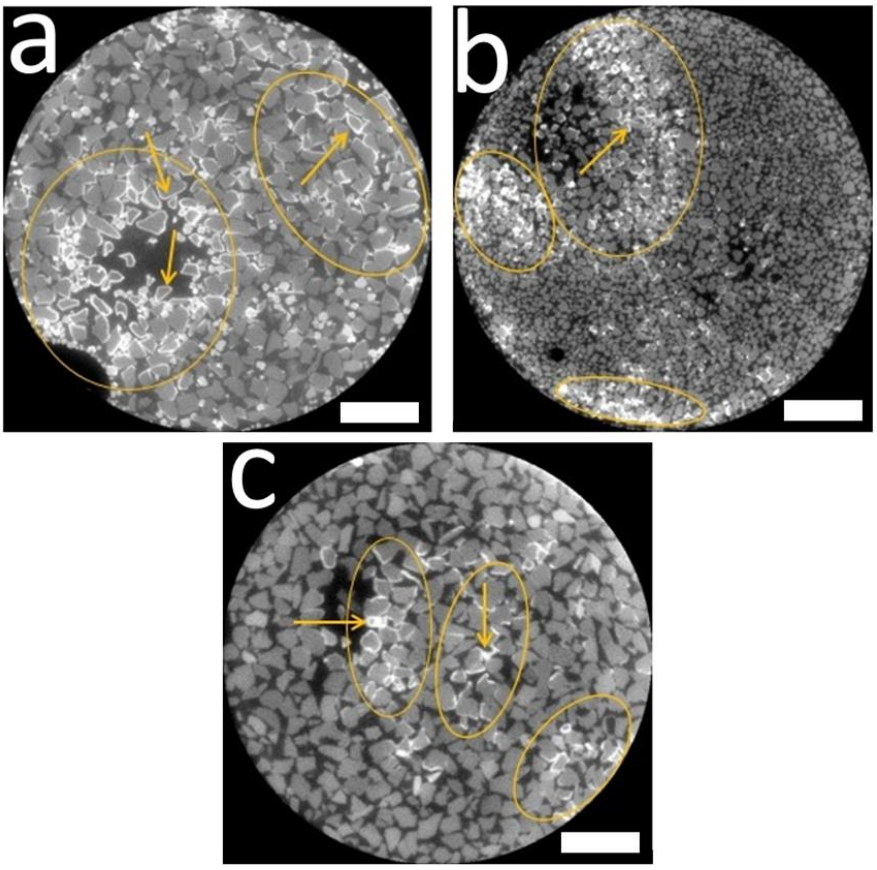

Figure 15. *Horizontal image slices from XCT images of silica and/ or alumina displaying the accumulation of PEG-AuNPs on the silica and alumina surfaces. These images are from a column of: a) silica and alumina mixed b) alumina c) silica. Gold nanoparticle accumulation on the surface of silica and alumina particles is visible bright bands on the exterior of the particles. Regions of prominent accumulation are marked with yellow rings and yellow arrows. Scale bars are 1 mm long.*

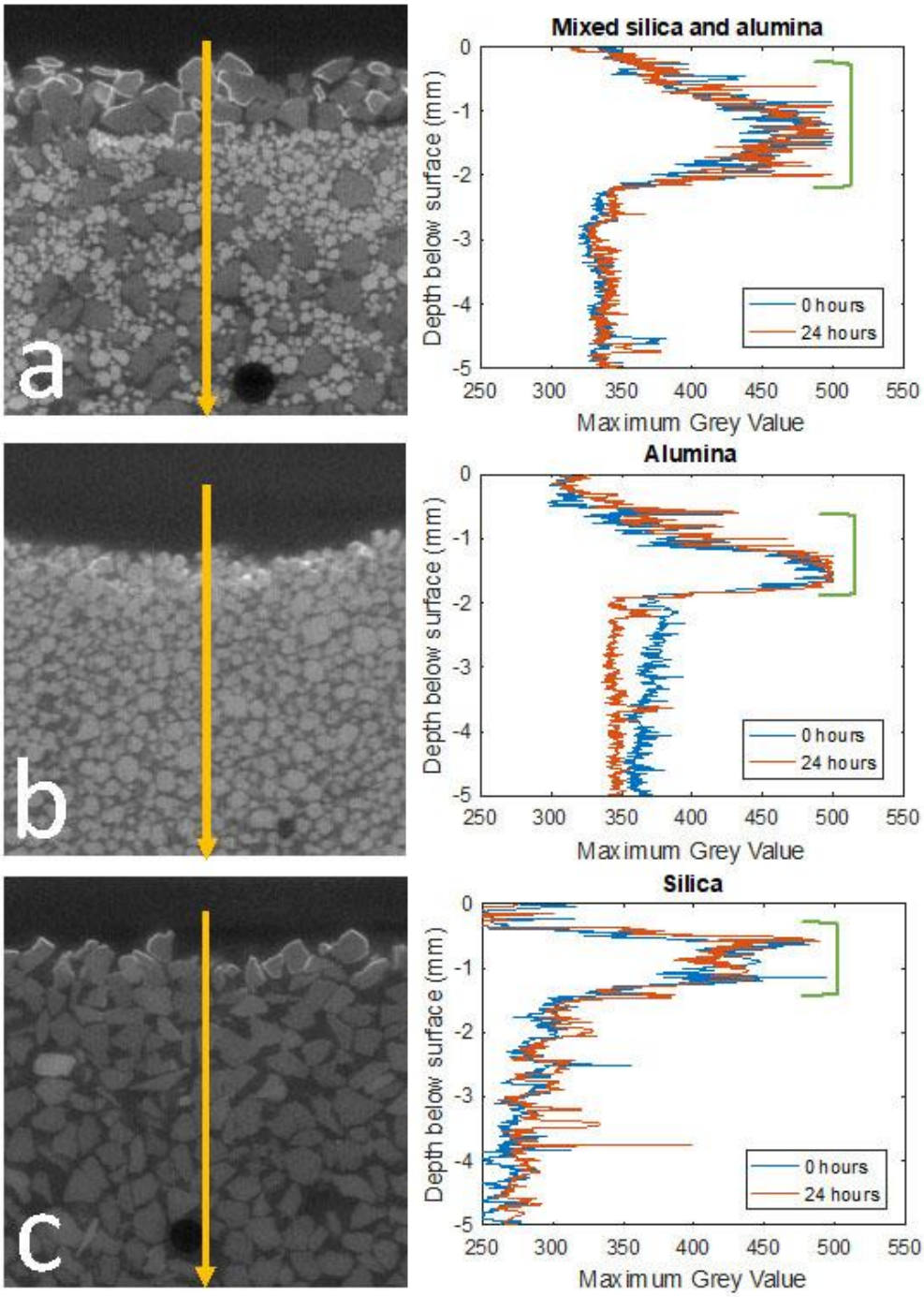

Figure 16. *XCT images of silica and/ or alumina confirming the accumulation of PEG-AuNPs on the very surface of the silica and alumina in the columns. Right: histograms display the maximum grey levels down the column for a) mixed silica and alumina b) alumina c) silica. Immediately after AuNP addition is displayed in blue and 24 hours after PEG-AuNP addition is displayed in orange. The gold nanoparticle induced peak is indicated in green. Left: a representative vertical slice through the image stack and the orange arrow displays the region from which data was extracted. Fluctuations in the grey value recorded above the surface of the silica and alumina are likely due to image artefacts.*

The SEM images of the silica and alumina displayed the accumulation of the AuNPs on the silica and alumina particles in greater detail. The AuNPs appear to be unevenly accumulated and generally on the uppermost exposed surfaces (***Figure 17***). At the highest magnification (30,000×) it was observed that both individual and aggregated groups of AuNPs were present on the alumina and silica surfaces (***Figure 17*d**).

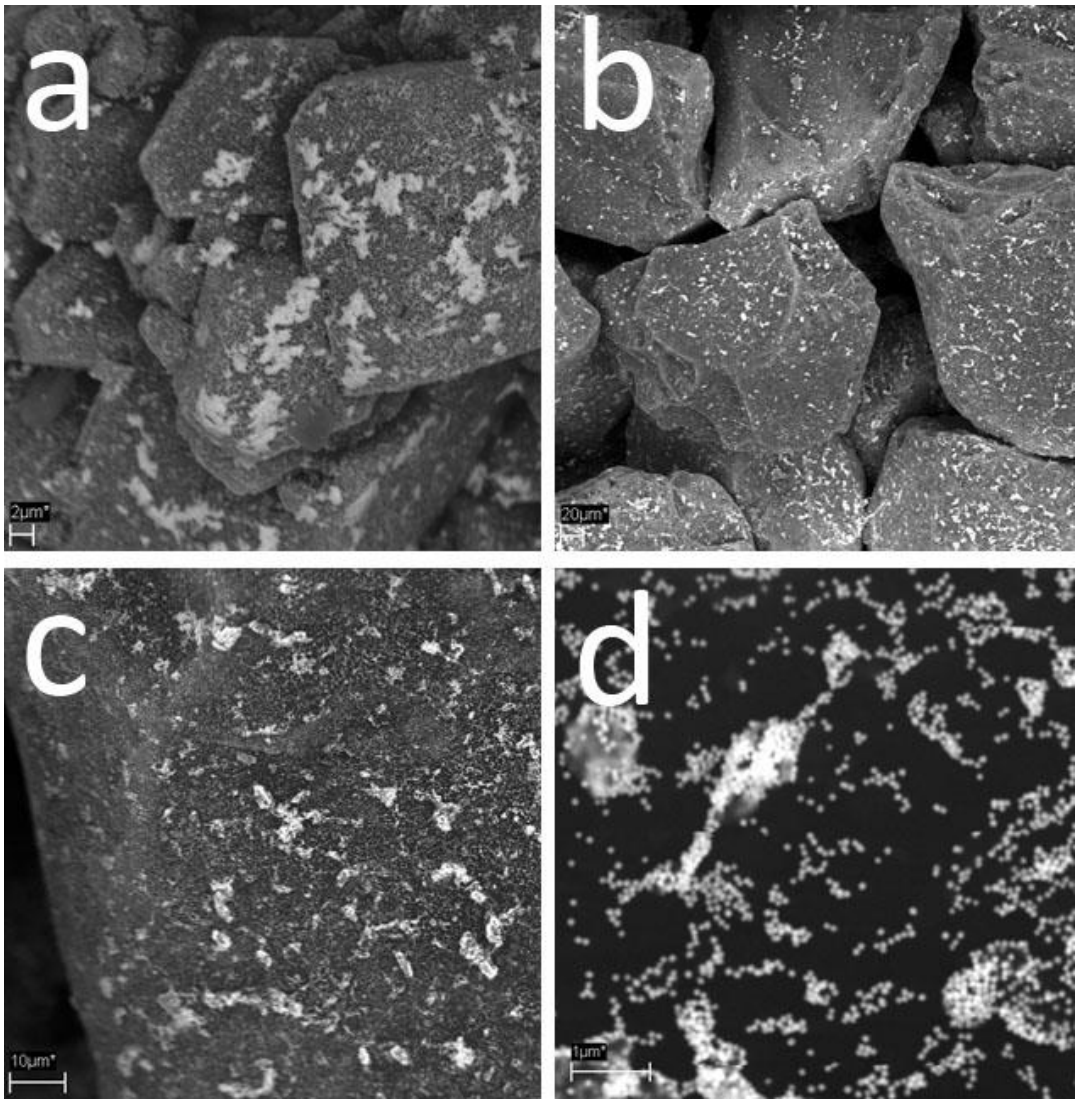

Figure 17. *Gold nanoparticles accumulated on the surface of silica or alumina particles captured using scanning electron microscopy (SEM) imaging. Gold nanoparticles are visible as the brighter regions. The four images are: the surfaces of alumina particles at 4,000× magnification (a), and silica particle surfaces at 400× (b), 2,000× (c) and 30,000× (d) magnification, respectively.*

Silica and Alumina Buffer Power Approximation Results

A lower bound estimate of the buffer power was determined by increasing b in the model until a similar rate of immobilisation was observed in the simulation results as captured in the experimental results (***Figure 16***). It was demonstrated that the difference in the distance travelled by AuNPs over a period of 24 hours between the XCT image results and the solution curve for b = 70 was 75 µm (***Figure 18***). When the buffer power was lower than 70 the difference between image and simulation results for the distance travelled by AuNPs increased (***Figure 18***). Therefore, this solution curve indicates that the PEG-AuNP pulse had become immobilised at the surface of the silica and alumina. Consequently, the approximate lower bound for the buffer power of silica and alumina on PEG-AuNPs was determined to be $b \approx 70$.

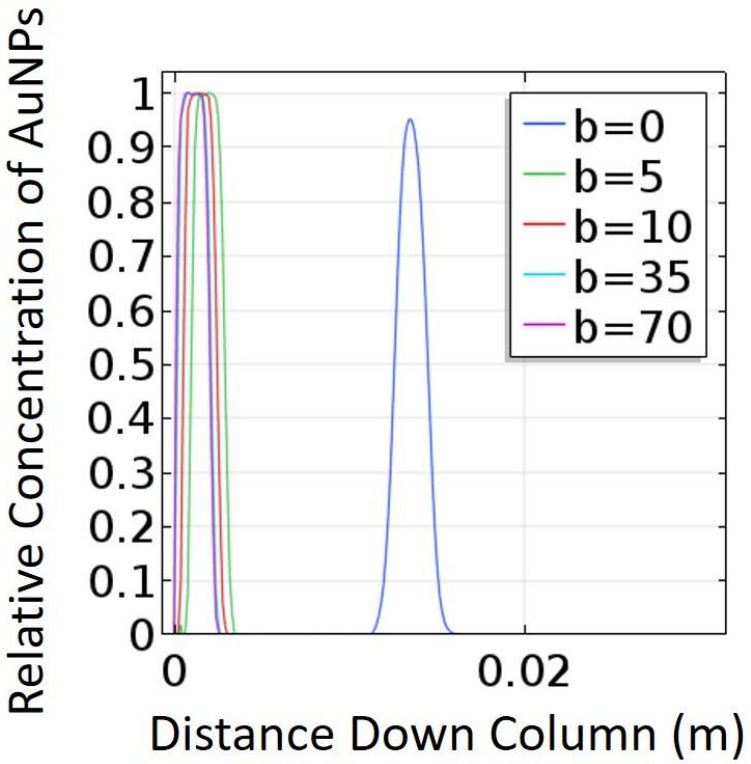

Figure 18. *The results of the 1D advection-diffusion model for the movement of AuNPs down a flow column over a period of 24 hours with an AuNP pulse placed atop 4 cm of silica and alumina. The buffer powers applied in these simulations were b = 70, b = 35, b = 10, b = 5 and b = 0. The difference in distance travelled by AuNPs down the column between the XCT image results and the solution curve for b = 70 was 75 µm indicating that the buffer power of 70 was sufficient to simulate the immobilisation of AuNPs on the silica and alumina surface.*

Soil Experimental Results

The columns containing each of the three soils were imaged every day for the full three days and displayed no indication of the AuNP aggregation observed within the silica and alumina columns (***Figure 19***). Visibly the PEG-AuNPs could be seen passing down through the column between imaging time steps, pulled by the syringe pump. XCT images showed that there were no brighter regions encapsulating primary soil grains, though there is the appearance of more X-ray attenuating materials inside grains - particularly in the Dundee soil (***Figure 19*****c**). However, these brighter regions are most likely naturally occurring minerals within the soil grains**.**

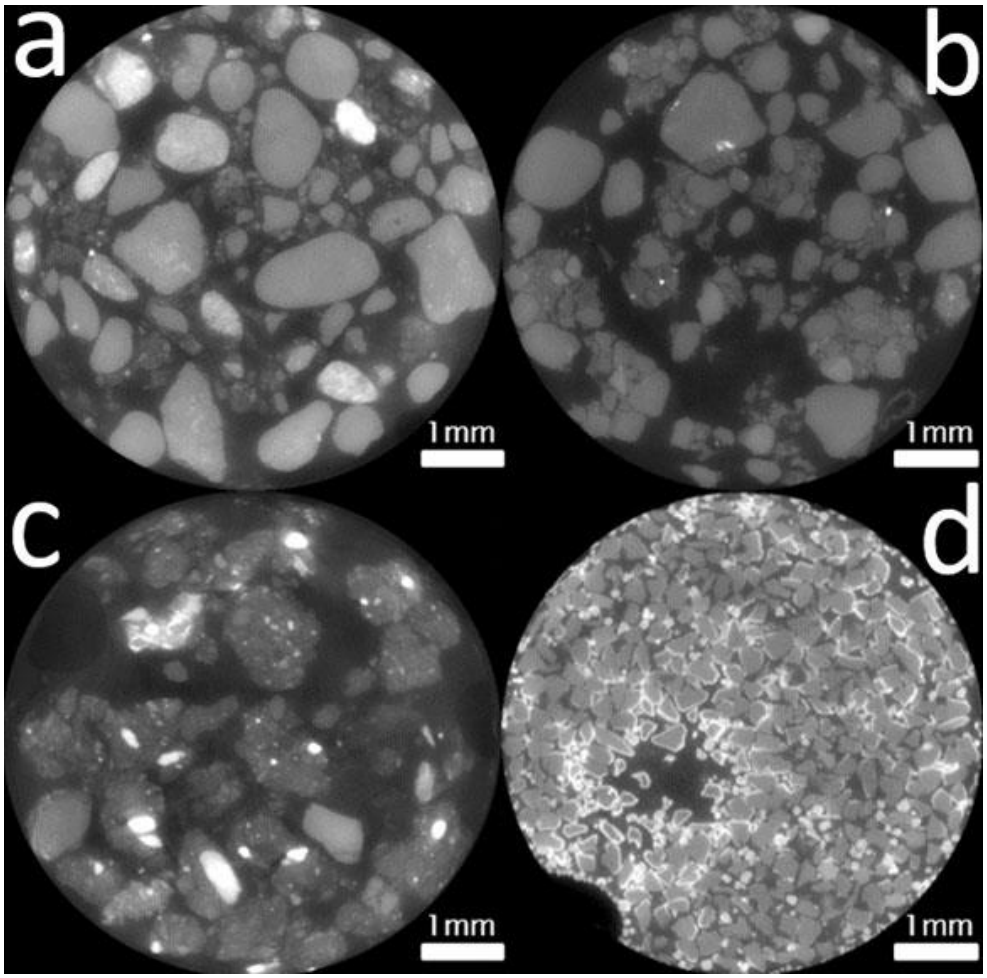

Figure 19. *Example image slices from XCT images of the PEG coated AuNP flow columns of Bangor (a), Nottingham (b), Dundee (c) and silica/ alumina mixture (d). The silica/ alumina mixture is included as a point of reference for the expected appearance of destabilisation. The surface deposition visible in the silica and alumina mixture is not present in the soil images suggesting aggregation has not taken place.*

The results of the UV-Vis undertaken on the solutions extracted from the soil columns displayed the characteristic 100 nm AuNP absorption peak between the wavelengths of 572 and 580 (***Figure 20***). This peak is still present within the XCT imaged Nottingham soil sample (***Figure 20*****a**), however it is visible as a 'shoulder' within the spectrum. The UV-Vis results of ***Figure 20*****a** contained more background noise than ***Figure 20*****b** and previous UV-Vis data. This noise was likely caused by small soil particulates which were not removed – the solutions presented in ***Figure 20*****b** were left to stand for 3 hours in order for soil particles to precipitate out of suspension prior to UV-Vis, whereas the solutions presented in ***Figure 20*****a** did not undergo such precipitation. Unlike previous soil-water solutions, these solutions could not undergo such thorough filtration due to the risk of also removing the AuNPs.

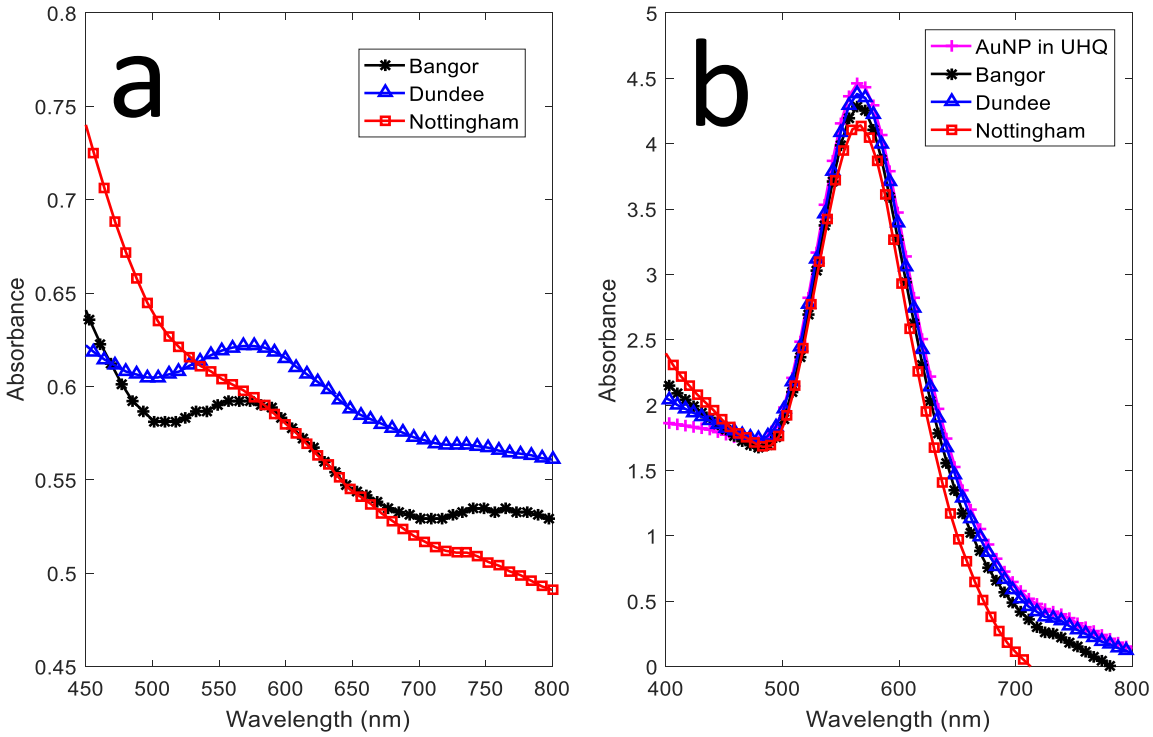

Figure 20. *The presence of stable PEG coated AUNPs in soil-water solutions extracted from soil columns as demonstrated by the results of UV-Vis analysis. This analysis was undertaken on solutions extracted from columns of each of the three soils (Bangor, Dundee, and Nottingham). This included those columns which were XCT imaged (**a**) and those flow columns which were run exclusively for UV-Vis analyses (**b**). The peaks between wavelengths 572 and 580 nm indicates the presence of 100 nm gold nanoparticles which had remained stable in suspension. The appearance of peaks at wavelengths below 500 nm is most likely the result of small soil particles within the suspension that were not removed by filtration.*

2.5.4 Confirming AuNP XCT Contrast and Stability

In the XCT images of the soils saturated with PEG-AuNPs, the contrast between the soil and PEG-AuNP solution was evident (***Figure 21***). The PEG-AuNP suspension was visibly more attenuating than the soil phase and grey level histograms of regions containing both soil and PEG-AuNP phases display a bi-modal distribution. The peak value in the histograms for the soil phase in the 8bit images was at a pixel value of approximately 89 and for the PEG-AuNP suspension the peak is at 124. This PEG-AuNP suspension produced artefacts such was the extent of the attenuation. Had the PEG-AuNP suspension been replaced by water, the grey value peaks would be reversed. The soil particles (peak A in ***Figure 21***) would produce the highest grey values whilst the fluid phase (peak B in ***Figure 21***) would produce distinctly lower grey values.

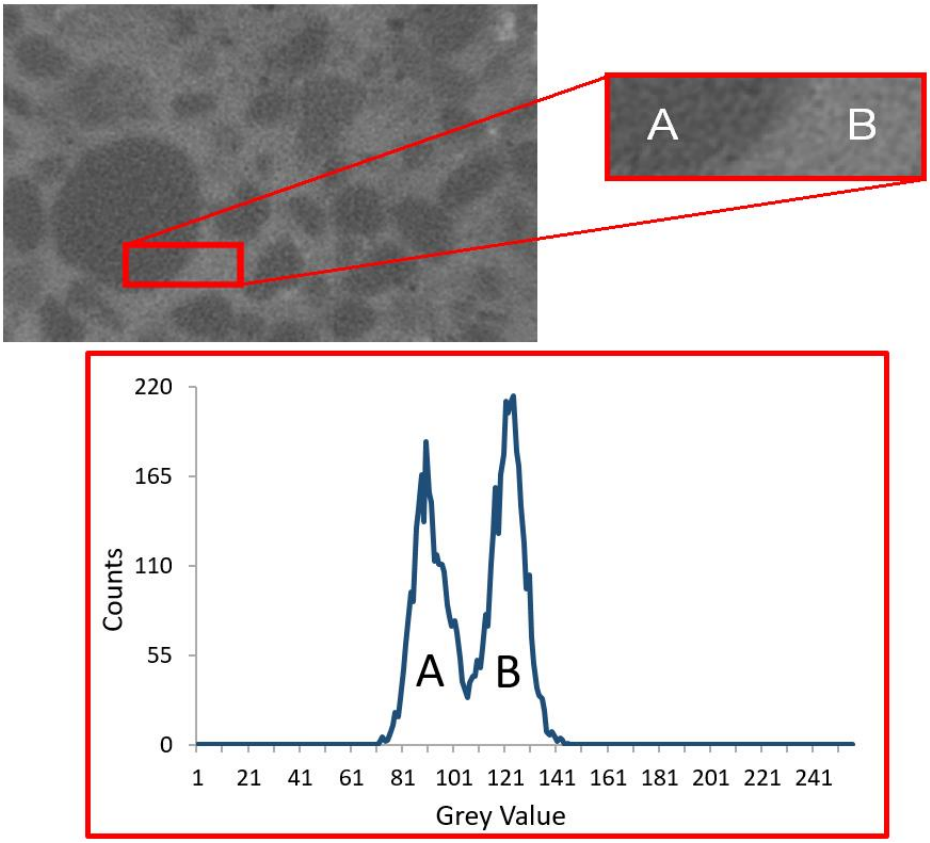

Figure 21. *The XCT contrast provided by a suspension of PEG-AuNPs within a syringe barrel containing soil particles. Top left: an XCT image region of a PEG coated gold nanoparticle suspension, at a concentration of 3.84 mg Au / mL, fully saturating Bangor soil. Top right: the PEG coated gold nanoparticle suspension (B) is visibly more attenuating than the soil (A). However, there were artefacts present within the images, which are most likely due to beam hardening resulting from the greater attenuation of PEG-AuNPs. Bottom: this contrast between the attenuation of soil (A) and PEG coated gold nanoparticles (B) in the top right image is also visible in the histogram of grey values.*

The contrast between PEG-AuNPs and soil means that the PEG-AuNP suspension can also be segmented using only a simple grey value threshold (***Figure 22***). There were artefacts present within the images, which are most likely due to beam hardening resulting from the greater attenuation of PEG-AuNPs. There is also no evidence of the formation of bright rings around soil particles as was visible in the silica and alumina images.

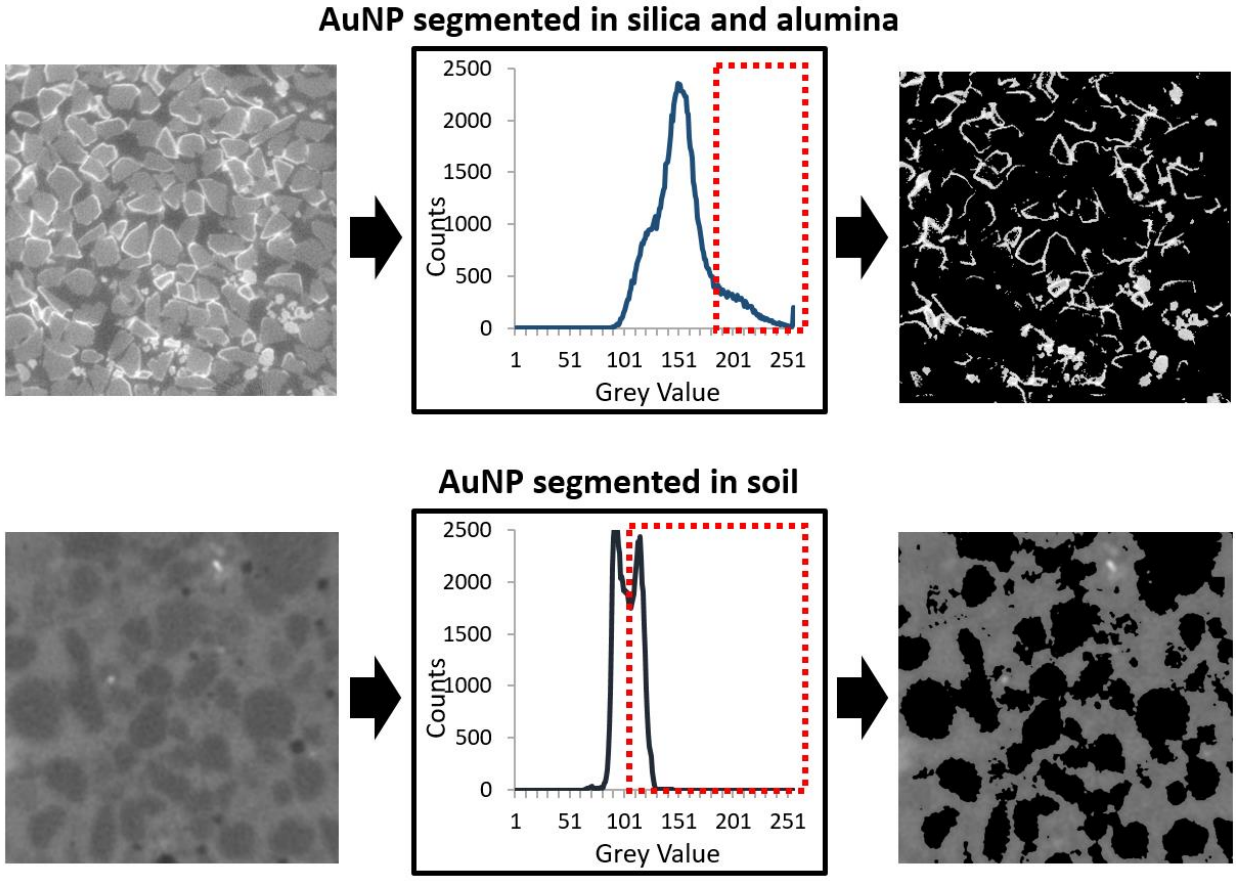

Figure 22. *A demonstration that AuNPs can be segmented from silica and alumina (top row) and from soil (bottom row) using a simple grey value threshold. The images on the left are unaltered 8bit images. In the centre are the histograms of grey values for the unaltered images. The red boxes with the dashed outline indicate the grey value range of AuNPs and which would be segmented by a grey value threshold. The images on the right are the segmented AuNPs and the result of the grey value threshold.*

2.5.5 Estimated Gold Nanoparticle Diffusion Rate

Experimentally the image results suggest we were able to capture the movement of AuNPs and ingress of water into the imaged domain. This is captured in the declining grey values with depth between time steps (***Figure 23***) following image processing. The model was then fit to this image data.

Model fitting results are illustrated in ***Figure 23***. When considering a constant porosity (***Figure 23a***), the optimization suggests the diffusivity of the AuNPs in free water is $D_f = 6.5\times10^{-9}\ m^2\ s^{-1}$. The diffusivity reduced to $D_f = 2.5\times10^{-9}\ m^2\ s^{-1}$ when considering the actual porosity at each depth (***Figure 23a***). This 'actual' porosity was captured as the cross sectional porosity within an image slice and was primarily affected by the manner in which the soil particles had settled within the flow column with depth. Both diffusivity values are on the same order of magnitude of other typical plant nutrients diffusing in free water (Barber, 1995). Simulated results suggest that AuNPs diffuse into the free water domain prior to being flushed from the system. Furthermore, AuNPs do not appear to be completely flushed from the system at the final time point.

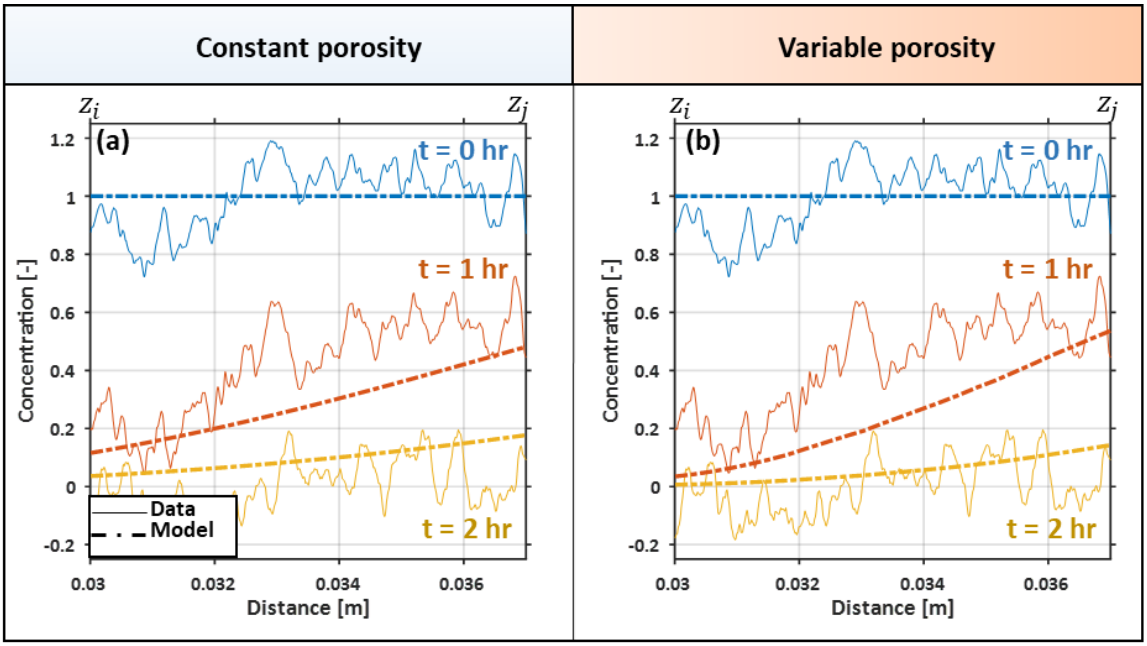

Figure 23. *Modelled and experimental gold nanoparticle concentrations along the depth of the imaged region considering (a) a constant value for porosity and (b) a spatially varying porosity. Experimentally determined normalized concentrations are given as solid curves, while modelled normalized concentrations are given as dashed curves. The model was fit for three different time points (0, 1, and 2 hours), which are colour coded as blue, orange, and yellow respectively. Fit curves to the data estimate that nanoparticles have a diffusivity in free water of (a) $6.5\times10^{-9}\ m^2\ s^{-1}$ for a fixed porosity value of $\phi = 0.4\ m^3_{fluid}\, m^{-3}_{bulk}$, and (b) $2.5\times10^{-9}\ m^2\ s^{-1}$ for a spatially varying porosity.*

2.6 Discussion

This study investigated the stability of AuNPs in soil environments. The conditions provided by soil-water solutions were confirmed by UV-Vis to induce aggregation of NC-AuNPs. This effect was mitigated by applying a PEG-SH coating to the AuNPs which proved sufficient for maintaining stability within soil-water solutions. When applied to flow columns of silica and alumina the destabilisation of AuNPs in porous media was characterised using a combination of XCT and SEM imaging techniques. The PEG-AuNPs were then added to flow columns containing soils where it was confirmed using XCT and UV-Vis that the PEG-AuNPs had remained stable. This stability was further demonstrated in the columns where soil was fully saturated with PEG-AuNPs and which provided sufficient distinct contrast.

The ICP-MS analysis of soil solutions indicated that the Dundee soil likely had the highest clay content of the three soils. This is because the Dundee soil contained higher concentrations of metals associated with clay-minerals (***Table 5***) such as aluminium, iron, magnesium and alkali metals such as potassium, rubidium and caesium (Driessen *et al.*, 2000). Additionally, the ICP-MS results suggested the Bangor and Nottingham soils may contain more sand minerals than the Dundee soil, as evidenced by the higher calcium content (Driessen *et al.*, 2000). These variations in soil composition could be quantified in future, for example by using a sedimentation method (Miller & Miller, 1987; Moritsuka *et al.*, 2015). It is possible that these variations in soil composition meant that the Dundee soil contained different soluble salts than the other two soils. Given the known susceptibility of NC-AuNPs to destabilising conditions (Diegoli *et al.*, 2008), it was expected that they would undergo aggregation in the soil solutions, observable as a peak shift in UV-Vis analysis (***Figure 14*a, c, e**). This could have meant the salts within the Dundee soil solution had a less severe destabilising effect than those of the other two soils hence the NC-AuNPs remained stable for longer within this soil solution – up to 72 hours (***Figure 14*c**). This reduced aggregation was unlikely to be acidity-related, since all three soil solutions were relatively neutral in pH and an absence of soil particles indicates that the differences were not related to surface charge effects. However, given the similar pH of all three soil water solutions, further investigation into the influence of acidity on the stability of AuNP suspensions in soil should be considered - potentially using pH buffered treatments at a broad range of pH values.

In all cases the NC-AuNPs remained stable for less than 72 hours. In contrast, the PEG-AuNPs introduced to soil solutions remained stable for at least one week (***Figure 14*b, d, f**). This indicated that the 5 kDa PEG-SH coating was sufficient to prevent aggregation in the presence of soluble soil salts and acids. The success of PEG-AuNPs for preventing aggregation is also corroborated by the

findings of Sun *et al.,* (2009), who observed that PEG coated AuNPs remained stable at concentrations of 100 mg Au/ mL and Bergen *et al.,* (2006) who noted that PEG coating prevented destabilisation from mild saline and acidic conditions.

The XCT images of the soil-analogue columns demonstrated that both silica and alumina (with contrasting negative and positive charges) had compromised the stability of the PEG-AuNP suspension as expected. The experimental results indicated significant and rapid immobilisation, suggesting that adhesion occurred within an hour. The XCT images used to characterise the destabilisation of the PEG-AuNPs acted as a reference for comparison against the soil column images (***Figure 15* & *Figure 16***). Where AuNPs had become immobilised, they were visible as bright regions on the surface of silica and alumina particles in XCT images. These regions provided considerable contrast (***Figure 15* & *Figure 16*)** and also meant the PEG-AuNPs could be segmented from the silica/ alumina using a grey value threshold (**Figure 22**). The XCT images of soil-analogue columns and the significant contrast provided by accumulated AuNPs did however demonstrate the potential of AuNPs as contrast agents within porous media systems. If AuNPs could in future be developed to accumulate on target structures, for example root systems, they could be a useful tool in root/ soil XCT studies.

The SEM imaging enabled further characterisation of AuNP destabilisation. The resulting images indicated that the accumulation was not uniform with AuNPs binding on the uppermost surface. Furthermore, SEM imaging showed that the AuNPs did not necessarily aggregate with one another (***Figure 17***). This further supports the observation that the immobilisation was fast as the suspension was not able to penetrate through the column beyond the uppermost surface. It should be noted that macropore structure would likely influence the flow of the AuNPs through the porous media system. However, it is unlikely that the AuNPs have simply been deposited onto the surface of the silica and alumina as a result of the smaller pore volume of the silica/ alumina systems than soil systems. Since the flux induced by the syringe pump was unable to draw the AuNPs further down the flow columns, it would appear that AuNPs were instead bound to the surface of the silica and alumina particles. Had the AuNPs been deposited onto the surface of silica and alumina particles it would be expected that the flux from the syringe pump would be capable of drawing them deeper.

The XCT images of the columns of soil were compared against those of silica and alumina columns. The bright surface coatings that were characteristic of AuNP aggregation in the silica and alumina columns were notably absent within the soil column images. Additionally, whereas the AuNPs were visible by eye on the surface of the silica and alumina as a dark brown region at the surface, within

the soil columns the PEG-AuNP suspension could be seen moving further down the column between imaging time steps. XCT images of the soils without the addition of AuNPs indicated that the bright contrasting regions embedded inside Dundee primary soil grains (***Figure 19*c)** are likely regions of naturally occurring soil minerals with a high X-ray attenuation rather than AuNPs. Not only were the primary soil grains not permeable enough for AuNP infiltration, but there is also no indication of AuNP accumulation on external soil grain surfaces, as had been observed in the silica and alumina. Given the complexity of the chemical environment provided by soil and the variability in soil mineral attenuation it would likely be worthwhile to undertake future investigations initially using sand. This would provide a less complex chemical environment and the X-ray attenuation of sand mineral grains would likely be more homogeneous.

The reason the AuNPs did not produce contrast while in suspension against soil or water, despite the initial high concentration, is likely because a small volume of water (approximately 10 µL) remained above fully saturated soil prior to the addition of the AuNPs. Once the AuNPs were applied to the surface they were likely diluted by this water volume as the high velocity with which the droplet of AuNPs entered the water may have been turbulent. Hence this would explain why the AuNP suspension became undetectable in XCT at a faster rate than standard diffusion would anticipate. This phenomena has been demonstrated by Taylor (1954), Fischer (1973) and Rein (1993). These imaging results therefore suggested that the PEG-SH coating had enabled AuNPs to remain stable in the soil columns.

UV-Vis results for solutions extracted from both the imaged and non-imaged soil columns confirmed that 100 nm PEG-AuNPs in suspension remained stable after the three days of imaging (***Figure 20***) for all three soil types. This was indicated by the presence of the characteristic absorption peak between the wavelengths of 572 and 580. In particular, the absorption values for the characteristic AuNP peaks in ***Figure 20*b** demonstrate this AuNP stability. This is because the concentration of AuNPs extracted from the base of the columns was almost equal to that of the AuNP suspensions applied to the soil surface in the column three days earlier. The increased noise present within this UV-Vis data was likely the result of small soil particles which could not be removed from the solution by filtration or dissolved organic carbon. The region below a wavelength of 500 nm partially obscured the characteristic peak between 572 and 580 nm in the Nottingham spectra in the imaged columns as a 'shoulder' (***Figure 20*a**) and this is an example of such noise.

Soil fully saturated with PEG-AuNPs provided further confirmation that the PEG coating ensured stability (***Figure 21***). The bright rings of destabilised AuNPs that were visible on the surface of silica and alumina were not present in these samples. In addition, the X-ray attenuation of the PEG-AuNP

suspension appeared uniform and was greater than that of the soil particles. The contrast between the PEG-AuNPs and the soil particles also meant that the PEG-AuNPs can be easily segmented using only a simple grey value threshold (***Figure 22***). This uniformity indicates that the PEG-AuNPs remained stable in suspension in the presence of the soil particles even at high concentration. There did however appear to be artefacts within the image most likely resulting from beam hardening caused by the greater attenuation of PEG-AuNPs. The contrast provided by the PEG-AuNP suspension and the bi-modal nature of the contrast between the PEG-AuNPs and soil particles also demonstrated that the 3.84 mg Au / mL concentration of AuNPs was sufficient for contrast against soil grains when not exposed to dilution. Furthermore, this result reinforces the suitability of AuNPs for future development as contrast agents in soil systems.

The diffusivity of the AuNPs in free water was estimated as D_f= 2.5×10^{-9} m^2 s^{-1} when the actual porosity was considered at each depth (***Figure 23*b**) indicating that PEG-AuNPs diffuse at a similar rate to other typical plant nutrients (Barber, 1995). This indicates that they may diffuse too quickly to be effective as a tracer contrast agent given the high concentration that is required for producing sufficient contrast. However, for use as a proposed functionalised contrast agent in soil PEG-AuNPs remain a promising candidate.

2.7 Conclusions

In summary, the PEG coating applied to the AuNPs was sufficient to maintain stability of the AuNPs in soils. This is evidenced by both UV-Vis and XCT imaging results. The stabilisation of AuNPs for use in soil environments can act as a platform from which development of AuNPs as XCT contrast agents can be pursued. Whilst there are limitations to the use of AuNPs as 'bulk flow' contrast agents (such as the high required concentration and estimated diffusion rate in free water) there is evidently potential for use in applications where AuNPs accumulate in high concentrations at a target surface, which may be enabled through functionalisation.

2.8 Author Contributions

CPS, AvV, SDK, ID and TR designed the study. CPS collected the UV-Vis data. CPS and AvV collected the ICP-MS data. CPS and SDK collected the XCT data. MMH and ID developed the PEG coating method. MMH, ID and CPS undertook the coating procedure. CPS collected the SEM data. SJD and SAR developed the modelling. CPS undertook the data analysis. CPS wrote the manuscript and all other authors provided critical revision and approval before submission and publication.

2.9 Acknowledgements

CPS, AvV, SDK and TR are funded by ERC Consolidator grant 646809 (Data Intensive Modelling of Rhizosphere Processes). SR and TR are funded by BBSRC SARISA BB/L025620/1. TR is also funded by BBSRC SARIC BB/P004180/1, EPSRC EP/M020355/1 and NERC NE/L00237/1. SJD is funded by BBSRC Syngenta Case PhD Studentship BB/L5502625/1. The authors acknowledge the μ-VIS X-ray Imaging Centre at the University of Southampton for provision of tomographic imaging facilities, supported by EPSRC grant EP-H01506X. The authors acknowledge the Scanning Electron Microscope Facility and High Resolution ICP-MS Facility at the National Oceanography Centre Southampton. The authors would also like to acknowledge Davey Jones (Bangor University), Tim George and Glyn Bengough (James Hutton Institute) and Sacha Mooney and Malcolm Bennett (University of Nottingham) for providing the soil samples used within this investigation.

3 X-ray Computed Tomography of Solute Movement in Ridged & Flat Plant Systems

3.1 Authors

Callum P. Scotson[1], Simon J. Duncan[1], Katherine A. Williams[1], Siul A. Ruiz[1], Tiina Roose[1,]

[1]Bioengineering Sciences Research Group, Mechanical Engineering, Faculty of Engineering and Physical Sciences, University of Southampton, Southampton, UK

3.2 Abstract

The aim of this investigation was to experimentally compare the movement of a solute through soils with two field-representative surface geometries: ridge and furrow surfaces *vs*. flat surfaces. XCT imaging was undertaken to trace the movement of a soluble iodinated contrast agent, here used as an XCT-visible analogue for field-applied solutes, through soil columns with either a ridge and furrow or flat soil surface geometry. In addition to the soil surface geometry, the experimental treatments included the presence or absence of plants and surface water ponding. Experimental results were compared to existing numerical simulations adapted to represent the present experimental column systems. Similar infiltration patterns were observed in imaging results and the numerical simulations for most treatments. The experimental results suggest that plant roots present a significant localised effect to reduce the infiltration depth of solutes particularly in planted ridges where the infiltration depth of the contrast agent was minimal. There is variability within the results since the number of replicates was limited to three due to the exploratory nature of the study (testing eight different treatments) and the cost and availability of XCT facilities capable of imaging such physically large samples. Discrepancies between the imaged infiltration depth of the solute and the numerical simulations are attributed to variation in plant root distribution and also spatial soil moisture, as measured using resistive soil moisture sensing. The results of this investigation elucidate the nature of solute movement through soil surface geometries - indicating that plant root water uptake can reduce solute infiltration depth on average by approximately 23% in flat systems and 61% in ridge and furrow systems. However, surface ponding can negate this, increasing infiltration depths on average by approximately 200% in flat systems and 138% in ridge and furrow systems, relative to systems with a plant but no ponding. These results suggest that soil surface shape, plant age and the timing of solute application with anticipated rainfall could be important considerations for reducing solute leaching and improving solute application efficiency.

3.3 Introduction

Numerous methods are used to cultivate crops in arable systems, including those which alter soil surface geometries (Fahong *et al.*, 2004). Two such approaches widely used in the United Kingdom are 'flat planting' and 'ridge and furrow planting' (Robinson, 1999). Flat planting uses a uniform soil surface with no significant spatial geometric changes, whereas ridge and furrow planting involves the creation of a system of periodic peaks and troughs across an arable field. Determining the most suitable soil surface treatment for a crop system depends on several factors including, but not limited to, the crop species, soil type, climate, water availability, nutrient status and ease of harvesting (Finch *et al.*, 2014). Ridge and furrow planting is the preferred choice for certain crops (*e.g.* potatoes) because it aids in nutrient replenishment of the soil (Feddes *et al.*, 1976) and the capacity to provide adequate water to plant roots without inducing waterlogging of the rooting region during periods of heavy rainfall (Tisdall & Hodgson, 1990).

Although ridge and furrow systems provide some clear advantages over flat planted systems, studies have shown that the mechanisms of water movement within ridge and furrow systems may make them more vulnerable to solute leaching (Alletto *et al.*, 2010; Kettering *et al.*, 2013). Typical solutes applied in agricultural systems include soluble fertilisers or pesticides. Solute leaching in agricultural systems is of importance as it can cause environmental damage (vanderWerf, 1996) and is cost inefficient for farmers. For example, excessive leaching of nitrogenous fertilisers not only means that the crop plants cannot utilise this nitrogen as intended, but can lead to eutrophication of water bodies wherein oxygen depletion can adversely damage populations of aquatic life (Harper, 1992; Conley *et al.*, 2009) and can also contaminate groundwater (Duttweiler & Nicholson, 1983; Huang & Uri, 1989; Power & Broadbent, 1989). Previously, field-scale agronomic studies have identified spatial variation in the solute infiltration depths in arable ridge and furrow systems (Smelt *et al.*, 1981; Kung, 1988; Leistra & Boesten, 2010). These studies found that solutes present within the furrows moved to a greater absolute depth compared to flat soil surface geometries in all instances. Moreover, a report from the European Food Safety Authority indicated that the severity of leaching in ridge and furrow systems can be up to six times that of flat systems (EFSA, 2013). However, solute management techniques can be employed to mitigate solute leaching in ridge and furrow systems. For example, Jaynes & Swan, (1999) observed that leaching was significantly reduced when nitrogen fertiliser was applied only to the ridge and not to the furrow. Such techniques can reduce damaging environmental effects of solute leaching (Hatfield *et al.*, 1998) to

the extent at which ridge and furrow systems are less vulnerable to leaching than flat systems (Ressler *et al.*, 1997).

Duncan *et al.*, (2018a; 2018b) modelled the movement of water and solutes in a ridge and furrow surface and a flat surface geometry (Duncan *et al.*, 2018b), illustrating the effects of dynamic furrow ponding on solute movement. Importantly, these systems were simulated with and without the presence of plant roots. These simulation results indicated that a ridge and furrow geometry could either increase or reduce the infiltration depth of solutes relative to flat systems depending on the rainfall activity following solute application and the presence of roots within the soil. In simulations where solute application to a planted ridge and furrow geometry was followed by a comparatively low frequency and intensity of rainfall, the infiltration depth of solutes was reduced compared to flat systems. Solutes accumulated in ridges in the rooting zone as a result of the root water uptake drawing in solutes via advection. However, when high intensity rainfall followed the solute application, the infiltration depth of the solute was increased in planted ridge and furrow geometries compared to flat systems. In this instance, water infiltration from ponding was the dominant transport mechanism, thus causing the solutes to infiltrate deeper and increase the likelihood of solute leaching. This effect was more severe in the simulations without plant roots due to a lack of water uptake from roots in the ridges of the system. While the simulation results elucidate much of the contrasting empirical evidence regarding ridge-furrow systems *vs* flat systems, there are few measurement techniques that can validate the model.

One established method for observing and tracing fluid flow is through the use of radiographic contrast agents coupled with imaging via X-ray computed tomography (XCT). For example, Heijs *et al.* (Heijs *et al.*, 1996), Koestel and Larsbo (2014) and Sammartino *et al.,* (Sammartino *et al.*, 2015) used XCT imaging to trace contrast agent solutions through porous media to assess preferential solute transport in the context of macropore structure and characteristics. These methods offer opportunities to obtain information which cannot be captured using traditional destructive methods such as dissections or soil coring. These methods allow for the examination and quantification of 3D patterns of fluid movement in an intact soil system containing live plants. In particular, non-ionic iodinated contrast agents are commonly used as fluid flow tracers – for example, for gastrointestinal and vascular flow imaging in biomedicine (Gertz *et al.*, 1985; Blachar *et al.*, 2001; Lusic & Grinstaff, 2013). These contrast agents are used as flow tracers because they possess several favourable traits. Firstly, they are generally less reactive compared to alternative contrast agents – for example, ionic iodinated contrast agents (Aspelin, 2006; Lusic & Grinstaff, 2013). This is advantageous when the contrast agent is required to translocate freely and for applications involving organic tissues. Additionally, non-ionic iodinated contrast agents are highly

soluble and possess a viscosity similar to water (Lusic & Grinstaff, 2013). These attributes make these contrast agents an ideal surrogate for mobile solutes in soil under variable agricultural settings.

The objective of this study was to experimentally observe the patterns of solute movement through ridge and furrow or flat soil surface geometries. This was achieved via XCT imaging, used to trace the flow of a soluble non-ionic iodinated contrast agent through soil columns, 10.5 cm in diameter and 31 cm in depth, with ridge and furrow or flat soil surfaces. The experimental imaging results were compared to numerical modelling simulations originally developed by Duncan *et al.* (2018a; 2018b), but adapted to represent the specific experimental system here. Resistive soil moisture sensing (RSMS) was also then used to record spatio-temporal soil moisture. Planted and non-planted treatments were incorporated, as well as treatments which vary in watering regime following solute application. These different watering regime treatments represented either no rainfall or excessive rainfall scenarios. By demonstrating that solute infiltration observed in the XCT imaging can be reproduced using numerical models, the conclusions of this work may lead to better informed management of solute application in areas exposed to intermittent heavy rainfall.

As informed by previous modelling results Duncan *et al.* (2018a; 2018b), we hypothesised that the advection of water uptake by plant roots would cause the contrast agent to accumulate close to the soil surface for both soil surface geometries. We predicted that this accumulation would take place to a greater extent in ridge and furrow systems which were not exposed to heavy watering following the addition of the contrast agent. This was because it was anticipated that the advective force of root water uptake would be able to exert greater influence in ridges, in accordance with the results of Duncan *et al.* (2018a; 2018b). We also hypothesised that where ponding is present ponding could force deeper infiltration of solutes. We predicted that this would take place as a result of the pressure exerted by ponded water.

3.4 Materials and Methods

3.4.1 Experimental System

In order to trace the movement of the contrast agent through the soil using imaging experiments, column mesocosm systems, designed to be suitable for XCT, were constructed (***Figure 24***). The requirements for achieving compatibility with XCT were: i) radial symmetry of the sample, ii) a constrained density and scale of the sample so that sufficient X-ray transmission and resolution could be achieved, and iii) low X-ray attenuation of the materials relative to the contrast agent.

Consequently, experimental column systems used for this investigation were largely constructed from unplasticised polyvinyl chloride (uPVC) components.

The major structural component of the mesocosm columns was a uPVC tube with an internal diameter of 10.2 cm and total height of 36 cm. On the basal end of the uPVC tube was a uPVC end-cap which featured ten evenly spaced holes of 5 mm diameter. A single layer of nylon mesh with an aperture of 300 µm (Plastok, UK) was laid into the base of the tube immediately over the holes in the end cap to prevent soil and sand aggregates from leaking out of the column via the holes. Coarse sand paper of 40 Grit (Flexovit, France) lined the inside of the uPVC tube with the abrasive surface facing soil-ward to increase surface connectivity at the interface between the edge of the soil and the inner wall of the tube. This would minimise the chance that preferential fluid flow pathways emerged. Sand of British Standard Fraction A (1.18 - 2.36 mm grain size) was placed onto the basal nylon mesh to a depth of 45 mm – the height of the end cap. A sand-textured Eutric Cambisol field soil (the same soil as the 'Bangor' soil used in Chapter 3 and which was collected from a surface plot at Abergwyngregyn, North Wales) was sieved to below 1 mm and placed on top of the sand until the soil was 25 cm deep. A sheet of the nylon mesh was laid onto the surface of the soil. This mesh was gently laid onto the surface of the soil, rather than pushed onto the surface, to reduce the risk of excess soil packing.

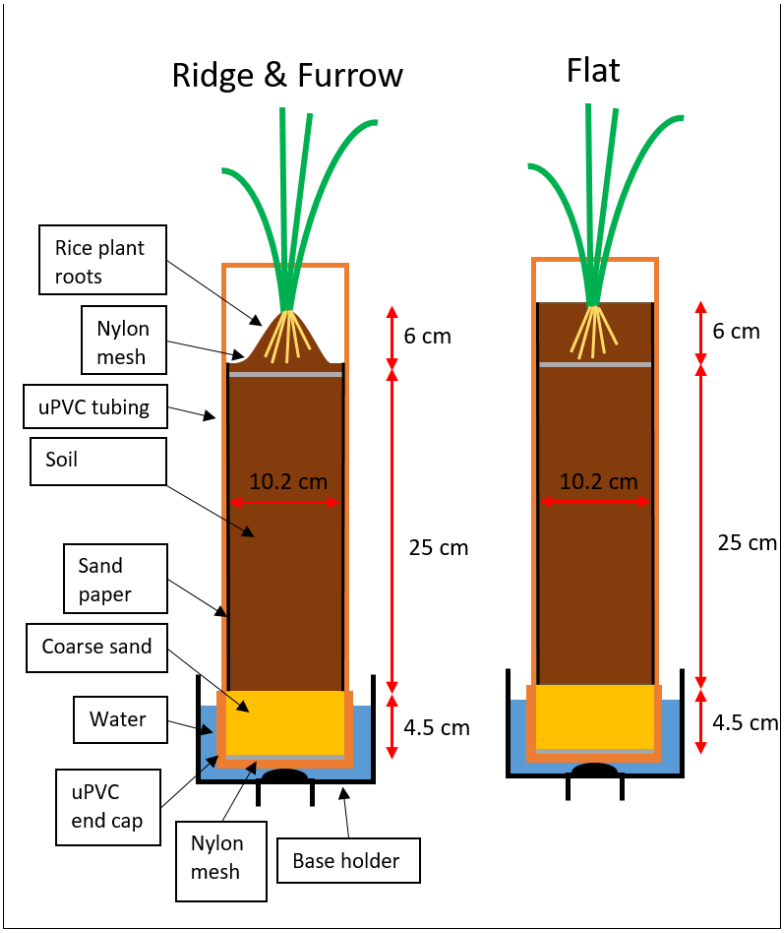

Figure 24. *Diagram of the column system featuring ridge and furrow (left) and flat (right) soil surface geometries.*

Two soil surface geometries were considered: a ridge and furrow geometry and a flat geometry. Additionally, an inverted ridge and furrow surface geometry was used to assess the significance of an edge effect (further details in 'Additional Inverted Ridge and Furrow System' below). For the flat soil surface geometry another 6 cm deep layer of soil was placed above the nylon mesh. For the ridge and furrow geometry a central mound was formed of the soil which was 6 cm in height from peak to trough. This resulted in a ridge width to ridge height ratio equivalent to that which can typically be found in agricultural field systems where this ratio can vary from 1:1 to 1:4 (Li & Gong, 2002; Tian *et al.*, 2003). This central mound formed a radially symmetrical representation of the ridge and furrow geometry. Pre-germinated rice seedlings (*Oryza sativa* subsp. *Indica* var. IR64) were placed in planted treatments into these top regions of the soil. This is discussed in more detail in the section 'Growth Conditions for Planted Treatments'. The upper layer of nylon mesh, buried 6 cm under the soil surface, confined maximum root growth to this top region of soil since it was necessary to downscale the soil system such that it would be XCT compatible. In particular, the

roots were not to grow to a greater relative depth than would be the case in a field system. In the field the root system would not substantially develop beyond the base of the ridge. We therefore use the nylon mesh to constrain maximum root growth to an equivalent depth for our scaled down system.

Additional Inverted Ridge and Furrow System

There was an inverted ridge and furrow surface geometry featuring no plant and no ponding for which the purpose was to assess the significance of an edge effect in the ridge and furrow geometry. For this surface geometry the experimental soil columns were setup in much same manner as the other soil columns (***Figure 25***). Where this surface geometry differed from the flat and ridge and furrow surface geometries was the structure of the top 6 cm of soil above the nylon mesh. For the inverted ridge and furrow system soil was added to a depth of 6 cm above the nylon mesh. The soil in the centre of the column was then removed to a depth of 6 cm. This soil surface setup is displayed in (***Figure 25***). There were three replicates for the inverted ridge and furrow surface geometry which underwent the same XCT imaging and image analysis as the flat and ridge and furrow soil columns.

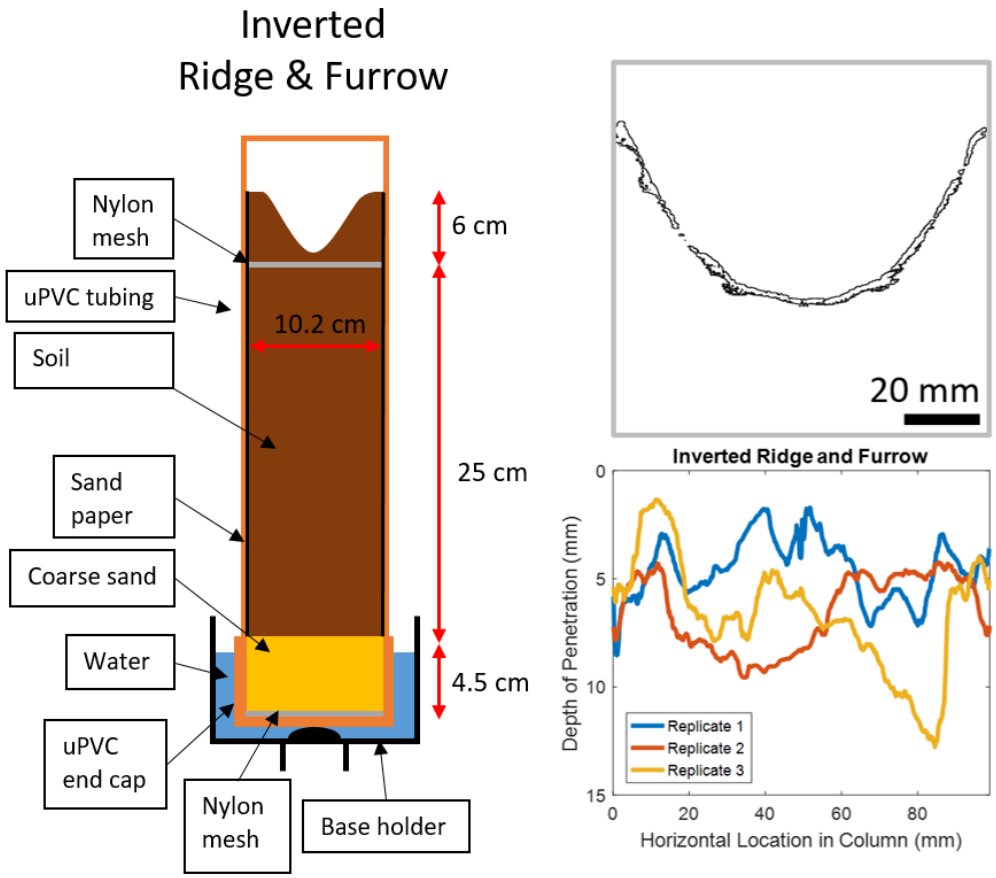

Figure 25. *The distance moved by the contrast agent vertically down the non-planted and non-ponded inverted ridge and furrow columns after 4 hours. On the left is a schematic of the inverted ridge and furrow column. The image on the top right is the segmented vertical-reslice image of the final contrast agent position (final position is outlined in black). Bottom right is the resulting plots from the Matlab script displaying distance moved vertically downward by contrast agent in the adjacent reslice image.*

Soil Bulk Density

Soil bulk density of all columns was recorded prior to watering and addition of plants. Soil bulk density was recorded for all of the columns by measuring the mass of all the column components, including sand, sanding paper and mesh, prior to the addition of the soil and then subtracting this value from the mass recorded once the soil had been added. The volume was calculated using the known internal diameter of the uPVC tubing and depth of soil. The mean soil bulk density was calculated as was the standard deviation presented in text as: mean ± standard deviation.

Base Holder and Basal Water Provision

The entire column was moved onto a raised central ridge in a 'base holder' consisting of a cylindrical uPVC tray of 15 cm internal diameter and 7.5 cm height. Three bolts of 4 cm length, which were radially evenly spaced, were drilled through the side of the larger cylinder at a height of 2 cm from the cylinder's top edge. Bolts were tightened such that the column was held securely and straight. Distilled water was then poured into the cylindrical tray to a depth of 4 cm around the outside of the column. The raised central ridge, which the column base rested on, allowed water in the tray to enter the column through holes in the basal end-cap and thus passively provide water to the soil system. The base holder featured an additional smaller cylinder, 6.2 mm internal diameter and 2.5 cm height, which extended downward from beneath the tray. This smaller additional cylinder allowed the base holder, which held the column, to later be secured in place on the stage of the XCT scanner using a 3-jaw chuck.

3.4.2 Experimental Treatments

The main treatments were combinations of either planted or non-planted systems, ridge and furrow soil surface geometries or flat soil surface geometries and either with ponding of water on the soil surface or without, summarised in ***Table 6.*** This combination of treatments is similar to those previously modelled by Duncan *et al.*, (2018a; 2018b). There were three replicate columns for each of the eight treatments (total 24 columns).

Table 6. *The experimental treatments undertaken. "Flat" indicates a flat soil surface geometry and "R&F" indicates a ridge and furrow soil surface geometry.*

	Without ponding	**With ponding**
No plant (Flat)	Treatment 1	Treatment 2
Plant (Flat)	Treatment 3	Treatment 4
No plant (R&F)	Treatment 5	Treatment 6
Plant (R&F)	Treatment 7	Treatment 8

3.4.3 Growth Conditions for Planted Treatments

Indica rice cultivar IR64 (*Oryza sativa* subsp. *Indica* var. IR64) was selected for planted treatments due to its high water uptake rate (Kramer, 1983; Li *et al.*, 2017) and shallow root architecture (Uga

et al., 2011; Uga *et al.*, 2013). Therefore, this rice cultivar was capable of successful development even with shall root growth as was necessary to downscale the soil system suitably for XCT imaging, whilst maintaining approximate root distribution and water mechanics of a field system. Whilst the nylon mesh was intended to confine maximum root growth, it was only likely to be necessary in the instance of exceptional root growth as the root architecture had been observed to remain sufficiently shallow during the four week duration of growth. Therefore the formation of root mats on the nylon mesh was unlikely and was in fact not observed within any replicates. Prior to transplanting into columns, the rice was pre-germinated. This germination involved submerging the seeds in water for 10 days using a photoperiod of 12 hours per day at a temperature of 30 ˚C / 27.5 ˚C during "day time" and "night time", respectively, controlled in a Conviron CMP6010 Growth Chamber (Controlled Environments Ltd, Canada). The humidity inside the chamber remained at 70% throughout the germination period.

Once germinated, rice seedlings were transplanted into the columns and placed 0.5 cm beneath the soil surface in the centre, orientated such that the leaf shoot emerged through the surface of the soil. In the ridge and furrow systems the seedlings were transplanted into the ridge. The entire column setup was then moved into the growth chamber, including the base holders in which the columns were held. The columns remained in the growth chamber for a total of four weeks until imaging. The water in the base holder trays was refilled regularly to maintain the provision of water to the columns of soil through the end-cap. Additionally, 15 mL of distilled water was mist-sprayed in a fine droplet size onto the soil surface of each column every other day until two days before imaging to ensure the plants received sufficient water. Supplying the plants with water through the basal end-cap and through mist-spraying reduced the risk of soil erosion from large water droplets on the soil surface.

After the imaging experiments had concluded, the plants were immediately harvested and weighed for a fresh mass value. The harvested plants were then dried in an oven at 60 °C for three days and the dry mass was recorded. The mean mass was calculated for plants from flat systems, plants from ridge and furrow systems and the overall mean of all plants. Standard deviation is reported alongside the mean in the format: mean ± standard deviation. A one tailed student's t-test assuming unequal variance was used to assess significant difference between the mass of plants from flat or ridge and furrow systems where significant difference was considered $P < 0.05$.

3.4.4 X-ray Computed Tomography Imaging

A contrast assessment was undertaken to ascertain the quantity and concentration of contrast agent that would need to be applied to columns for sufficient contrast. This assessment also provided the XCT parameters used for the column imaging. All XCT and radiography imaging was accomplished using the Custom 450kVp Hutch at the µ-VIS X-ray Imaging Centre, University of Southampton, UK. The contrast assessment column was set up in the same system as the main experimental treatments. The contrast agent used for these experiments was Niopam 370 (Bracco, UK), an iopamidol based contrast agent containing 370 mg iodine / mL. A dilution series of the contrast agent with distilled water was produced at milligrams of iodine per millilitre of solution concentrations of: 370 (100% of as supplied concentration), 333 (90%), 277.5 (75%), 185 (50%), 92.5 (25%) and 37 (10%). These concentrations were decanted into 2mL Eppendorf tubes (Eppendorf, Germany). For each contrast assessment image three tubes containing the contrast agent and one tube of distilled water were embedded into the soil of the contrast assessment column in a ring. The tube containing water acted as a reference value. The depth of the tubes was such that the tube caps were level with the soil surface. The first contrast assessment featured the 370, 33 and 277.5 mg iodine / mL concentrations and the second contrast assessment featured the 185, 92.5 and 37 mg iodine / mL concentrations.

The fluid mass density of the contrast agent was also recorded at the concentration determined to be most appropriate during the contrast assessment. This was achieved by recording the mass of 1 mL of the contrast agent solution. This was recorded to assess whether this was substantially different to water and thus likely to influence preferential flow.

During all XCT imaging, the columns were affixed to the XCT scanner stage by placing the smaller cylinder on the underside of the base holder (as shown in ***Figure 26***) into a three jaw chuck. For the contrast assessment imaging, the stage was raised such that the top 8 cm region of soil, which included the Eppendorf tubes containing the contrast agent, was imaged. The stage was lowered for the experimental columns to ensure that scans captured the region from 2 cm above the soil surface through to 12 cm below. Capturing this region would ensure that the top 10 cm of soil would be clearly visible, whilst allowing an additional 2 cm zone of non-essential image information at the top and bottom of the scan. This was because cone beam artefacts were expected to form within these 2 cm zones at the top and bottom creating streaks of high grey values which would make later image processing more complex.

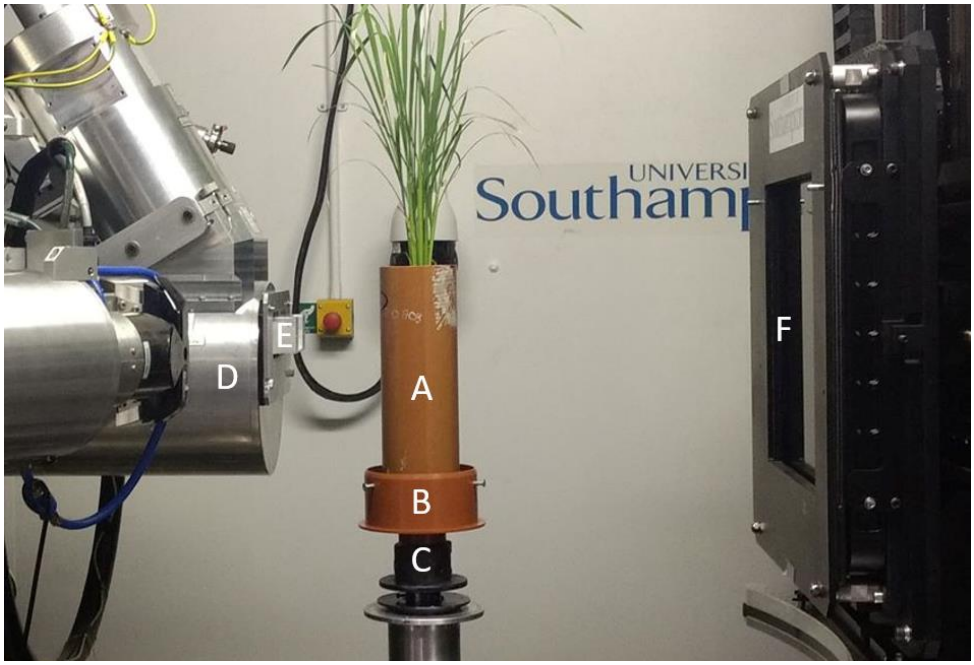

Figure 26. *Planted soil column (A) in a base holder (B) affixed to the XCT scanner stage using a 3 jaw chuck (C). X-ray source (D), including aluminium bow tie filter (E), and flat panel detector (F) are visible.*

Contrast agent was added to the experimental column soils 1 minute before the start of image acquisition. A 25 mL volume of the contrast agent was sprayed evenly over the surface of the soil at a concentration of 185 mg I / mL, as determined as most appropriate by the contrast assessment. For the treatments with ponding, 15 mL of water was then sprayed onto the soil surface such that ponding occurred above the soil surface. The treatments without ponding did not undergo the addition of water to the soil surface after contrast agent application.

The XCT imaging utilised an X-ray tube with a tungsten target to generate X-rays of 400kVp in energy. An aluminium bow tie filter was applied to reduce edge effects and artefacts resulting from greater X-ray transmission at the edges of the columns. A comprehensive list of imaging parameters are given in ***Table 7***.

Table 7. *The parameters used for the XCT imaging. All XCT and radiography imaging was accomplished using the Custom 450kVp Hutch at the μ-VIS X-ray Imaging Centre, University of Southampton, UK.*

Parameter	Value
Voltage (kV)	400
Amperes (μA)	513
Power (W)	205.2
Exposure (ms)	88
Analogue Gain	2
Binning	x2
Number of Projections	1201
Frames per Projection	2
Target Material	W
Detector	Flat Panel (2000x2000 pixels)
Filtration	Al (bow tie)
Resulting Voxel Size (μm)	130

One XCT scan was captured of each contrast assessment column. The experimental columns were imaged once before the application of the contrast agent to produce a 'control' image. The contrast agent was then applied and four hours later the columns were imaged again to produce a 'final' image. The resulting XCT images were reconstructed using the software CTPro 3D (Nikon, Tokyo, Japan) with a fine scale dual centre of rotation detection. The images were reconstructed as 32bit 3D image stacks.

3.4.5 Image Analysis

Segmentation of Contrast Agent

The image segmentation of the XCT data was undertaken using the Fiji distribution of the image processing software ImageJ (Schindelin *et al.*, 2012; Rueden *et al.*, 2017). The image segmentation workflow is summarised in ***Figure 27***. First, a 3D Gaussian blur operation with a radius of 6 pixels in each dimension was applied to the 'control' image (the image captured before contrast agent was

applied). This reduced speckle from individual particles, from pores where there were some small changes in pore structure with time and variation in localised contrast particularly at the soil surface and in ridges where total linear attenuation can be variable. The next stage in the workflow was the subtraction of the smoothed control image from the 'final' image (the image captured approximately four hours after the contrast agent was applied). This removed the contrast resulting just from the attenuation of the soil and not the contrast agent and allowed the contrast agent distribution to be segmented.

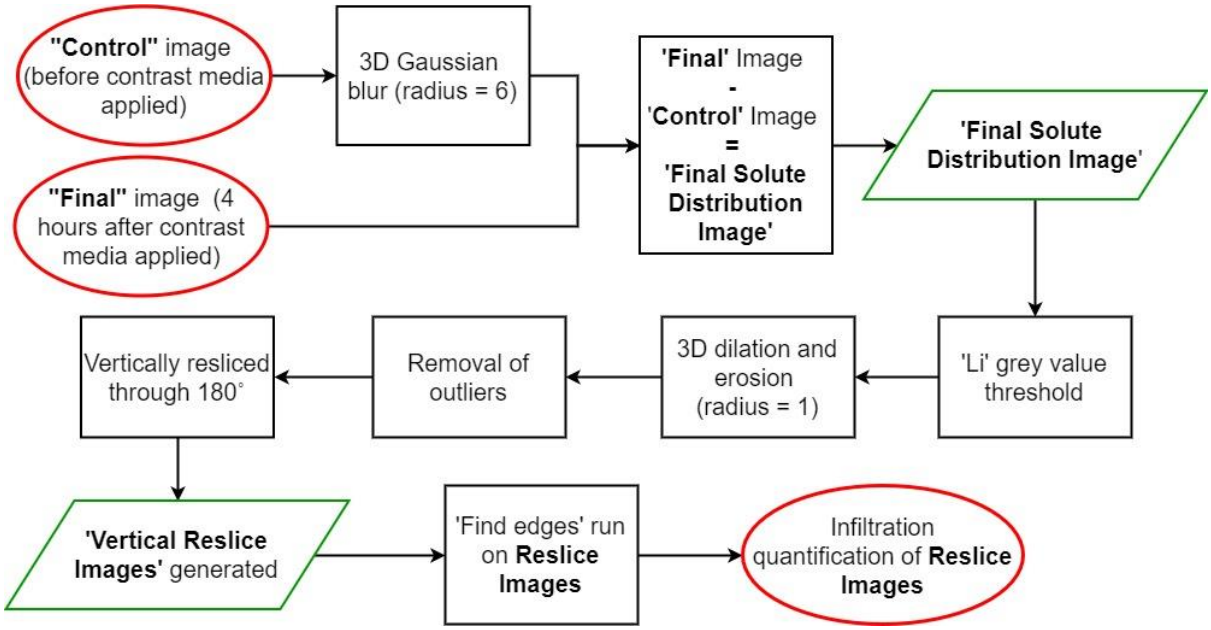

***Figure 27**. A flowchart outlining the workflow for image segmentation of the contrast agent distribution. The red ellipses represent the first and last images in the segmentation workflow. The green parallelograms are output images, with the title of the images in bold and in quotation marks. The black rectangles are the operations that were applied.*

The post subtraction image stack was then cropped and a 'clear outside' operation was performed which removed image data outside an oval outline such that the image stack only included the area inside the column. This oval outline around the inside of column was set by segmenting the uPVC tube using a grey value threshold, obtaining the dimensions of the inner wall of the tube and then using this to set the oval. A 'Li' binary threshold (Li & Tam, 1998) was applied to the image stack to segment the high grey value pixels of the contrast agent from any remaining pixels of soil or column

material. The 'Li' binary threshold is an iterative method which uses a one-point iteration to determine the threshold which minimizes the cross entropy of the unsegmented image and the segmented image (Li & Lee, 1993; Li & Tam, 1998). This was followed by a 3D ball dilation and then an erosion of 1 pixel in each direction using the FIJI 'Morphological Filters 3D' tool from the plugin package 'MorphoLibJ' (Legland *et al.*, 2016). A 'remove outliers' was then applied to the stack which removed any groups of pixels of less than three pixels in diameter. Both the 'dilation'/ 'erosion' and 'remove outliers' operations were intended to reduce 'speckle' from individual pixels of high grey value which had resulted from particularly attenuating soil grains that had been over-segmented.

Following contrast agent segmentation, a '180˚ rotation vertical reslice' stack was produced for each column (***Figure 28***). The reslice stacks would enable analysis of vertical contrast agent infiltration depth in the context of the radial symmetry of the column systems. To produce these stacks, first the segmented image stack was duplicated. The duplicate stack was then rotated by one degree and resliced along the centre line of the vertical (Z) axis to produce a 2D reslice image (***Figure 28***). This duplication and reslicing process was repeated 180 times and each time the angle of rotation performed on the duplicate stack was increased by one. Using this method, a stack was produced containing the 2D reslice images of the full 180˚ rotation. A 'find edges' operation was performed on the stack of reslices in preparation for the next stage of analysis and this stack was then saved.

Finally, the infiltration depth of the contrast agent within the columns was quantified. To achieve this, each 2D image of the vertical reslice image stack was read into Matlab (MathWorks, US) as arrays of pixel values. A custom script calculated the difference between the top (soil surface) and bottom edge position (deepest point of solute infiltration) for every column within the arrays. This calculated value was the approximate infiltration depth vertically down columns by the contrast agent within the four hours. The values for the infiltration depth of contrast agent were then averaged across the rotation images and the radial mean average infiltration depth of the contrast agent was plotted from the outside edge to the centre of the columns. The overall mean infiltration depth for each replicate was also calculated in addition to the standard deviation also using Matlab. Standard deviation is reported alongside the mean infiltration depth in the format: mean infiltration depth ± standard deviation.

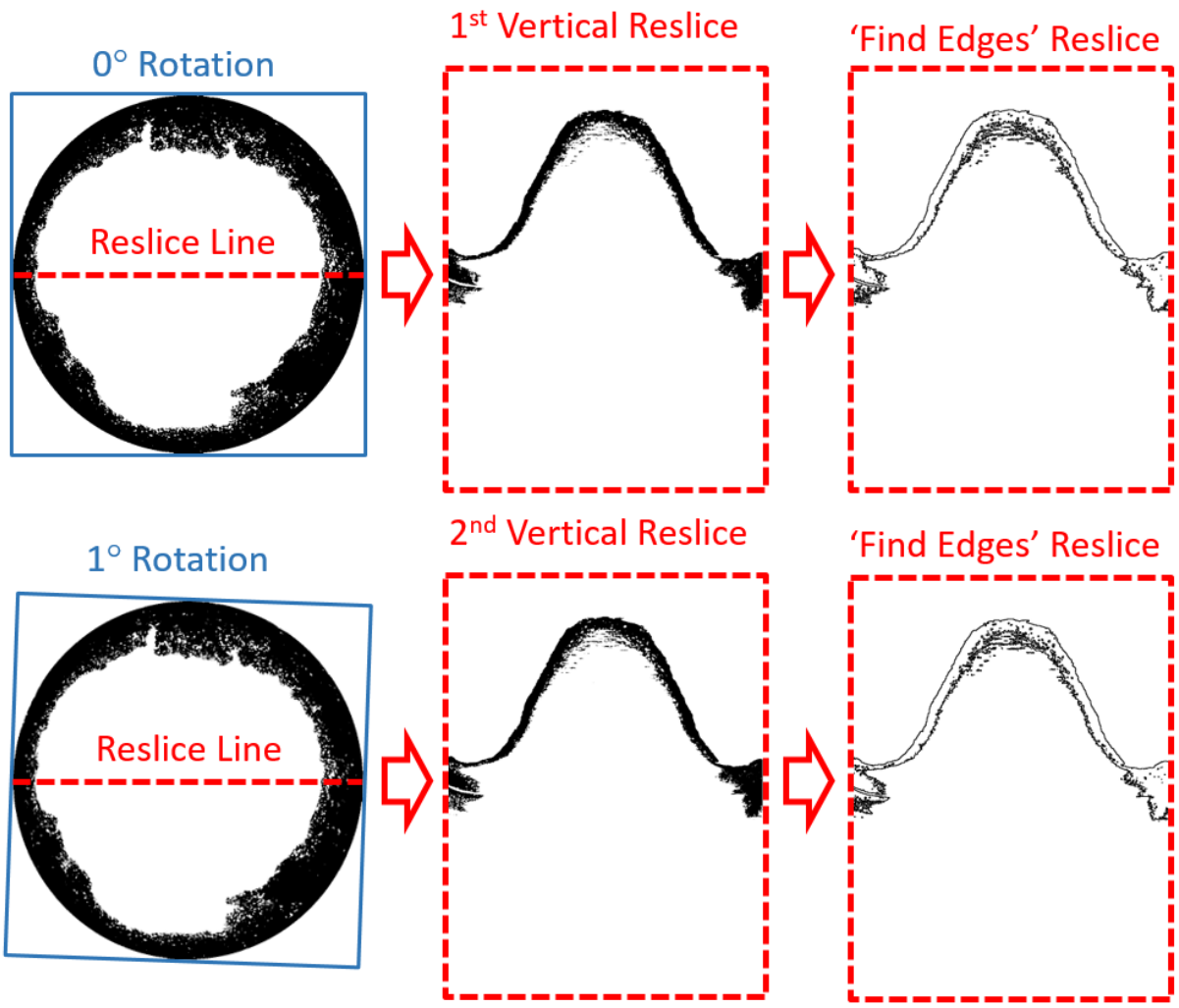

Figure 28. *A diagram demonstrating the vertical reslice and find edges operations performed during the image analysis. The top row are the initial images before rotation. The bottom row is the images after the first rotation of 1°. The resliced images are produced by performing a 'reslice' operation along a central horizontal line through the image stacks. This is demonstrated by red dashed lines in the images on the left which represents the line along which the resliced operation is performed.*

Root Surface Area Density

Image processing was undertaken on Replicate One of the planted flat system with ponding to segment the roots and to quantify the density of the surface area of the roots with distance from the column centre. This image processing was undertaken using the FIJI distribution of the software ImageJ (Schindelin *et al.*, 2012; Rueden *et al.*, 2017). These data were then used to parameterise the density of root surface area in an additional model simulation rather than the homogenous root distribution used in all other simulations of this investigation. The purpose of this image processing and parameterised simulation was to demonstrate that discrepancies between infiltration patterns

observed in the imaging experiments and patterns observed in the other modelling simulations could partly be a result of the implementation of homogenous root distribution.

To segment the roots the 'control' image stack (without contrast agent) was first changed from 32bit to 8bit in order to reduce computational time. The image stacks were then cropped such that only the inside of the columns remained. This was achieved by using the 'make oval' tool to place an oval around the inside of the wall of the uPVC column followed by the 'crop' and 'clear outside' tools. Slices outside of the range 498 to 731 were removed as slices outside this range did not contain roots as they were either above the soil or beneath the nylon mesh. A grey value threshold between 1 and 71 was applied which captured the roots in soil. The 'remove outliers' tool was applied with a radius of 3 pixels to remove some soil particles which had also been segmented by the threshold. Following this, some over-segmented soil particles remained and these had to be manually removed from the images using the 'paint brush' tool. Given the elements of manual segmentation involved, it was not possible to apply this labour intensive image processing to all twelve columns containing plants. For the other imaged columns the nylon mesh would constrain the root growth to only the top region of the soil and this would control the maximum region of root growth without requiring this labour intensive process of segmenting the root systems. The root map which was produced following this segmentation is displayed in ***Appendix Figure A1***.

The first step in quantifying the root surface area density was the creation of a new image stack with every pixel value set to zero and the same dimensions as the cropped segmentation image of the roots using the 'new image' tool. A single pixel in the centre of each image slice of this new stack was set to a value of 255. A Euclidean distance transform was then applied from the central pixels set to 255 outwards using the tool '3D Distance Map' from the '3D ImageJ Suite' of plugins (Ollion *et al.*, 2013). The resulting distance transform stack was duplicated three times. A grey value threshold of 0 to 58 was applied to the first duplicate stack which created a central circle in each slice of the stack with a radius of 16.66 mm. A threshold of 59-118 was applied to the second duplicate stack which created a ring with an internal radius of 16.66 mm and an external radius of 33.33 mm. A threshold of 119-178 was applied to the third duplicate stack which created an outer ring with an internal diameter of 33.33 mm and an external diameter of 50 mm. Essentially in each of these duplicate stacks were concentric rings of equal thickness to one another (16.66 mm).

The segmentation image stack of the roots was then multiplied by each of these distance transform concentric ring image stacks. This produced three image stacks containing: only the roots present between the centre of the column and 16.66 mm out, only the roots present within a ring between 16.66 and 33.33 mm out from the centre and only the roots present within a ring between

33.33 mm from the centre to the very outer edge of the column, respectively. The plugin '3D Objects Counter' (Bolte & Cordelieres, 2006) was then applied to each of these three concentric ring image stacks of segmented roots to record the surface area of the roots present. The total surface area of roots present within each ring was then divided by the total volume of the ring to provide data for the density of root surface area with distance from the centre of the column. The root surface area density values were as follows: 0.063 mm^2 / mm^3 in the central volume (with a radius of 16.66 mm), 0.015 mm^2 / mm^3 in the middle ring between the central volume and outer ring (with an internal radius of 16.66 mm and an external radius of 33.33 mm) and finally 0.004 mm^2 / mm^3 in the outer ring.

3.4.6 Resistance Sensors for Spatial Soil Moisture

Resistive soil moisture sensing (RSMS) is a technique used to assess soil moisture (Zazueta *et al.*, 1994) and was applied here to assess spatial variation in soil moisture. RSMS was utilised to monitor soil moisture in this investigation as an alternative to weighing the soil columns throughout the experiments. Whilst the mass of soil columns could have been an interesting additional dataset, we did not know the mass of the plants which were present so it would not have been possible to use changes in soil column mass to determine soil moisture. Duplicate columns were made for the RSMS experiments as RSMS probes are physical structures that could create macro pores in the soil. RSMS-related macro pores could act as preferential pathways which would enable faster movement of contrast agent compared with the rest of the soil and bias the measured distances in the images. The columns used for the RSMS experiments featured the same combination of treatments as the imaged columns (***Table 6***). The custom built RSMS system consisted of a Raspberry Pi Zero W (Raspberry Pi Foundation, UK) connected to a soil moisture probe (The Pi Hut, UK) via an analogue to digital converter (ADS1015, Adafruit, USA) that recorded analogue voltage impedance between forks of the probe as a proxy for soil moisture. In each column were three soil moisture probes which each had a total width of 2 cm and functional probe fork length of 3 cm. The first probe was placed into the centre of column, the second halfway to the outside of the column and the third 1 cm in from the column edge. Each probe was placed vertically down through the soil surface so that the soil just covered the top of the probe fork. A diagram which visually displays the positioning of the probes is given in ***Appendix Figure A2***.

The Raspberry Pi-based system was constructed from the design given by The Pi Hut (Hut, 2019) and the Python code (Python version 2.7) used for recording the voltage impedance values was based upon the Python code 'Adafruit_ADS1x15' which is open source and available on GitHub

(Fried *et al.*, 2013). The same and similar methodologies have been used numerous times for soil moisture sensing applications (Chate & Rana, 2016; Jadhav & Hambarde, 2016; Ishak *et al.*, 2017). The published Python code was however modified for this experiment in order to take five voltage recordings on the hour – each recording separated by five seconds. The times when these voltage recordings were taken were recorded and the mean and standard deviation of the five recordings were calculated. These hourly voltage recordings were taken for a full five days, four weeks after the transplanting of the seedlings into the columns for planted treatments (equivalent to the first XCT imaging time point in the imaged columns).

The device was calibrated to ensure the accuracy of the recordings and to correspond the measured voltage values to soil moisture values. The soil used in the RSMS columns was the same soil type as used in the imaged columns. This soil for the RSMS columns was oven dried at 110 °C for five days. The soil calibration samples were wetted using distilled water to volumetric water contents ranging from 0 to 50% at 5% increments. The voltage data recorded by the probes was linearly correlated with the known soil water percentage. The slope of this correlation was -1.0817, the intercept was 1.2079 and the r^2 value for the correlation fit was 0.966. The standard deviation is reported alongside the mean in the format: mean ± standard deviation. A one tailed t-test assuming unequal variance was used to assess significant difference where significant difference was considered $P < 0.05$.

3.4.7 Implementation of Model

We used the water-solute-pond model developed in Duncan *et al*. (2018a), which is used to study water and solute movement in a cross section of a ridge and furrow (or flat) soil surface geometry. The model consists of a coupled system of Partial Differential Equations (PDEs) and Ordinary Differential Equations (ODEs) that describe water and solute movement, and surface ponding in a ridge and furrow system.

Within the model the movement of water in soil is described by the effects of capillary forces, pressure gradients and gravity, all of which is coupled via a feedback loop to the pond depth on the soil surface. The pond depth is described by a combination of surface runoff, rainfall and infiltration into the soil. Furthermore, the transport of solutes, *i.e.*, contrast agent in soil under the influence of water movement is also included. The mechanisms driving solute movement are described by the processes of diffusion and advection, which are influenced by the movement of water and the resulting pressure gradients that form in the soil. The diffusivity of the solutes considers the diffusivity of iodine in free water under different soil saturation conditions and a tortuosity

impedance factor. This allows for a coupled system of equations to describe the simultaneous movement of water and solutes in soil. It should be noted that we assume solutes do not create osmotic pressure gradients influencing fluid flow, *i.e.,* water movement influences solute movement, but not *vice versa*. Furthermore, for the scales and rates of the fluid flow and the consideration of advective fluxes in the model, we neglect hydromechanical dispersion, which could more significantly impact solute transport on larger scales.

The model described is developed for generalised curved soil surface, *i.e.*, to account for the ridge and furrow geometry. However, this can be easily adapted for a flat surface. The details and necessary equations for the model used for this investigation can be found in the Appendix. For a full derivation and validation, see Duncan *et al*. (2018a).

3.5 Results

3.5.1 Contrast Assessment

The contrast assessment of the XCT images revealed that the contrast agent provided adequate contrast against both the soil and the Eppendorf tube containing the distilled water at all concentrations of the dilution series (***Figure 29***). However, it was found that concentrations of 222 mg iodine / mL and above were vulnerable to crystallisation. For these reasons, the 185 mg iodine / mL contrast agent concentration was determined to be the suitable concentration for application in this investigation: it produced sufficient contrast against both soil and water whilst not being vulnerable to crystallisation. Concentrations as low as 37 mg iodine / mL at least (a fifth of the concentration applied to the soil surface in the imaging experiments) provided sufficient contrast against soil and water so as to be segmented by the grey value threshold during the image processing.

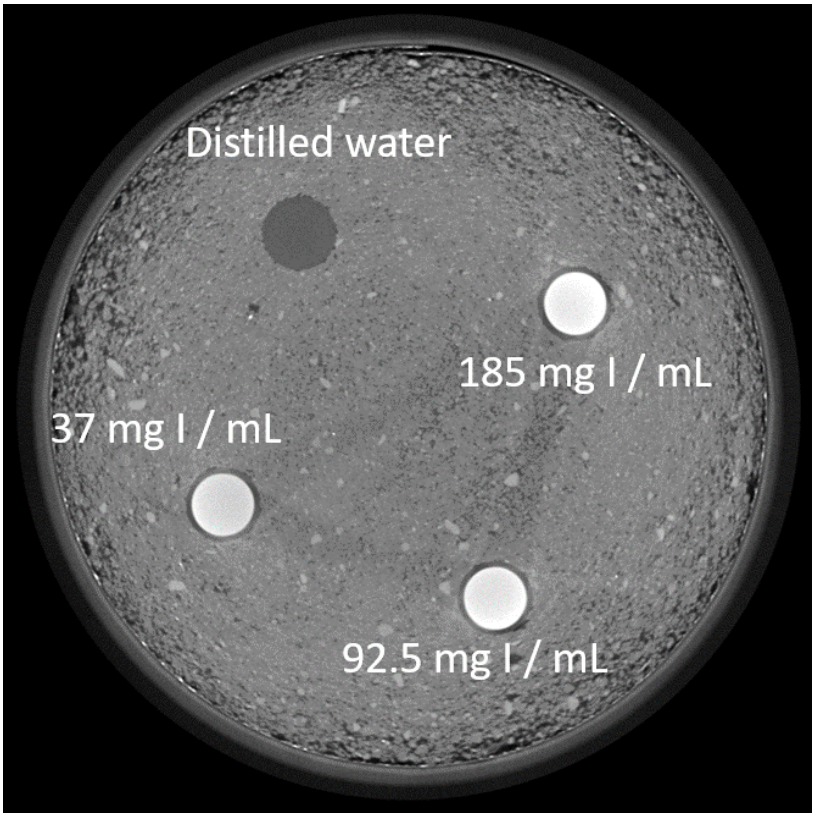

Figure 29. *A two dimensional image slice captured horizontally through Contrast Assessment Two. The three bright 'disks' are the Eppendorf tubes containing a contrast agent dilution series. All three tubes containing the contrast agent visibly produced sufficient contrast (a discrete peak in the histogram of grey values) against both the soil and the tube of distilled water.*

The fluid mass density of the contrast agent at a concentration of 185 mg iodine / mL was also recorded (1.0732 g / mL) and was similar to that of water (1.0021 g / mL). It is important to note that large differences in mass density between solutions in porous media can induce preferential flow and displacement fronts. Therefore if agrochemical solutions applied to soil possess a significantly different mass density to soil water then it is possible that flow behaviour may differ from that observed of the contrast agent solution in this investigation.

3.5.2 Soil Bulk Density and Plant Mass

The mean soil bulk density recorded for the columns at setup was 1.01 g / cm^3 ± 0.013. This soil bulk density is within the normal range for a sand-textured Eutric Cambisol field soil containing organic matter (Soane, 1990; Li *et al.*, 2002). A full table of soil bulk density values is presented in ***Appendix Table A1***.

The harvested fresh and dry plant mass was recorded for all of the planted columns. The overall mean mass of fresh plant material, dry plant material and water content was 16.69 ± 3.60 g, 2.72 ± 0.79 g and 5.65 ± 2.22 g, respectively. The student's t-test to assess significant difference between plants from flat systems and from ridge and furrow systems did not indicate there was significant difference for fresh plant mass (P = 0.84), dry plant mass (P = 0.57) or mass of water content (P = 0.67). A full table of plant mass values is presented in ***Appendix Table A2***.

3.5.3 Inverted Ridge and Furrow

The results of the inverted ridge and furrow imaging experiments indicated that the dominant influence over infiltration pattern was the treatment applied to the ridge and furrow columns and not an edge effect. In these inverted ridge and furrow experiments there was no evidence that the contrast agent had infiltrated to a greater depth at the edges compared with the centre (***Figure 25***). The contrast agent should have been greater at the edge instead had there been a significant edge effect. This indicated that experimental observations regarding infiltration depth at the edge of the ridge and furrow columns are the most likely the result of the experimental treatment rather than an edge effect.

3.5.4 Ridge and Furrow Geometry Overview

<u>Experimental Results</u>

The XCT image results of non-ponded treatments indicated that roots impede the infiltration depth of the contrast agent (***Figure 30***). In the ridge and furrow system with a plant but without ponding, the contrast agent infiltrated to an average depth of 3.88 ± 2.53 mm and a maximum depth of 10 mm over the course of the four hours (***Figure 30*****b**). When no plant was present, the infiltration of the contrast agent was greater – to an average depth of 9.98 ± 3.3 mm (***Figure 30*****a**). In ridge and furrow treatments with ponding and plants, the impedance of contrast agent infiltration depth was varied (***Figure 30*****d**). In the ridge, the infiltration depth was less than 10 mm in two of the three replicates. However, in the furrow the infiltration depth was between 15 and 25 mm. This is further than in the planted systems without ponding (***Figure 30*****b**). The pattern of contrast agent infiltration in the planted system with ponding (***Figure 30*****d**) was in many cases similar to that of both the ponded and non-ponded systems with no plant (***Figure 30*****a** and **c)**. There is some variation between replicates within the imaging experiments (***Figure 30*** and ***Figure 33*****)**.

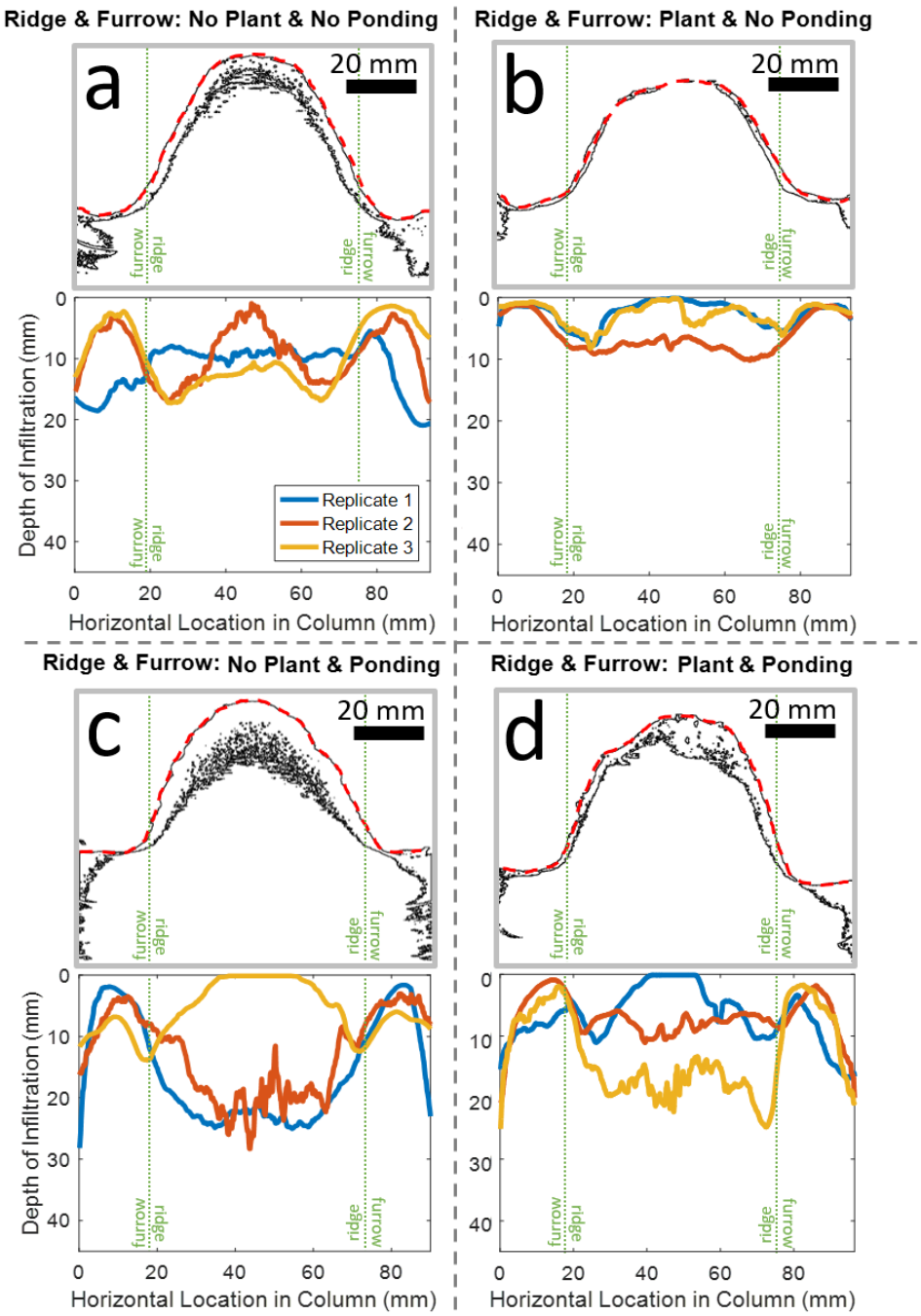

Figure 30. *The distance moved by the contrast agent vertically down the columns after 4 hours. The images on the top of each section are segmented vertical-reslice images of the final contrast agent position in one example replicate for each treatment (this final position is the region outlined in black). The soil surface in these images is indicated by the red dashed line. On the bottom of each section are the resulting plots from the Matlab script which display distance moved vertically downward by the contrast agent in the adjacent reslice images. (**a**) is the non-planted ridge and furrow system without ponding. (**b**) is the planted ridge and furrow system without ponding. (c) is the non-planted ridge and furrow system with ponding. (**d**) is the planted ridge and furrow system with ponding.*

Simulation Results

In the model, the transport depths for the planted ridge and furrow simulations without the addition of ponding was uniformly 10 mm from ridge to furrow (***Figure 31***), which is similar to the maximum depth observed in the imaging (***Figure 30*b**). However, the numerical simulations did not capture variation in contrast agent infiltration depth from ridge to furrow as observed in some imaged replicates for this treatment. Also, unlike the imaging results, the depth of contrast agent infiltration observed in simulation results was the same in the systems with no plant and no ponding as in the systems with a plant and no ponding. Images of the planted ridge and furrow system with ponding displayed some differences in contrast agent infiltration pattern compared to the numerical simulations. The 2D resliced images showed that the infiltration depth in the furrow was generally greater than in the ridge (***Figure 30*d**), which is consistent with the numerical simulations (***Figure 31***). The imaged contrast agent infiltration pattern was observed to be similar between the systems with a plant and ponding (8.99 ± 4.76 mm), with ponding but no plant (11.61 ± 6.99 mm) and the system with no plant and no ponding (9.98 ± 3.3 mm) (***Figure 30*a, c and d**). This was not true of simulations where results for these treatments were different. In the simulation for the system with a plant and no ponding the solute in furrows remained nearer to the surface than in the other two treatments.

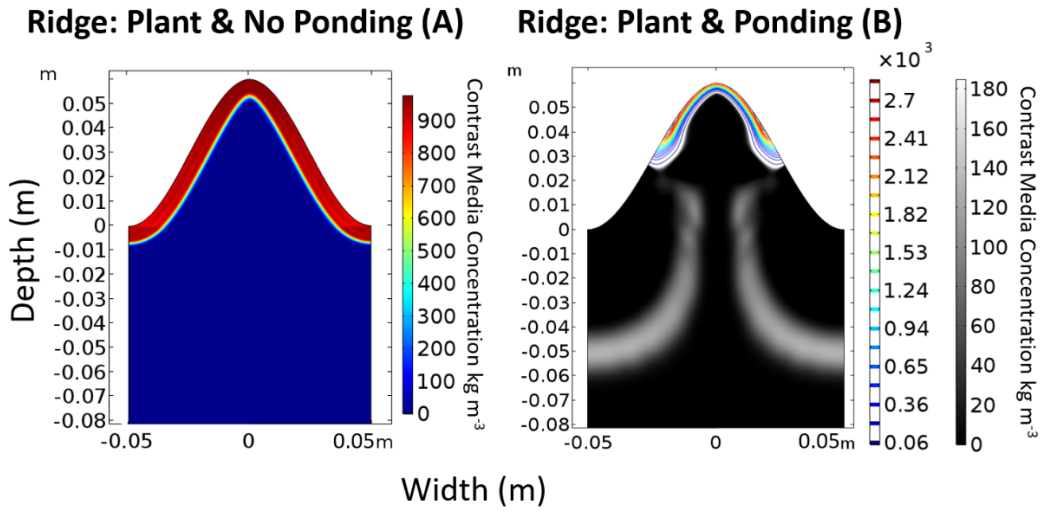

Figure 31. *Model simulation results for the planted ridge and furrow geometry without ponding (left) and with ponding (right) after four hours. The concentration of contrast agent is represented by colour gradients. For the ridge and furrow geometry with ponding the concentration of contrast agent is represented by a grey scale gradient for lower concentrations and a colour contour gradient for higher concentrations such that the full range of concentrations present can be visualised. In part B of the figure, a multicolour scale is used for higher concentrations of contrast agent and a greyscale is used for lower concentrations.*

3.5.5 Flat Geometry Overview

Experimental Results

The infiltration pattern was complex for the flat treatments. There was evidence of an inward movement of contrast agent horizontally toward the centre of column in the flat planted treatment without ponding (***Figure 32***).

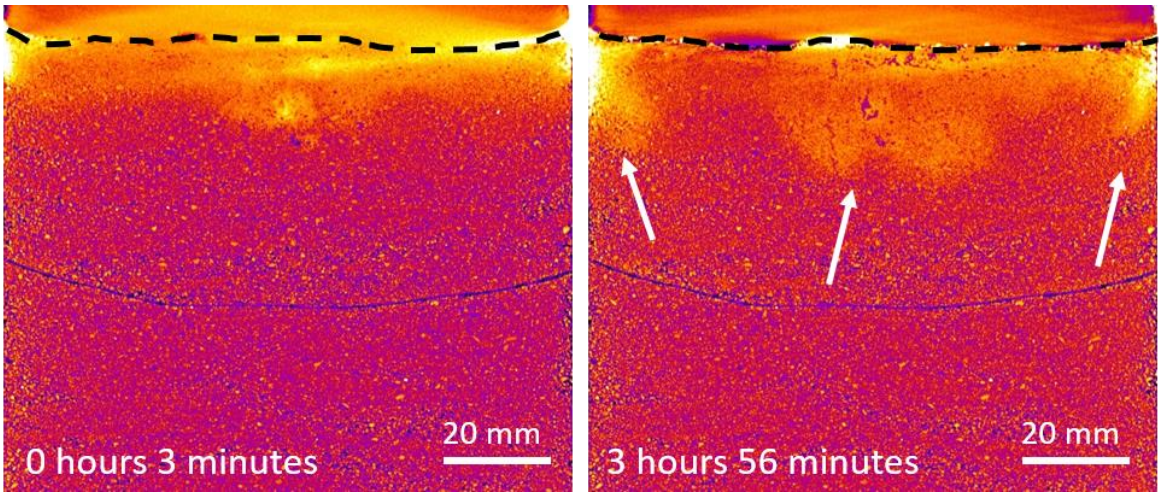

Figure 32. *Vertical reslice images displaying the initial (left) and final position of the contrast agent after almost four hours (right) in the planted flat geometry treatment without ponding. The image has undergone application of an alternative look up table. The more white the region of the image the higher the concentration of contrast agent and the more blue the lower the concentration of contrast agent was at that location. This reslice of the top region of the column was obtained through the centre line of the column at 0˚ of rotation. Deeper infiltration of the contrast agent in the central region and at the edges, indicated by white arrows, by the final time step is clearly visible. The centre is predicted to have had the greatest roots density.*

The contrast agent at the edges of the columns, i.e. furthest from where the rice seedling was planted, appeared to move freely downward in the column (***Figure 33*****b**). In the planted system with ponding the infiltration depth of the contrast agent was greater (16.19 ± 6.99 mm) than in systems without ponding (5.41 ± 3.38 mm) (***Figure 33*****d**). The infiltration patterns observed in the imaged flat system with no plant and no ponding were variable (***Figure 33*****a**) and the standard deviation for infiltration depth was high (6.99 ± 4.25 mm).

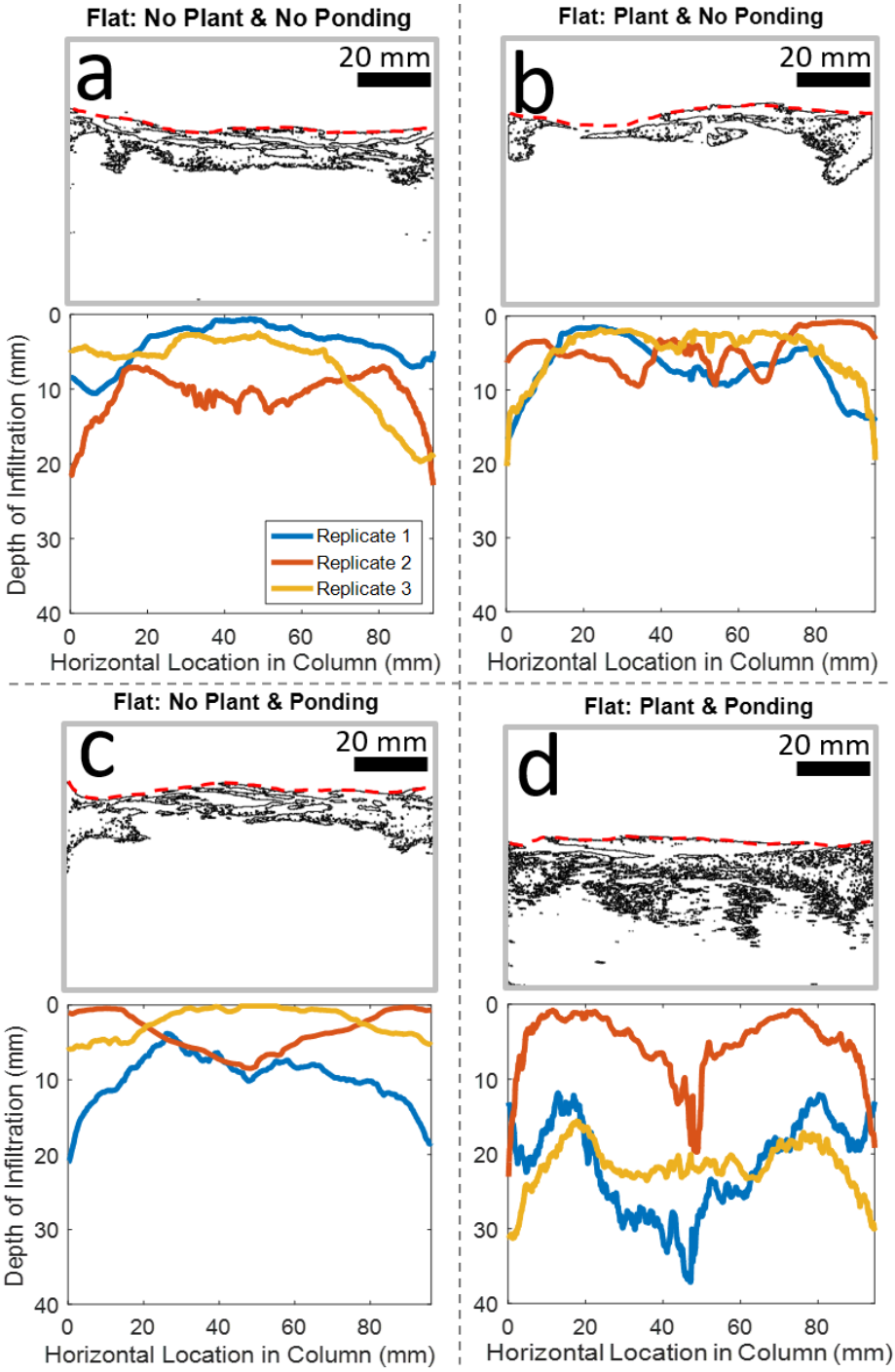

Figure 33. *The distance moved by the contrast agent vertically down the columns after 4 hours. The images on the top of each section are segmented vertical-reslice images of the final contrast agent position in one example replicate for each treatment (this final position is the region outlined in black). The soil surface in these images is indicated by the red dashed line. On the bottom of each section are the resulting plots from the Matlab script which display distance moved vertically downward by the contrast agent in reslice images. (**a**) is the non-planted flat system without ponding. (**b**) is the planted flat system without ponding. (**c**) is the non-planted flat system with ponding. **(d)** is the planted flat system with ponding.*

Simulation Results

When the patterns and depth of contrast agent infiltration in imaged flat systems were compared to those of the simulated flat systems with homogenous root distribution, disparities in infiltration patterns were apparent. The depth of infiltration was generally observed to be non-uniform from the edge to the centre of the column in the imaging experiments (***Figure 33***), whereas the simulation results showed no horizontal variation in infiltration depth (***Figure 34***). In the imaging results, the infiltration depth in the centre of the planted system with no ponding was up to 10 mm in the centre and 20 mm at the edges, whereas in the simulation results the infiltration depth was horizontally uniform. However, in the additional simulation which instead used root distribution data extracted from XCT imaging results a non-uniform infiltration depth can be observed (***Figure 35***). The simulation results for the planted flat system with ponding suggested that contrast agent infiltration would be uniform and to a greater depth (60 mm) than observed in the imaging experiments (16.18 ± 6.99 mm) (***Figure 33*****d** **&** ***Figure 34*****b**).

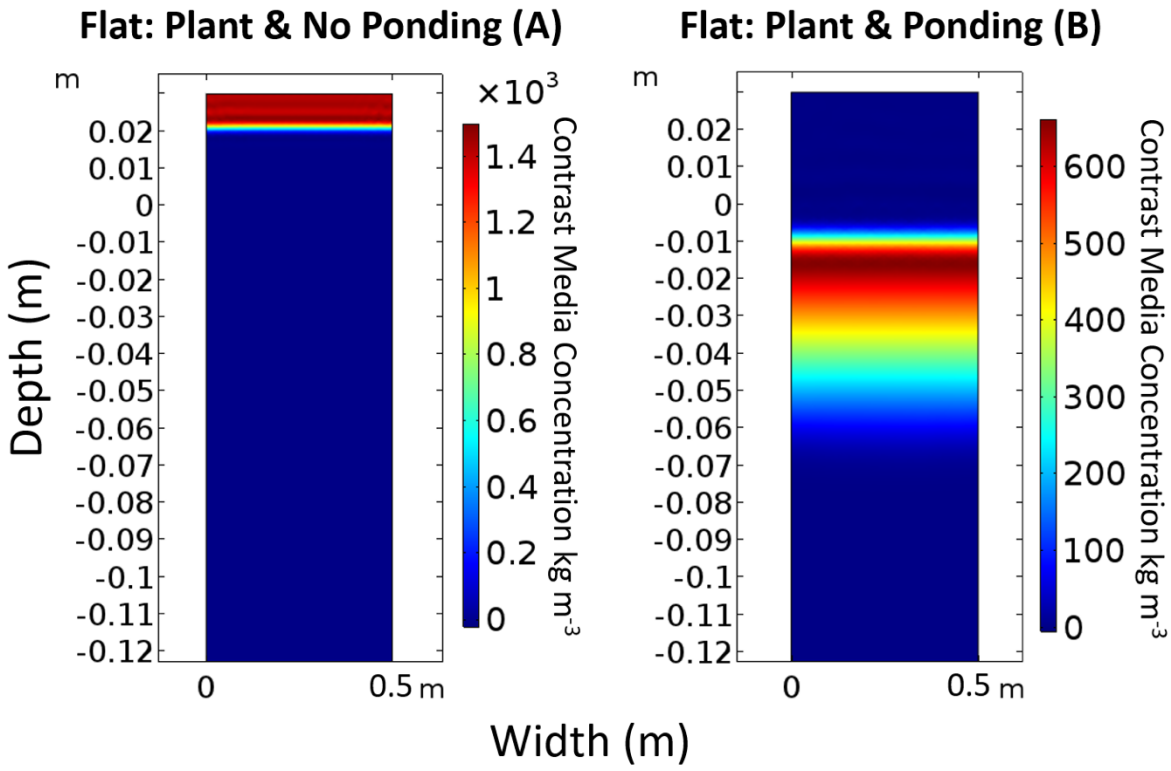

Figure 34. *Model simulation results for the planted flat geometry without ponding (left) and with ponding (right) after four hours. The concentration of contrast agent is represented by a colour gradient. The contrast agent infiltrates considerably deeper after a period of four hours in the ponded system (right) than the non-ponded system (left).*

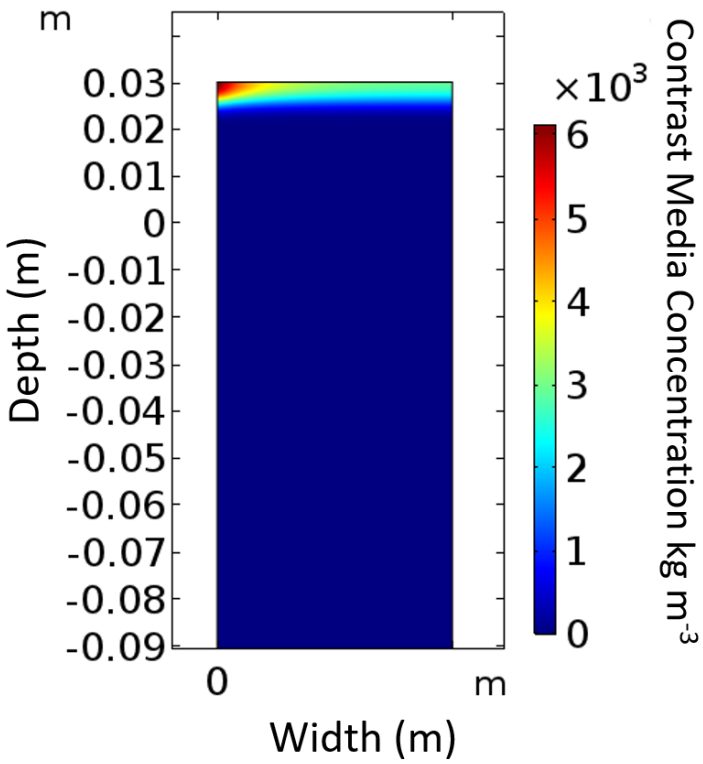

***Figure 35**. Model simulation results for the additional simulation of planted flat geometry without ponding after four hours. This additional simulation featured a root surface area distribution extracted from XCT imaging results whereas all other simulations in this investigation featured a homogenous root distribution. The concentration of contrast agent is represented by a colour gradient. The infiltration depth and concentration of the solute is observably greater in the root-dense centre of the column (0 m in width).*

3.5.6 RSMS Spatial Soil Moisture

The soil moisture values indicated two trends. Firstly, soil in both flat systems and ridge and furrow systems containing plants was significantly drier than in the systems without plants. For soil moisture values captured one hour before each watering event, there was significant difference between the soil moisture in the planted (11% VWC ± 0.057) and non-planted systems (20.4% VWC ± 0.026). This was true of both flat ($P = 8.65\times10^{-8}$) and ridge and furrow ($P = 0.0006$) surface geometries. The full data is displayed in ***Figure 36*.**

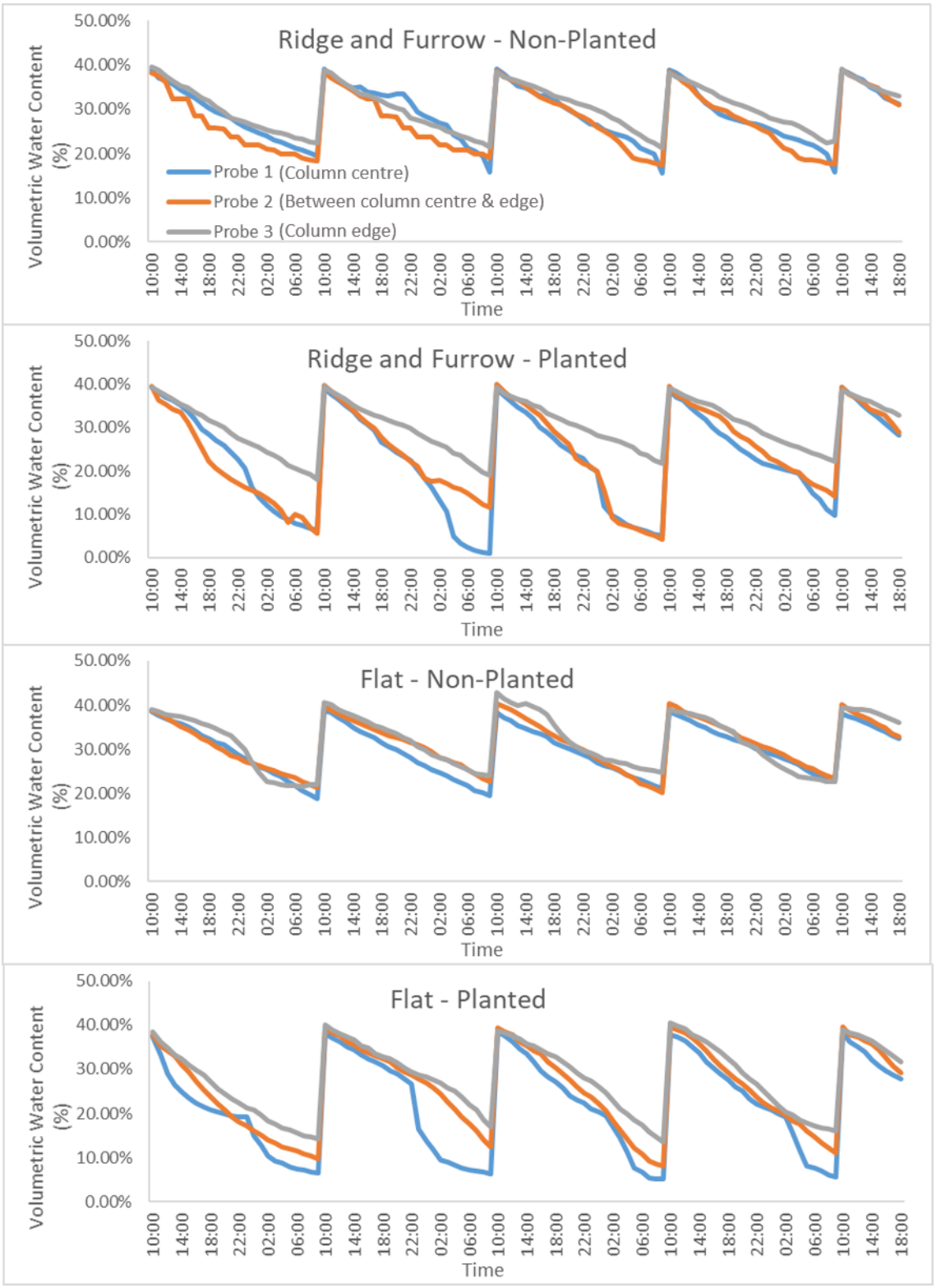

Figure 36. *Volumetric water content recorded as a percentage using a Raspberry Pi based resistive soil moisture sensing system. Probe One was in the centre of the column, Probe Two was halfway to the edge of the column and Probe Three was at the outer edge of the column. The probes were 3 cm in length each and were placed just beneath the soil surface.*

The second observable trend was that in planted systems, with either surface geometry, the probes nearest to the centre of the columns recorded the lowest soil moisture values. The central region of the columns was likely the most root-dense, as was observed in the image analysis of the root surface area density for Replicate One of the planted flat system with ponding (segmented to parameterise the additional model simulation with non-homogenous root distribution). Due to the labour intensive nature of this image processing it was not possible to segment the root surface area density in other planted columns. However, most roots were found in the central region of the columns upon visual inspection of the other planted replicates. In the intervals between watering events the soil in the centre of the columns dried at a faster rate than at the edges of the columns. For soil moisture values captured one hour before each watering event, there was significant difference between the soil moisture in the centre of the column and at the edges of the column for both planted flat ($P = 0.001$) and planted ridge and furrow ($P = 0.003$) systems.

3.6 Discussion

The aim of this study was to capture the movement of a solute through ridge and furrow and flat soil surface geometries using XCT imaging of contrast agent as it infiltrated soil columns. The treatments applied to the experimental systems were similar to those investigated using mathematical modelling by Duncan *et al.* (2018a; 2018b). The contrast agent iopamidol (trade name: Niopam) was applied to the surface of each of the columns. The position of the contrast agent was traced over a period of four hours using XCT. These experimental results were then compared to numerical simulations, initially developed by Duncan *et al.* (2018a; 2018b) though adapted to directly represent the experimental system.

3.6.1 Ridge and Furrow Surface Geometry

In the planted ridge and furrow treatment without ponding the infiltration depth of the contrast agent was minimal and the contrast agent accumulated near the soil surface in the ridge as was hypothesised (***Figure 30*b**). The infiltration depth of the contrast agent in the non-planted ridge and furrow system was substantially greater in both the ridge and furrow regions (***Figure 30*a**). However, in the simulation results the infiltration was the same in the systems with no plant and no ponding as in the systems with a plant and no ponding. This is possibly because of the difference in soil moisture in experimental columns compared with model simulations. The RSMS results had

suggested that the ridge of planted columns was significantly drier than non-planted columns, likely the result of root water uptake. If this were the case then the advection induced by the root water uptake could have also influenced the reduced vertical infiltration in the planted systems. This is in agreement with previous modelling investigations (Duncan *et al.*, 2018a; Duncan *et al.*, 2018b). However, it should be noted that, whilst RSMS results can give some insights into soil moisture, the RSMS results do not directly distinguish between the effects of root water uptake and evaporation. Therefore in future it would be useful to explicitly record transpiration rate and or root water uptake data in order to better decipher the influence of these factors.

In planted ridge and furrow systems with ponding, the infiltration depth in the furrows was greater than in the planted ridge and furrow systems without ponding (***Figure 30*b** and **d**). The infiltration depth in the furrow was more similar to the columns which contained no plant at all when ponding took place (***Figure 30*a** and **c**). This suggests that ponding can negate the capacity of roots to hold the solute near the surface of the soil. The infiltration depth in the furrow was likely further exacerbated by the greater initial water content in the furrow compared to the ridge prior to the addition of the contrast agent (***Figure 36***). The hydraulic conductivity of the soil in the furrow was therefore reduced even before the hydrostatic pressure, resulting from the addition of the ponding water, was considered. This deeper infiltration of contrast agent in the furrow for ponded systems was also observed in the simulation results (***Figure 31***). This suggests that the roots can have an observable effect on reducing the solute transport depth, particularly in regions nearest to where the rice seedling was planted. It should also be noted that in Replicate 1 of the ridge and furrow system without a plant or ponding there was the appearance of some minimal initial ponding in the furrow. This was likely caused by soil surface run-off of contrast agent from the ridge into the furrow. This soil surface run-off was not captured in the model as it assumed solute application is normal to the soil surface. These results could explain why some previous agronomic studies have found ridge and furrow geometries to be particularly susceptible to solute leaching (Smelt *et al.*, 1981; Kung, 1988; Leistra & Boesten, 2010). A period of significant rainfall or soil surface run-off of solutes during these agronomic studies could have exacerbated the solute leaching effect in the furrow.

3.6.2 Flat Surface Geometry

The pattern of contrast agent infiltration captured during XCT imaging of the planted flat system without ponding did not reflect that of the model simulations which featured homogenous root distribution. The contrast agent accumulated in the centre of the column in the imaging

experiments (***Figure 32*).** The numerical simulations for this treatment had suggested that the contrast agent infiltration would be horizontally uniform (***Figure 34***). In the additional simulation for the planted flat system without ponding, which featured the root distribution from the imaging results (***Appendix Figure A1***), this pattern of accumulation in the root dense centre of the columns can be observed suggesting a greater density of roots may have influenced this accumulation (***Figure 35***). This would appear to support the suggestion that a greater density of plant roots in the centre of the imaged columns could induce an accumulation in the centre of the columns. However, given the small number of replicates and the labour intensive nature of the root segmentation procedure meant that only one column could be analysed, this cannot be stated with certainty. It should also be noted that the root distribution of the rice plants used within this investigation could vary from those crops typically grown in such soil systems in the field. For example, the rice roots in this investigation were generally fine and spread laterally (***Appendix Figure A1***) and therefore did not generally produce heterogeneously distributed macropores further down within the soil. However, crops which produce a taproot or tubers, *i.e.* potatoes or carrots, would create such macropores around the taproot or tuber. This could lead to the formation of an 'edge' effect at the interface between the taproot or tuber and the soil which could induce heterogeneous preferential flow. Such a pattern would not have been captured by the fine rice roots of our system.

In the planted flat system without ponding the centre of the columns was also the driest region as indicated by the RSMS results (***Figure 36***). This central accumulation of contrast agent in this treatment may have been further influenced by the significantly drier soil surface in the experimental samples than in the model simulations prior to contrast agent applications. This was likely due to a combination of drainage, surface evaporation, and root water uptake effects (Hanks *et al.*, 1969; Nye & Tinker, 1977). The low soil water matric potential may have contributed to this water redistribution analogous to soil water sorptivity effects (Philip, 1957; Wooding, 1968; Philip, 1969). The drier soil subdomain could have induced a strong water potential gradient (Nye & Tinker, 1977) - hence the contrast agent redistributed through the soil toward the dry central region. This could explain why an inward movement of contrast agent is experimentally observed in the flat planted system without ponding (***Figure 32***). In the system without ponding, the contrast agent near to the centre was likely drawn further inward by this water potential gradient, which resulted from the advective root water uptake.

In this treatment the contrast agent was also observed to infiltrate to a depth of up to 30 mm through the soil at the edges of the column (***Figure 33*b**). It is possible the contrast agent at edges of these columns could have been too far from where the rice seedling was planted to be observably influenced by the roots and so was able to move freely deeper into the soil. It is also possible that

the deeper infiltration at the edges of the column is the result of an edge effect at the column wall as this is also observable in the flat system without a plant or ponding. Though, it should also be noted that in the RSMS experiments for both the flat system with a plant and without a plant the soil in the centre of the columns was frequently drier than at the edge (***Figure 36***) – possibly a result of surface evaporation. If the central soil was drier prior to the application of the contrast agent then the capillary action of the soil may have held more of the contrast agent fluid in in the centre nearer to the surface. However, there is ultimately too much variation between the replicates to determine the cause with certainty.

In the systems with a plant and ponding the contrast agent appears to infiltrate to a greater depth, particularly in the centre of the columns, than in those with no plant but which undergo ponding (***Figure 33*****c** and **d**). This is potentially a result of the ponded water forcing the contrast agent deeper into root-generated pores (Phillips, 2007; Milleret *et al.*, 2009; Ruiz *et al.*, 2015). This enhanced flow through root-generated pores is not included in the model. When there is no ponding treatment applied to the soil surface advection of the root water uptake remains dominant. However, when water is applied to the soil surface for the ponding treatment it is possible that the hydrostatic pressure of this surface water drives the contrast agent down through these root-generated pores. Therefore advection driven by roots water uptake to hold the contrast agent near the surface may be negated by the hydrostatic pressure from ponding water. In the equivalent ridge and furrow systems this is potentially not observed because the pond in those systems largely accumulates in the furrow whereas in the flat systems the ponding occurred across the surface. Therefore in the flat systems the ponding is over the area of the surface from which the plant emerges and is able to enter root generated pores with more ease thus forcing the contrast agent deeper. This is not captured by the continuum-based modelling methodology used in this study because it assumes uniform root distribution and does not consider anomalous pore structures that might have been caused by root-induced bioturbation.

3.6.3 Agricultural Implications and Further Work

The results of this work have several implications for the application of soluble agrochemicals to soil systems with either flat or ridge and furrow surface geometries. However, these potential implications should be viewed in the context of the limitations of the scale and technology deployed in this investigation. For example, there is variation between replicates within the imaging experiments (***Figure 30***, ***Figure 33*** and ***Figure 25***). The use of XCT technology meant that the replicate number was constrained to three. Given the exploratory nature of the study (testing

different eight different treatments), we were limited by the cost and availability of XCT facilities capable of imaging samples as physically large as the soil columns. Individual scenarios which are more specific in nature warrant focus on individual treatments with a greater number of replicates. This would also facilitate a greater use of statistical testing to analyse trends between treatments which could not be validly implemented within this investigation.

In addition, the physical downscaling of the ridge and furrow system, necessary for XCT imaging, has implications for the applicability the results of this investigation may have for agricultural field systems. We maintained a ridge height to ridge width ratio which was equivalent to that of field systems however, in field systems the height of ridges is typically between 15 and 60 cm whilst the width of ridges is typically between 30 and 60 cm (Li & Gong, 2002; Tian *et al.*, 2003). This physical downscaling would have for example reduced the surface area of the soil surface which would have had implications for evaporation of water from the soil. The heterogeneous aspects of soil systems also has implications for comparisons. For example, the soil aggregate sizes used in this investigation were more homogenous than would be expected in the field – though this was a necessary control measure for the reproducibility of the experiments. This could have implications for some aspects of the hydromechanics of the system such as the extent of capillary action taking place as well as hydromechanical dispersion. Previous studies have indicated that the relative influence of soil heterogeneity on solute movement can be considerable, for example compared to advection from root water uptake mechanisms (Schroder *et al.*, 2012; Koch *et al.*, 2019). In addition to soil heterogeneity, the soil bulk density used in this study was fairly low and thus the influence of different soil densities should be considered in future investigations. A final additional suggestion for future studies is that it could worthwhile to incorporate the interaction between evapotranspiration and the influence it has on mobilising contrast agents in soil. By utilising a root transpiration model, the Penmen Monteith equation (Monteith, 1965) could potentially be linked to the transport of contrast agents in the soil domain.

Given that the results indicate that when ponding takes place in a ridge and furrow system solutes will infiltrate to a considerable depth, it might be important to consider the timing of solute application with respect to anticipated rainfall. Results suggest that farmers may wish to consider how early into the growing season they need to apply solutes, particularly in ridge and furrow systems. If solutes are applied early in the growing season when root systems are less developed then the capacity for the advective force of plant roots to hold the solute near the soil surface may be reduced (Somma *et al.*, 1998; Crush *et al.*, 2005). With regards to flat planting systems the density of planting and accuracy of solute application could be important for reducing solute leaching. The results of this investigation suggest that the effect of plant roots to prevent solute

leaching could be localised to root zones. In addition to our observations, previous agronomic studies have observed that greater root density reduces solute leaching (Hauggaard-Nielsen *et al.*, 2001; Mariotti *et al.*, 2015). As such if solutes are applied to areas of soil with low root density then leaching could be exacerbated. It would therefore be worthwhile to consider a future investigation in which plants with different root architectures and distributions were trialled. This would enable the study of factors such as the influence of extensive lateral roots, shallow/ deep roots or perhaps taproots as these would all likely affect patterns of solute flow.

3.7 Conclusions

It was hypothesised that for treatments containing a plant the contrast agent would accumulate near to the soil surface. It was also hypothesised that where ponding is present, it could force deeper infiltration of solutes. In summary, we observed that plant roots have a significant impact on reducing the depth of vertical solute transport. This is particularly true of plants growing within ridge and furrow systems, where plants were absent from these systems the depth of contrast agent infiltration was observed to be greater. The effect of roots on solute infiltration was however observed to be relatively localised to root dense regions. We also observed that ponding induced deeper solute infiltration in flat soil surface geometries which contained a plant – thought to be a result of hydrostatic pressure from ponding forcing contrast agent into root generated bio-pores. The results indicate that plant roots, soil surface structure and soil moisture can affect the infiltration depth of solutes. These results also indicate that the timing of solute application with anticipated rainfall could be an important consideration for the agricultural industry. However, there is variability within the results since the number of replicates was limited to three due to the exploratory nature of the study and the availability and cost of XCT facilities capable of imaging physically large soil column samples. Giving consideration to the limitations imposed by the scale of the system and technology used for this investigation, further work is required before implications for agriculture can be stated with certainty.

3.8 Author Contributions

CPS, SJD and TR designed the study. CPS collected the XCT image data. CPS developed the image processing protocol with advice and input from KW. CPS undertook the image processing and analysis on XCT data. SJD developed and undertook the modelling with input from SR. CPS constructed the Raspberry Pi soil moisture probe setup and undertook the RSMS experiments. CPS

wrote the manuscript and all other authors provided critical revision and approval before submission and publication.

3.9 Acknowledgements

CPS, KW and TR are funded by ERC Consolidator grant 646809 (Data Intensive Modelling of Rhizosphere Processes). SJD is funded by BBSRC Syngenta Case PhD Studentship BB/L5502625/1. SR and TR are funded by BBSRC BBSRC SARIC BB/P004180/1. TR is also funded by EPSRC EP/M020355/1 and NERC NE/L00237/1. The authors acknowledge the μ-VIS X-ray Imaging Centre at the University of Southampton for provision of tomographic imaging facilities, supported by EPSRC grant EP-H01506X. The authors would also like to acknowledge Davey Jones (Bangor University) for providing the soil used within this investigation and Max Smith for providing a Raspberry Pi.

4 Developing a System for In Vivo Imaging of Maize Roots Containing Iodinated Contrast Agents in Soil using Synchrotron XCT and XRF

4.1 Authors

Callum P. Scotson[1], Arjen van Veelen[1,2,3], Katherine A. Williams[1], Nicolai Koebernick[1,4], Daniel McKay Fletcher[1], Tiina Roose[1]

[1]Bioengineering Sciences Research Group, Department of Mechanical Engineering, Faculty of Engineering and Physical Sciences, University of Southampton, Southampton, UK

[2]Material Science and Technology Division, Los Alamos National Laboratory, Los Alamos, NM 87545, United States

[3]Stanford Synchrotron Radiation Lightsource, SLAC National Accelerator Laboratory, Menlo Park, CA 94025, United States

[4]Soil Science and Soil Protection, Martin Luther University Halle-Wittenberg, Von-Seckendorff-Platz 3, 06120 Halle (Saale), Germany

4.2 Abstract

A significant issue when imaging plant root and soil systems using X-ray computed tomography is the low contrast to noise ratio between roots and soil-water. In this study a novel experimental system was developed to overcome this low contrast to noise ratio and facilitate imaging of different tissues in plant roots. The system was to enable the application of iodinated contrast agents to *in vivo* plant roots in soil and be compatible with time-resolved synchrotron X-ray computed tomography imaging. We demonstrate the efficacy of the experimental system for *in vivo* imaging of live root systems and capture the translocation of the contrast agent through root vasculature into the leaves with novel use of both synchrotron X-ray computed tomography and synchrotron X-ray fluorescence mapping. With the application of the contrast agent we are able to identify fluid flow in root vasculature and visualise anatomical root features, which are otherwise often only observable in *ex vivo* microscopy samples, including: the xylem, metaxylem, pith, fibres in aerenchyma and leaf venation. Finally, we provide examples of features which can be studied using this new system, such as the interaction between aerenchyma cross sectional area and solute transport in root vasculature with root depth. We also outline how our system could be used to parameterise models for fluid flow in plants.

4.3 Introduction

X-ray computed tomography (XCT) is a commonly employed technique for biomedical imaging research (Kalender, 2006), and it is increasingly used for non-destructive 3D imaging of plant root and soil systems (Mooney *et al.*, 2012; Roose *et al.*, 2016). However, due to overlapping X-ray attenuation of soil pore water and root tissues, the ability to distinguish between soil and plant roots remains a challenge (Mooney *et al.*, 2012) – the resulting poor contrast complicates image segmentation and subsequent quantifications. Additionally, higher X-ray energies are required to penetrate larger samples and these higher energies are proportionally less sensitive to attenuation. Therefore the maximum attainable contrast-to-noise ratio generally decreases as sample diameter increases (Attix, 2008) and thus contrast issues can also limit sample sizes.

When similar issues occur within biomedical soft tissue imaging, it is common practice to use solutions containing radiopaque elements as contrast agents – iodine in particular (Lusic & Grinstaff, 2013). More specifically, in biomedical imaging non-ionic iodinated contrast agents are commonly used since they possess several favourable traits (Lusic & Grinstaff, 2013). Firstly, they are generally less reactive compared to alternative contrast agents – for example, ionic iodinated contrast agents (Aspelin, 2006; Lusic & Grinstaff, 2013). Non-ionic iodinated contrast agents are also highly soluble and possess a viscosity similar to water (Lusic & Grinstaff, 2013). This is advantageous when the contrast agent is used in organic tissues and particularly when the intention is to utilise the contrast agent in time-resolved studies where excessive toxic effects resulting from the reactivity of the contrast agent could damage tissues over time and thus alter tissue structures.

There are currently very few examples of the use of contrast agents within *in vivo* plant material; most existing studies have employed staining of harvested material (Ahn *et al.*, 2010; Dhondt *et al.*, 2010; Blonder *et al.*, 2012). However, when imaging *ex vivo* or harvested plant material it is not possible to capture plant processes over time and much structural information can be lost – particularly when studying root systems which are removed from soil. Karunakaran *et al.,* (2015) and Keyes *et al.,* (2017b) are two of only very few examples of the use of contrast agents for *in vivo* XCT imaging of plants. Karunakaran *et al.,* (2015) used the non-ionic iodinated contrast agent Ioversol to undertake synchrotron X-ray computed tomography (SRXCT) phase contrast imaging of wheat seed spikes and canola stems by introducing the contrast agent directly into the vasculature via injection. The resulting images effectively captured the internal structure of the wheat seed spikes and canola stems and indicated the potential for using iodinated contrast agent as an effective flow tracer in *in vivo* phytological systems. The study suggested that translocation via plant vasculature is a promising avenue to deliver contrast agents to different plant tissues for SRXCT

imaging. However, the plant samples featured in this study were imaged against a background of air which is considerably less attenuating than soil and thus the complications of limited contrast introduced when imaging plant material in soil were not present.

Keyes *et al.*, (2017b) submerged cut leaf material of a live winter pea plant in non-ionic iodinated contrast agents (both Gastrografin and Niopam contrast agents) and after 24 hours undertook XCT imaging of the *in vivo* soil borne roots to capture contrast agent which had translocated from the leaves to the roots via the plant's vasculature. This further confirmed the promising potential for using iodinated contrast agents to image *in vivo* root systems. However, the difficulty of this experimental setup is that it is complex to estimate the time required for the contrast agents to translocate through the plant to the root system and also that it could be difficult to know how much contrast agent is likely to reach the root system in plants of various size and scale.

In the work of Scotson *et al.* (2020a) an iodinated contrast agent was utilised to capture solute flow through large soil columns of 10 cm in diameter which contained live plants. This study sought to investigate the influence of soil surface structure and of surface ponding on solute infiltration into soil systems. The study demonstrated that iodinated contrast agents could effectively be used as an XCT-visible analogue for agrochemical solutes to trace flow patterns in soil systems where live plants were present. However, agrochemical solute uptake and translocation within the plant roots were not investigated within the study.

The aim of our study was to develop an experimental system in which iodinated contrast agents, acting as an XCT-visible analogue for agrochemical solutes, can be applied directly to an exposed section of root to investigate root uptake and translocation within a live root, and which is also compatible with time-resolved SRXCT to facilitate *in vivo* imaging of plant root material in soil. We hypothesised that by supplying the contrast agent directly to the roots we would circumnavigate the issues of translocation highlighted above in the work of Karunkaran *et al*., (2015) and Keyes *et al*., (2017b). In this study we demonstrate the efficacy of this experimental setup and present example data which can be gathered using such a system. For example, we study the influence of aerenchyma cross sectional area on solute translocation through the cortex – aerenchyma is a plant tissue which contains enlarged gas spaces, often an indicator of environmental stresses such as hypoxia, and has previously been observed to impede axial transport through the root cortex (Evans, 2004; Fan *et al.*, 2007; Hu *et al.*, 2014). We explored the SRXCT imaging of maize roots which had been partially submerged in iodinated contrast agent whilst the remainder of the root material remained in soil. From these data we were able to observe the translocation of the iodinated contrast agent through the root cortex to the stele and into above ground tissues such as the leaves

and stem. We also used synchrotron X-ray fluorescence (SRXRF) to confirm the presence of iodine in above ground plant tissues.

4.4 Materials and Methods

4.4.1 Experimental System

Soil Imaging Experimental System Assembly

The experimental system used for the imaging of roots in soil consisted of two main components: a 3D printed top chamber and, connected to the base of this top chamber, a root growth channel constructed from 1 mL syringe barrels (***Figure 37***). This system was setup to enable *in vivo* SRXCT imaging of roots in the basal root growth channel and was designed for ease of exposure of the root tip to the contrast agent by removal of a section of soil after root growth. The 3D printed top chamber was a cylinder of 2 cm in diameter and 3 cm in depth. The top end of this cylinder was open but the basal end was closed except for a 3 mm hole in the centre over which the root growth channel would be placed. The root growth channel was composed of two 4 cm lengths of 1 mL syringe barrels (BD Plastipak, NJ, USA) with an internal diameter of 4.88 mm. The two lengths of syringe barrel were joined end to end by waterproof insulation tape. Where the two lengths of the syringe barrels join the internal diameter was just narrow enough (approximately 1 mm diameter) for only primary maize roots to pass through from the top section of the root growth chamber into the bottom section of the root growth chamber. The exposed end of the top section of root growth channel was attached to the base of the top chamber over the basal hole (***Figure 37*a**). The exposed end of the basal section of the root growth channel was covered with a single layer of nylon mesh with an aperture of 300 µm (Plastok, UK) such that water could enter the syringe barrel, but larger soil particles would not be able to leave. Three such systems were assembled to produce three replicates.

Plant Growth Conditions

Maize seeds (*Zea mays* L. cv. tasty sweet trophy F1) were germinated and then planted in the top chamber of the system. To germinate these seeds, they were placed onto damped laboratory blue roll in a petri dish for a period of 10 days at 25°C and covered from light. After this ten day period the seedling root had emerged and was approximately 1 cm in length. The seedling was placed into the top chamber of the experimental system and the seedling root was manoeuvred through the

basal hole in the top chamber into the top of the root growth channel. A sand-textured Eutric Cambisol field soil (collected from a surface plot at Abergwyngregyn, North Wales, UK: 53.0140'N, −4.0010'W), sieved to 2 mm and below, was then poured into the top chamber and tapped down gently until it filled the root growth chamber and covered the seedling in the top chamber.

To facilitate growth of the maize seedlings in the experimental systems, the systems were placed into a Conviron CMP6010 Growth Chamber (Controlled Environments Ltd, Canada) for a period of ten days prior to the imaging experiments. Ten days was sufficient to ensure that the roots had grown through the top root chamber and into the bottom root chamber section without being too long a length of time such that the roots would begin to grow too large for the system. The temperature in the cabinet was maintained at 25 °C at a relative humidity of 60%. The cabinet had a 'daylight' period of 14 hours and a 'night' period of 10 hours. The seedlings were watered every day by pipetting 1 mL of water onto the soil in the top chamber and the basal end of the root chamber, covered by the nylon mesh, was placed into a tray of water to a depth of 1 cm. The three replicates of our system were referred to as 'Maize 1', 'Maize 2' and 'Maize 3' or in shorter form as M1, M2 and M3.

Addition of Contrast Agent

Following the capture of the 'Control' images, contrast agent was added. First, the bottom section of the root growth channel was detached from the top section of the root growth chamber (***Figure 37*b**), leaving a length of root exposed but undamaged. The removed section was then replaced with an empty section which was sealed watertight at one end and filled with iopamidol iodinated contrast agent, Niopam 370 (Bracco, UK), at a concentration of 185 mg iodine / mL (***Figure 37*c**) - the roots extending from the base were thus submerged in the contrast agent. This concentration was determined by previous work (Scotson *et al.*, 2020a) and was confirmed as appropriate with the use of a phantom containing the contrast agent and soil which displayed sufficient contrast between materials. The phantom consisted of a length of syringe identical to those used for the root growth chamber. This length of syringe was sealed at one end, filled with soil and then the soil was saturated with contrast agent at the concentration of 185 mg iodine / mL. An SRXCT image of the phantom was then captured and the concentration was deemed adequate when a discrete grey value peak was produced by the contrast agent within grey value histograms.

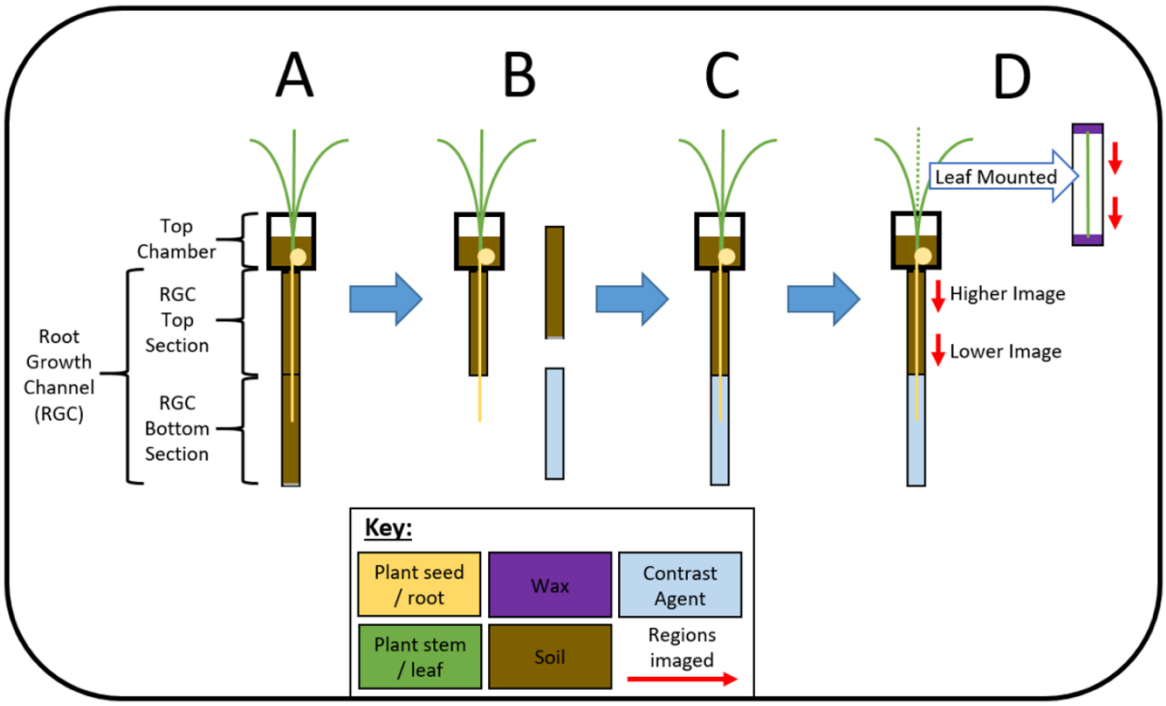

Figure 37. *Schematic of the experimental systems used for growth and imaging of the maize plants. This displays all four stages of the experimental setup including: the initial system setup for plant growth and root development (A), the removal of the basal section of the root chamber (B), the replacement of the basal section of the root chamber with the contrast agent (C) and the final setup displaying the various regions which underwent SRXCT imaging of both the roots and excised leaf material (D). Red arrows indicate the regions of the roots and leaves which were imaged using SRXCT. A colour key is placed at the bottom of the schematic indicating the colour of plant roots, plant leaves, soil, iopamidol contrast agent and the SRXCT imaged region.*

4.4.2 Synchrotron X-ray CT Imaging

The synchrotron X-ray computed tomography (SRXCT) imaging was undertaken at three time-points: once before the addition of contrast agent ('Control'), 11 hours after the addition of the contrast agent ('T1') and 23 hours after the addition of the contrast agent ('T2'). The plants were not imaged more frequently than this owing to concerns over the effects of prolonged X-ray exposure on plant health. Zappala *et al.,* (2013) previously observed that plant health was not significantly affected provided plants were not exposed to X-rays for prolonged periods. This has also been confirmed by Keyes *et al*., (2017a) who monitored microscale plant root growth using SRXCT and were able to mitigate the negative effects of X-rays on plant health by limiting exposure. Finally, sections of leaf and stem, excised and mounted as described below, were imaged 25 hours after the initial addition of contrast agent ('Leaf Images'). The synchrotron XCT imaging was carried

out at the I13-1 beamline at Diamond Light Source (DLS), Didcot, UK. The energies used for the SRXCT was 15-20 keV ('pink beam'). A total of 1601 equiangular projections were recorded through 180° with an exposure time of 0.15 seconds per projection – leading to a total scan time per scan acquired of four minutes. A 500 µm cadmium tungstate ($CdWO_4$) scintillator was used and the detector used was a PCO edge 5.5 CMOS detector. A fourfold optical magnification microscope system was used with a field of view of 4 × 3.5 mm and pixel size of 1.6 µm. With a propagation distance of 63.5 mm there was an intermediate amount of phase contrast. The attenuation data were reconstructed into 3D volumes of 2160 slices of 2560 × 2560 pixels each using a filtered back projection algorithm. These reconstructed 3D volumes had a 32bit dynamic range upon reconstruction but were then down-sampled to 8bit for ease of computational handling. During the 8bit conversion, all images were down-sampled to the same fixed ranged which was set according to the minimum and maximum values found across all images. The list of SRXCT parameters is given in ***Table 8***.

Table 8. *Synchrotron data acquisition parameters for X-ray computed tomography (SRXCT) imaging and X-ray fluorescence (XRF) mapping.*

SRXCT Parameter	**Value**	**SRXRF Parameter**	**Value**
DLS Beamline	I13-1	**DLS Beamline**	I18
Energy (keV)	15-20	**Energy (keV)**	5
Projections	1601	**Edges excited**	L2 and L3 iodine edges
Projection Exposure Time (s)	0.15	**Pixel Size Resolution -Equivalent to Spot Size (µm)**	10
Total scan time (min)	4	**Monochromator**	Si (111)
Scintillator	Cadmium tungstate ($CdWO_4$)	**Detector**	Four-element Vortex Si drift detector
Detector	PCO edge 5.5 CMOS	**X-ray flux**	10^{10}–10^{11} photons s^{-1}
Magnification	Fourfold optical magnification	**Standards used**	Apatite mineral and spessartine garnet
Field of View (mm)	4 × 3.5	**Calibrated Peaks**	Mg, Al, Si, P, S, K, Ca, I, I (L alpha 2) and I (L beta 2).
Resulting Pixel Size Resolution (µm)	1.6		
Image Dimensions	2160 slices (2560 × 2560 pixels each)		

Soil and Root SRXCT Imaging

An SEM stub mount was used to mount the experimental systems for SRXCT imaging. This stub mount was modified to hold a syringe vertically tip-down by securing the tip with a luer connection. The design of this modified SEM stub is detailed in previous studies (Keyes *et al.*, 2013; Daly *et al.*, 2016; Keyes *et al.*, 2017a). The basal tip of the bottom section of the root growth channel was inserted into this modified SEM stub such that the experimental system was held vertically. The SRXCT imaging consisted of capturing 4 mm (diameter) by 3.5 mm (height) field of view regions of roots in soil at two different heights in the top section of the root growth channel. The top image was captured in a region between 13 and 16.5 mm below the base of top chamber (between 23.5 and 29 mm above the chamber containing contrast agent) and the bottom image was capture in a

region between 30 and 33.5 mm beneath the base of the top chamber (between 6.5 and 10 mm above the chamber containing contrast agent) (***Figure 37*d**).

Leaf and Stem SRXCT Imaging

Following the imaging of roots in soil, sections of leaf and stem were excised from the maize plants and mounted for SRXCT imaging. Stem and leaf material was cut 5 mm above the soil and labelled according to a system where the central stem is labelled 'Stem', the most basal leaf is 'Leaf 1' and the second most basal leaf is 'Leaf 2' and so on. For the mount, a 2.5 mL syringe was cut in half along its vertical length though leaving the syringe tip intact. 3D printed blocks were then slotted into either end of the halved syringe (***Figure 37*d**). These 3D printed blocks had a flat surface facing out from the cutaway syringe onto which the tips of leaves could be mounted. Wax was melted using a low heat soldering iron onto the flat surfaces of the blocks at either end of the syringe. To mount sections of leaf and stem this wax was reheated, either end of the leaf material were held in the molten wax on the two blocks and as the wax cooled the leaves would become fixed in place ready for imaging (***Figure 37*d**). The syringe tip could then be placed into the modified SEM stub and thus be held vertical as described for the soil imaging system above. The imaged sections consisted of two different 3.5 mm lengths of leaf or stem material with a field of view diameter of 4 mm.

4.4.3 SRXCT Image Analysis

The image analysis consisted of two main steps: manual segmentation of the root systems using Avizo 9.3.0 (Thermo Fisher Scientific, Waltham, MA, USA) and then all further analysis and quantification was completed using the FIJI distribution of ImageJ (Schindelin *et al.*, 2012; Rueden *et al.*, 2017). The further analysis included recording the average grey value of the cortex and of the stele and the aerenchyma cross sectional area (***Figure 38***).

The initial stage of image processing was segmenting the roots in the original absorption image stack. This segmentation was completed using the 'manual segmentation' tool. Each root present within an image stack was listed as a different 'material' and as such attributed a different colour label in the segmentation root mask image. This allowed for individual roots to be analysed separately using a colour threshold to select masks for individual roots – for example, the primary root could be analysed separately. The segmented root stack was saved as a 3D .tiff file.

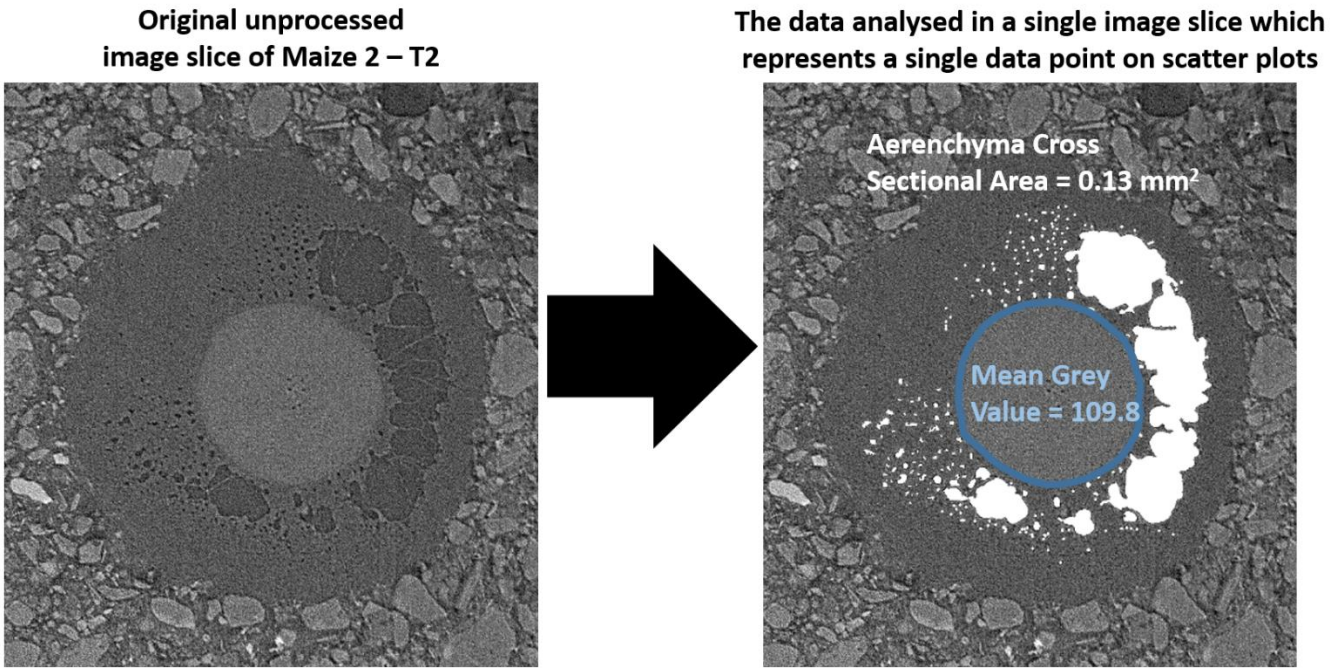

Figure 38. *An example of the data lifted from an image slice which is then represented by data points on the scatter plots of stele grey value and aerenchyma cross sectional area. A comparison is provided between an original unprocessed image (left) and an image displaying an overlay of the regions analysed for stele grey value and aerenchyma cross sectional area (right).*

Aerenchyma Segmentation and Area Quantification

Next, the aerenchyma was segmented and the cross-sectional area of aerenchyma was quantified. This was particularly focused on the primary roots as many of the smaller secondary roots were either partially outside the field of view of the image stacks or at the artefact-rich edges. This image processing was implemented using the FIJI distribution of ImageJ and the algorithm developed is outlined in ***Figure 39***. First, a threshold of 1-255 was applied to the root mask image of the roots. This removed the background pixels with a grey value of zero. This image was then converted to 8bit from 8bit colour and the resulting image stack was divided by 255 to provide a mask for the segmented roots where any pixels containing root material had a grey value of 1. The 'Gaussian Blur (3D)' tool was applied to the original unsegmented image stack using a radius of 1 in X and Y horizontal dimensions and 0 in the vertical Z dimension. The Gaussian blur was not applied to the Z dimension as there were not significant speckle artefacts in the vertical Z dimensions as there were in the horizontal X and Y dimensions. The mask stack for the segmented roots (where a grey value of 1 was assigned to pixels containing root material) was then multiplied by the original image stack to produce an image stack containing just the segmented roots.

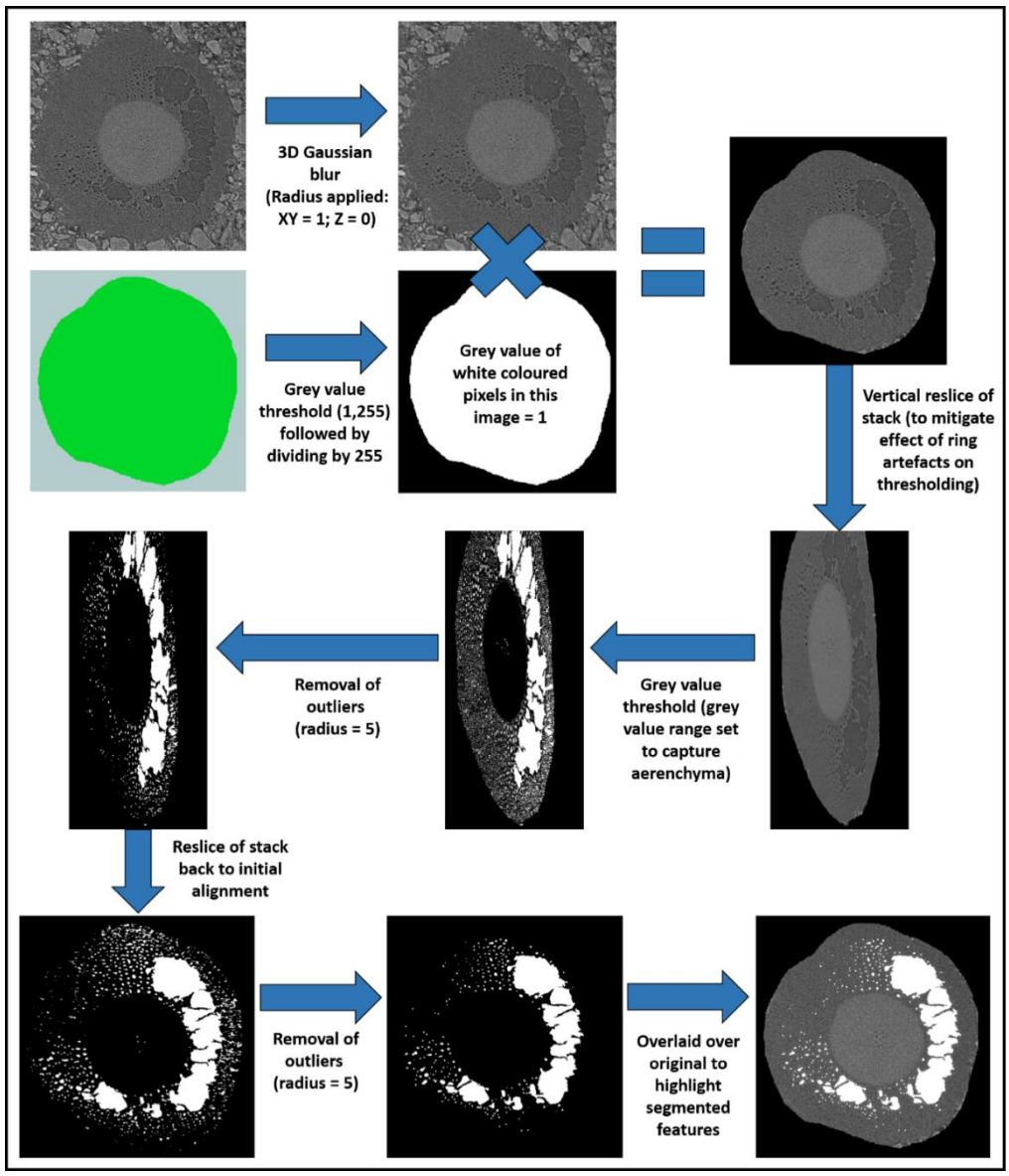

Figure 39. *A visual flow chart describing the image processing algorithm used for segmenting the root aerenchyma. The purpose of the vertical reslice step was to mitigate for the effects of ring artefacts on grey value thresholding. The green root mask image was generated using manual segmentation in Avizo 9.3.0 (Thermo Fisher Scientific, Waltham, MA, USA) and all other image processing was completed in the Fiji distribution of ImageJ (Schindelin et al., 2012; Rueden et al., 2017).*

Next, the new image stack, containing just the segmented roots, was horizontally resliced using the 'Reslice' tool. This reduced the effects of ring artefacts on aerenchyma segmentation. The effect of these ring artefacts on grey values in the cortex can be seen in ***Figure 40***. A grey value threshold

was applied to the resliced stack to segment voxels containing the aerenchyma. The grey value range used for this threshold was set from 1 to an upper limit of 10 beneath the modal grey value (the same as displayed in ***Figure 40***). The 'Remove Outliers' tool was applied to the image stack with a radius of 5 to remove some over-segmented noise. The 'Reslice' tool was then used to return the stack to the original orientation. Following this, the 'Remove Outliers' tool was applied again with a radius of 5 pixels to remove remaining over-segmented noise from the stack. The 'Remove Outliers' tool was applied twice, once in the 'reslice' orientation and once in the standard orientation, because it is a 2D method and thus by using it in both orientations it is applied in the X, Y and Z dimensions. The aerenchyma cross-sectional area was then quantified in each slice using the 'Measure' tool to count the number of pixels present with a grey value of 255 in a given 2D image slice.

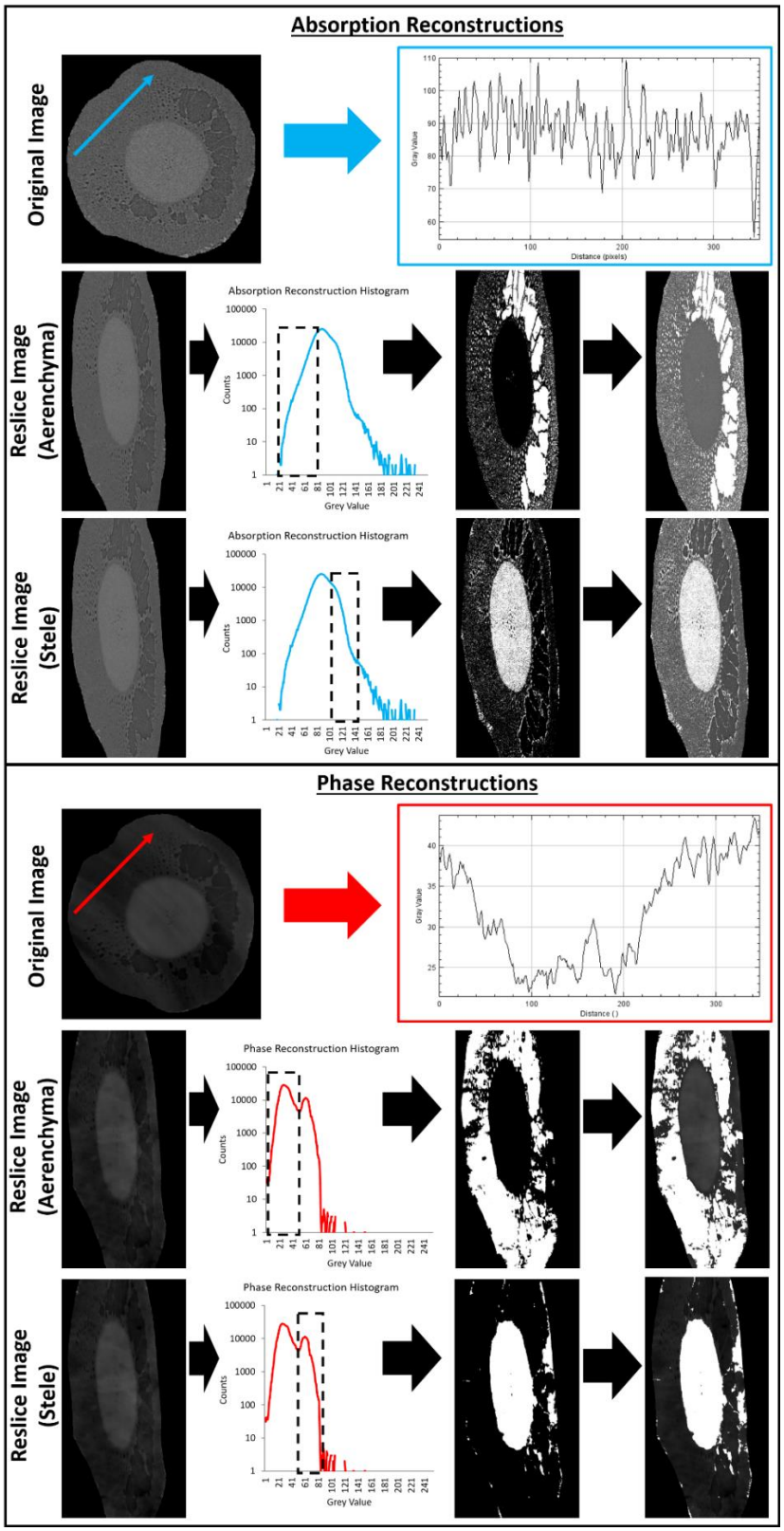

Figure 40. *A comparison between the merits of absorption and phase reconstruction for segmentation of root anatomical features. Absorption images enable more reliable thresholding of aerenchyma whereas phase images enable more reliable thresholding of the stele. Ring artefacts complicated segmentation in the phase images to a greater extent than in absorption images.*

Quantifying Stele Grey Value with Depth

Average grey value in cross sectional areas of the root stele was quantified with depth in the main roots as an indicator of contrast agent presence. To achieve this, first the stele of the main roots in each original unsegmented image stack were manually segmented as a mask using the 'manual segmentation' tool in Avizo 9.3.0. The segmented root 'Stele Mask' image stack was saved as a 32bit 3D .tiff file.

The next stage was quantification of the average grey value which was implemented using the FIJI distribution of ImageJ. As with the aerenchyma segmentation, a new image stack which contained only the voxels of the stele of main roots was generated by multiplying the original unsegmented image stack with the Stele Mask image. The background voxels in the new image stack were assigned a grey value of 0. Finally, the mean grey value within the range 1 to 255 (the full grey value range for 8bit images excluding zeros) was calculated for each slice sequentially using the 'Measure' tool. This range was imposed on the mean grey value measurement to remove background pixels.

Quantifying Cortex Grey Value with Depth

As with the other analyses, the quantification of the grey value of the cortex was implemented using the FIJI distribution of ImageJ. First, the binarised root stele mask was subtracted from the segmented root stack (containing only the root and not the soil) using the 'Image Calculator' tool. The binarised aerenchyma mask was then also subtracted from the segmented root stack to remove the aerenchyma from the image stack. This produced a new image stack which only contained voxels of the main root cortex. As with the stele grey value quantification, the background voxels in the image stack were assigned a grey value of 0 and the mean grey value within the range 1 to 255 was calculated for each slice sequentially using the 'Measure' tool.

4.4.4 Synchrotron X-ray Fluorescence Mapping and Analysis

The primary purpose of the synchrotron X-ray fluorescence (SRXRF) analysis was to observe where iodinated contrast agent had accumulated in the plant in a cumulative iodine map produced from the XRF dataset which would allow visual observation (***Figure 41***). Once SRXCT imaging had concluded, the plant material was flash frozen using a liquid nitrogen bath and then kept in a -80 °C freezer. Five days after the conclusion of the SRXCT imaging a length of Stem and Leaf 1 of Maize 2

were removed from the freezer and were mounted side by side using a sticky carbon SEM stub (***Figure 41***). The XRF map was captured at I18 at the Diamond Light Source synchrotron, Didcot, UK. To capture the XRF map the SEM stub was mounted on an x-y-z stage, rastered relative to the fixed incident beam. In order to obtain signal of low Z elements, the samples were held under a helium atmosphere. This beamline at DLS uses Kirkpatrick-Baez mirrors to produce spot sizes of 2-10 µm and the pixel size was chosen to be 10 µm. A Si(111) monochromator was used to select the incident beam energy and a four-element Vortex Si drift detector was used to detect X-rays. X-ray flux was estimated to be 10^{10}–10^{11} photons s^{-1}, the energy used was 5 keV and both the L2 and L3 edges of iodine were excited. The full energy dispersive spectrum was recorded for each pixel of the XRF map and the completed map was saved as an .nxs file. Fitting was undertaken using the freeware PyMCA X-ray Fluorescence Toolkit (Sole et al., 2007) from fundamental parameters of the experiment using standards of apatite mineral and spessartine garnet with known elemental concentrations for calibration. A table of SRXRF parameters is given in ***Table 8***.

The analysis of the XRF maps was implemented using the PyMCA X-ray Fluorescence Toolkit (Sole *et al.*, 2007). Reference peaks were calibrated for the following elements: Mg, Al, Si, P, S, K, Ca, I, I (L alpha 2) and I (L beta 2). The cumulative iodine map was then produced from the dataset to allow visual observations (***Figure 41***).

4.5 Results

4.5.1 Confirmation of Iodine Induced Contrast

In comparisons of SRXCT images of the main maize roots before the addition of the contrast agent (Control) and 11 hours after the addition of contrast agent (T1) the contrast agent is visible as regions of comparatively higher grey values (***Figure 42***). The stele, in the centre of the root where the root vasculature can be found, can be observed with the use of contrast agent. Considerable contrast of the stele against the cortex material can be seen with the contrast agent (***Figure 44***, ***Figure 45***, ***Appendix Figure A9*** and ***Appendix Figure A10***), whereas without contrast agent the stele is not distinguishable from the cortex (***Figure 42***). In addition, the contrast agent enabled visualisation of finer scale anatomical root features such as the xylem and metaxylem (***Figure 42***). In particular, the additional contrast in the plant vasculature provided by the contrast agent means that it is possible for metaxylem to be visualised when it both contains pulses of contrast agent and between pulses of contrast agent (***Figure 42***) – a feature which is otherwise difficult to observe using SRXCT owing to the limited contrast to noise ratio within root material. Whilst the stele can be observed in both absorption and phase reconstructions, the stele is more accurately segmented

using thresholding in phase images (***Figure 40***). In phase images the stele is represented by a clear second peak in grey value histograms whereas, in absorption images the peak in grey value histograms which represents the stele is only visible as a non-discrete 'shoulder' (***Figure 40***). In contrast, the aerenchyma is more accurately segmented in absorption rather than phase reconstructions (***Figure 40***). The grey value ranges of the histograms presented in ***Figure 40*** with zero counts would have included elements of the soil in non-segmented image stacks.

The XRF map which was produced for the mounted section of leaf and stem material from Maize 2 confirmed that iodine had travelled through the plant vasculature from the roots to the leaf and stem material. This is indicated by the high cumulative iodine concentration observed in both the stem and leaf material in the iodine map of the sample (***Figure 41***). The iodine was particularly concentrated in the vasculature of the leaves and stem, *i.e.*, in the parallel leaf venation. High concentrations were visualised as the green regions in ***Figure 41***. The accumulation of contrast agent in the leaf venation is also visible in the leaf SRXCT data in both cross sectional images and in vertical reslices of image stacks which have undergone a maximum z-projection (***Figure 41***).

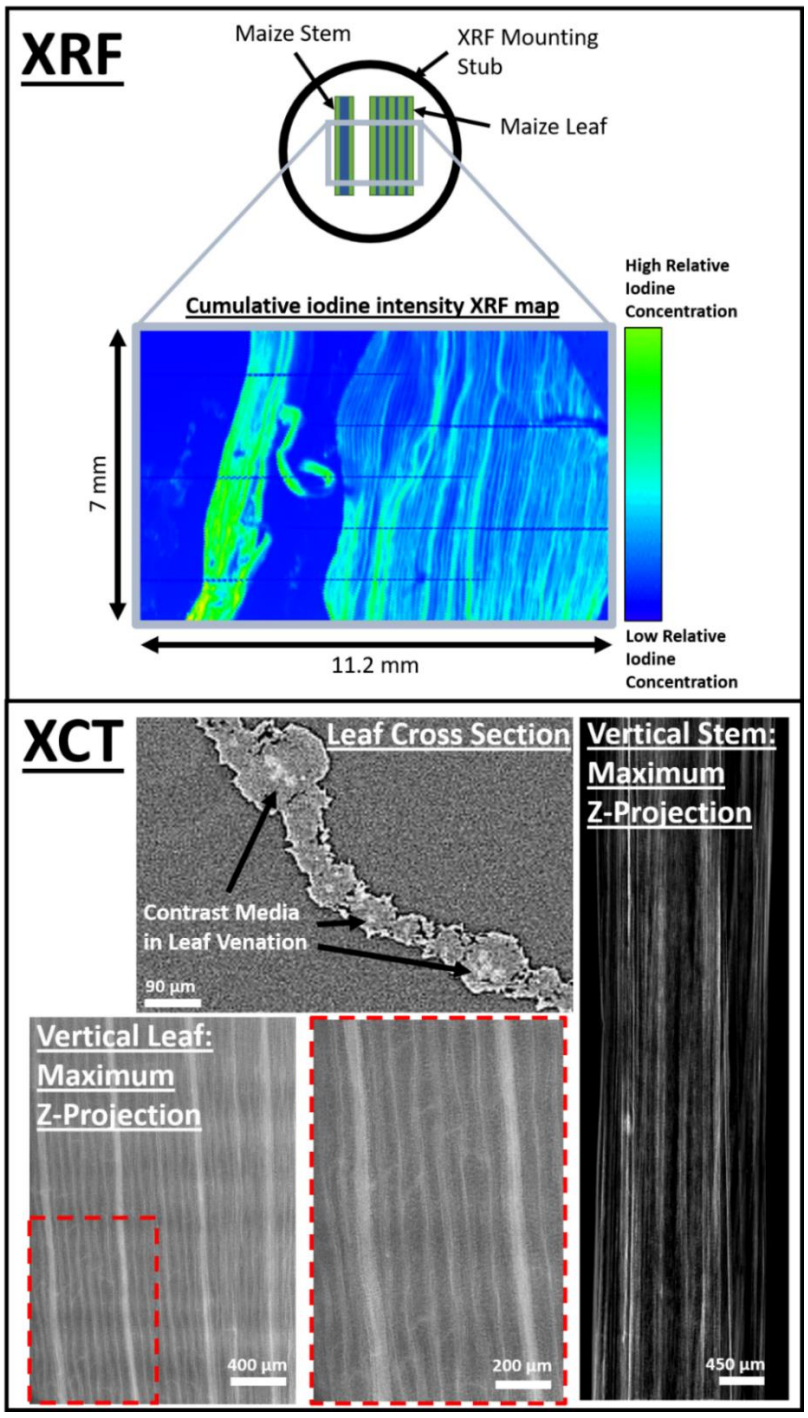

Figure 41. *Top is the SRXRF map of cumulative iodine intensity in stem and leaf material from 'Maize 2'. The SRXRF panel displays a schematic diagram of the stem and leaf material mounted onto an 'SEM stub' for mapping indicating the region that was mapped (top of panel) and also the relative cumulative iodine SRXRF intensity map of the stem and leaf material (bottom of panel). On the bottom are SRXCT images displaying that contrast agent was present in leaf venation and visible as the pixels of higher grey values. The SRXCT panel displays a leaf cross sectional slice (top) and a vertical reslice of a leaf which has undergone a maximum z-projection (bottom). In the vertical reslice images of the leaf it is possible to observe individual leaf vessels.*

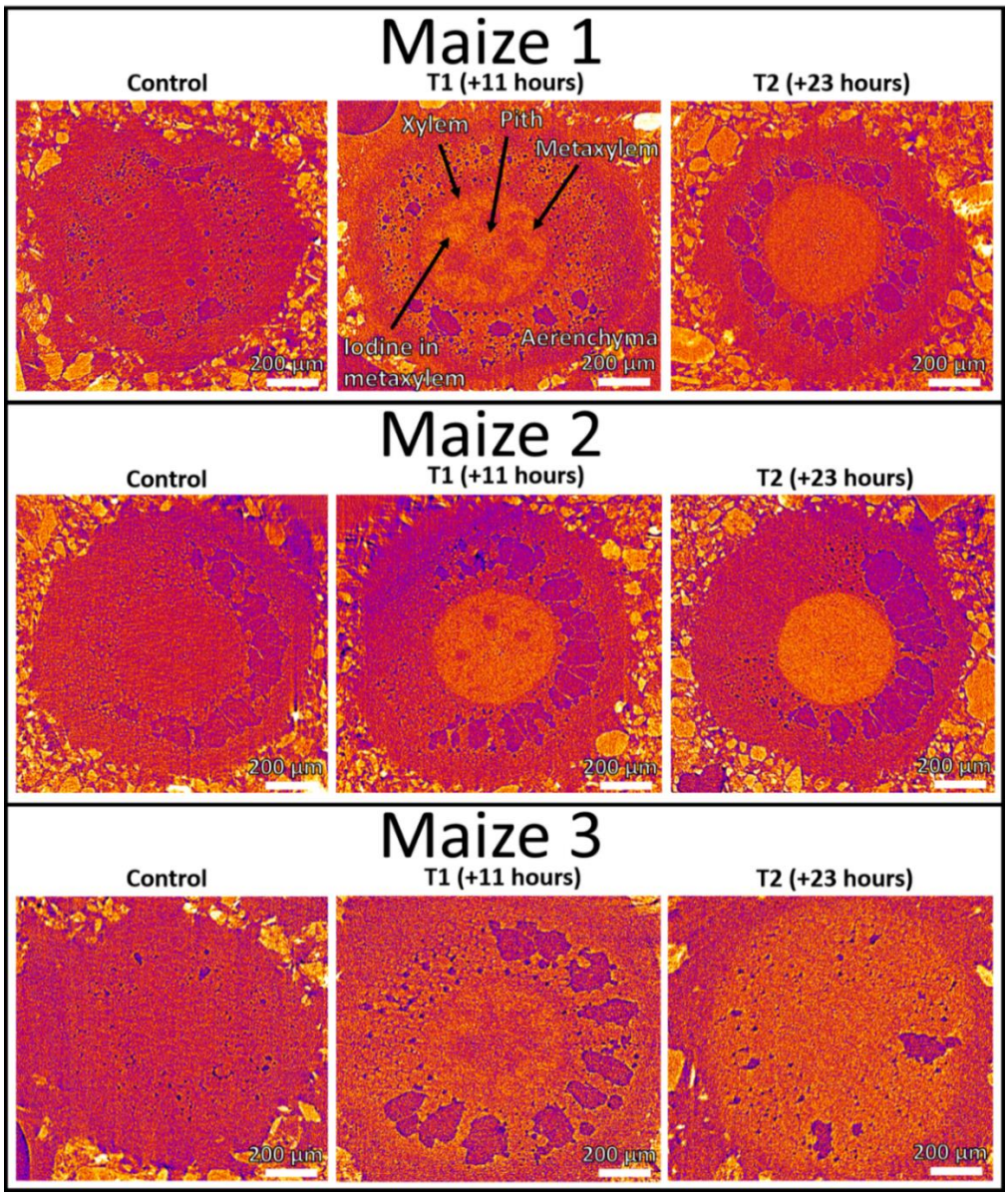

Figure 42. *A collection of comparisons of SRXCT images of the main maize roots before the addition of the contrast agent (Control), 11 hours after the addition of contrast agent (T1) and 23 hours after the addition of contrast agent (T2). Comparisons are made for each of the three replicates: Maize 1, Maize 2 and Maize 3. Contrast agent is visible as the pixels of higher grey values (yellow) and background pixels are lower in grey value (dark purple). The contrast agent enabled visualisation of anatomical root features otherwise not easily observable in SRXCT images such as xylem and metaxylem. In particular, the additional contrast in the plant vasculature provided by the contrast agent means that metaxylem both containing contrast agent pulses and which does not contain contrast agent pulses can be visualised. With the addition of contrast agent the stele, in the centre of the root where the root vasculature can be found, considerably contrasts against the cortex material outside whereas without contrast agent the stele is not easily distinguished. Fibres can also be visualised in the aerenchyma.*

4.5.2 Average Stele Grey Value

The average grey value along the length of the primary root stele increased with time (***Figure 43***). This appeared to be true of the higher and lower imaged sections of the primary roots in all three replicates. In the lower imaged section the average grey values increased from 96, 83.4 and 94.8 at T1 to 107.3, 90.4 and 101.6 at T2 for M1, M2 and M3, respectively (***Figure 43***). In the higher imaged section the average grey values increased from 93.3, 69.5 and 74.8 at T1 to 93.8, 77.5 and 101.3 at T2 for M1, M2 and M3, respectively (***Figure 43***). For all three replicates the initial average grey value in the main root stele was similar between the lower and higher imaged sections at the control time point, i.e., before contrast agent was added. However, at T1 and T2 (11 and 23 hours after the addition of contrast agent, respectively) average grey value increased though by a smaller amount in the higher imaged section of the primary roots than the lower imaged section (***Figure 43***).

This was explored in greater detail where the grey value in the stele with depth was investigated within image stacks (***Figure 44*** **and** ***Figure 45***). For every Pearson correlation coefficient (PCC) analysis undertaken on this data, the P-Value indicated that the correlation coefficients were significant ($P < 0.005$). In all image stacks the grey value was higher in the stele at greater depths (nearer to the basal tip of the roots (***Figure 44*** **and** ***Figure 45***). Additionally, the grey value in the lower sections of root increased at a greater rate with depth (***Figure 44***) than in the higher sections (***Figure 45***). The changes in the average stele grey value with depth are substantial in comparison with the smaller changes in cortex grey value with depth where there appears to be no discernible trend present across the data (***Appendix Figure A9*** **and** ***Appendix Figure A10***).

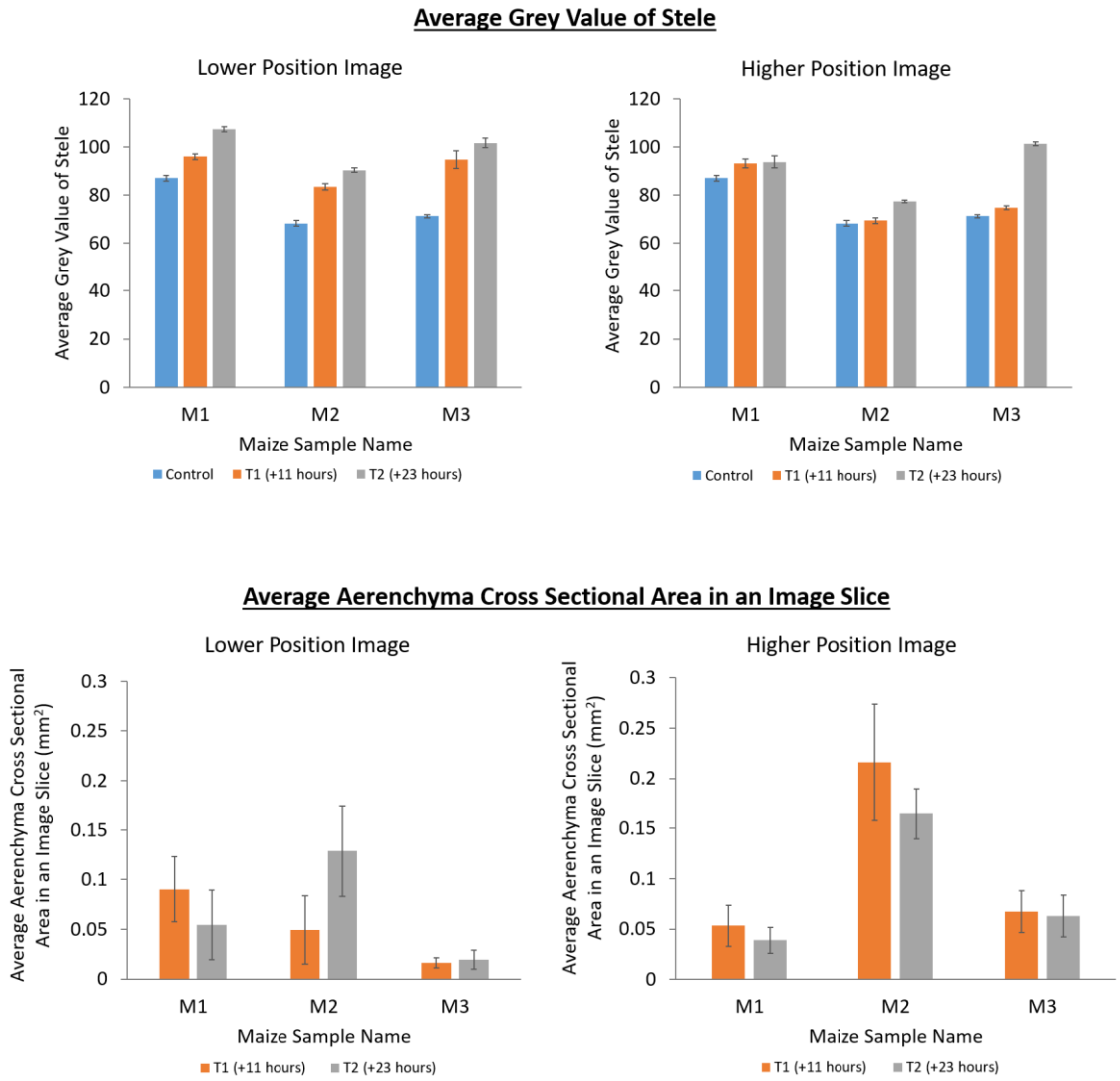

Figure 43. *The average grey value along lengths of root stele in main roots (top) and the average aerenchyma cross sectional area (bottom) at different imaging time points. This is presented for both the lower image positions (left) and the higher image position (right). The control time point (blue) was prior to the addition of contrast agent, the T1 time point (orange) was 11 hours after the addition of contrast agent and the T2 time point (grey) was 23 hours after the addition of the contrast agent. Control time points are included for the average stele grey value plots as a baseline for comparison and to demonstrate that the contrast agent increased the grey value in the stele relative to the control. This is not relevant to the aerenchyma cross sectional area plots as these are simply to demonstrate that there is no significant differences in cross sectional area between T1 and T2 - these are the relevant time points for the comparisons made in* ***Figure 44*** *and* ***Figure 45****. Standard error bars are also provided.*

4.5.3 Stele Grey Value and Aerenchyma Cross Sectional Area Over Depth

The P-Value for every Pearson correlation coefficient for this comparison was $P < 0.005$ and thus the correlation coefficients were significant. In ten of the twelve comparisons analysis reported a negative correlation between the average grey value of primary root stele with aerenchyma cross sectional area over all root depths (***Table 9, Appendix Figure A5*** **and** ***Appendix Figure A6***). Of those ten which featured a negative correlation, six could be considered to report a comparatively strong negative correlation (PCC < -0.6). There was no clear relationship between the strength and direction (positive or negative) of the reported PCC and whether the comparison is made in the lower or higher of the imaged root sections (***Table 9***). There was also no clear relationship between the strength and direction (positive or negative) of the reported PCC and whether the comparison is made at T1 or T2 (***Table 9***). This is reflected in the variation of aerenchyma cross sectional area with depth where no apparent consistent trends are present between imaging time points or image position (***Figure 43*** **and** ***Appendix Figure A7*** **and** ***Appendix Figure A8***).

Table 9. *Pearson Correlation Coefficient of average grey value of root stele versus aerenchyma cross sectional are over depth. T1 is the time point for scans acquired 11 hours after the addition of contrast agent and T2 is the time point for scans acquired 23 hours after the addition of contrast agent. Position refers to whether the data is from the upper or lower imaged region of root length captured at different heights. Upper means the region of root imaged which was nearer to the above soil material and Lower means the region of root imaged which was nearer to the root tip. M1, M2 and M3 are the names of each of the plant samples. The P-Value for every correlation coefficient was P < 0.005 and therefore significant. Full scatter plots of this data for the lower and higher image positions can be found in* ***Appendix Figure A5 and Appendix Figure A6*** *respectively.*

TIME - POSITION	M1	M2	M3
T1 - Lower	-0.415	0.188	-0.301
T1 - Upper	-0.662	-0.349	-0.843
T2 - Lower	-0.712	-0.381	-0.769
T2 - Upper	0.396	-0.839	-0.773

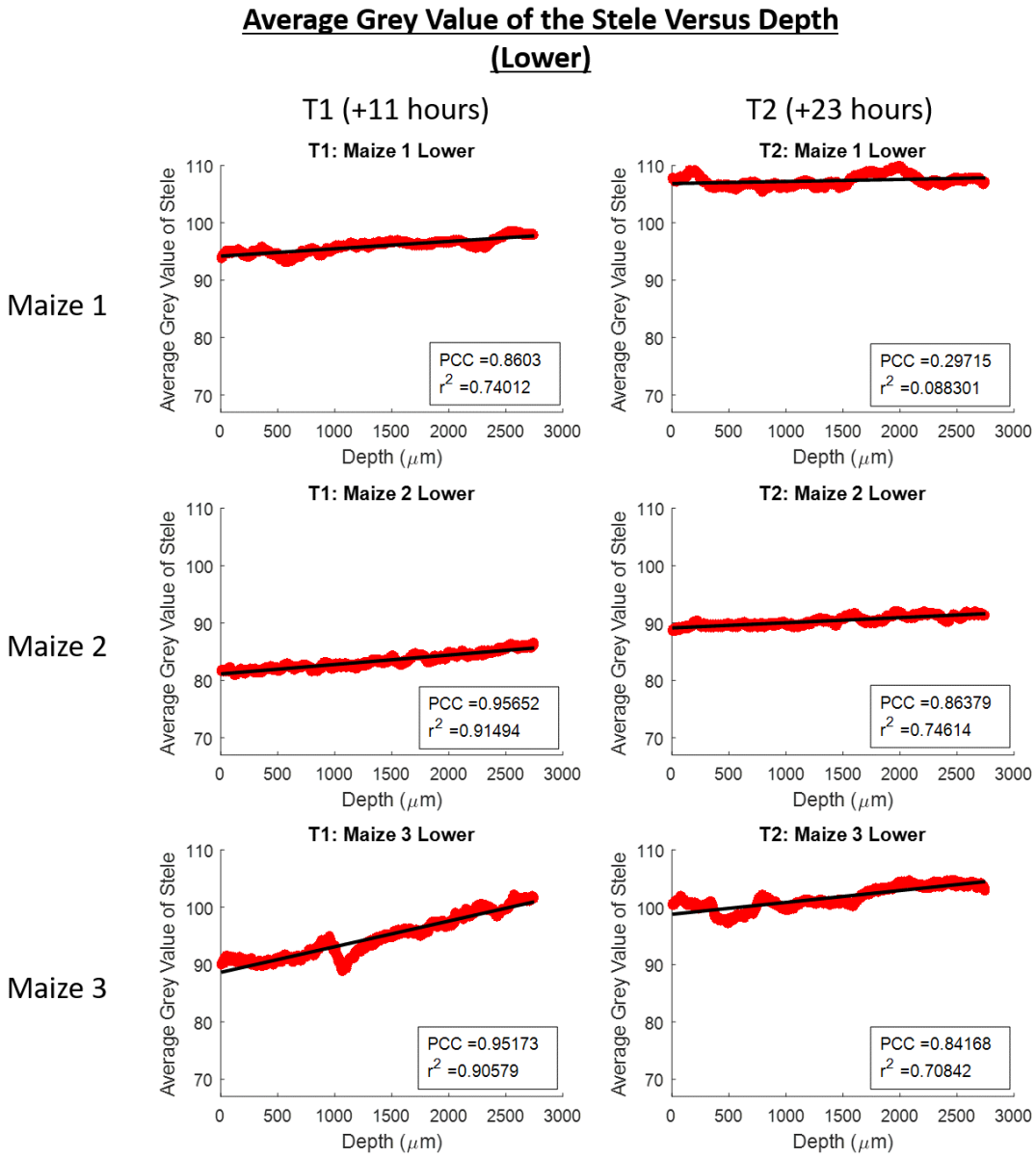

Figure 44. *Scatter plots of average grey value of the root stele versus depth down the root growth channel for the lower imaged section of roots. Zero on the depth axis is the top of the image. T1 is the time point for scans acquired 11 hours after the addition of contrast agent and T2 is the time point for scans acquired 23 hours after the addition of contrast agent. Maize 1, Maize 2 and Maize 3 are the names of each of the plant samples. The Pearson correlation coefficient, r^2 value and linear best fit lines are provided for each scatter plot.*

The correlation plots indicated that for the two comparisons which reported a weak positive correlation, Maize1-T2-Higher and Maize3-T2-Lower, the full data were variable with a low r^2 value of 0.15 or below (***Appendix Figure A5*** **and** ***Appendix Figure A6***). The correlation plots for the six

comparisons which reported a strong negative correlation (PCC < -0.6) also indicated evidence of lower variability with all reporting an r^2 value of 0.4 or above (***Appendix Figure A5*** **and** ***Appendix Figure A6***). It should be noted that for Maize3-Lower the correlation plots at both T1 and T2 displayed considerably smaller values for the aerenchyma cross sectional area - approximately an order of magnitude smaller than in other samples (***Figure 43***).

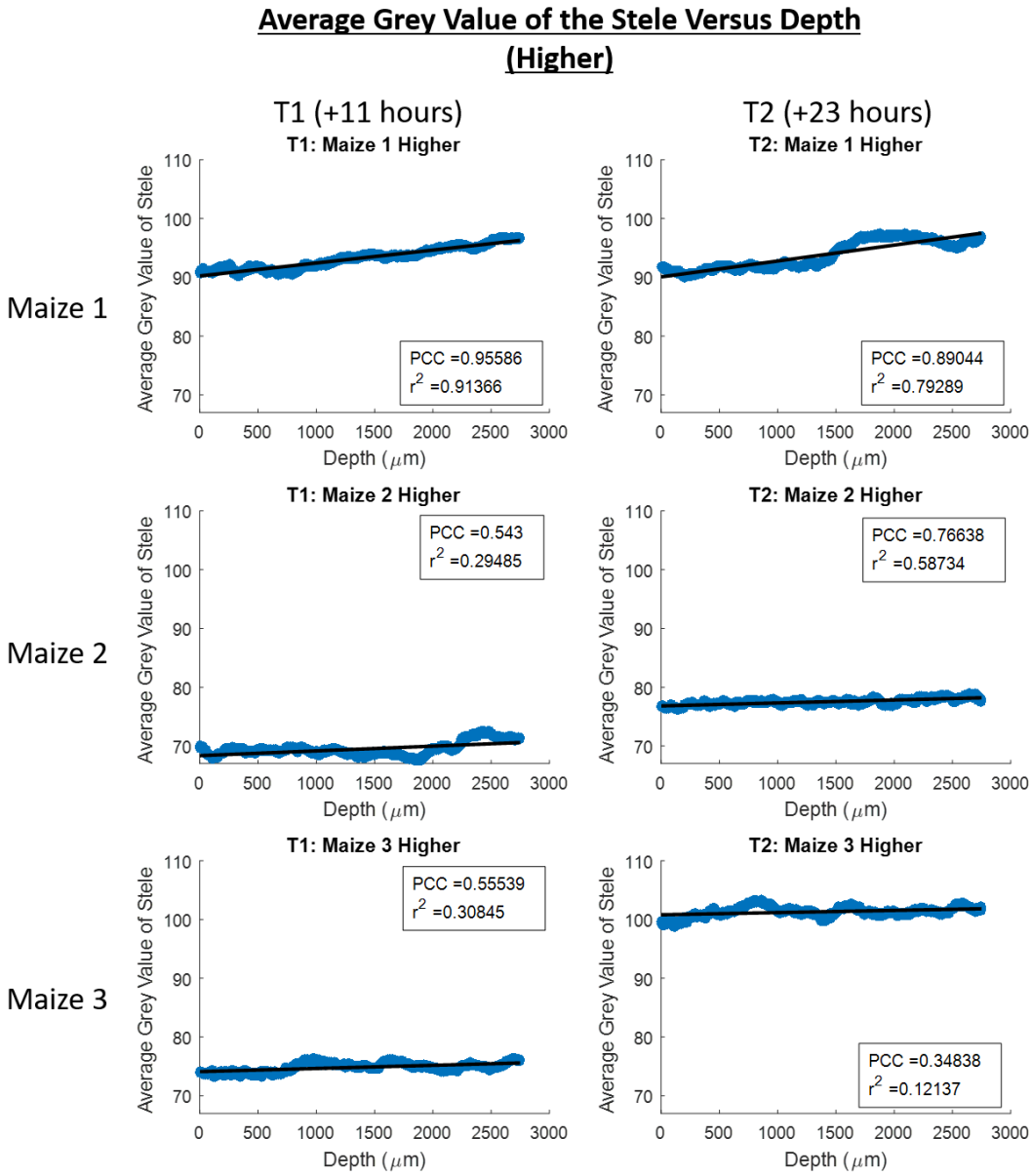

Figure 45. *Scatter plots of average grey value of the root stele versus depth down the root growth channel for the higher imaged section of roots. Zero on the depth axis is the top of the image. T1 is the time point for scans acquired 11 hours after the addition of contrast agent and T2 is the time point for scans acquired 23 hours after the addition of contrast agent. Maize 1, Maize 2 and Maize 3 are the names of each of the plant samples. The Pearson correlation coefficient, r^2 value and linear best fit lines are provided for each scatter plot.*

4.6 Discussion

We developed an experimental system which enabled iodinated contrast agents to be supplied directly to plant roots for uptake and translocation compatible with time-resolved SRXCT to facilitate *in vivo* imaging of plant root material in soil. We intended to overcome issues of low contrast to noise within XCT images of plant roots and soil environments which can complicate image processing and can result in the loss of physiological/ anatomical information (Mooney *et al.*, 2012). The experimental setup performed its intended purpose enabling *in vivo* imaging of live root systems and capturing the translocation of the contrast agent through root vasculature into the leaves, revealing additional root anatomical information.

4.6.1 Capturing Root Anatomy

The successful translocation of the contrast agent from the roots to the leaves, evidenced by both SRXCT and SRXRF data (***Figure 41***), indicated that this system performed equally well to Keyes *et al.,* (2017b) with regards to achieving contrast agent distribution in *in vivo* plant material. However, our system provided some additional benefits, *i.e.*, enabling visualisation of anatomical features of the root system (***Figure 42***). We were able to capture details such as the position of the stele, the vascular structure, fibres in aerenchyma and identify the accumulation of contrast agent in leaf / stem venation (***Figure 41*** **and** ***Figure 42***). In particular, examples of xylem and metaxylem can be observed both containing contrast agent and also empty within the same image stack identifying the location of different vascular features (***Figure 42***). This was possible in both the phase and absorption reconstructions, though each offered different benefits with regards to segmenting specific root features. In absorption images it was possible to more accurately to segment aerenchyma, as ring artefacts in the phase images make thresholding more complex (***Figure 40***). However, the presence of a discrete second peak in the grey value histogram of phase images meant the stele could be segmented with greater accuracy using phase reconstructions (***Figure 40***). Since the contrast agent accumulated in the vasculature the position of the leaf venation could be mapped using both SRXCT and SRXRF (***Figure 41***) – this was not possible in SRXCT images without the application of the contrast agent. This also meant that we were able to capture individual leaf vessels in both the SRXCT and SRXRF images (***Figure 41***). Often to capture such features the tissue is removed from the plant and stained for microscopy rather than remaining intact *in vivo*. Additionally, with the development of nanoparticulate contrast agents for use in soil (Scotson *et al.*, 2019), it is possible that in future the *in vivo* anatomical imaging achievable with our experimental system could be further enhanced with the use of AuNPs functionalised to

accumulate on particular plant tissues or organs. Particularly with the use of AuNPs of approximately 3.5 nm in size, which have previously been observed to pass into roots and then be translocated throughout the plant to the leaves (Sabo-Attwood *et al.*, 2012).

A further benefit of our system is that it involves application of the contrast agent directly to the root. This could be of importance given the potential for iodinated contrast agents to have osmotoxic effects over time, as identified by Keyes *et al*., (2017b). By applying the contrast agent directly to the root it is possible to capture the contrast agent within root tissues in soil without the need to cut leaf material or the time delay necessary for translocation from the leaf to the roots as in the Keyes *et al.*, (2017b) system (all the while osmotoxic effects may be developing and plant health may be deteriorating). Using our system it would also be possible to study further dynamics of root and soil interactions, such as the effect of soil porosity or soil compaction on soil-water uptake. This could be achieved by applying the contrast agent through a partially saturated soil rather than submerging the root in a contrast agent solution. Such an approach of application via partially saturated soil could be paired with studies which seek to capture root-water interactions, such as Scotson *et al*., (2020a), to monitor effects of root water uptake on soil pore water. However, it should be noted that it is likely that this method of application could result in lower concentrations of contrast agent within the root system relative to direct application to roots.

4.6.2 Translocation of Contrast Agent

Our system was also capable of tracking the translocation of the contrast agent through the root vasculature with time. This translocation was observed as the change in grey value over time in the lower and higher imaged sections of the roots (***Figure 43***). Over time as more contrast agent entered the root stele, the grey value inside the root in the lower imaged section increased and then more gradually the grey value also increased in the higher imaged section of the root as the contrast agent was translocated further up the vasculature (***Figure 43***). This translocation of the contrast agent into the stele and up the root vasculature was further evidenced by the average grey value of the stele with depth in individual image stacks. Within all individual image stacks the average grey value of the stele increased with time and was greater with depth (***Figure 44*** **and** ***Figure 45***). However, this increase was again more gradual within the image stacks captured at the higher position (***Figure 45***) – potentially a result of the time required for the contrast agent to translocate up through the root from the lower to higher imaging position. Whilst the grey value within the stele does increase with time in all instances, there is some variation within the rate increase - possibly a result of slight variations in root growth and development between plants.

Given that we assume that the grey value in the stele is indicative of the plant solute uptake rate, more developed roots, or those plants with longer lengths of root submerged into the contrast agent, would likely have a faster rate of contrast agent uptake (Gardner, 1991; Roose & Schnepf, 2008).

In contrast, the average grey value within the cortex showed no such trend of consistently increasing as contrast agent was translocated further up the root material (***Appendix Figure A9*** **and** ***Appendix Figure A10***) which would suggest that the upwards translocation of the contrast agent did take place through the vasculature in the stele, rather than in an apoplastic manner through the cortex. Were the contrast agent to be translocated upward through the cortex it would be expected that there would be a trend of average grey values in the cortex increasing with time, as is observed in the stele (***Figure 44*** **and** ***Figure 45***), though this trend is not present (***Appendix Figure A9*** **and** ***Appendix Figure A10***). There are variations in the cortex grey value with depth (correlations in M2-lower in addition to M1-higher and M3-higher are negative whilst all other correlations are positive). It is possible that this is a result of contrast agent leaking from the stele through damaged endodermis tissues. Keyes *et al*., (2017b) observed similar leaking of contrast agents from the stele into the cortex which was thought to be a result of osmotic stress effects of the contrast agents over time. It is also possible that the apparent 'disappearance' of aerenchyma over time in some samples (***Figure 42***) is caused by contrast agent leaking through damaged tissues – if contrast agent has also leaked into the aerenchyma then the grey value inside the aerenchyma could be raised such that there is insufficient contrast generated between the cortex and aerenchyma. This is likely to be further exacerbated with prolonged exposure, for example where time is required for contrast agent to translocate from leaves to the root system as in Keyes *et al*., (2017b), and thus the benefit of our system delivering contrast agent immediately to the roots is reinforced. However, we did not visually observe such tissue damage in SRXCT images.

The grey value data could be correlated with other anatomical characteristics of the roots such as the aerenchyma cross sectional area with depth (***Appendix Figure A5*** **and** ***Appendix Figure A6***). In half of the image stacks we were able to capture strong negative correlations between aerenchyma cross sectional area and grey value (***Table 9*** **and** ***Appendix Figure A5*** **and** ***Appendix Figure A6***), despite little evidence of a consistent trend in aerenchyma cross sectional area with depth (***Appendix Figure A7*** **and** ***Appendix Figure A8***). This potentially indicates that aerenchyma may act as a barrier to solutes moving through the cortex and into the stele as has previously been observed (Fan *et al.*, 2007; Hu *et al.*, 2014). Owing to the exploratory nature of this study, the replicate number is too small to rigorously answer biological questions relating to the effect of aerenchyma cross sectional area on the transport of solutes through the cortex and into the stele. However, we

can present this as an example avenue for future study using our experimental system. For example, if this system was used in larger studies with more replicates, such data could be used to parametrise models for plant solute or water transport, such as those of Payvandi *et al.*, (2014), under different environmental conditions.

4.6.3 Considerations and Further Work

Iodinated contrast agents have been used previously to study larger soil and plant systems and one future avenue for exploration could be upscaling the experimental system developed in this study and using it to capture solute movement through roots in considerably larger soil systems. Previous studies have investigated fluid flow through soil cores of 10 cm in diameter or larger using radiographic contrast agents (Heijs *et al.*, 1996; Koestel & Larsbo, 2014; Scotson *et al.*, 2020a) and, were such methodologies to be combined with the principles of the experimental system used in this study, fluid flow and nutrient movement through both the soil and through the root system could be studied simultaneously. Such data could then be used to parameterise mathematical models of solute movement through soil to roots and then transport within the plants. Additionally, using larger soil systems would facilitate the use of larger and more mature plants which would likely tolerate contrast agents better than juvenile plants. By applying the principles of our experimental system, contrast agents could still be delivered immediately to the roots of larger plants without the increased time delay required by the system established by Keyes *et al.,* (2017b) for translocation of the contrast agent from the leaves to the roots of larger plants. Not only could this enable fluid flow tracing through the root system, but it would also likely simplify segmentation of roots by increasing the contrast to noise ratio of the roots against soil water within larger soil samples which can otherwise present segmentation issues (Attix, 2008; Mooney *et al.*, 2012). However, one limitation of using a system containing more mature plants is that such a root system would likely include more branching and it could therefore take longer for contrast agent to translocate into secondary roots if the agent is only applied to the primary root. In addition, larger root systems would likely require a greater volume of contrast agent be taken up by the plant in order for sufficient contrast to be maintained. The larger volume of applied contrast agent and the increased duration of exposure of the roots to the contrast agent would have implications for plant health and the capacity of plant tissues to mitigate the osmotoxic effects of the contrast agent.

In addition to the opportunities outlined above, it is important to note that there are potential considerations in the use of this experimental system which could affect future applications and implementation. As mentioned, iodinated contrast agents can induce osmotic stress effects over

time resulting in internal plant tissue damage which may affect normal plant function and growth (Zhang *et al.*, 2016; Keyes *et al.*, 2017b). There is no visible evidence for tissue damage within the SRXCT images of this study – plant vascular tissues remained sufficiently healthy to transport the contrast agent to the leaves. We would not have captured changes in root growth caused by the addition of contrast agent as the contrast agent was only applied to the roots for the imaging period of 24 hours and the root tips themselves were not captured in SRXCT images. The purpose of this investigation was to assess whether our system would facilitate contrast agent uptake however, were growing root tips to be imaged, such as in the work of Keyes *et al*., (2017a), it would be possible to capture effects of contrast agents on root growth over time. In order to mitigate these effects, non-ionic iodinated contrast agents should be used, such as the iopamidol used in this investigation, as ionic alternatives have previously been observed to induce more significant osmotic stress effects in biological tissues (Haller & Hizoh, 2004; Heinrich *et al.*, 2005; Hasebroock & Serkova, 2009; Sendeski, 2011). Additionally, the osmolality, closely associated with osmotic shock effects (Lusic & Grinstaff, 2013), of non-ionic contrast agents has been reported to be at least four times lower than that of ionic contrast agents of comparable iodine concentrations (Aspelin, 2006). Osmotoxic effects of iodinated contrast agents could be further mitigated if using more dilute contrast agents since more dilute contrast agents are likely to draw less water from nearby plant cells (Lusic & Grinstaff, 2013). It would therefore be worthwhile to conduct further optimisation studies to assess the necessary contrast agent concentrations for achieving sufficient contrast within plant tissues whilst considering a minimisation of osmotoxic effects. However, it should be noted that, even when using diluted non-ionic contrast agents, prolonged exposure to iodinated contrast agents will still have implications for plant health - particularly where juvenile plants are used. Therefore, there are limitations on the duration of experiments which require continuous exposure of plants to contrast agents. This perhaps reinforces that upscaling the experimental system to a size similar to Heijs *et al.*, (1996), Koestel and Larsbo (2014) and Scotson *et al.*, (2020a) to support more mature plants, which are more stress tolerant (Derera *et al.*, 1969; Choudhury & Kumar, 1980; Singh *et al.*, 2012), would be a positive progression of our system which could also aid mitigation of osmotoxic water stress effects of the contrast agent.

4.6.4 Conclusions

In conclusion, we have demonstrated that our experimental system, which utilises contrast agent applied to intact *in vivo* plant roots within soil, can enhance SRXCT imaging of the root system and elucidate details of the internal root structure. We confirmed the translocation of the contrast agent throughout the plants with the novel use of both SRXCT and SRXRF imaging. With the

application of the contrast agent it was possible to visualise anatomical information including the stele, the root vasculature, fibres in the aerenchyma and the leaf venation. Examples were then provided of the features which could be studied using our system such as the effect of aerenchyma cross sectional area on fluid and nutrient transport in plant root systems. Our system could be used in future to study many different aspects of solute transport, root anatomy and structure, much of which would otherwise require microscopy of stained *ex vivo* plant tissues. The data from such studies could then be utilised to parameterise mathematical models of solute transport through varying internal root structures to investigate optimal root structure for efficient solute transport.

4.7 Author Contributions

CPS, TR designed the study. CPS designed and constructed the plant growth setup for in vivo imaging. CPS, DMF, AvV and NK collected the SRXCT and SRXRF data. CPS developed the image processing protocols with advice and input from KAW. CPS undertook the image processing and analysis on SRXCT data. CPS and AvV undertook the analysis on the SRXRF data. CPS wrote the manuscript and all other authors provided critical revision and approval before submission and publication.

4.8 Acknowledgements

CPS, AvV, KAW, NK, DMF and TR were funded by ERC Consolidator grant 646809 (Data Intensive Modelling of Rhizosphere Processes). TR is also funded by BBSRC SARIC BB/P004180/1, BBSRC SARISA BB/L025620/1, EPSRC EP/M020355/1 and NERC NE/L00237/1. The authors acknowledge the Diamond Light Source synchrotron, Didcot, UK, and in particular grants MT18762 (I13-1) and SP19399 (I18) for provision of SRXCT and SRXRF facility and for assistance with facility operation. The authors would also like to acknowledge Davey Jones (Bangor University) for providing the soil samples used within this investigation. We gratefully acknowledge the support of the U.S. Department of Energy through the LANL/LDRD Program and the G. T. Seaborg Institute for this work. Los Alamos National Laboratory is operated by Triad National Security, LLC, for the National Nuclear Security Administration of U.S. Department of Energy (Contract No. 89233218CNA000001).

5 Conclusions and Further Work

The aims of the body of work presented in this thesis was to develop strategies for using contrast agents to overcome issues of low contrast within XCT images of plant/ soil systems and to then use contrast agents to study patterns of solute movement and transport through soil and plant roots. In Chapter 1 we established that the low contrast to noise ratio that results from the similar X-ray attenuation characteristics of plant roots and soil-water is a major challenge in using XCT imaging to capture plant root and soil interactions. We determined that this is particularly an issue where higher X-ray energies are required for larger samples in order to achieve sufficient X-ray penetration - contrast is often reduced in these instances owing preferential attenuation of lower energy X-ray photons (Flannery *et al.*, 1987). We noted that in biomedical applications these issues of low contrast are often overcome with the use of radiocontrast agents (Lusic & Grinstaff, 2013). We then determined the necessary attributes of contrast agents for use in soil systems containing plants, primarily the properties of: minimal toxicity, ease of mobility, sustained stability in soil and plant environments and to contain an X-ray attenuating material (Lusic & Grinstaff, 2013). Against these criteria we then compared the attributes and limitations of various contrast agents and identify suitable candidates for use in plant and soil systems. We noted that non-ionic iodinated contrast agents are commonly used as flow tracers in biomedicine (Gertz *et al.*, 1985; Blachar *et al.*, 2001; Lusic & Grinstaff, 2013). They also had some limited use in soil science (Karunakaran *et al.*, 2015; Keyes *et al.*, 2017b), as a result of the comparatively low reactivity and toxicity to organic tissues of this class of contrast agent. Additionally, we noted that gold nanoparticles (AuNPs) have been used before in biomedical imaging for tissue-specific approaches (Rabin *et al.*, 2006; Sun *et al.*, 2009; Lusic & Grinstaff, 2013). This is because they can be modified in order to adhere to specific tissues or materials with the application of coatings possessing functional groups. However, the major obstacle to the use of AuNPs in soil environments was the instability of suspensions in the presence of acids, salts or surface charges – all of which can be present in soil.

In the three research chapters of this thesis, we have demonstrated the capacity for both metal nanoparticulate and iodinated contrast agents to generate sufficient contrast in plant and soil systems. In our review of the literature we have assessed the challenges of imaging plant and soil systems using XCT, investigated how contrast agents can be used to overcome limited contrast in soil/ plant XCT images and studied the benefits or limitations of different categories of contrast agent. In Chapter Two we developed AuNPs which remain stable in soil conditions, which are capable of producing contrast in soil and which we determined had a similar approximate diffusion coefficient to typical plant nutrients. An iodinated contrast agent was used in Chapter Three to

trace solute movement through soil columns featuring different soil surface geometries – demonstrating that soil water status, surface geometry and root water uptake can all influence solute infiltration. Finally, in Chapter Four we captured internal plant fluid transport and anatomical features otherwise not observable in XCT imaging by using a novel experimental system to deliver contrast agent directly to the roots. A conceptual diagram displaying how all three research chapters of this thesis relate to one another is given in ***Figure 46***.

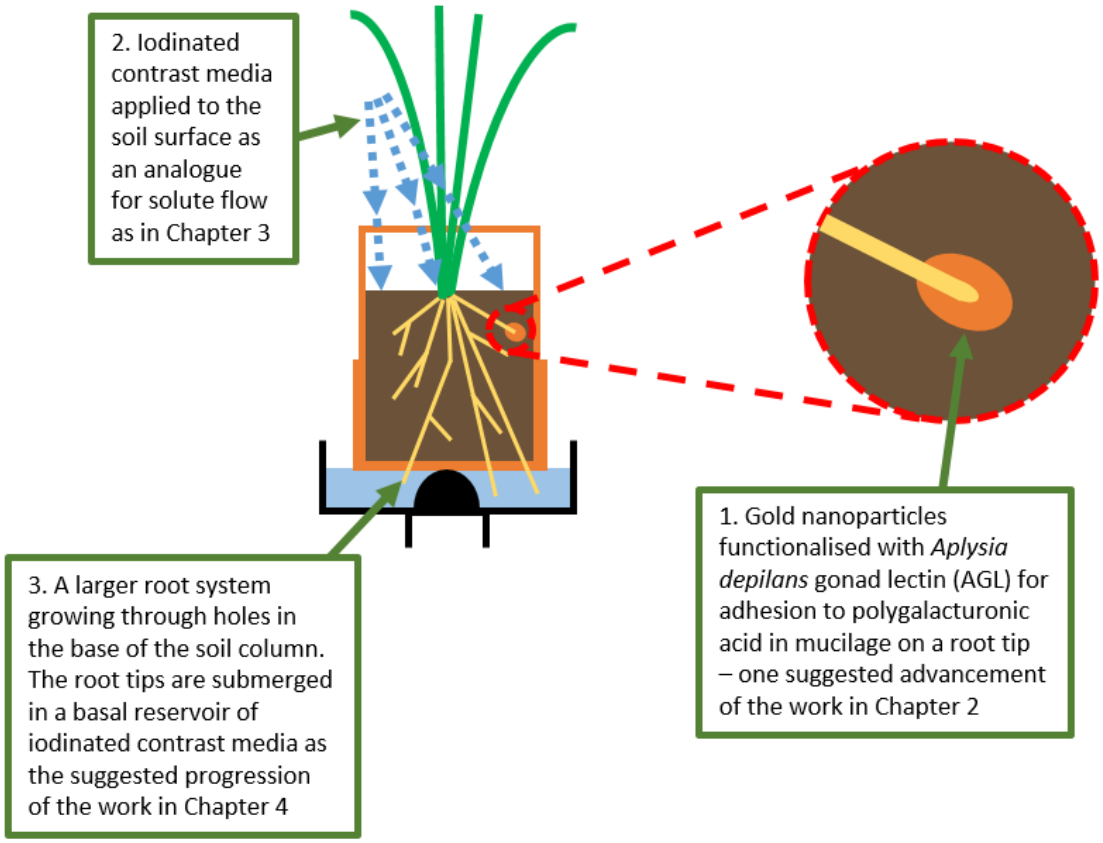

Figure 46. *A conceptual diagram displaying how the three research chapters of this thesis relate to one another. In a proposed development of the work in Chapter Two, gold nanoparticles could be functionalised with Aplysia depilans gonad lectin (AGL) for adhesion to polygalacturonic acid in order to map root tip mucilage (1). The application of iodinated contrast agent, acting as an XCT-visible analogue for agrochemical solutes, to the soil surface enables the study of patterns of solute infiltration in different soil and plant systems as in Chapter Three (2). The experimental system conceived in Chapter Four could be scaled up to the size of the system used in Chapter Two wherein roots of a larger root architecture would grow through the base of the soil column and into a basal reservoir of iodinated contrast agent (3).*

5.1 Strategies for Overcoming Low Contrast

In all three scientific chapters we have achieved the aim of demonstrating that contrast agents can overcome issues of low contrast in soil and plant root systems. Once stabilised, we produced a concentrated suspension of AuNPs to confirm that the AuNPs can provide sufficient contrast against soil at high concentrations. We were able to observe in XCT images that a distinct peak was produced by the AuNPs in grey value histograms and thus the applicability of using AuNPs to overcome the limited contrast in soil was demonstrated. With functionalisations developed for plant and soil science applications AuNPs could be induced to accumulate at high concentrations on target tissues, such as Sun *et al*., (2009) achieved in a biomedical context, and contrast would be generated.

In Chapter Three sufficient contrast was produced by the non-ionic iodinated contrast agent, iopamidol, such that we could segment the contrast agent from the soil automatically using a custom algorithm. In contrast assessments we demonstrated that the iodinated contrast agent provided contrast against soil even at 37 mg iodine / mL – a fifth that of the concentration we applied to the soil surface and a tenth of the as-supplied concentration. This meant the contrast agent could still be segmented after the full four hours and even when applied with surface water ponding. Non-ionic iodinated contrast agents, such as iopamidol, are therefore capable candidates for similar future use where the intention is to capture the influence of plant roots on fluid flow through large soil columns over time.

Using our novel experimental system, in Chapter 4 we could successfully trace internal plant fluid transport using an iodinated contrast agent. The contrast agent provided observably increased contrast within root and by quantifying the grey value of the stele we could track contrast agent transport through the roots. Without the iodinated contrast agent it would also not have been possible to achieve visualisation of the anatomical root features and destructive staining microscopy techniques would instead have been required. With our system it would be possible to develop further studies to investigate the dynamics of internal plant fluid transport and solute uptake as a direct result of the contrast provided by the iodinated contrast agent.

5.2 Patterns of Solute Movement and Transport

Our second aim, to use contrast agents to study patterns of solute movement and transport through soil and plant root systems, was approached from a different perspective in each chapter. In Chapter Two we captured the movement of AuNPs through flow columns using XCT imaging and

by collecting UV-Vis spectra prior to and following the passage of the nanoparticulate suspension through the flow columns – in doing so we were able to confirm stability of PEG-coated AuNPs in soil environments. Upon confirmation of stability, we used time-resolved XCT imaging to capture the diffusion of AuNPs through fully saturated soil. We then used this as a reference dataset against which the diffusion rate of AuNPs in soil could be approximated. The approximate diffusion coefficient, similar to other plant nutrients (Barber, 1995), can be used to provide insight for future studies into the movement of gold nanoparticulate suspensions in soils.

In Chapter Three, we were able to use an iodinated contrast agent as an XCT-visible analogue for soluble agrichemicals to capture the dynamics of solute infiltration through ridge and furrow or flat soil surface geometries. Using the contrast agent we were able to observe that plant roots can reduce the infiltration depth of solutes, though this effect was localised to the likely root-dense centre of the columns. This central accumulation is suspected to be further influenced by drier soil in the centre of the columns, as recorded in RSMS results, inducing a strong water potential gradient (Nye & Tinker, 1977) as a result of a combination of drainage, surface evaporation, and root water uptake effects (Hanks *et al.*, 1969; Nye & Tinker, 1977). The contrast agent also enabled us to note that the hydrostatic pressure of surface ponding, especially in furrows, was sufficient to negate the influence of plant roots and drive the contrast agent to greater infiltration depths. These results provide further evidence to support the findings of previous agronomic studies which had suggested ridge and furrow systems can be more vulnerable to leaching (Smelt *et al.*, 1981; Kung, 1988; Leistra & Boesten, 2010). Had there been periods of significant rainfall during these studies, solute leaching in the furrow could have been exacerbated. In addition, we observed that ponding induced deeper solute infiltration in flat soil surface geometries which contained a plant. This is thought similarly to be a result of hydrostatic pressure from ponding forcing the contrast agent into root generated bio-pores (Phillips, 2007; Milleret *et al.*, 2009; Ruiz *et al.*, 2015). We concluded that applying solutes to soil systems containing well developed plant root systems with a greater root density (which can therefore exert greater advective forces) could be an important consideration for reducing solute leaching in agricultural systems (Hauggaard-Nielsen *et al.*, 2001; Mariotti *et al.*, 2015). Similarly, targeted application of solutes to root-dense ridges in ridge and furrow systems, implemented through precision agriculture approaches similar to those suggested by Ressler *et al*., (1997), would also likely be beneficial for reducing leaching in the furrow and improving overall application efficiency. However we noted that, in both flat and ridge furrow systems, numerous processes which affect soil water status would likely also influence solute movement including root water uptake, drainage and surface evaporation.

As mentioned, by using our experimental system discussed in Chapter Four we could capture the dynamics of internal fluid and solute transport within plant roots. We observed that as the contrast agent was taken up by the plant and translocated upward towards the leaves, the grey value increased in the higher and lower imaged sections of roots with time. First, the grey value increased in the stele in the lower position images as the contrast agent entered the roots and then as the contrast agent was translocated up the root system with time the grey value increased in the stele in upper position images. The increase in the average grey value of the stele increased with time and was greater with depth in individual image stacks also. However, we did note that there was variation in the rate of increase of grey values and we stated this could be a result of slight differences in root growth and development – more developed roots with longer lengths of root tissue submerged in the contrast agent would be expected to maintain a higher rate of uptake (Gardner, 1991; Roose & Schnepf, 2008). Another feature which we determined may affect stele grey is the aerenchyma cross sectional area – aerenchyma has previously been observed to impede axial solute transport (Evans, 2004; Fan *et al.*, 2007; Hu *et al.*, 2014). We correlated aerenchyma cross sectional area and stele grey value with depth and were able to identify strong negative correlations between these features in half of all image stacks, indicating that this impedance effect may be present. However, more replicates would be required before this could be rigorously established. Finally, we were able to determine that the contrast agent likely did not translocate via an apoplastic pathway through the cortex. Unlike in average stele grey values, there is no evidence of average grey value in the cortex increasing with time and no evidence of a trend with depth. We also noted variation in the cortex grey value between imaging time points was possibly the result of contrast agent leaking from the stele into the cortex through damaged endodermis tissue – though we did not visually observe such damage in SRXCT images. Such damage was previously observed by Keyes *et al.,* (2017b) and thought to be caused by osmotic stress effects of prolonged exposure of plant tissues to contrast agents (Lusic & Grinstaff, 2013; Zhang *et al.*, 2016).

5.3 Further Work

The research work presented within this thesis has the potential to be further developed and applied for crop and soil science research applications. We determined that the use of AuNPs as bulk fluid flow tracers is not feasible. Given the required high concentration (Xu *et al.*, 2008; Sun *et al.*, 2009) and that the AuNP diffusion rate is estimated to be high, functionalisation is necessary. To build on the successes of this work, the next stage in AuNP development would be to assess the stability and practicability of using PEG-coated AuNPs in soil systems containing live plant roots. For

example, it would be necessary to ascertain whether plant exudates affect AuNP stability and to investigate strategies for applying the AuNP suspensions to complex soil systems i.e., through injection into the soil. Following this, the intention would be to identify a suitable surface functionalisation for plant science research. One potential avenue for future investigation would be functionalising AuNP coatings with the addition of *Aplysia depilans* gonad lectin (AGL) which has previously been observed to bind to polygalacturonic acids (Benhamou *et al.*, 1988; Benhamou, 1989) – a major constituent of plant root mucilage. Using such a functionalisation it could be possible to accumulate AuNPs on root mucilage to provide contrast in XCT images and, perhaps in an experimental system similar to Keyes *et al.*, (2017a), capture the dynamics and behaviour of root exudates. However, a consideration in using an AGL functionalisation is that polygalacturonic acids are also found in soil organic matter and often on soil particle surfaces. Therefore there is a risk that AGL functionalised AuNPs could also bind to these soil features. In demonstrating that a PEG coating is sufficient to achieve stability of AuNPs in soil and that contrast is generated at high concentration, we believe that we have successfully developed a platform from which functionalisation of AuNPs for use as a tissue-specific contrast agent can be pursued.

In Chapter Three we observed that the RSMS data suggested that the centre of planted columns was significantly drier than the outer edge and that this likely influenced solute infiltration patterns. However we also noted that RSMS cannot distinguish between the influences of drainage, root water uptake and evaporation on spatial soil moisture. Therefore, to further develop this research we suggest in future it would be useful to explicitly record transpiration rate and root water uptake data in order to better decipher the influence of root advective forces. However, boundary effects, resulting from the solid walls of the column system, could impact water dynamics and these would also need to be considered. For example, the significance of these boundary conditions could be examined by studying the impact of different soil column diameters on solute movement. Due to the exploratory nature of the study and the availability and cost of XCT facilities capable of imaging physically large soil column samples, the number of replicates was limited to three and as such there is some variability within the imaging results. Limitations imposed by the scale of the system and technology necessary for this investigation means further work, which features fewer treatments, but more replicates, is warranted before specific implications for agriculture can be stated with certainty. By narrowing the scope of future studies, but increasing the number of replicates, individual effects could be studied in more detail and a greater depth of statistical testing could be facilitated. In addition, this variability could also be reduced by altering the water content of the soil, as informed by RSMS results, such that it was similar between replicates prior to the application of the contrast agent – the initial water content of the soil could have influenced the

infiltration patterns of solutes. Despite limitations, this work did indicate that plant roots, soil surface structure and soil moisture can affect the infiltration depth of solutes. Whilst further work is required to better understand the interactions between these influences, it would appear that if agriculturalists wish to improve the application efficiency of solutes and reduce leaching then anticipated rainfall, the extent of root development and the accuracy of application to root dense-zones should all be considered.

The experimental system which we designed and constructed, discussed in Chapter Four, presents numerous possible avenues for future research. Osmotic stress effects can hinder plant growth and development by damaging and reducing the turgidity of plant cells. This is a result of water being drawn out from plant tissues along an osmotic gradient induced by the contrast agent. Therefore a possible direction for study could be to combine our experimental system for applying contrast agents directly to roots with the imaging protocols of Keyes *et al*., (2017a) to capture the influence of contrast agents at varying concentrations on root growth. This would enable us to capture a time-resolved image series of microscale root growth dynamics and how these are impeded or altered by stress effects. An additional proposed development of this work would be to upscale our experimental system to a size similar to the experiments of Heijs *et al.*, (1996), Koestel and Larsbo (2014) and Scotson *et al.*, (2020a) – large soil columns of up to 10 cm in diameter. Primarily, this would improve the segmentation of roots in large soil systems by increasing the contrast between soil and plant material but also would enable the use of mature plants which are more tolerant to stress effects (Derera *et al.*, 1969; Choudhury & Kumar, 1980; Singh *et al.*, 2012). However, as mentioned in Chapter Four, a limitation of using a larger root system is that such root systems would be expected to include more branching. In larger root systems with more branching it could take longer for the contrast agent to translocate from the primary root, to which the contrast agent was applied, and into secondary roots. In addition to a longer duration of application, the total volume of contrast agent applied would also likely need to be greater if sufficient contrast were to be maintained. Facing a similar challenge of translocating iodinated contrast agents around biological structures, though in a biomedical context, Sun *et al.* (2009) observed that the iodinated contrast agent eXIA-160 could not achieve full coverage of the complex structures of murine liver tissues. Though such mammalian tissues evidently differ from root architecture, it would indicate that achieving full coverage of complex biological tissues using iodinated contrast agents can be challenging. This increase in the duration of application and the volume applied to roots could have implications for the capacity of plant tissues to mitigate the osmotoxic effects of the contrast agent and therefore implications for general plant health. The capacity for our SRXCT compatible system to successfully deliver contrast agents to live plant roots in soil represents a significant

advancement upon previous approaches. Using this system, we were able to increase the contrast of roots against soil-water – presenting opportunities for improving the segmentation of roots. In addition, our system enabled us to capture internal plant fluid transport and to visualise anatomical root features. We propose that this system could be used in future to study aspects of solute transport and root structure *in vivo*, which would otherwise likely require microscopy imaging of stained *ex vivo* plant tissues.

In this thesis we aimed to develop strategies to overcome low contrast in XCT images of plant and soil systems using contrast agents and use contrast agents to study solute movement and transport. In stabilising AuNPs for use in soil, using iodinated contrast agents to trace solute infiltration and by constructing a system for applying contrast agents directly to roots, we have made significant contributions to the development of strategies for using contrast agents in soils. We have captured the diffusion of AuNPs in soil (as a reference for approximating the diffusion coefficient), demonstrated that plant roots can have a localised effect on reducing the depth of solute infiltration and recorded the rate of increase in grey value of root steles as plants take up contrast agents. These observations provide insight into the dynamics of solute movement in both plant and soil systems. Though further work is required to progress development, we have made significant contributions in identifying strategies for contrast agent use and demonstrating the capacity for contrast agents to trace solute movement in soil and plant systems.

Appendix I – Chapter 3 Supplementary Material

Implementation of Model

We used the water-solute-pond model developed in Duncan *et al*. (2018a), which is used to study water and solute movement in a cross section of a ridge and furrow (or flat) soil surface geometry. The model consists of a coupled system of Partial Differential Equations (PDEs) and Ordinary Differential Equations (ODEs) that describe water and solute movement, and surface ponding in a ridge and furrow system.

Within the model the movement of water in soil is described by the effects of capillary forces, pressure gradients and gravity, all of which is coupled via a feedback loop to the pond depth on the soil surface. The pond depth is described by a combination of surface runoff, rainfall and infiltration into the soil. Furthermore, the transport of solutes, *i.e.*, contrast agent in soil under the influence of water movement is also included. The mechanisms driving solute movement are described by the processes of diffusion and advection, which are influenced by the movement of water and the resulting pressure gradients that form in the soil. This allows for a coupled system of equations to describe the simultaneous movement of water and solutes in soil. It should be noted that we assume solutes do not create osmotic pressure gradients influencing fluid flow, *i.e.,* water movement influences solute movement, but not *vice versa*.

The model described is developed for generalised curved soil surface, *i.e.*, to account for the ridge and furrow geometry. However, this can be easily adapted for a flat surface. For a full derivation and validation, see Duncan *et al*. (2018a).

Water Movement in Variably Saturated Soil

The movement of water in soil is described by the effects of capillary forces, pressure gradients and gravity. Variably saturated soil is described by Richards' equation (Bear, 2012). Richards' equation in mixed form is given by (Richards, 1931; Kavetski *et al.*, 2001),

$$\boldsymbol{\phi}\frac{\partial \boldsymbol{S}}{\partial \boldsymbol{t}} + \nabla \cdot \left[-\frac{\boldsymbol{\kappa}(\boldsymbol{S})}{\boldsymbol{\mu}}\left(\nabla \boldsymbol{p} + \boldsymbol{\rho}\boldsymbol{g}\hat{k}\right)\right] = -\boldsymbol{F}_{\mathbf{w}}, \quad x \in \boldsymbol{\Lambda}, \tag{1}$$

where ϕ is the soil porosity, S is the relative saturation (*i.e.,* $S = \phi_l/\phi$, where ϕ_l is the volumetric water content), $\kappa(S)$ is the unsaturated permeability, μ is the viscosity of the fluid, *i.e.*, water, p is the soil water pore pressure, ρ is the density of the fluid, g is the acceleration due to gravity, $\widehat{\boldsymbol{k}}$ is a

unit vector in the upwards direction, Λ is a generalised ridge and furrow geometry (***Appendix Figure A3*a**), and F_{w} is a sink term that describes water uptake via plant roots.

Richards' equation (1) can be written in terms of soil water pore pressure p using two van Genuchten formulae (van Genuchten, 1980); one for the suction characteristic,

$$\boldsymbol{S(p) = \left[\left(\frac{p_a - p}{p_c}\right)^{\frac{1}{1-m}} + 1\right]^{-m}}, \tag{2}$$

and one hydraulic permeability,

$$\boldsymbol{\kappa(S) = \kappa_s S^{\frac{1}{2}}\left[1 - \left(1 - S^{\frac{1}{m}}\right)^{m}\right]^{2}}, \tag{3}$$

where p_c is the characteristic suction pressure, m is a van Genuchten parameter, κ_s is the saturated soil water permeability and p_a is the atmospheric pressure. Substituting (3) – (4) into (1) gives Richards' equation in the pressure form.

The domain used to describe a general ridge and furrow system Λ (***Appendix Figure A3*a**) is split into two regions Λ_{U} and Λ_{A}. Λ_{U} is the region of soil in which roots take up water and Λ_{A} is the region in which there are no roots. F_{w} is assumed to be active only where roots are present. Hence, we write,

$$\boldsymbol{F_w} = \begin{cases} \boldsymbol{\lambda_c(p - p_r)}, & x \in \boldsymbol{\Lambda_U} \\ \boldsymbol{0}, & x \in \boldsymbol{\Lambda_A}, \end{cases} \tag{4}$$

whered p_r is the pressure in the root xylem and λ_c is the product of the root surface area density and water conductivity of the plant root cortex described as:

$$\boldsymbol{\lambda_c = k_r l_d(t)}, \tag{5}$$

where k_r(≈10^{-9} [$m^2 s^{-1} MPa^{-1}$]) is radial conductivity of the root cortex per unit of root length, and $l_d(t)$ is the root length density, which we describe as:

$$\boldsymbol{l_d(t), = 10^3 t,\ 0 \le t < 30\ days}. \tag{6}$$

Thus, $\lambda_c \approx 3\times10^{-4}$ [$MPa^{-1}s^{-1}$] after 30 days. Root xylem pressure was not explicitly measured in the experiments of this investigation. Instead to parameterise the water uptake rate values for rice root xylem pressure from the literature were used. The root xylem pressure was assumed to be 0.1 MPa. This is a conservative value given that root xylem pressure can be up to 2 MPa, though both are well within the range of realistic values. The water uptake rate in the model changes with root surface area density over time and in accordance with fluctuations in soil moisture. The root xylem hydraulic conductivity value used in this model, 7.85×10^{-8} $m^3m^{-2}s^{-1}MPa^{-1}$, is within bounds given by Henry *et al.,* (2012).

An additional simulation for the flat surface geometry was undertaken to investigate discrepancies between the imaging results and the results of the simulations which feature homogenous root distribution. Implementation of the root region Λ_{U} in this additional simulation of the flat system explicitly considered the spatially resolved root surface distribution obtained from the XRCT images. The measured root surface area density was defined as,

$$\widetilde{\boldsymbol{\gamma}}(\boldsymbol{r_i}) = \frac{\boldsymbol{A_s}(\boldsymbol{r_i})}{\boldsymbol{\pi}\left(\boldsymbol{r_i^2} - \boldsymbol{r_{i-1}^2}\right)\boldsymbol{\Delta z}}, \tag{7}$$

where r_i and r_{i-1} are the inner and outer annulus radii respectively, Δz is the experimental depth of the control volume where the root area is measured, and $A_s(r_i)$ is the root surface area in in the control volume (between r_{i-1} and r_i). To induce the spatial component of the root surface distribution without changing the magnitude of λ_c, the spatially dependent root surface area density $\tilde{\gamma}$ is normalized with respect to its spatial mean. The total root surface area in the pot is defined as,

$$\boldsymbol{A_{s,tot}} = \sum_{\boldsymbol{i=1}}^{\boldsymbol{n}} \boldsymbol{A_s}(\boldsymbol{r_i}), \tag{8}$$

where n is the final annulus control volume index. Substituting 5 into 6 yields,

$$\boldsymbol{A_{s,tot}} = \sum_{\boldsymbol{i=1}}^{\boldsymbol{n}} \boldsymbol{\pi}\widetilde{\boldsymbol{\gamma}}(\boldsymbol{r_i})\boldsymbol{\Delta z}(\boldsymbol{r_i} + \boldsymbol{r_{i-1}})(\boldsymbol{r_i} - \boldsymbol{r_{i-1}}). \tag{9}$$

Since $A_{s,tot}$ is constant for an domain arbitrary partitioning, (7) could be re-written as,

$$\boldsymbol{A_{s,tot} = \lim_{|r_i - r_{i-1}| \to 0} \sum_{i=1}^{n} 2\pi \tilde{\gamma}(r_i) r_i (r_i - r_{i-1}) \Delta z,} \tag{10}$$

which is equivalent to,

$$\boldsymbol{A_{s,tot} = 2\pi \Delta z \int_{r_{0=0}}^{r_n} \tilde{\gamma}(r) r dr.} \tag{11}$$

The mean root surface area density across the full domain is described as,

$$\boldsymbol{\langle \tilde{\gamma} \rangle = \frac{A_{s,tot}}{\pi \Delta z r_n^2},} \tag{12}$$

which is equivalent to,

$$\boldsymbol{\langle \tilde{\gamma} \rangle = \frac{2\pi \Delta z \int_0^{r_n} \tilde{\gamma}(r) r dr}{2\pi \Delta z \int_0^{r_n} r dr}.} \tag{13}$$

Thus, the normalized root surface density is expressed as:

$$\boldsymbol{\gamma(r_i) = \frac{\tilde{\gamma}(r_i)}{\langle \tilde{\gamma} \rangle}.} \tag{14}$$

As the expression above is only defined for discrete data points, the data was fit to an analytic distribution that is continuous with respect to r.

$$\boldsymbol{\gamma(r) \approx \alpha e^{-\beta r},} \tag{15}$$

where α and β are fitting coefficients and cofactors respectively. As such, the root water uptake term is changed to the following,

$$\boldsymbol{F_w = \begin{cases} \lambda_c (p - p_r) \gamma(r), & x \in \Lambda_U \\ 0, & x \in \Lambda_A \end{cases},} \tag{16}$$

where the total magnitude of the water uptake term is preserved while considering the explicit spatial dependence of the system.

Soil Surface Boundary Condition

To form a complete description of the ridge and furrow system, we derive boundary conditions that are imposed on the edges of the soil domain Λ, and a model for dynamic water ponding on the soil surface coupled to Richards' equation for water movement in soil (see Duncan *et al*. (2018a)).

To represent surface ponding, the surface $\partial\Lambda_{\mathrm{S}}$ (see ***Appendix Figure A3*****a**) is split into two distinct regions. This is shown in ***Appendix Figure A3*****b**, where $\partial\Lambda_{\mathrm{R}}$ is the surface of soil that is not ponded, *i.e.*, where rainfall infiltrates the soil directly, and $\partial\Lambda_{\mathrm{P}}$ is the ponded region. The interface between the two regions is defined by the moving boundary point $x_0(t)$ (***Appendix Figure A3*****b**).

On the soil surface directly under the pond $\partial\Lambda_P$ we apply the hydrostatic pressure that is a result of the height of the water column in the pond above it, *i.e.,*

$$\boldsymbol{p} = \boldsymbol{\rho g h}(\boldsymbol{x}, \boldsymbol{t}), \quad x \in \boldsymbol{\partial\Lambda_P}, \tag{17}$$

where $h(x,t)$ [m] is the depth of the pond.

Precipitation landing on the bare soil $\partial\Lambda_R$ enters the soil domain via a combination of capillary forces and gravitational effects. Hence, we implement a normal fluid flux condition on $\partial\Lambda_{\mathrm{R}}$ (Yang *et al.*, 1996), *i.e.*,

$$n \cdot \left\{ \frac{\boldsymbol{\kappa}[\boldsymbol{S}(\boldsymbol{p})]}{\boldsymbol{\mu}} \left(\nabla \boldsymbol{p} + \boldsymbol{\rho g} \hat{k} \right) \right\} = \boldsymbol{\omega}(\boldsymbol{t}), \quad x \in \boldsymbol{\partial\Lambda_R}, \tag{18}$$

where $\omega(t) = \min\{\Gamma(t), I_c\}$ [m s^{-1}] is the volume flux of water entering the soil per unit soil surface area, $\Gamma(t)$ [m s^{-1}] is the volume flux of water per unit soil surface area, *i.e.,* application of ponding water, I_c [m s^{-1}] is the infiltration capacity of the soil. The value for this infiltration capacity of the soil was 1.6×10^{-6} m s^{-1} (Morin & Benyamini, 1977).

We denote $\chi(x)$ to be the generalised curve of the surface $\partial\Lambda_S$, which takes the form of the function,

$$\boldsymbol{\chi(x) = A\cos(Bx) + C}, \tag{19}$$

where A is the variation in soil depth, B is the ridge wave number, and C is the average soil depth (***Appendix Figure A3***). It should be noted that for the flat geometry $\chi(x)$ is constant with the average soil depth, *i.e.*, $\chi(x) = C$.

The position of the interface between the ponded and un-ponded regions $x_0(t)$ along the soil surface is then given as a function of rainfall landing directly into the pond $R_F(t)$, infiltration of water from the pond into the soil $I_f(t)$, and surface runoff $R_o(t)$ (see Duncan *et al*. (2018a) for details), *i.e.*,

$$\boldsymbol{\frac{dx_0(t)}{dt} = f\left(R_F(t), I_f(t), R_0(t)\right)}. \tag{20}$$

Lateral Boundary Condition

For the lateral boundaries $\partial\Lambda_E$ and $\partial\Lambda_W$, we set a zero flux boundary condition to emulate the soil column, *i.e.,*

$$\boldsymbol{n \cdot \left\{\frac{\kappa[S(p)]}{\mu}\left(\nabla p + \rho g\hat{k}\right)\right\} = 0, \quad x \in \partial\Lambda_E \cup \partial\Lambda_W}. \tag{21}$$

Hence, there is no lateral water movement into or out of Λ.

Boundary Condition at the Base of the Soil

The base of the domain is submerged in water. For the boundary on the base of the domain $\partial\Lambda_B$, we set a Dirichlet boundary condition (Feddes *et al.*, 1988; Banti *et al.*, 2011), *i.e.*,

$$\boldsymbol{p = p_0, \quad x \in \partial\Lambda_B}. \tag{22}$$

Initial Conditions

For the initial pressure condition $p|_{t=0}$, we impose the steady state pressure profile that forms when roots are not present, *i.e.*,

$$\boldsymbol{p}|_{\boldsymbol{t=0}} = \boldsymbol{p}_{\infty}(x), \quad x \in \boldsymbol{\Lambda}. \tag{23}$$

Furthermore, we implement no surface ponding present on $\partial\Lambda_S$ at $t = 0$, *i.e.*,

$$\boldsymbol{x_o(t)}|_{\boldsymbol{t=0}} = \boldsymbol{\eta}, \tag{24}$$

such that the pond depth is 0, where η is the edge of the geometry Λ (***Appendix Figure A3***).

Solute Movement in Variably Saturated Soil

In this section, we introduce a model for solute movement in soil. It is coupled with the water movement model, thereby constructing a model for simultaneous water and solute movement in soil.

To model the movement of solutes in soil, we use the advection-diffusion-reaction equation (Guerrero *et al.*, 2009), *i.e.,*

$$\frac{\boldsymbol{\partial}}{\boldsymbol{\partial t}}[(\boldsymbol{\phi_l} + \boldsymbol{b})\boldsymbol{c}] + \nabla \cdot (\boldsymbol{c}u) = \nabla \cdot (\boldsymbol{\phi_l D}\nabla \boldsymbol{c}), \tag{25}$$

where D is the solute diffusion coefficient in the soil pore water, ϕ_l is the volumetric water content, c is the solute concentration in the pore water, $\boldsymbol{u}$ is the volume flux of water and b is the buffer power of the solute, *i.e.*, the ratio of the solute adsorption and desorption rates. It should be noted, consistent with the experimental assay given the time scale of the imaging experiments, we assume that there is no solute uptake by plant roots.

The volumetric water content ϕ_l is related to p by the suction characteristic $\phi_l = \phi S(p)$. In addition, we state that $\boldsymbol{u}$ is described by Darcy's law, *i.e.*,

$$u = -\frac{\boldsymbol{\kappa}[\boldsymbol{S(p)}]}{\boldsymbol{\mu}}\left(\nabla \boldsymbol{p} + \boldsymbol{\rho g}\hat{k}\right). \tag{26}$$

Finally, we assume D can be expressed by the power law,

$$\boldsymbol{D} = \boldsymbol{D_f \phi^d S(p)^d}, \tag{27}$$

where D_f is the diffusion coefficient in free liquid and d is the impedance factor of the solute that accounts for the tortuosity of the solute moving through the pore space (Reddy & Doraiswamy, 1967; Nye & Tinker, 1977).

Combining equations (13) - (15), and using the governing water movement equations (1) - (4), the model for solute movement is given by,

$$\begin{gathered}\frac{\boldsymbol{\partial c}}{\boldsymbol{\partial t}}[\boldsymbol{b} + \boldsymbol{S(p)\phi}] + \frac{\boldsymbol{\partial p}}{\boldsymbol{\partial t}}\left\{\frac{\boldsymbol{\partial S(p)}}{\boldsymbol{\partial p}}\boldsymbol{\phi c}\right\} + \nabla \cdot \left[-\boldsymbol{D_f \phi^{d+1} S(p)^{d+1} \nabla c}\right] + \\ \nabla \cdot \left\{-\frac{\boldsymbol{c\kappa[S(p)]}}{\boldsymbol{\mu}}\left(\nabla \boldsymbol{p} + \boldsymbol{\rho g}\hat{k}\right)\right\} = -\boldsymbol{\Gamma_c},\ x \in \boldsymbol{\Lambda}.\end{gathered} \tag{28}$$

The solute model (16) is coupled to the water movement model (1) – (4) to achieve a system of PDEs that describes simultaneous water and solute movement in soil.

Soil Surface Boundary Condition

On the boundary of the soil $\partial\Lambda_S$ we impose a solute flux condition such that,

$$n \cdot \left(\left[\boldsymbol{D_f \phi^{d+1} S(p)^{d+1} \nabla c}\right] + \left\{\frac{\boldsymbol{c\kappa[S(p)]}}{\boldsymbol{\mu}}\left(\nabla \boldsymbol{p} + \boldsymbol{\rho g}\hat{k}\right)\right\}\right) = \boldsymbol{c_m(t)}, \quad x \in \boldsymbol{\partial\Lambda_S}, \tag{29}$$

where $c_m(t)$ is the volume flux of solute per unit soil surface area per unit time entering the soil domain.

Lateral Boundary Condition

For the boundaries $\partial\Lambda_E$ and $\partial\Lambda_W$, we set a zero flux boundary condition, *i.e.,*

$$n \cdot \left(\left[\boldsymbol{D_f \phi^{d+1} S(p)^{d+1} \nabla c}\right] + \left\{\frac{\boldsymbol{c\kappa[S(p)]}}{\boldsymbol{\mu}}\left(\nabla \boldsymbol{p} + \boldsymbol{\rho g}\hat{k}\right)\right\}\right) = \boldsymbol{0}, \quad x \in \boldsymbol{\partial\Lambda_E} \cup \boldsymbol{\partial\Lambda_W}. \tag{30}$$

Hence, there is no lateral solute movement into or out of Λ.

Boundary Condition at the Base of the Soil

On the boundary $\partial\Lambda_B$ we impose a Dirichlet boundary condition that it set to the initial concentration of the solute contained in the two geometries, *i.e.*,

$$\boldsymbol{c = c|_{t=0}}, \quad x \in \boldsymbol{\partial\Lambda_B}. \tag{31}$$

Initial Condition

We model solute movement in previously solute free soil. Hence, we impose a uniform zero initial concentration across Λ, *i.e.*,

$$\boldsymbol{c|_{t=0} = 0}, \quad x \in \boldsymbol{\Lambda}. \tag{32}$$

Estimation of Transpiration

The water flux through the rooting zone is defined as,

$$u_r = \boldsymbol{k_r} \frac{\boldsymbol{p - p_r}}{\boldsymbol{2\,\pi\, r_{root}}} \tag{33}$$

and we assume that all of the water taken up by the root is transpired. We define r_{root} as the approximate average radius of the roots extracted from the columns (0.5 mm). In systems containing a plant and ponding with flat or ridge and furrow surface geometries, we observe that transpiration is approximately 80% greater in the flat geometry than in the ridge and furrow geometry (***Appendix Figure A4***). This is possibly because of the volume of soil occupied by the 'root zone' in the flat geometry is greater and therefore there is a greater volume of liquid for the plant to draw in for transpiration. There are however several limitations of this equation (33). Firstly, only a mean radius is considered for the root system though a more precise approach would be to consider the distribution of root radii. Furthermore, the root pressure is considered fixed for the entire subdomain whereas it is known that the xylem pressure changes along the depth of the root system (Ruiz *et al.*, 2020). Lastly, this formulation does not consider above ground processes that might augment transpiration rates. However, this study utilized a growth cabinet, thus auxiliary environmental conditions (*i.e.* wind velocity, temperature, thermal conductivity, irradiance, etc.) were not necessary.

Appendix I Tables & Figures

Appendix Table A1. *Soil bulk density information recorded for all 24 of the columns. RF = ridge and furrow, F = flat, INV = inverted ridge and furrow, PL = planted, NPL = no plant, NP = no ponding, P = ponding, number = replicate number. For example the second replicate of the planted ridge and furrow system with ponding would be: RF_PL_P_2*

Column	Empty Column Mass (g)	Sand Column Mass (g)	Full Column Mass (g)	Soil Mass (g)	Soil Bulk Density (g / cm3)
RF_PL_NP	638.2	1293.9	9117	7823.1	1.02
RF_PL_P	653	1285.3	9102.7	7817.4	1.02
RF_NPL_NP	641.3	1290.7	9113.5	7822.8	1.02
RF_NPL_P	644.8	1316.8	9101	7784.2	1.02
F_PL_NP	642.9	1319	9082.3	7763.3	1.02
F_PL_P	645	1299.8	9139.2	7839.4	1.03
F_NPL_NP	645.5	1287.3	9227.7	7940.4	1.04
F_NPL_P	646	1305.4	9093.5	7788.1	1.02
RF_PL_NP_2	648.8	1348	9002.6	7654.6	1.00
RF_PL_P_2	643.5	1315.5	8917.3	7601.8	1.00
RF_NPL_NP_2	638.3	1359.6	8902.3	7542.7	0.99
RF_NPL_P_2	655.1	1329.9	8966.8	7636.9	1.00
F_PL_NP_2	645.5	1308	9069.3	7761.3	1.02
F_PL_P_2	651.8	1397.5	8898.6	7501.1	0.98
F_NPL_NP_2	653.2	1346.3	8902.7	7556.4	0.99
F_NPL_P_2	673.6	1363	8895.9	7532.9	0.99
RF_PL_NP_3	641.3	1315.3	9035.2	7719.9	1.01
RF_PL_P_3	644.8	1340.7	8973.5	7632.8	1.00
RF_NPL_NP_3	646	1334.2	8986.6	7652.4	1.00
RF_NPL_P_3	638.3	1307.2	9024.3	7717.1	1.01
F_PL_NP_3	638.2	1320.5	8996.6	7676.1	1.01
F_PL_P_3	653	1317.3	9006.8	7689.5	1.01
F_NPL_NP_3	642.9	1327.5	9012.5	7685	1.01
F_NPL_P_3	645	1332.1	8998.7	7666.6	1.00
RF_INV_01	645.5	1331.8	9025.6	7693.8	1.01
RF_INV_02	651.8	1328.7	8993.9	7665.2	1.00
RF_INV_03	648.8	1338.2	9006.7	7668.5	1.00

Appendix Table A2. *Plant mass information collected for the plants from planted treatments. RF = ridge and furrow, F = flat, PL = planted, NP = no ponding, P = ponding, number = replicate number. For example the second replicate of the planted ridge and furrow system with ponding would be: RF_PL_P_2.*

Column	Wet Plant Mass (g)	Dry Plant Mass (g)	Water Content at Harvest (g)
RF_PL_NP	16.64	2.83	4.88
RF_PL_P	13.68	2.27	5.02
RF_PL_NP_2	22.41	4.33	4.17
RF_PL_P_2	15.30	2.19	6.00
RF_PL_NP_3	17.37	2.46	6.07
RF_PL_P_3	15.04	2.17	5.92
F_PL_NP	10.12	2.91	2.48
F_PL_P	19.58	1.47	12.35
F_PL_NP_2	16.30	2.57	5.35
F_PL_P_2	19.59	3.19	5.14
F_PL_NP_3	14.07	2.35	4.98
F_PL_P_3	16.83	2.59	5.49

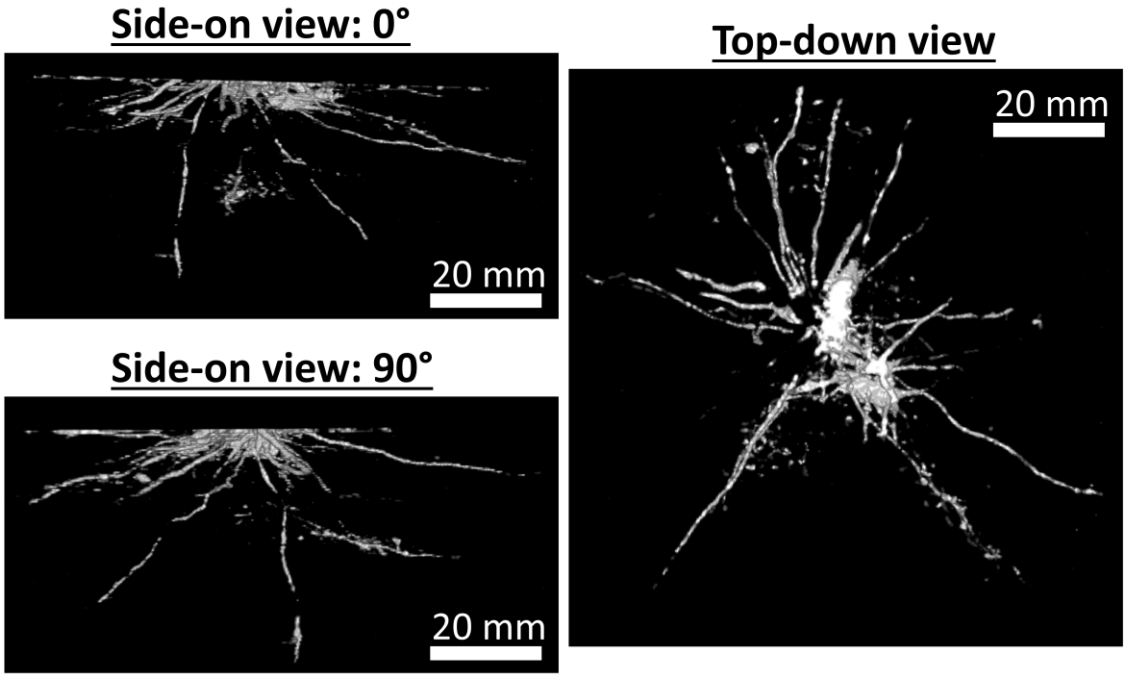

Appendix Figure A1: *Three dimensional views of the root map of Replicate One of the flat planted system with ponding. This root map was used to parameterise the image-based modelling for root surface area density. On the left are two side-on views of the root map at 0° and 90°. On the right is a top-down view of the root map.*

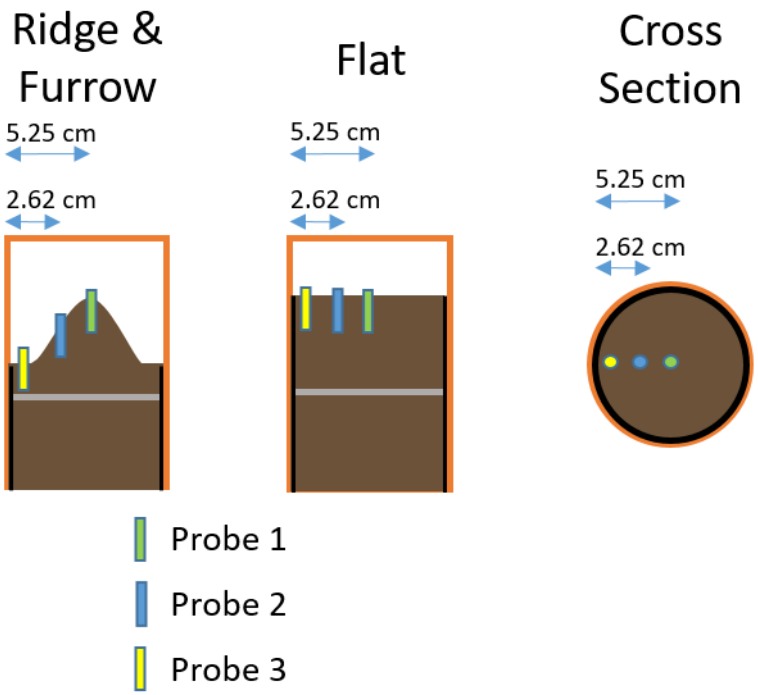

Appendix Figure A2: *A schematic diagram outlining the positioning of resistive soil moisture sensing (RSMS) probes within the soil columns. Probe 1 is displayed in green and located in the centre of the column, Probe 2 is displayed in blue and located halfway between the centre and outer edge of the column and Probe 3 is displayed in yellow and located 1 cm in from the column edge.*

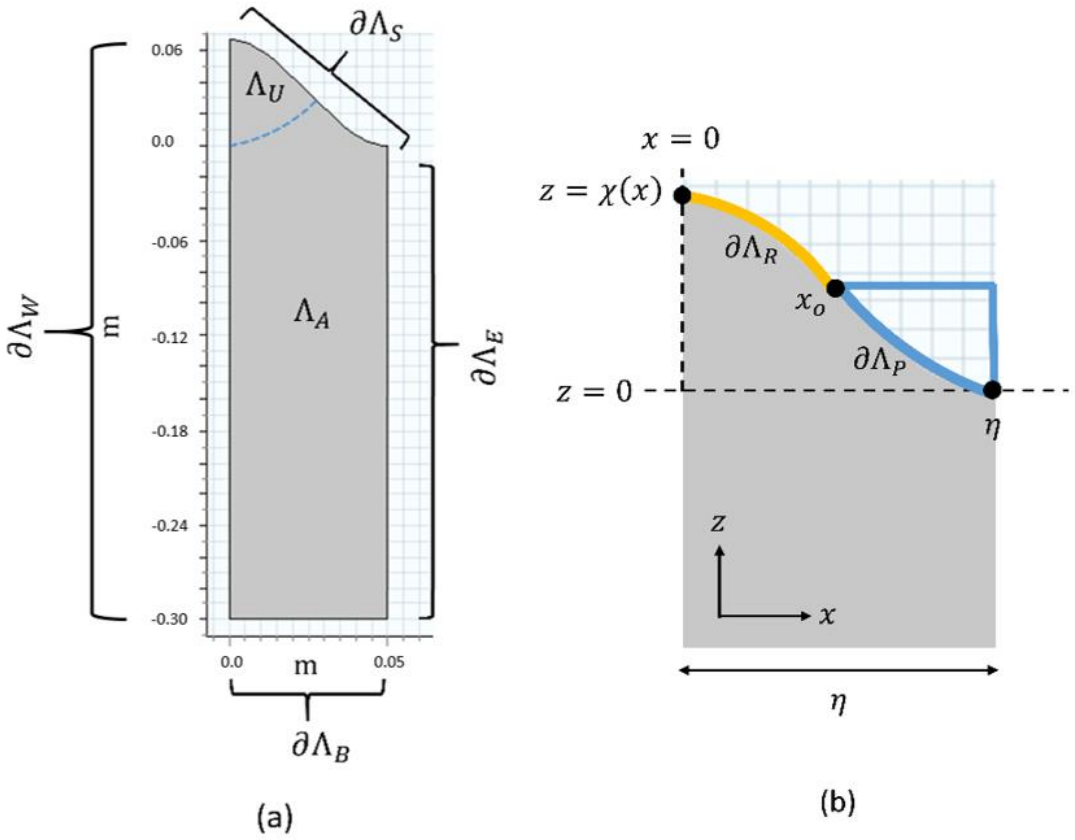

Appendix Figure A3. *(a) Half a ridge and furrow period, where Λ is the total soil domain such that $\Lambda = \Lambda_A \cup \Lambda_U$, Λ_A is the region of soil absent of roots, Λ_U is the region of soil where roots are present, $\partial\Lambda_S$ is the soil surface boundary, $\partial\Lambda_B$ is the base of the domain, $\partial\Lambda_W$ is the left boundary adjacent to the ridge and $\partial\Lambda_E$ is the right boundary adjacent to the furrow. The curve $\partial\Lambda_S$ is generated from the values $A = C = \frac{1}{6}m$ and $B = 2\pi\ m^{-1}$ used in the periodic function $\chi(x)$, i.e., equation (7), where A is the variation in soil depth, B is the ridge wave number, and C is the average soil depth. (b) Half a ridge and furrow period, where $\partial\Lambda_P$ is the soil surface boundary on which ponding occurs, $\partial\Lambda_R$ is the soil surface that is not ponded, x_0 is the point on the soil surface $\partial\Lambda_S$ where the pond begins, η is the width of the half period of ridged domain, and $\chi(x)$ is the curve for the soil surface $\partial\Lambda_S$.*

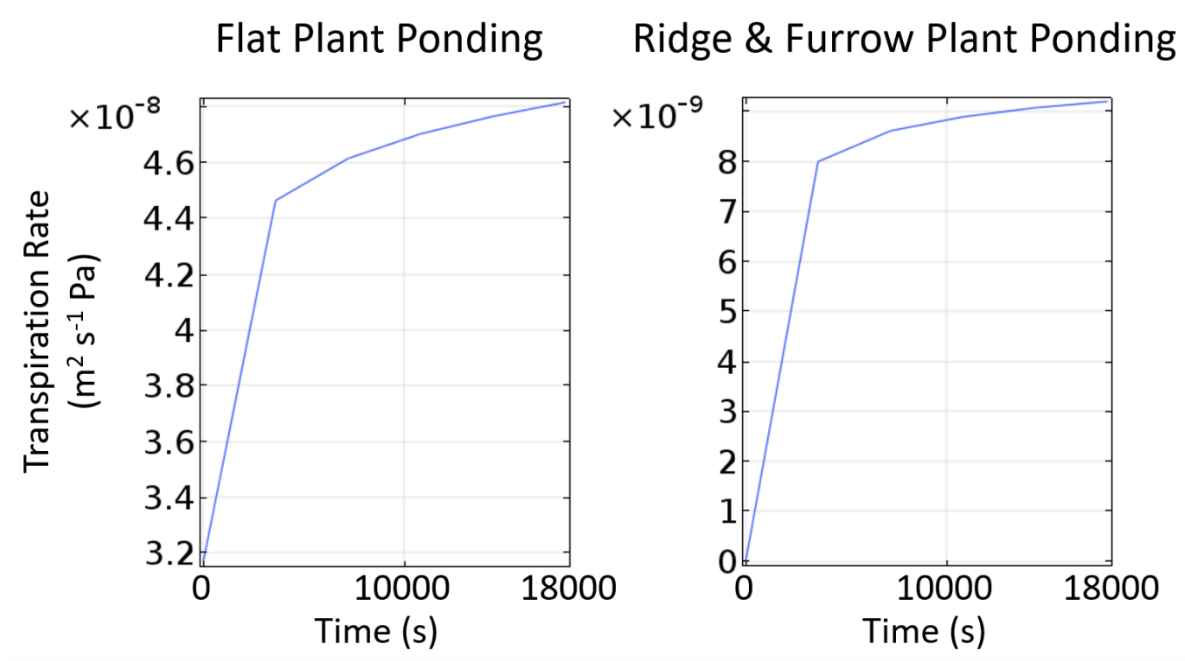

Appendix Figure A4. *Model derived estimates for transpiration in systems containing a plant and ponding with flat (left) or ridge and furrow (right) soil surfaces. The estimated transpiration rate in the flat geometry is approximately 80% greater than in the ridge and furrow geometry. This is possibly because of the volume of soil occupied by the 'root zone' in the flat geometry is greater and therefore there is a greater volume of liquid for the plant to draw in for transpiration.*

Appendix II - Chapter 4 Supplementary Material

Appendix II Tables & Figures

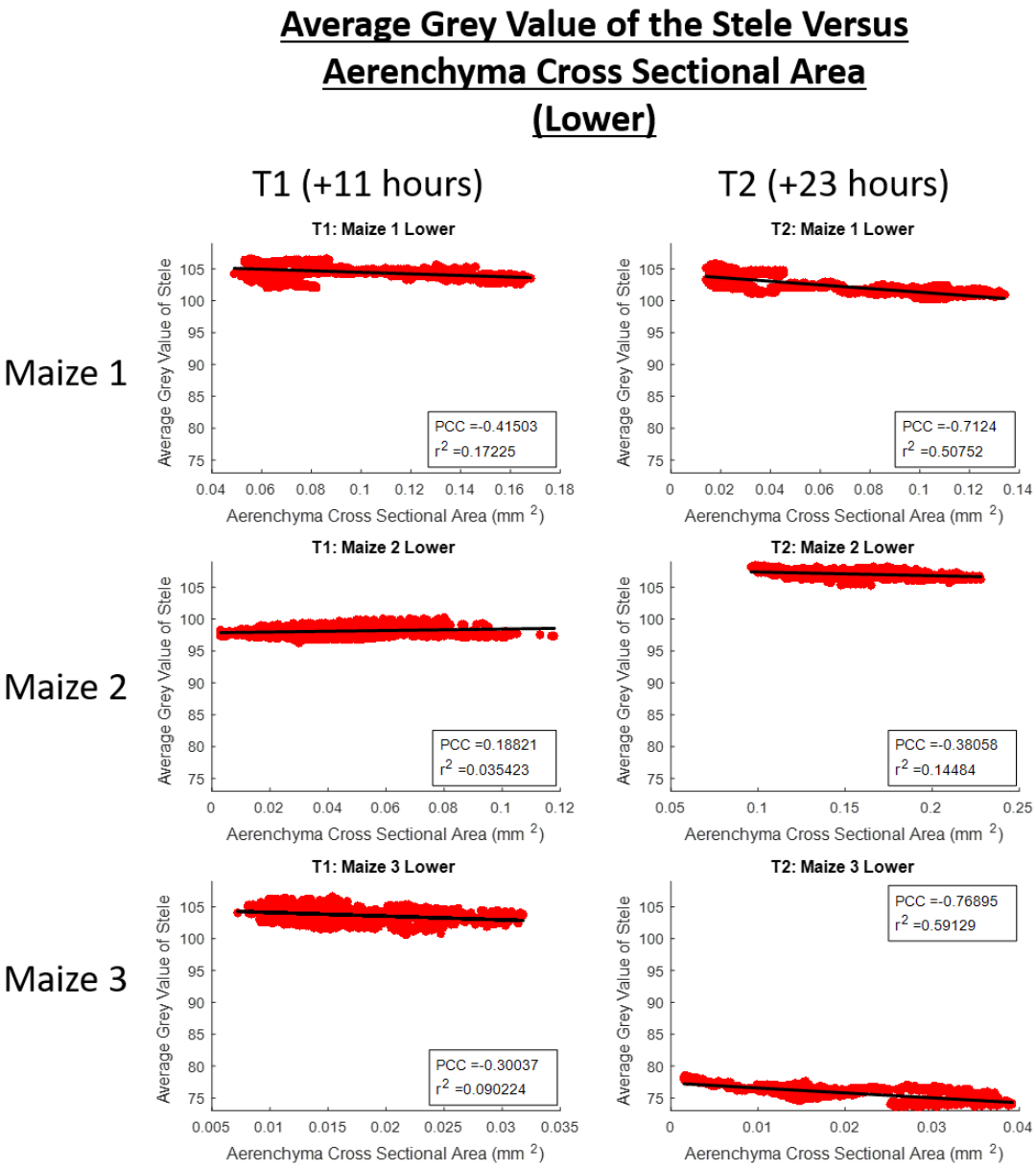

Appendix Figure A5. *Scatter plots of average grey value of root stele versus aerenchyma cross sectional area over depth for the lower imaged section of roots. Each individual data point on the scatter plots represents the average grey value of the stele and the aerenchyma cross sectional area recorded in a single slice from within the image stack (**Figure 38**). T1 is the time point for scans acquired 11 hours after the addition of contrast agent and T2 is the time point for scans acquired 23 hours after the addition of contrast agent. Maize 1, Maize 2 and Maize 3 are the names of each of the plant samples. The Pearson correlation coefficient, r^2 value and linear best fit lines are provided for each scatter plot.*

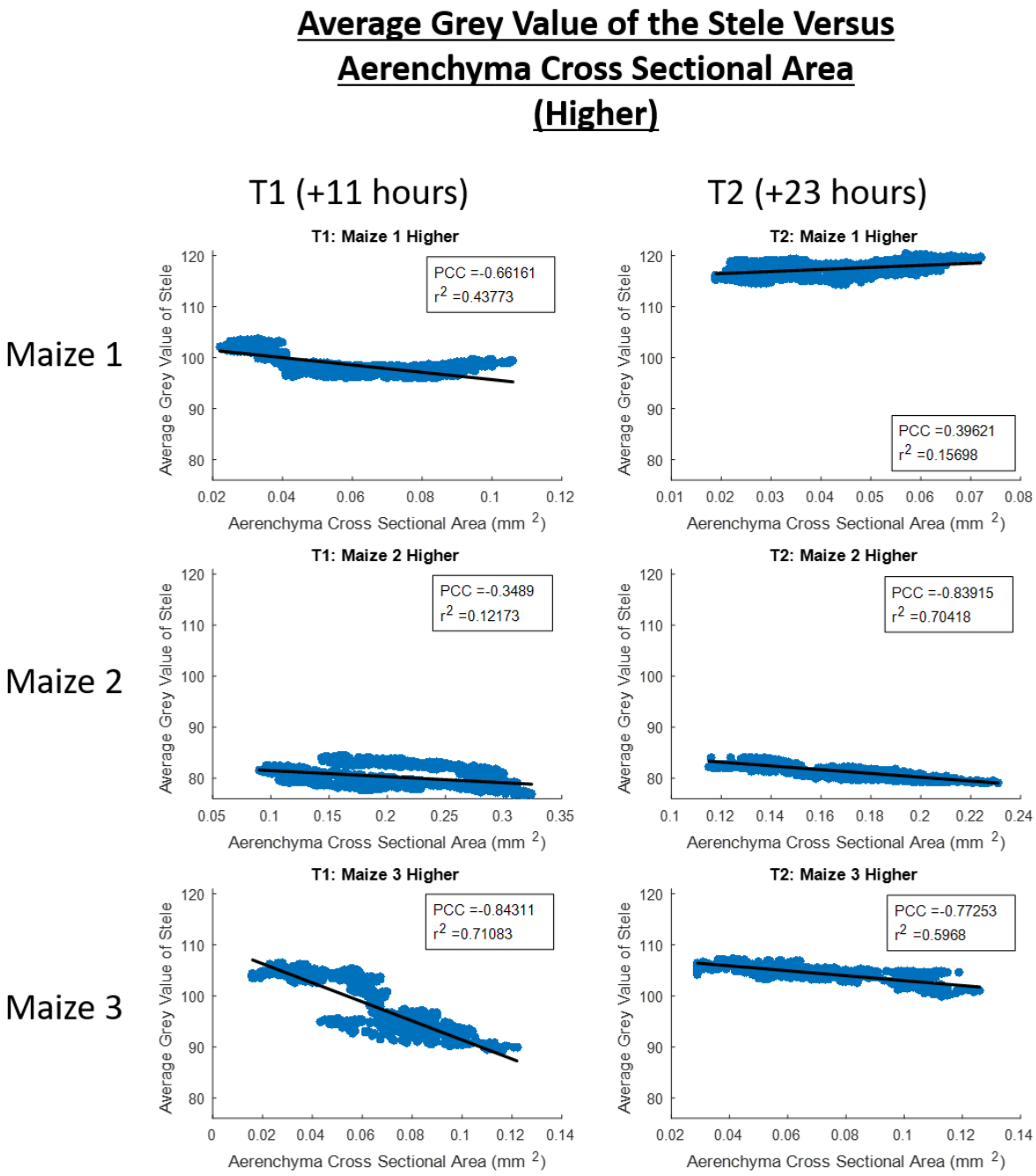

Appendix Figure A6. *Scatter plots of average grey value of root stele versus aerenchyma cross sectional area over depth for the higher imaged section of roots. Each individual data point on the scatter plots represents the average grey value of the stele and the aerenchyma cross sectional area recorded in a single slice from within the image stack (**Figure 38**). T1 is the time point for scans acquired 11 hours after the addition of contrast agent and T2 is the time point for scans acquired 23 hours after the addition of contrast agent. Maize 1, Maize 2 and Maize 3 are the names of each of the plant samples. The Pearson correlation coefficient, r^2 value and linear best fit lines are provided for each scatter plot.*

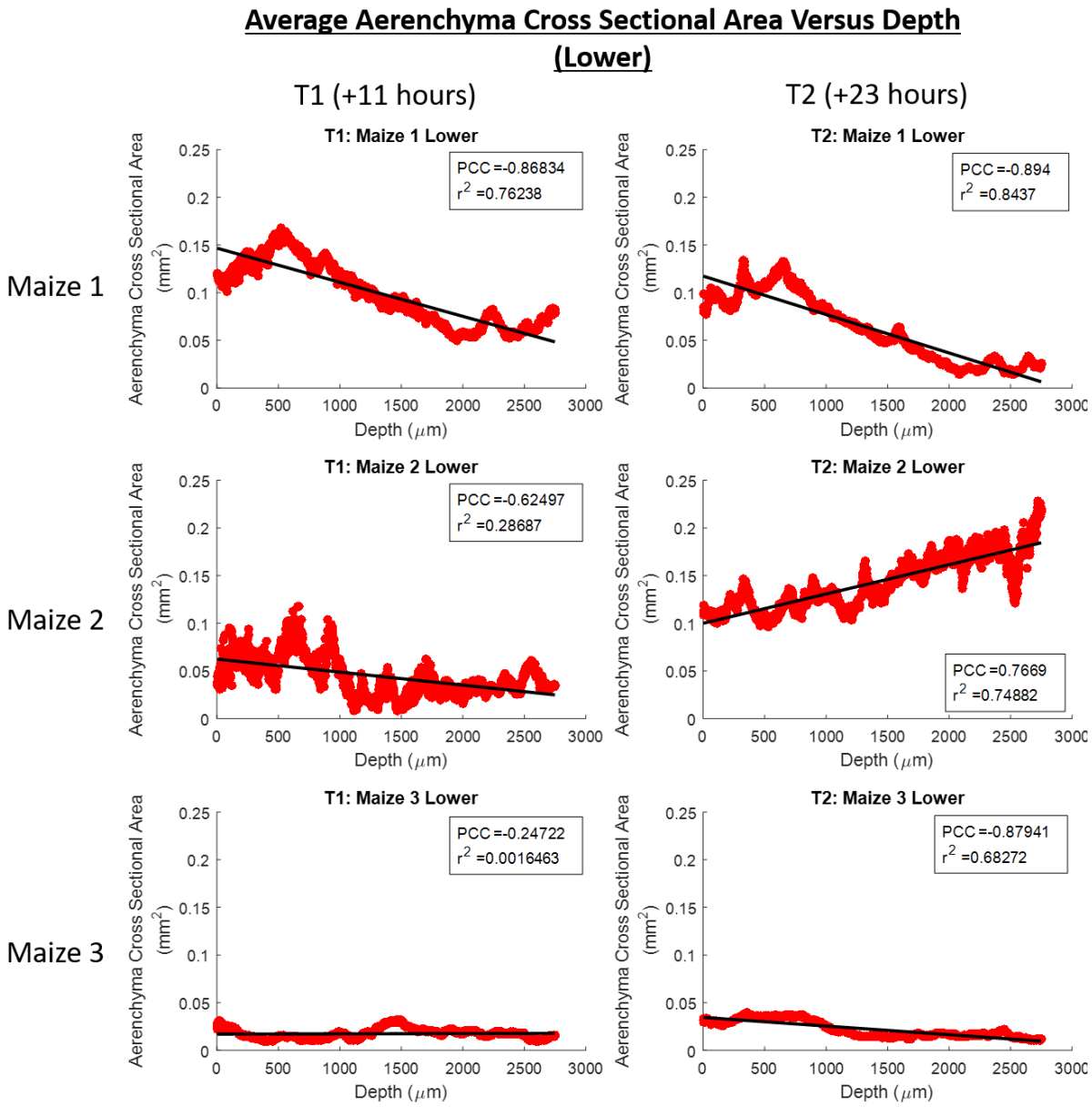

Appendix Figure A7. *Scatter plots of aerenchyma cross sectional area versus depth down the root growth channel for the lower imaged section of roots. T1 is the time point for scans acquired 11 hours after the addition of contrast agent and T2 is the time point for scans acquired 23 hours after the addition of contrast agent. Maize 1, Maize 2 and Maize 3 are the names of each of the plant samples. The Pearson correlation coefficient, r^2 value and linear best fit lines are provided for each scatter plot.*

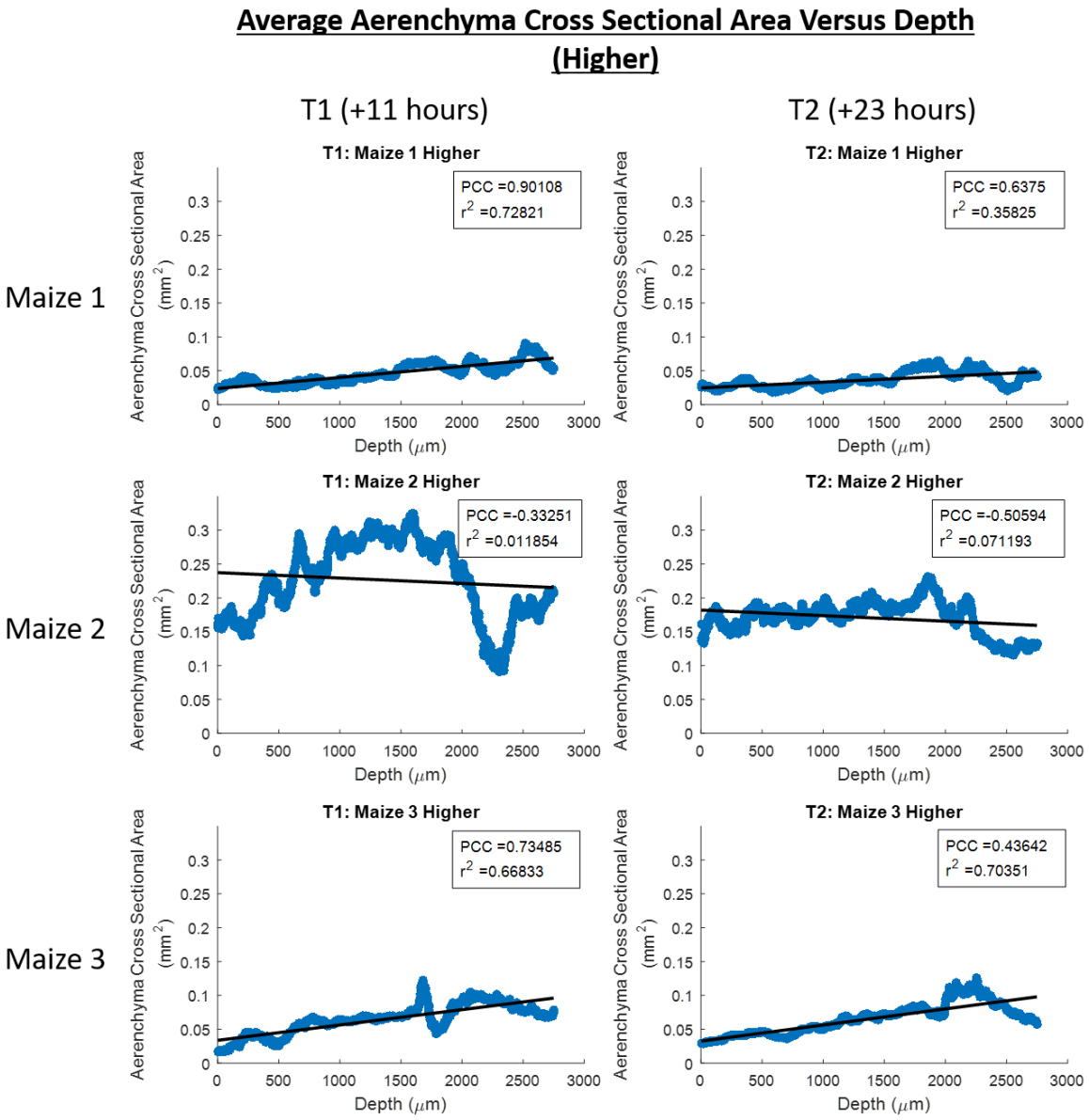

Appendix Figure A8. *Scatter plots of aerenchyma cross sectional area versus depth down the root growth channel for the higher imaged section of roots. T1 is the time point for scans acquired 11 hours after the addition of contrast agent and T2 is the time point for scans acquired 23 hours after the addition of contrast agent. Maize 1, Maize 2 and Maize 3 are the names of each of the plant samples. The Pearson correlation coefficient, r^2 value and linear best fit lines are provided for each scatter plot.*

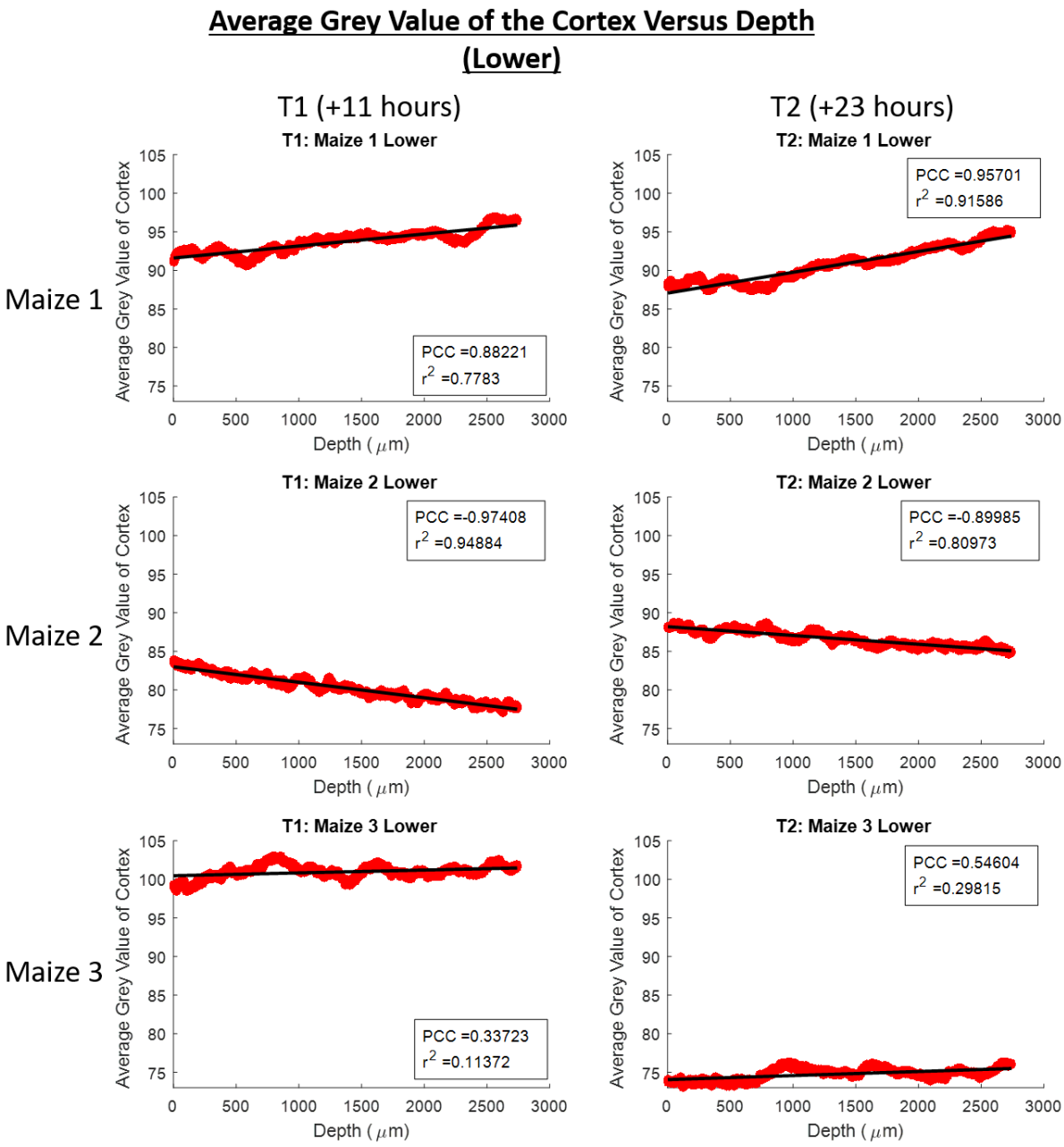

Appendix Figure A9. *Scatter plots of average cortex grey value versus depth down the root growth channel for the lower imaged section of roots. T1 is the time point for scans acquired 11 hours after the addition of contrast agent and T2 is the time point for scans acquired 23 hours after the addition of contrast agent. Maize 1, Maize 2 and Maize 3 are the names of each of the plant samples. The Pearson correlation coefficient, r^2 value and linear best fit lines are provided for each scatter plot.*

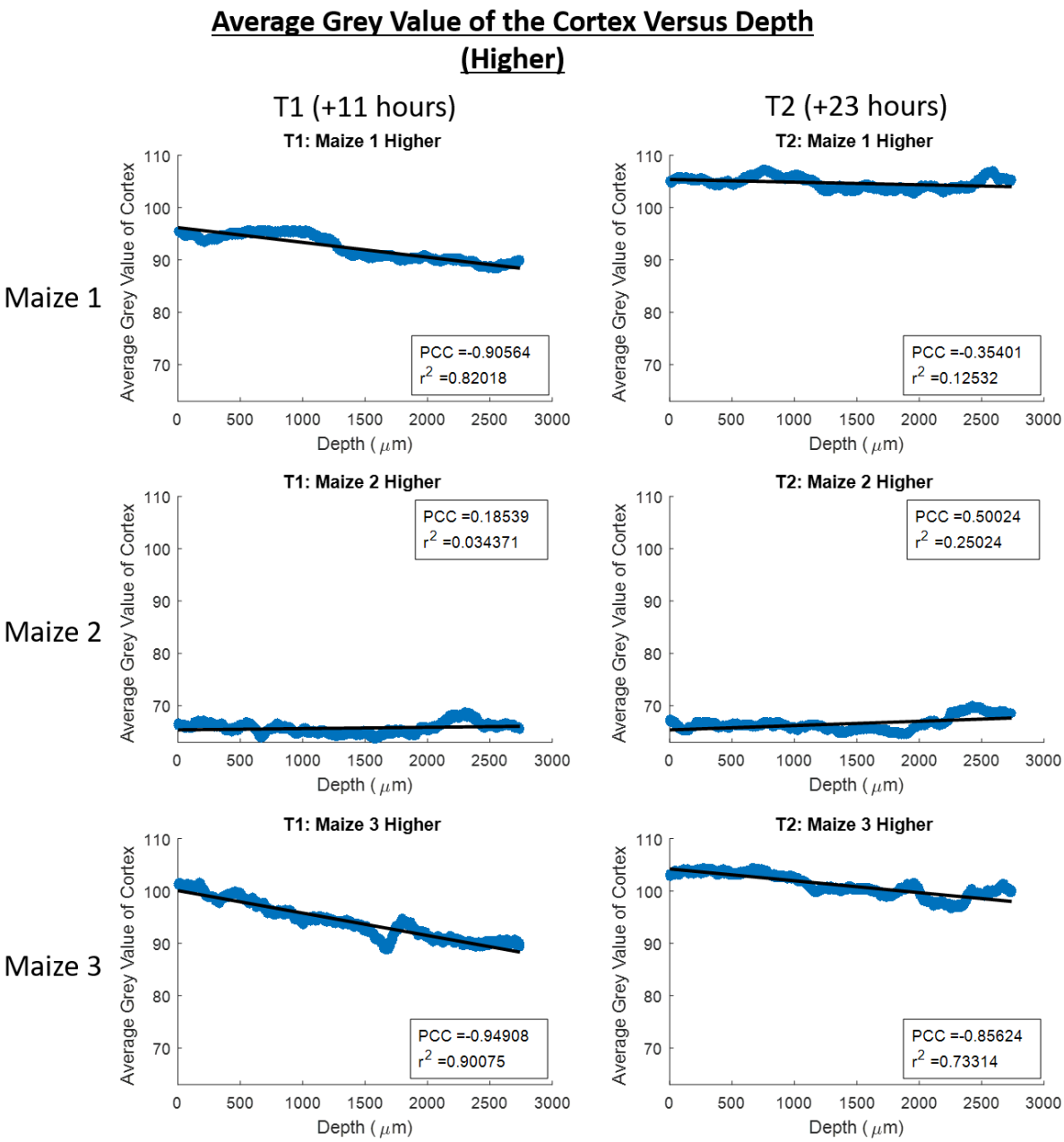

Appendix Figure A10. *Scatter plots of average cortex grey value versus depth down the root growth channel for the higher imaged section of roots. T1 is the time point for scans acquired 11 hours after the addition of contrast agent and T2 is the time point for scans acquired 23 hours after the addition of contrast agent. Maize 1, Maize 2 and Maize 3 are the names of each of the plant samples. The Pearson correlation coefficient, r^2 value and linear best fit lines are provided for each scatter plot.*

References

Abdul Razak HR, Shaffiq Said Rahmat SM, Md Saad WM. 2013. Effects of different tube potentials and iodine concentrations on image enhancement, contrast-to-noise ratio and noise in micro-CT images: a phantom study. *Quant Imaging Med Surg* **3**(5): 256-261. DOI: 10.3978/j.issn.2223-4292.2013.10.04

Ahn S, Jung SY, Lee JP, Kim HK, Lee SJ. 2010. Gold nanoparticle flow sensors designed for dynamic X-ray imaging in biofluids. *Acs Nano* **4**(7): 3753-3762. DOI: 10.1021/nn1003293

Ahn S, Jung SY, Lee SJ. 2013. Gold nanoparticle contrast agents in advanced X-ray imaging technologies. *Molecules* **18**(5): 5858-5890. DOI: 10.3390/molecules18055858

Alletto L, Coquet Y, Benoit P, Heddadj D, Barriuso E. 2010. Tillage management effects on pesticide fate in soils. A review. *Agronomy for Sustainable Development* **30**(2): 367-400. DOI: 10.1051/agro/2009018

Anderson NG, Butler AP, Scott NJ, Cook NJ, Butzer JS, Schleich N, Firsching M, Grasset R, de Ruiter N, Campbell M, et al. 2010. Spectroscopic (multi-energy) CT distinguishes iodine and barium contrast material in MICE. *Eur Radiol* **20**(9): 2126-2134. DOI: 10.1007/s00330-010-1768-9

Anderson S, Wang H, Peyton R, Gantzer C. 2003. Estimation of porosity and hydraulic conductivity from X-ray CT-measured solute breakthrough. *Geological Society, London, Special Publications* **215**(1): 135-149

Asli S, Neumann PM. 2009. Colloidal suspensions of clay or titanium dioxide nanoparticles can inhibit leaf growth and transpiration via physical effects on root water transport. *Plant Cell and Environment* **32**(5): 577-584. DOI: 10.1111/j.1365-3040.2009.01952.x

Aspelin P. 2006. Why choice of contrast medium matters. *European Radiology Supplements* **16**(4): D22-D27. DOI: 10.1007/s10406-006-0183-4

Attix FH. 2008. *Introduction to radiological physics and radiation dosimetry*. John Wiley & Sons

Babula P, Adam V, Opatrilova R, Zehnalek J, Havel L, Kizek R. 2008. Uncommon heavy metals, metalloids and their plant toxicity: a review. *Environmental Chemistry Letters* **6**(4): 189-213. DOI: 10.1007/s10311-008-0159-9

Balastre M, Argillier JF, Allain C, Foissy A. 2002. Role of polyelectrolyte dispersant in the settling behavior of barium sulphate suspension. *Colloids and Surfaces a-Physicochemical and Engineering Aspects* **211**(2-3): 145-156. DOI: 10.1016/S0927-7757(02)00240-6

Banti M, Zissis T, Anastasiadou-Partheniou E. 2011. Furrow Irrigation Advance Simulation Using a Surface–Subsurface Interaction Model. *Journal of Irrigation and Drainage Engineering* **137**(5): 304-314. DOI: doi:10.1061/(ASCE)IR.1943-4774.0000293

Barber SA. 1995. *Soil nutrient bioavailability: a mechanistic approach*. John Wiley & Sons

Barranco FT, Dawson HE, Christener JM, Honeyman BD. 1997. Influence of aqueous pH and ionic strength on the wettability of quartz in the presence of dense non-aqueous-phase liquids. *Environmental Science & Technology* **31**(3): 676-681. DOI: 10.1021/es960217m

Bear J. 2012. *Hydraulics of groundwater*. Courier Corporation

Benhamou N. 1989. Ultrastructural-study of galacturonic acid distribution in some pathogenic fungi using gold-complexed Aplysia-depilans gonad gectin. *Canadian Journal of Microbiology* **35**(3): 349-358. DOI: 10.1139/m89-054

Benhamou N, Gilboagarber N, Trudel J, Asselin A. 1988. A new lectin-gold complex for ultrastructural-localization of galacturonic acids. *Journal of Histochemistry & Cytochemistry* **36**(11): 1403-1411. DOI: 10.1177/36.11.3049790

Bergen JM, Recum HAv, Goodman TT, Massey AP, Pun SH. 2006. Gold nanoparticles as a versatile platform for optimizing physicochemical parameters for targeted drug delivery macromolecular bioscience. Volume 6, Issue 7. *Macromolecular Bioscience*

Blachar A, Federle MP, Dodson SF. 2001. Internal hernia: Clinical and imaging findings in 17 patients with emphasis on CT criteria. *Radiology* **218**(1): 68-74. DOI: 10.1148/radiology.218.1.r01ja5368

Blonder B, De Carlo F, Moore J, Rivers M, Enquist BJ. 2012. X-ray imaging of leaf venation networks. *New Phytologist* **196**(4): 1274-1282. DOI: 10.1111/j.1469-8137.2012.04355.x

Böhm W. 1979. *Methods of studying root systems*. Springer Verlag, Berlin. DOI: 10.1007/978-3-642-67282-8

Bolte S, Cordelieres FP. 2006. A guided tour into subcellular colocalization analysis in light microscopy. *Journal of Microscopy-Oxford* **224**: 213-232. DOI: 10.1111/j.1365-2818.2006.01706.x

Bontrager KL, Lampignano J. 2013. *Textbook of radiographic positioning and related anatomy*. Elsevier Health Sciences

Brunot F. 1933. The Toxicity of Osmium Tetroxide (Osmic Acid). *Journal of Industrial Hygiene* **15**: 136-143

Chate BK, Rana J. 2016. Smart irrigation system using Raspberry pi. *International Research Journal of Engineering and Technology (IRJET)* **3**(05): 247-249

Choudhury PN, Kumar V. 1980. The sensitivity of growth and yield of dwarf wheat to water-stress at 3 growth-stages. *Irrigation Science* **1**(4): 223-231

Clark DP, Ghaghada K, Moding EJ, Kirsch DG, Badea CT. 2013. In vivo characterization of tumor vasculature using iodine and gold nanoparticles and dual energy micro-CT. *Physics in Medicine and Biology* **58**(6): 1683-1704. DOI: 10.1088/0031-9155/58/6/1683

Clark LJ, Whalley WR, Leigh RA, Dexter AR, Barraclough PB. 1999. Evaluation of agar and agarose gels for studying mechanical impedance in rice roots. *Plant and Soil* **207**(1): 37-43

Clausnitzer V, Hopmans JW. 2000. Pore-scale measurements of solute breakthrough using microfocus X-ray computed tomography. *Water Resources Research* **36**(8): 2067-2079. DOI: 10.1029/2000wr900076

Conley DJ, Paerl HW, Howarth RW, Boesch DF, Seitzinger SP, Havens KE, Lancelot C, Likens GE. 2009. ECOLOGY Controlling Eutrophication: Nitrogen and Phosphorus. *Science* **323**(5917): 1014-1015. DOI: 10.1126/science.1167755

Cook S, Peacock M, Evans CD, Page SE, Whelan MJ, Gauci V, Kho LK. 2017. Quantifying tropical peatland dissolved organic carbon (DOC) using UV-visible spectroscopy. *Water Research* **115**: 229-235. DOI: 10.1016/j.watres.2017.02.059

Coursey CA, Nelson RC, Boll DT, Paulson EK, Ho LM, Neville AM, Marin D, Gupta RT, Schindera ST. 2010. Dual-energy multidetector CT: How does it work, what can it tell us, and when can we use it in abdominopelvic imaging? *Radiographics* **30**(4): 1037-1055. DOI: 10.1148/rg.304095175

Crank J, Nicolson P. 1996. A practical method for numerical evaluation of solutions of partial differential equations of the heat-conduction type. *Advances in Computational Mathematics* **6**(3-4): 207-226. DOI: Doi 10.1007/Bf02127704

Crush JR, Waller JE, Care DA. 2005. Root distribution and nitrate interception in eleven temperate forage grasses. *Grass and Forage Science* **60**(4): 385-392. DOI: 10.1111/j.1365-2494.2005.00488.x

Daly KR, Keyes SD, Masum S, Roose T. 2016. Image-based modelling of nutrient movement in and around the rhizosphere. *Journal of Experimental Botany* **67**(4): 1059-1070. DOI: 10.1093/jxb/erv544

Derera N, Marshall D, Balaam L. 1969. Genetic variability in root development in relation to drought tolerance in spring wheats. *Experimental Agriculture* **5**(4): 327-338

Dhondt S, Vanhaeren H, Van Loo D, Cnudde V, Inze D. 2010. Plant structure visualization by high-resolution X-ray computed tomography. *Trends in Plant Science* **15**(8): 419-422. DOI: 10.1016/j.tplants.2010.05.002

Diegoli S, Manciulea AL, Begum S, Jones IP, Lead JR, Preece JA. 2008. Interaction between manufactured gold nanoparticles and naturally occurring organic macromolecules. *Science of the Total Environment* **402**(1): 51-61. DOI: 10.1016/j.scitotenv.2008.04.023

Driessen P, Deckers J, Spaargaren O, Nachtergaele F. 2000. *Lecture notes on the major soils of the world*. Food and Agriculture Organization (FAO)

Duncan SJ, Daly KR, Sweeney P, Roose T. 2018a. Mathematical modelling of water and solute movement in ridge plant systems with dynamic ponding. *European Journal of Soil Science* **69**(2): 265-278. DOI: 10.1111/ejss.12503

Duncan SJ, Daly KR, Sweeney P, Roose T. 2018b. Mathematical modelling of water and solute movement in ridged versus flat planting systems. *European Journal of Soil Science* **69**(6): 967-979. DOI: 10.1111/ejss.12711

Duttweiler D, Nicholson H. 1983. *Environmental problems and issues of agricultural nonpoint source pollution [USA]*. Iowa State University Press, Iowa, USA.

Effersoe H, Rosenkilde P, Groth S, Jensen LI, Golman K. 1990. Measurement of renal-function with Iohexol - a comparison of Iohexol, Tc-99m-Dtpa, and Cr-51 Edta Clearance. *Investigative Radiology* **25**(7): 778-782. DOI: 10.1097/00004424-199007000-00005

EFSA. 2013. Scientific Opinion on the report of the FOCUS groundwater working group (FOCUS, 2009): assessment of lower tiers. *EFSA Journal* **11**(2): 3114. DOI: 10.2903/j.efsa.2013.3291

Evans DE. 2004. Aerenchyma formation. *New Phytologist* **161**(1): 35-49. DOI: 10.1046/j.1469-8137.2003.00907.x

Fahong W, Wang X, Sayre K. 2004. Comparison of conventional, flood irrigated, flat planting with furrow irrigated, raised bed planting for winter wheat in China. *Field Crops Research* **87**(1): 35-42. DOI: 10.1016/j.fcr.2003.09.003

Fan MS, Bai RQ, Zhao XF, Zhang JH. 2007. Aerenchyma formed under phosphorus deficiency contributes to the reduced root hydraulic conductivity in maize roots. *Journal of Integrative Plant Biology* **49**(5): 598-604. DOI: 10.1111/j.1744-7909.2007.00450.x

Feddes RA, Kabat P, Van Bakel P, Bronswijk J, Halbertsma J. 1988. Modelling soil water dynamics in the unsaturated zone—state of the art. *Journal of Hydrology* **100**(1): 69-111

Feddes RA, Kowalik P, Kolinskamalinka K, Zaradny H. 1976. Simulation of Field Water-Uptake by Plants Using a Soil-Water Dependent Root Extraction Function. *Journal of Hydrology* **31**(1-2): 13-26. DOI: 10.1016/0022-1694(76)90017-2

Federle MP, Chang PJ, Confer S, Ozgun B. 1998. Frequency and effects of extravasation of ionic and nonionic CT contrast media during rapid bolus injection. *Radiology* **206**(3): 637-640

Finch S, Samuel A, Lane GP. 2014. *Lockhart and Wiseman's Crop Husbandry Including Grassland*. Elsevier

Fischer HB. 1973. Longitudinal dispersion and turbulent mixing in open-channel flow. *Annual Review of Fluid Mechanics* **5**: 59-78. DOI: 10.1146/annurev.fl.05.010173.000423

Flannery BP, Deckman HW, Roberge WG, Damico KL. 1987. 3-dimensional X-ray microtomography. *Science* **237**(4821): 1439-1444. DOI: 10.1126/science.237.4821.1439

Fried L, Townsend K, Sklar M. 2013.). Adafruit library code for Raspberry Pi. Retrieved from: https://github.com/adafruit/Adafruit-Raspberry-Pi-Python-Code/tree/legacy [accessed on 01 August, 2018]

Gardner WR. 1991. Modeling water-uptake by roots. *Irrigation Science* **12**(3): 109-114

Gertz EW, Wisneski JA, Chiu D, Akin JR, Hu C. 1985. Clinical superiority of a new nonionic contrast agent (Iopamidol) for cardiac angiography. *Journal of the American College of Cardiology* **5**(2): 250-258. DOI: 10.1016/S0735-1097(85)80044-9

Geso M. 2007. Gold nanoparticles: a new X-ray contrast agent. *British Journal of Radiology* **80**(949): 64-65. DOI: 10.1259/bjr/28250432

Golshahi J, Nasri H, Gharipour M. 2014. Contrast-induced nephropathy; A literature review. *J Nephropathol* **3**(2): 51-56. DOI: 10.12860/jnp.2014.12

Griffith W. 1974. Osmium tetroxide and its applications. *Platinum Metals Review* **18**(3): 94-96

Guerrero JP, Pimentel LCG, Skaggs T, van Genuchten MT. 2009. Analytical solution of the advection–diffusion transport equation using a change-of-variable and integral transform technique. *International Journal of Heat and Mass Transfer* **52**(13): 3297-3304

Hainfeld JF, Slatkin DN, Focella TM, Smilowitz HM. 2006. Gold nanoparticles: a new X-ray contrast agent. *Br J Radiol* **79**(939): 248-253. DOI: 10.1259/bjr/13169882

Haiss W, Thanh NT, Aveyard J, Fernig DG. 2007. Determination of size and concentration of gold nanoparticles from UV-vis spectra. *Analytical Chemistry* **79**(11): 4215-4221. DOI: 10.1021/ac0702084

Haller C, Hizoh I. 2004. The cytotoxicity of iodinated radiocontrast agents on renal cells in vitro. *Investigative Radiology* **39**(3): 149-154. DOI: 10.1097/01.rli.0000113776.87762.49

Hanks RJ, Klute A, Bresler E. 1969. A numeric method for estimating infiltration, redistribution, drainage, and evaporation of water from soil. *Water Resources Research* **5**(5): 1064-1069. DOI: 10.1029/WR005i005p01064

Harper D 1992. What is eutrophication? *Eutrophication of Freshwaters*: Springer, 1-28.

Hasebroock KM, Serkova NJ. 2009. Toxicity of MRI and CT contrast agents. *Expert Opinion on Drug Metabolism & Toxicology* **5**(4): 403-416. DOI: 10.1517/17425250902873796

Hatfield JL, Allmaras RR, Rehm GW, Lowery B. 1998. Ridge tillage for corn and soybean production: environmental quality impacts. *Soil & Tillage Research* **48**(3): 145-154. DOI: 10.1016/S0167-1987(98)00141-X

Hauggaard-Nielsen H, Ambus P, Jensen ES. 2001. Temporal and spatial distribution of roots and competition for nitrogen in pea-barley intercrops - a field study employing P-32 technique. *Plant and Soil* **236**(1): 63-74. DOI: 10.1023/A:1011909414400

Heijs AWJ, Ritsema CJ, Dekker LW. 1996. Three-dimensional visualization of preferential flow patterns in two soils. *Geoderma* **70**(2-4): 101-116. DOI: 10.1016/0016-7061(95)00076-3

Heinrich MC, Kuhlmann MK, Grgic A, Heckmann M, Kramann B, Uder M. 2005. Cytotoxic effects of ionic high-osmolar, nonionic monomeric, and nonionic iso-osmolar dimeric iodinated contrast media on renal tubular cells in vitro. *Radiology* **235**(3): 843-849. DOI: 10.1148/radiol.2353040726

Henry A, Cal AJ, Batoto TC, Torres RO, Serraj R. 2012. Root attributes affecting water uptake of rice (Oryza sativa) under drought. *Journal of Experimental Botany* **63**(13): 4751-4763. DOI: 10.1093/jxb/ers150

Hostetler MJ, Stokes JJ, Murray RW. 1996. Infrared spectroscopy of three-dimensional self-assembled monolayers: N-alkanethiolate monolayers on gold cluster compounds. *Langmuir* **12**(15): 3604-3612. DOI: 10.1021/la960249n

Hotze EM, Phenrat T, Lowry GV. 2010. Nanoparticle aggregation: Challenges to understanding transport and reactivity in the environment. *Journal of Environmental Quality* **39**(6): 1909-1924. DOI: 10.2134/jeq2009.0462

Hu B, Henry A, Brown KM, Lynch JP. 2014. Root cortical aerenchyma inhibits radial nutrient transport in maize (Zea mays). *Annals of Botany* **113**(1): 181-189. DOI: 10.1093/aob/mct259

Huang WY, Uri ND. 1989. The Determination of an Optimal Policy for Protecting Ground-Water Quality. *Water Resources Bulletin* **25**(4): 775-782

Hut TP. 2019.). Raspberry Pi plant pot moisture sensor. Retrieved from: https://thepihut.com/blogs/raspberry-pi-tutorials/raspberry-pi-plant-pot-moisture-sensor-with-email-notification-tutorial [accessed on 01 August, 2018]

Ishak SN, Abd Malik NNN, Latiff NMA, Ghazali NE, Baharudin MA. 2017. Smart home garden irrigation system using Raspberry Pi. *2017 Ieee 13th Malaysia International Conference on Communications (Micc)*: 101-106

Jadhav S, Hambarde S. 2016. Android based Automated Irrigation System using Raspberry Pi. *International Journal of Science and Research* **5**(6): 2345-2351

Jaynes DB, Swan JB. 1999. Solute movement in uncropped ridge-tilled soil under natural rainfall. *Soil Science Society of America Journal* **63**(2): 264-269. DOI: 10.2136/sssaj1999.03615995006300020002x

Jokerst JV, Lobovkina T, Zare RN, Gambhir SS. 2011. Nanoparticle PEGylation for imaging and therapy. *Nanomedicine* **6**(4): 715-728. DOI: 10.2217/Nnm.11.19

Jost G, Pietsch H, Lengsfeld P, Hutter J, Sieber MA. 2010. The impact of the viscosity and osmolality of iodine contrast agents on renal elimination. *Investigative Radiology* **45**(5): 255-261. DOI: 10.1097/RLI.0b013e3181d4a036

Jost G, Pietsch H, Sommer J, Sandner P, Lengsfeld P, Seidensticker P, Lehr S, Hutter J, Sieber MA. 2009. Retention of iodine and expression of biomarkers for renal damage in the kidney after application of iodinated contrast media in rats. *Investigative Radiology* **44**(2): 114-123

Kaestner A, Schneebeli M, Graf F. 2006. Visualizing three-dimensional root networks using computed tomography. *Geoderma* **136**(1-2): 459-469. DOI: 10.1016/j.geoderma.2006.04.009

Kalender WA. 2006. X-ray computed tomography. *Physics in Medicine and Biology* **51**(13): R29-R43. DOI: 10.1088/0031-9155/51/13/R03

Karunakaran C, Lahlali R, Zhu N, Webb AM, Schmidt M, Fransishyn K, Belev G, Wysokinski T, Olson J, Cooper DML, et al. 2015. Factors influencing real time internal structural visualization and dynamic process monitoring in plants using synchrotron-based phase contrast X-ray imaging. *Scientific Reports* **5**. DOI: 10.1038/srep12119

Kavetski D, Binning P, Sloan S. 2001. Adaptive time stepping and error control in a mass conservative numerical solution of the mixed form of Richards equation. *Advances in Water Resources* **24**(6): 595-605

Kemmochi I, Maru H. 2004. Nondestructive discrimination of cabbage plants infected with verticillium wilt using contrast media and an X-ray apparatus. *Journal of the Japanese Society for Horticultural Science* **73**(5): 484-490

Kettering J, Ruidisch M, Gaviria C, Ok YS, Kuzyakov Y. 2013. Fate of fertilizer N-15 in intensive ridge cultivation with plastic mulching under a monsoon climate. *Nutrient Cycling in Agroecosystems* **95**(1): 57-72. DOI: 10.1007/s10705-012-9548-3

Keyes SD, Cooper L, Duncan S, Koebernick N, Fletcher DMM, Scotson CP, van Veelen A, Sinclair I, Roose T. 2017a. Measurement of micro-scale soil deformation around roots using four-dimensional synchrotron tomography and image correlation. *Journal of the Royal Society Interface* **14**(136). DOI: 10.1098/rsif.2017.0560

Keyes SD, Daly KR, Gostling NJ, Jones DL, Talboys P, Pinzer BR, Boardman R, Sinclair I, Marchant A, Roose T. 2013. High resolution synchrotron imaging of wheat root hairs growing in soil and image based modelling of phosphate uptake. *New Phytologist* **198**(4): 1023-1029. DOI: 10.1111/nph.12294

Keyes SD, Gostling NJ, Cheung JH, Roose T, Sinclair I, Marchant A. 2017b. The application of contrast media for in vivo feature enhancement in X-ray Computed Tomography of soil-grown plant roots. *Microscopy and Microanalysis*: 1-48

Kim J, Lawler DF. 2005. Characteristics of zeta potential distribution in silica particles. *Bulletin of the Korean Chemical Society* **26**(7): 1083-1089

Kim T, Lee CH, Joo SW, Lee K. 2008. Kinetics of gold nanoparticle aggregation: Experiments and modeling. *Journal of Colloid and Interface Science* **318**(2): 238-243. DOI: 10.1016/j.jcis.2007.10.029

Kim T, Lee K, Gong MS, Joo SW. 2005. Control of gold nanoparticle aggregates by manipulation of interparticle interaction. *Langmuir* **21**(21): 9524-9528. DOI: 10.1021/la0504560

Kinsella JM, Jimenez RE, Karmali PP, Rush AM, Kotamraju VR, Gianneschi NC, Ruoslahti E, Stupack D, Sailor MJ. 2011. X-ray computed tomography imaging of breast cancer by using targeted peptide-labeled bismuth sulfide nanoparticles. *Angewandte Chemie-International Edition* **50**(51): 12308-12311. DOI: 10.1002/anie.201104507

Koch A, Meunier F, Vanderborght J, Garre S, Pohlmeier A, Javaux M. 2019. Functional-structural root-system model validation using a soil MRI experiment. *Journal of Experimental Botany* **70**(10): 2797-2809. DOI: 10.1093/jxb/erz060

Koestel J, Larsbo M. 2014. Imaging and quantification of preferential solute transport in soil macropores. *Water Resources Research* **50**(5): 4357-4378. DOI: 10.1002/2014wr015351

Kosmulski M. 2009. Compilation of PZC and IEP of sparingly soluble metal oxides and hydroxides from literature. *Advances in Colloid and Interface Science* **152**(1-2): 14-25. DOI: 10.1016/j.cis.2009.08.003

Kramer PJ. 1983. Drought resistance in crops with special emphasis on rice - International Rice Research Institute. *American Scientist* **71**(4): 418-418

Kung K 1988. Ground truth about water flow pattern in a sandy soil and its influences on solute sampling and transport modeling. *International conference and workshop on the validation of flow and transport models for the unsaturated zone*. 224-230

Lee N, Choi SH, Hyeon T. 2013. Nano-sized CT contrast agents. *Adv Mater* **25**(19): 2641-2660. DOI: 10.1002/adma.201300081

Legland D, Arganda-Carreras I, Andrey P. 2016. MorphoLibJ: integrated library and plugins for mathematical morphology with ImageJ. *Bioinformatics* **32**(22): 3532-3534. DOI: 10.1093/bioinformatics/btw413

Leistra M, Boesten JJTI. 2010. Measurement and computation of movement of bromide ions and carbofuran in ridged humic-sandy soil. *Archives of Environmental Contamination and Toxicology* **59**(1): 39-48. DOI: 10.1007/s00244-009-9442-4

Li CH, Lee CK. 1993. Minimum cross entropy thresholding. *Pattern Recognition* **26**(4): 617-625. DOI: 10.1016/0031-3203(93)90115-D

Li CH, Ma BL, Zhang TQ. 2002. Soil bulk density effects on soil microbial populations and enzyme activities during the growth of maize (Zea mays L.) planted in large pots under field exposure. *Canadian Journal of Soil Science* **82**(2): 147-154. DOI: Doi 10.4141/S01-026

Li CH, Tam PKS. 1998. An iterative algorithm for minimum cross entropy thresholding. *Pattern Recognition Letters* **19**(8): 771-776. DOI: 10.1016/S0167-8655(98)00057-9

Li M, Brasseur JG, Kern MK, Dodds WJ. 1992. Viscosity measurements of barium sulfate mixtures for use in motility studies of the pharynx and esophagus. *Dysphagia* **7**(1): 17-30

Li S, Zuo Q, Wang XY, Ma WW, Jin XX, Shi JC, Ben-Gal A. 2017. Characterizing roots and water uptake in a ground cover rice production system. *Plos One* **12**(7). DOI: 10.1371/journal.pone.0180713

Li XY, Gong JD. 2002. Effects of different ridge : furrow ratios and supplemental irrigation on crop production in ridge and furrow rainfall harvesting system with mulches. *Agricultural Water Management* **54**(3): 243-254. DOI: Doi 10.1016/S0378-3774(01)00172-X

Lusic H, Grinstaff MW. 2013. X-ray-computed tomography contrast agents. *Chemical Reviews* **113**(3): 1641-1666. DOI: 10.1021/cr200358s

Mariotti M, Masoni A, Ercoli L, Arduini I. 2015. Nitrogen leaching and residual effect of barley/field bean intercropping. *Plant Soil and Environment* **61**(2): 60-65. DOI: 10.17221/832/2014-Pse

Mattrey RF, Aguirre DA. 2003. Advances in contrast media research. *Academic Radiology* **10**(12): 1450-1460. DOI: 10.1016/S1076-6332(03)00642-1

McClellan JA 2001. Osmium tetroxide modification and the study of DNA-protein interactions. *DNA-Protein Interactions*: Springer, 121-134.

Miller WP, Miller DM. 1987. A Micro-Pipette Method for Soil Mechanical Analysis. *Communications in Soil Science and Plant Analysis* **18**(1): 1-15. DOI: Doi 10.1080/00103628709367799

Milleret R, Le Bayon RC, Lamy F, Gobat JM, Boivin P. 2009. Impact of roots, mycorrhizas and earthworms on soil physical properties as assessed by shrinkage analysis. *Journal of Hydrology* **373**(3-4): 499-507. DOI: 10.1016/j.jhydrol.2009.05.013

Monteith JL. 1965. Evaporation and environment. *Symp Soc Exp Biol* **19**: 205-234

Mooney SJ, Pridmore TP, Helliwell J, Bennett MJ. 2012. Developing X-ray computed tomography to non-invasively image 3-D root systems architecture in soil. *Plant and Soil* **352**(1-2): 1-22. DOI: 10.1007/s11104-011-1039-9

Morin J, Benyamini Y. 1977. Rainfall infiltration into bare soils. *Water Resources Research* **13**(5): 813-817. DOI: 10.1029/WR013i005p00813

Moritsuka N, Izawa G, Katsura K, Matsui N. 2015. Simple method for measuring soil sand content by nylon mesh sieving. *Soil Science and Plant Nutrition* **61**(3): 501-505. DOI: 10.1080/00380768.2015.1016864

Nowack B, Bucheli TD. 2007. Occurrence, behavior and effects of nanoparticles in the environment. *Environmental Pollution* **150**(1): 5-22. DOI: 10.1016/j.envpol.2007.06.006

Nye PH, Tinker PB. 1977. *Solute movement in the soil-root system*. Univ of California Press

Ollion J, Cochennec J, Loll F, Escude C, Boudier T. 2013. TANGO: a generic tool for high-throughput 3D image analysis for studying nuclear organization. *Bioinformatics* **29**(14): 1840-1841. DOI: 10.1093/bioinformatics/btt276

Pahlsson AMB. 1989. Toxicity of heavy-metals (Zn, Cu, Cd, Pb) to vascular plants - a literature-review. *Water Air and Soil Pollution* **47**(3-4): 287-319. DOI: 10.1007/Bf00279329

Payvandi S, Daly KR, Jones DL, Talboys P, Zygalakis KC, Roose T. 2014. A mathematical model of water and nutrient transport in xylem vessels of a wheat plant. *Bulletin of Mathematical Biology* **76**(3): 566-596. DOI: 10.1007/s11538-013-9932-4

Peacock M, Freeman C, Gauci V, Lebron I, Evans CD. 2015. Investigations of freezing and cold storage for the analysis of peatland dissolved organic carbon (DOC) and absorbance properties. *Environmental Science-Processes & Impacts* **17**(7): 1290-1301. DOI: 10.1039/c5em00126a

Peth S, Chenu C, Leblond N, Mordhorst A, Garnier P, Nunan N, Pot V, Ogurreck M, Beckmann F. 2014. Localization of soil organic matter in soil aggregates using synchrotron-based X-ray microtomography. *Soil Biology & Biochemistry* **78**: 189-194. DOI: 10.1016/j.soilbio.2014.07.024

Philip J. 1957. The theory of infiltration: 1. The infiltration equation and its solution. *Soil science* **83**(5): 345-358

Philip JR 1969. Theory of infiltration. *Advances in hydroscience*: Elsevier, 215-296.

Phillips JD. 2007. Development of texture contrast soils by a combination of bioturbation and translocation. *Catena* **70**(1): 92-104. DOI: 10.1016/j.catena.2006.08.002

Pieper M, Aman S, Tomas J. 2012. Agglomeration kinetics of submicron barium sulfate precipitates. *Chemical Engineering Science* **77**: 228-234. DOI: 10.1016/j.ces.2011.12.043

Power J, Broadbent F 1989. Proper accounting for N in cropping systems. *Developments in Agricultural and Managed Forest Ecology*: Elsevier, 159-181.

Rabin O, Perez JM, Grimm J, Wojtkiewicz G, Weissleder R. 2006. An X-ray computed tomography imaging agent based on long-circulating bismuth sulphide nanoparticles. *Nature Materials* **5**(2): 118-122. DOI: 10.1038/nmat1571

Rawlins BG, Wragg J, Reinhard C, Atwood RC, Houston A, Lark RM, Rudolph S. 2016. Three-dimensional soil organic matter distribution, accessibility and microbial respiration in macroaggregates using osmium staining and synchrotron X-ray computed tomography. *Soil* **2**(4): 659-671. DOI: 10.5194/soil-2-659-2016

Reddy K, Doraiswamy L. 1967. Estimating liquid diffusivity. *Industrial & Engineering Chemistry Fundamentals* **6**(1): 77-79

Rein M. 1993. Phenomena of liquid-drop impact on solid and liquid surfaces. *Fluid Dynamics Research* **12**(2): 61-93. DOI: 10.1016/0169-5983(93)90106-K

Ressler D, Horton R, Baker J, Kaspar T. 1997. Testing a nitrogen fertilizer applicator designed to reduce leaching losses. *Applied Engineering in Agriculture* **13**(3): 345-350. DOI: 10.13031/2013.21617

Richards LA. 1931. Capillary conduction of liquids through porous mediums. *Journal of Applied Physics* **1**(5): 318-333

Robinson D. 1999. A comparison of soil-water distribution under ridge and bed cultivated potatoes. *Agricultural Water Management* **42**(2): 189-204. DOI: 10.1016/S0378-3774(99)00031-1

Roose T, Fowler AC. 2004. A model for water uptake by plant roots. *Journal of Theoretical Biology* **228**(2): 155-171. DOI: 10.1016/j.jtbi.2003.12.012

Roose T, Keyes SD, Daly KR, Carminati A, Otten W, Vetterlein D, Peth S. 2016. Challenges in imaging and predictive modeling of rhizosphere processes. *Plant and Soil* **407**(1-2): 9-38. DOI: 10.1007/s11104-016-2872-7

Roose T, Schnepf A. 2008. Mathematical models of plant-soil interaction. *Philosophical Transactions of the Royal Society a-Mathematical Physical and Engineering Sciences* **366**(1885): 4597-4611. DOI: 10.1098/rsta.2008.0198

Rueden CT, Schindelin J, Hiner MC, DeZonia BE, Walter AE, Arena ET, Eliceiri KW. 2017. ImageJ2: ImageJ for the next generation of scientific image data. *Bmc Bioinformatics* **18**. DOI: 10.1186/s12859-017-1934-z

Ruiz S, Koebernick N, Duncan S, Fletcher DM, Scotson C, Boghi A, Marin M, Bengough AG, George TS, Brown LK, et al. 2020. Significance of root hairs at the field scale - modelling root water and phosphorus uptake under different field conditions. *Plant and Soil* **447**(1-2): 281-304. DOI: 10.1007/s11104-019-04308-2

Ruiz S, Or D, Schymanski SJ. 2015. Soil penetration by earthworms and plant roots-mechanical energetics of bioturbation of compacted soils. *Plos One* **10**(6). DOI: 10.1371/journal.pone.0128914

Sabo-Attwood T, Unrine JM, Stone JW, Murphy CJ, Ghoshroy S, Blom D, Bertsch PM, Newman LA. 2012. Uptake, distribution and toxicity of gold nanoparticles in tobacco (Nicotiana xanthi) seedlings. *Nanotoxicology* **6**(4): 353-360. DOI: 10.3109/17435390.2011.579631

Sammartino S, Lissy AS, Bogner C, Van den Bogaert R, Capowiez Y, Ruy S, Cornu S. 2015. Identifying the functional macropore network related to preferential flow in structured soils. *Vadose Zone Journal* **14**(10). DOI: 10.2136/vzj2015.05.0070

Schild HH, Kuhl CK, Hubner-Steiner U, Bohm I, Speck U. 2006. Adverse events after unenhanced and monomeric and dimeric contrast-enhanced CT: A prospective randomized controlled trial. *Radiology* **240**(1): 56-64. DOI: 10.1148/radiol.2393050560

Schindelin J, Arganda-Carreras I, Frise E, Kaynig V, Longair M, Pietzsch T, Preibisch S, Rueden C, Saalfeld S, Schmid B, et al. 2012. Fiji: an open-source platform for biological-image analysis. *Nature Methods* **9**(7): 676-682. DOI: 10.1038/Nmeth.2019

Schnaar G, Brusseau ML. 2005. Pore-scale characterization of organic immiscible-liquid morphology in natural porous media using synchrotron X-ray microtomography. *Environmental Science & Technology* **39**(21): 8403-8410. DOI: 10.1021/es058370

Schroder N, Javaux M, Vanderborght J, Steffen B, Vereecken H. 2012. Effect of root water and solute uptake on apparent soil dispersivity: A simulation study. *Vadose Zone Journal* **11**(3). DOI: 10.2136/vzj2012.0009

Scotson CP, Duncan SJ, Williams KA, Ruiz SA, Roose T. 2020a. X-ray computed tomography imaging of solute movement through ridged and flat plant systems. *European Journal of Soil Science*

Scotson CP, Munoz-Hernando M, Duncan SJ, Ruiz SA, Keyes SD, van Veelen A, Dunlop IE, Roose T. 2019. Stabilizing gold nanoparticles for use in X-ray computed tomography imaging of soil systems. *Royal Society Open Science* **6**(10). DOI: 10.1098/rsos.190769

Scotson CP, van Veelen A, Williams KA, Koebernick N, Fletcher DM, Roose T. 2020b. Developing a system for in vivo imaging of maize roots containing iodinated contrast media in soil using synchrotron XCT and XRF. *Plant and Soil*: 1-19

Sendeski MM. 2011. Pathophysiology of renal tissue damage by iodinated contrast media. *Clinical and Experimental Pharmacology and Physiology* **38**(5): 292-299. DOI: 10.1111/j.1440-1681.2011.05503.x

Shalygo NV, Mock HP, Averina NG, Grimm B. 1998. Photodynamic action of uroporphyrin and protochlorophyllide in greening barley leaves treated with cesium chloride. *Journal of Photochemistry and Photobiology B-Biology* **42**(2): 151-158. DOI: 10.1016/S1011-1344(98)00067-0

Sinet M, Muffatjoly M, Bendaace T, Pocidalo JJ. 1985. Maintaining blood-pH at 7.4 during hypothermia has no significant effect on work of the isolated rat-heart. *Anesthesiology* **62**(5): 582-587. DOI: 10.1097/00000542-198505000-00007

Singh J, Daftary A. 2008. Iodinated contrast media and their adverse reactions. *J Nucl Med Technol* **36**(2): 69-74; quiz 76-67. DOI: 10.2967/jnmt.107.047621

Singh S, Gupta AK, Kaur N. 2012. Differential responses of antioxidative defence system to long-term field drought in wheat (Triticum aestivum L.) genotypes differing in drought tolerance. *Journal of Agronomy and Crop Science* **198**(3): 185-195. DOI: 10.1111/j.1439-037X.2011.00497.x

Sistrom CL, Gay SB, Peffley L. 1991. Extravasation of Iopamidol and Iohexol during contrast-enhanced CT - report of 28 cases. *Radiology* **180**(3): 707-710

Smelt JH, Schut CJ, Dekker A, Leistra M. 1981. Movement and conversion of aldicarb and its oxidation-products in potato fields. *Netherlands Journal of Plant Pathology* **87**(5): 177-191. DOI: 10.1007/Bf01976984

Smith H, Puddington I. 1960. Spherical agglomeration of barium sulphate. *Canadian Journal of Chemistry* **38**(10): 1911-1916

Smith IC, Carson BL, Ferguson TL. 1974. Osmium: an appraisal of environmental exposure. *Environmental health perspectives* **8**: 201-213

Soane BD. 1990. The role of organic-matter in soil compactibility - a review of some practical aspects. *Soil & Tillage Research* **16**(1-2): 179-201. DOI: 10.1016/0167-1987(90)90029-D

Sole VA, Papillon E, Cotte M, Walter P, Susini J. 2007. A multiplatform code for the analysis of energy-dispersive X-ray fluorescence spectra. *Spectrochimica Acta Part B-Atomic Spectroscopy* **62**(1): 63-68. DOI: 10.1016/j.sab.2006.12.002

Somma F, Hopmans JW, Clausnitzer V. 1998. Transient three-dimensional modeling of soil water and solute transport with simultaneous root growth, root water and nutrient uptake. *Plant and Soil* **202**(2): 281-293. DOI: 10.1023/A:1004378602378

Sperling RA, Parak WJ. 2010. Surface modification, functionalization and bioconjugation of colloidal inorganic nanoparticles. *Philosophical Transactions of the Royal Society a-Mathematical Physical and Engineering Sciences* **368**(1915): 1333-1383. DOI: 10.1098/rsta.2009.0273

Sperling RA, Rivera gil P, Zhang F, Zanella M, Parak WJ. 2008. Biological applications of gold nanoparticles. *Chemical Society Reviews* **37**(9): 1896-1908. DOI: 10.1039/b712170a

Street RL, Watters GZ, Vennard JK. 1996. *Elementary fluid mechanics*. J. Wiley

Sun IC, Eun DK, Na JH, Lee S, Kim IJ, Youn IC, Ko CY, Kim HS, Lim D, Choi K, et al. 2009. Heparin-coated gold nanoparticles for liver-specific CT imaging. *Chemistry* **15**(48): 13341-13347. DOI: 10.1002/chem.200902344

Taina IA, Heck RJ, Elliot TR. 2008. Application of X-ray computed tomography to soil science: A literature review. *Canadian Journal of Soil Science* **88**(1): 1-20

Taylor AF, Rylott EL, Anderson CWN, Bruce NC. 2014. Investigating the toxicity, uptake, nanoparticle formation and genetic response of plants to gold. *Plos One* **9**(4). DOI: 10.1371/journal.pone.0093793

Taylor GI. 1954. The dispersion of matter in turbulent flow through a pipe. *Proc. R. Soc. Lond. A* **223**(1155): 446-468

Thompson MV, Holbrook NM. 2004. Root-gel interactions and the root waving behavior of Arabidopsis. *Plant Physiology* **135**(3): 1822-1837. DOI: 10.1104/pp.104.040881

Tian Y, Su DR, Li FM, Li XL. 2003. Effect of rainwater harvesting with ridge and furrow on yield of potato in semiarid areas. *Field Crops Research* **84**(3): 385-391. DOI: 10.1016/S0378-4290(03)00118-7

Tinker PB. 1976. Roots and water - transport of water to plant roots in soil. *Philosophical Transactions of the Royal Society of London Series B-Biological Sciences* **273**(927): 445-461. DOI: 10.1098/rstb.1976.0024

Tinker PB, Nye PH. 2000. *Solute movement in the rhizosphere*. Oxford University Press

Tisdall JM, Hodgson AS. 1990. Ridge tillage in Australia - a review. *Soil & Tillage Research* **18**(2-3): 127-144. DOI: 10.1016/0167-1987(90)90055-I

Tourinho PS, van Gestel CAM, Lofts S, Svendsen C, Soares AMVM, Loureiro S. 2012. Metal-based nanoparticles in soil: Fate, behavior, and effects on soil invertebrates. *Environmental Toxicology and Chemistry* **31**(8): 1679-1692. DOI: 10.1002/etc.1880

Uga Y, Okuno K, Yano M. 2011. Dro1, a major QTL involved in deep rooting of rice under upland field conditions. *Journal of Experimental Botany* **62**(8): 2485-2494. DOI: 10.1093/jxb/erq429

Uga Y, Sugimoto K, Ogawa S, Rane J, Ishitani M, Hara N, Kitomi Y, Inukai Y, Ono K, Kanno N, et al. 2013. Control of root system architecture by DEEPER ROOTING 1 increases rice yield under drought conditions. *Nature Genetics* **45**(9): 1097. DOI: 10.1038/ng.2725

van Genuchten MT. 1980. A Closed-form Equation for Predicting the Hydraulic Conductivity of Unsaturated Soils1. *Soil Sci. Soc. Am. J.* **44**(5): 892-898. DOI: 10.2136/sssaj1980.03615995004400050002x

vanderWerf HMG. 1996. Assessing the impact of pesticides on the environment. *Agriculture Ecosystems & Environment* **60**(2-3): 81-96. DOI: 10.1016/S0167-8809(96)01096-1

Wang CL, Cohan RH, Ellis JH, Adusumilli S, Dunnick NR. 2007. Frequency, management, and outcome of extravasation of nonionic iodinated contrast medium in 69 657 intravenous injections. *Radiology* **243**(1): 80-87. DOI: 10.1148/radiol.2431060554

Wildenschild D, Hopmans JW, Vaz CMP, Rivers ML, Rikard D, Christensen BSB. 2002. Using X-ray computed tomography in hydrology: systems, resolutions, and limitations. *Journal of Hydrology* **267**(3-4): 285-297. DOI: 10.1016/S0022-1694(02)00157-9

Wooding R. 1968. Steady infiltration from a shallow circular pond. *Water Resources Research* **4**(6): 1259-1273

Xiong L, Zhu JK. 2002. Molecular and genetic aspects of plant responses to osmotic stress. *Plant Cell and Environment* **25**(2): 131-139. DOI: 10.1046/j.1365-3040.2002.00782.x

Xu CJ, Tung GA, Sun SH. 2008. Size and concentration effect of gold nanoparticles on X-ray attenuation as measured on computed tomography. *Chemistry of Materials* **20**(13): 4167-4169. DOI: 10.1021/cm8008418

Yang B, Blackwell PS, Nicholson DF. 1996. A numerical model of heat and water movement in furrow-sown water repellent sandy soils. *Water Resources Research* **32**(10): 3051-3061

Yu SB, Watson AD. 1999. Metal-based X-ray contrast media. *Chemical Reviews* **99**(9): 2353-2377. DOI: 10.1021/cr980441p

Zakaria HM, Shah A, Konieczny M, Hoffmann JA, Nijdam AJ, Reeves ME. 2013. Small molecule- and amino acid-induced aggregation of gold nanoparticles. *Langmuir* **29**(25): 7661-7673. DOI: 10.1021/la400582v

Zappala S, Helliwell JR, Tracy SR, Mairhofer S, Sturrock CJ, Pridmore T, Bennett M, Mooney SJ. 2013. Effects of X-ray dose on rhizosphere studies using X-ray computed tomography. *Plos One* **8**(6). DOI: 10.1371/journal.pone.0067250

Zazueta FS, Xin J, Smajstrla AG, Carrillo M. 1994. Comparison of soil-moisture sensors and rainfall shutoff devices for computer-based irrigation control. *Computers in Agriculture 1994 - Proceedings of the 5th International Conference*: 864-869

Zhang F, Niu G, Lin X, Jacobson O, Ma Y, Eden HS, He YL, Lu GM, Chen XY. 2012. Imaging tumor-induced sentinel lymph node lymphangiogenesis with LyP-1 peptide. *Amino Acids* **42**(6): 2343-2351. DOI: 10.1007/s00726-011-0976-1

Zhang Y, Lv T, Carvalho PN, Arias CA, Chen ZH, Brix H. 2016. Removal of the pharmaceuticals ibuprofen and iohexol by four wetland plant species in hydroponic culture: plant uptake

and microbial degradation. *Environmental Science and Pollution Research* **23**(3): 2890-2898. DOI: 10.1007/s11356-015-5552-x

Zhang ZY, Ross RD, Roeder RK. 2010. Preparation of functionalized gold nanoparticles as a targeted X-ray contrast agent for damaged bone tissue. *Nanoscale* **2**(4): 582-586. DOI: 10.1039/b9nr00317g